UNIVERSITY OF GENOVA

PHD PROGRAM IN PHYSICS AND NANOSCIENCE

Studies of the Drell-Yan process at the Large Hadron Collider

by

Alessandro Guida

Thesis submitted for the degree of *Doctor of Philosophy*

May 2022

Supervisors: James Ferrando
Simone Marzani

Table of contents

Acknowledgements

I would like firstly to thank DESY and the University of Genova for making this joint Ph.D. programs possible, in particular I acknowledge the special support given by the DESY ATLAS secretariat and the DESY ATLAS group during these years, making this experience almost problem-free.

A special thanks goes to my supervisors James and Simone M., James has always supported and encouraged me at every step of my Ph.D., with him I had illuminating discussion about physics, that helped keeping alive my passion for the subject. He closely and actively followed my work helping in the success of the projects. The same I can say about Simone, he expressed great interest for my work and was always available for discussions. He always promptly acted to answer any request of mine. My analysis team Francesco, Massimo and Uta deserve a special mention for the work with have done together, and the many things I learned during our meetings and the countless chat with Fra. I really enjoyed the stimulating discussions we had , these helped me growing as a scientist. I want to thank all the people participating to the Standard Model group at DESY for the interesting meetings and discussions we had. A particular thank goes to Simone A. Stefano C. Sasha G. and Ludovica for the projects we carried out together.

These years at DESY have been wonderful mainly thanks to all the friends and colleagues I met here in Hamburg. I can't thanks all of them here as the ackmowledgement would be longer than the thesis, but I want to mention Surabhi, Sara, Georgiana and Jan-Hendrik for being the best office mate possible, Jordi for being the funniest person on earth, and Emily for being the smartest of all of them. I can't forget the people in Genova and a special thanks goes to Luca, Enrico, Giulia e Nicola.

Finally I want to thank my family, my mother, my father and my brothers, Claudio e Roberto for being supportive and helping me going through all these years.

Chapter 1

Introduction

The study of the elementary constituents of matter has made exceptional progress in the last century. This has led to the establishment of a unified theoretical framework, the *Standard Model* (SM), that describe the elementary interactions between particles. Three out of the four known forces find a quantum description in this theory, these are: the strong, the electromagnetic and the weak interactions. The experiments conducted at the Large Hadron Collider (LHC) at CERN (Geneva), where proton beams collide at TeV energies, help to test the validity of the Standard Model. The greatest success of these experiments was the discovery in 2012 of the Higgs boson by the ATLAS and CMS collaboration [1, 2]. This new particle fits perfectly in the Standard Model and its observation yielded the final missing piece. The experiments at the LHC have have developed, from their inception, a wide physics program for precision measurements of the SM processes and investigation of possible deviations of the measurement outcomes from the theory.

The experimental conditions in proton-proton collisions can be challenging due to the effects of the strong interaction. This force keeps the proton together as a bound state of quark and gluons. Even though the strong interaction is described successfully inside the Standard Model by the Quantum ChromoDynamics (QCD), the theoretical predictions can be very difficult, not only for the complication of the calculation itself, but also because of some non-perturbative behaviour of the theory that affects the possibility of performing the calculations. Because of the proton composition and the strength of the interaction, QCD effects are important for each LHC measurement and a good understanding of the physics of the collisions is necessary. The primary element to perform any calculation is the knowledge of the structure of the proton in high energy collisions. This information cannot be obtained from first principles, but needs to be extracted from the data. The proton structure is encoded in distribution functions for the different partons (quarks or gluon)

that are interpreted as the probability of finding an interacting parton in the collision with a certain fraction of the proton energy. The parton distribution functions (PDF) are an input for the theoretical calculation of all the processes at the LHC. An important part of the knowledge about PDFs comes from the deep-inelastic-scattering measurements at the HERA collider [3]. The LHC has a wide program of measurements that can help to improve the PDF knowledge and that explores phase space regions that are complementary to the HERA ones. The improvement in the precision of the PDF knowledge is fundamental for present and future measurements at the LHC. The primary process that can be measured at the LHC and that carries information about the PDFs is the Drell-Yan (DY) process. This consists of the creation of a vector boson (γ^*/Z or a $W^{+/-}$) through the annihilation of quark anti-quark pair from the protons. The boson then immediately decays into a lepton pair. While the process is mediated via an electroweak boson (the DY process can be used for a measurement of electroweak parameters in the SM) the kinematics of the final state lepton encodes information on the proton dynamics. Cross section measurements of the DY process can be additional input in the extraction of the parton distribution functions.

Throughout this thesis various studies related to the Drell-Yan process at the LHC are presented. In chapter 3 an overview of the methods for precision QCD calculation of the DY process is reported and a study of the accuracy of the prediction is presented. In particular the effects of fiducial cuts on the accuracy is investigated. Some cut configurations induce a bias in the calculation methods and introduce some instability in the series expansion. A preliminary study of these effects on the PDF determination is also presented.

Starting from chapter 6.5 a measurement of the Drell-Yan process in proton-proton collision at the LHC is presented. The analysis uses data collected with the ATLAS detector in 2015, in collisions at the center of mass energy of $\sqrt{s} = 13\,\text{TeV}$. The measurement is performed in the di-muon channel only and targets a low invariant mass range of the final state, between 7.3 GeV and 56 GeV. In the thesis the measurement will be referred to as *low mass Drell-Yan* measurement. The measured observable are the single differential cross section in the dimuon invariant mass, $m_{\mu\mu}$, and the double differential cross sections in $m_{\mu\mu} - |y_{\mu\mu}|$ and $m_{\mu\mu} - p_T^{\mu\mu}$. This analysis extends to new data a previous ATLAS analysis that used collision data at 7 TeV [4]. The low mass range allows an extreme region of the phase space to be explored and to exploit the full potential of the ATLAS data. In particular, low values of x, where x is fraction of proton momentum carried by interacting partons, are explored. This measurement represents an input to improve the PDF knowledge in this kinematic region, and gives the possibility to test particular non-perturbative dynamics at small-x, such as the BFKL dynamics [5].

The structure of the thesis is the following: in Chapter 2 a review of the Standard Model theory and the physics of proton collisions is presented, as well as an introduction to the Drell-Yan process. Chapter 3 presents a review of the higher order QCD prediction methods for DY process and explores the effects of fiducial cuts on the accuracy of the calculations. In Chapter 4 the LHC and the ATLAS detector are introduced. Chapter 5 focuses on the tracking and reconstruction of muon particles, these will be the final state analysed in the low mass DY measurement. Starting from Chapter 6 the measurement is presented. After an introduction the selection requirements of the analysis are described. In Chapter 7 the methods for the estimation of the background events entering the data selection are described, with a particular focus on the estimation of the background represented by QCD events. In Chapter 8 the modelling of some key physical quantities entering the QCD background estimation method is investigated. Chapter 9 is dedicated to a description of the methods used in the analysis to extract the Drell-Yan cross section from the measurement. In Chapter 10 the systematic uncertainty affecting the measurement are carefully evaluated, while in chapter 11 the cross section results, compared to some theoretical predictions, are presented. Finally chapter 12 is devoted to the conclusion and the discussion of future projects and possible improvements regarding the measurement.

Chapter 2

The Standard Model and proton-proton collision

The Standard Model (SM) refers to the theoretical framework that describes the interaction between elementary particles. The SM provides a coherent description of three of the four forces known in nature. These are referred to as Electromagnetic, weak and strong interactions. An experimentally proved particle-level description of the gravitational interaction is instead still missing. The test of the SM predictions is the purpose of many experiments around the world. At the Large Hadron Collider at CERN, high energy proton beams [1], $E_p \sim 6.5\,\text{TeV}$, collide offering a probe of the interaction at a high energy scale. In previous runs collisions have occurred at 0.9, 2.76, 5.02, 7 and 8 TeV. Collision at 13.6 TeV are planned in 2022 in the upcoming Run3. Multipurpose experiment, such as ATLAS and CMS have been able to observe a wide range of SM processes and measure the related cross-sections. Figure 2.1 shows a summary of total cross-section measurements performed by the ATLAS collaboration and compared to the SM predictions. The measurements produced so far always show a good agreement with the predictions of the theory model. Some discrepancies with respect to the SM predictions are nevertheless observed by some experiments. For example, deviations in the anomalous magnetic momentum of the muon are measured at Fermilab [6], or hint of lepton flavour universality violation are found in the LHCb results [**lhcb-lep-flav-viol2**, 7]. Very recently the CDF experiment published ax precise measurement of the mass of the W boson [8] that is in disagreement with the Standard Model expectation.

In this chapter the main aspects of the SM are presented: section 2.1 presents the quantum chromodynamics, the theory of strong interactions, while section 2.2 focuses on

[1] In dedicate runs, also heavy ions, such as lead, are accelerated.

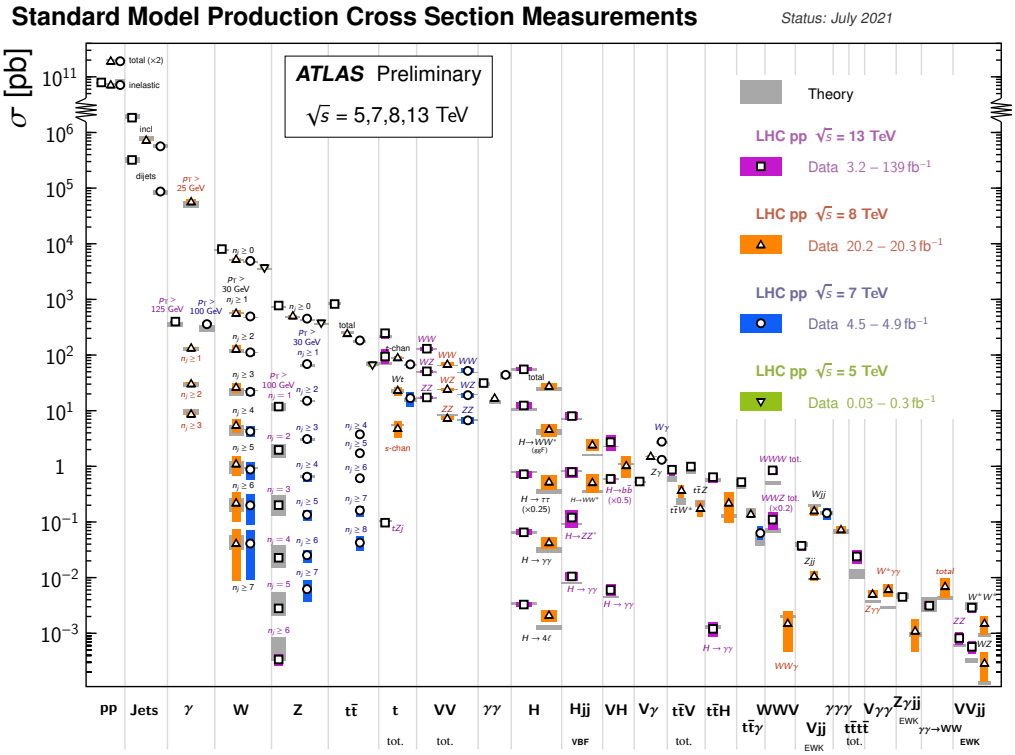

Figure 2.1 Total cross-section measurements performed by the ATLAS collaboration for a wide range of processes and compared to the SM predictions. Image from [9].

the Electroweak interactions, the Higgs boson and process of symmetry breaking of the theory. Next, in section 2.3, the physics of the proton collisions at the LHC is explored, in particular the *parton model*, used to obtain theoretical predictions for the processes, is described. In section 2.4 the Drell-Yan process is introduced, a formulation of the Leading Order differential cross-section is given, and the effects of higher order QCD contributions are also discussed.

2.1 Quantum Chromodynamics

Quantum ChromoDynamics (QCD) is the theory that describes the strong interaction. This interaction arises as a result of requiring the underlying field theory to be invariant under local gauge transformation. The local gauge group is $SU(3)$. The *quarks*, q_i, where $i = 1,2,3$, are interpreted as fundamental representation of $SU(3)$. The new degree of freedom i is referred to as color. Under a local $SU(3)$ transformation the quark fields transform as

$$q_i(x) \to q_i'(x) = (\exp[ig_S\alpha(x)_a T^a])_{ij} q_j(x) \tag{2.1}$$

where g_S is the strong coupling, T^a are the generators of the $SU(3)$ group and $\alpha^a(x)$ are the functions that parameterize the transformation. To write a Lagrangian density that is invariant under such transformations, the covariant derivative is introduced

$$D_\mu q_i = [\partial_\mu + ig_S G_\mu^a T^a] q_i \tag{2.2}$$

G_μ^a, $a = 1,\ldots,8$ are newly introduced vector fields, one for each of the eight $SU(3)$ generators. These are the fields describing the gluon. The definition in eq. 2.2 is covariant if G_μ^a transforms, under local gauge rotation, as

$$G_\mu^a \to G_\mu'^a = G_\mu^a + \partial\alpha^a(x) - g_S f_{abc}\alpha^b G_\mu^c \tag{2.3}$$

where $\alpha^a(x)$ is the same as in eq. 2.1. The last term in the above equation comes out as a consequence of the non-abelian nature of $SU(3)$. The constants f_{abc} describe the commutation relations for the generators: $[T^a, T^b] = if_{abc}T^c$. The Lagrangian density for the QCD is then built combining the quark and gluon dynamic terms

$$\mathscr{L}_{QCD} = \mathscr{L}_{quarks} + \mathscr{L}_{gluons} \tag{2.4}$$

where

$$\mathscr{L}_{quarks} = \sum_f \bar{q}_f(\gamma^\mu D_\mu - m)q_f \tag{2.5}$$

the sum is over the different quark flavours. Every quark carries the same color charge. The gluon term, $\mathscr{L}_{gluons}$, is given by

$$\begin{aligned}\mathscr{L}_{gluons} = -\frac{1}{4}Tr(F_{\mu\nu}F^{\mu\nu}) = &-\frac{1}{4}(\partial_\mu G^a_\nu - \partial_\nu G^a_\mu)(\partial^\mu G^\nu_a - \partial^\nu G^\mu_a) \\ &- g_S f_{abc}(\partial_\mu G^a_\nu)G^{\mu\, b}G^{\nu\, c} \\ &- g_S^2(f_{abc}G^{\mu\, b}G^{\mu\, c})(f_{ade}G^d_\mu G^e_\nu)\end{aligned} \tag{2.6}$$

From equations 2.5 and 2.6 it is possible to identify the quark-gluon vertex and the gluon self interaction vertexes, typical of non-abelian gauge theory. The QCD framework is similar to the Electromagnetic one, but the behaviour of the theory is rather different. Two of the most important aspects of QCD, confinement and asymptotic freedom, are presented in the next sections.

2.1.1 Confinement and Hadronisation

Even though much experimental evidence for the existence of quarks and gluons has been obtained, no free quark has ever been observed. This fact is explained with the hypothesis of *color confinement* according to which, colored objects are confined in color singlet states (hadrons) and no particle with non zero color charge can freely propagate. Confinement is explained qualitatively by fact that the energy stored in the field between two quarks, because the exchanged gluons self interact, increases linearly with the distance between the particles

$$V(r) \sim kr \tag{2.7}$$

with $k \sim 1\,\mathrm{GeV}/\mathrm{fm}$. As a result, quarks, when pulled apart, have enough energy to recombine into new hadron states.

This phenomena is observed in high energy collision experiments where highly energetic quarks and gluons produce jets of colorless hadrons in the final state. Hadronisation is a non-perturbative process and its details are poorly understood. Various phenomenological models, with many free parameters tuned to data measurements, are able however to give a reasonable description of the experiments.

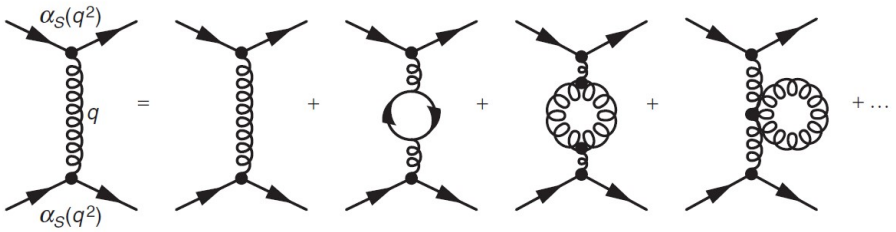

Figure 2.2 The renormalization of the coupling correspond to absorb the loop contribution into a redefinition of the coupling.

2.1.2 Asymptotic freedom of QCD

Experimentally, QCD shows the behaviour of being quasi-free at high energy. This means that the coupling, $\alpha_S = g_S^2/4\pi$, in the Lagrangian equations 2.5, 2.6 is not the same as the one measured experimentally. This is because the values in the Lagrangian correspond to the coupling value in tree level diagrams, but experimentally one measures contributions from all perturbative orders. Theoretically it is then needed to consider QCD contributions beyond the leading order, this leads to the problem of divergent diagram contributions. In particular the loop diagrams diverge in the upper limit of infinite momentum flowing inside the loop. These singular contributions are called ultraviolet divergences. The problem is solved by putting an upper cut-off energy M on the momentum integration and absorbing the loop contribution above an arbitrary energy scale μ into a re-definition of the coupling. After that, the upper cut-off M can be freely sent to infinity. This procedure of cancellation of the infinities is called *renormalization*. A schematic depiction of renormalization is shown in Figure 2.2, where an infinite series of one loop divergent diagrams are absorbed into the value of the coupling. If all the higher order diagrams were divergent, the theory could not be used to make any prediction. In a renormalizable field theory, only a certain class of diagrams is actually divergent and the renormalization can be applied systematically, recovering prediction power.

As a consequence of renormalization, the coupling acquires a dependence on the energy scale of the process, Q. This dependence is governed by the renormalization group equation

$$\frac{d}{d\ln(Q^2)}\alpha_S = \beta(\alpha_S(\mu^2)) \tag{2.8}$$

where

$$\beta(\alpha_S) = -\alpha_S^2(\beta_0 + \beta_1\alpha_S + \beta_2\alpha_S^2 + \ldots) \tag{2.9}$$

and the power expansion coefficients β_i are calculable by considering the loop contribution absorbed into the coupling definition. Equation 2.9 shows as β is non zero only at order α_S^2, reflecting that the Q^2 dependence appears only at loop level. The diagrams contributing to β_0, for example, are the quark and gluon loop in Figure 2.2 and the β_0 value is equal to

$$\beta_0 = \frac{1}{12\pi}(11N_c - 2N_f) \tag{2.10}$$

where N_c is the number of colors and N_f is the number of flavours. Considering $N_c = 3$ and $N_f = 6$, $\beta_0 = 21/12\pi$. In particular the negative contribution eventually comes from the gluon diagrams while the quark loops contribute positively. Substituting in equation 2.8

$$\frac{d}{d\ln(Q^2)}\alpha_S = -\beta_0\alpha_S^2 \tag{2.11}$$

this can be easily integrated, obtaining

$$\alpha_S(Q^2) = \frac{\alpha_S(\mu^2)}{1+\beta_0\alpha_S(\mu^2)\ln(Q^2/\mu^2)} \tag{2.12}$$

This first order solution corresponds to the procedure of absorbing the one loop contribution, at each order, shown in Figure 2.2. Because β_0 is positive, eq. 2.10, α_S is decreasing in Q^2, that means, the coupling gets smaller when Q increases. This property is called *asymptotic freedom* of QCD. The sign of β_0 is crucial for this behaviour. In the case of QED the loop contributions to β_0 come only from the the leptons, as the photon doesn't self interact. β_0 is then negative and the energy dependence is the opposite, α_{QED} decreases as Q increases. The asymptotic freedom of QCD confirms the validity of perturbative calculations when considering high energy processes. When the scale of process becomes too small, around $\sim 1\,\text{GeV}$, the perturbative expansion is no longer valid.

2.2 Electroweak Interactions

Electroweak interactions are based on the symmetry gauge group $SU(2)\times U(1)$. This, together with the $SU(3)$ group of QCD, completes the picture of the SM symmetry group that is: $SU(3)\times SU(2)\times U(1)$. As in the case of the QCD, the interaction arises as a result of requiring the theory to be invariant under local transformations of the group. This introduces the gauge bosons W_μ^i, $i = 1,2,3$ for $SU(2)$ and B_μ for $U(1)$, as well as two couplings, g' and g, for the two groups respectively. The left-handed fermions are organized into $SU(2)$

doublets

$$\Psi_i = \begin{pmatrix} \nu_i \\ l_i^- \end{pmatrix} \text{ or } \begin{pmatrix} u_i \\ d_i' \end{pmatrix} \tag{2.13}$$

where the index i goes on the different lepton and quark flavours. d_i' are the electroweak quark eigenstates, these are related to the mass eigenstates through the Cabibbo-Kobayashi-Maskawa matrix [10, 11], $d_i' = \sum_j V_{ij} d_j$. The right handed fermions are instead $SU(2)$ singlets.

Additionally, as a way to generate the particle mass terms, a scalar Higgs doublet is considered

$$\phi = \begin{pmatrix} \phi^+ \\ \phi^- \end{pmatrix}. \tag{2.14}$$

The Higgs potential is given by

$$V(\phi) = \mu^2 \phi^\dagger \phi + \frac{\lambda^2}{2} (\phi^\dagger \phi)^2 \tag{2.15}$$

in the case of negative μ^2, the field has non zero vacuum expectation equal to $v/\sqrt{2} = \mu/\lambda$ where $v \simeq 246\,\text{GeV}$. Expanding ϕ around the minimum

$$\phi_0 = \frac{1}{\sqrt{2}} \begin{pmatrix} 0 \\ v \end{pmatrix} \tag{2.16}$$

and making use of the $SU(2)$ symmetry, one can write the field ϕ as

$$\phi = \frac{1}{\sqrt{2}} \begin{pmatrix} 0 \\ v + H(x) \end{pmatrix} \tag{2.17}$$

where $H(x)$ is the neutral Higgs scalar field. This leads to a partial breaking of the gauge symmetry and the appearing of gauge boson mass terms in the Lagrangian

$$\mathscr{L}_{mass} = |ig' \frac{1}{2} W_\mu^i \phi_0| = \frac{g'^2}{8} v^2 [(W_\mu^1)^2 + (W_\mu^2)^2 + (W_\mu^3)^2] \tag{2.18}$$

plus additional terms of interactions between the gauge bosons and the Higgs field.

A gauge symmetric Yukawa coupling term between the fermions and the Higgs doublet can also be added, generating mass terms for the leptons and quarks. In particular, after the

symmetry breaking, the Lagrangian for the fermion fields ψ_i is

$$\begin{aligned}\mathscr{L}_F = &\sum_i \bar{\psi}_i(i\gamma^\mu\partial_\mu - m_i - \frac{m_i H}{v})\psi_i \\ &- \frac{g}{2\sqrt{2}}\sum_i \bar{\psi}_i\gamma^\mu(1-\gamma^5)(T^+W_\mu^+ + T^-W_\mu^-)\psi_i \\ &- e\sum_i Q_i\bar{\psi}_i\gamma^\mu\psi_i A_\mu \\ &- \frac{g}{2\cos\theta_W}\sum_i \bar{\psi}_i\gamma^\mu(g_V^i - g_A^i\gamma^5)\psi_i Z_\mu\end{aligned} \tag{2.19}$$

Where the index i represent the different flavours. ψ are the Dirac spinors, for the electron for example, $\psi_e = \binom{e_L}{e_R}$. Here $\theta_W = \tan^{-1}(g'/g)$ is the weak angle; $|e| = g\sin\theta_W$ is the electric charge. The photon field A and the neutral and charged current boson fields, Z and $W^{+/-}$, are linear combination of the previously mentioned B and W^i $i = 1,2,3$, fields

$$\begin{aligned}A &= B\cos\theta_W + W^3\sin\theta_W \\ Z &= -B\sin\theta_W + W^3\cos\theta_W \\ W^\pm &= (W^1 \mp iW^2)/\sqrt{2}\end{aligned} \tag{2.20}$$

The first line in the Lagrangian contains the Yukawa coupling between the Higgs field and the fermions. The second line of equation 2.19 describes the charged current interaction, T^+ and T^- are the weak isospin raising and lowering operator and allows a compactness of the formula. The third line describes the Electromagnetic interactions with Q_i the charge in units of $|e|$. The last line is the Neutral Current term, the axial and vector coupling are given by

$$\begin{aligned}g_V^i &= t_{3L}^i - 2Q_i\sin^2\theta_W \\ g_A^i &= t_{3L}^i\end{aligned} \tag{2.21}$$

where t_{3L}^i is the weak-isospin of the fermion i and is $+1/2$ for u_i and ν_i while $-1/2$ for d_i and e_i.

The boson masses of the EW sector, at leading order in perturbation theory, are given by

$$\begin{aligned} M_H &= \lambda v, \\ M_W &= \frac{1}{2} g v = \frac{ev}{2\sin\theta_W}, \\ M_Z &= \frac{1}{2}\sqrt{g^2+g'^2}\, v = \frac{ev}{2\sin\theta_W\cos\theta_W} = \frac{M_W}{\cos\theta_W} \\ M_\gamma &= 0 \end{aligned} \tag{2.22}$$

2.3 Proton collisions at the LHC

At the LHC, proton beams are accelerated at high energy and collided. The proton is not a fundamental particle itself but it is composed of a bound state of valence quarks, two u quarks and one d quark, plus, as will be discussed later, a sea of other flavour quarks, antiquarks and gluons. The proton constituents in this context are also referred as *partons*. When the protons collide the constituent partons interact, some of these interactions happen with the exchange of high transverse momentum, meaning that perturbative QCD is applicable. In general, the SM theory presented in the previous sections can be expanded perturbatively in power series of the couplings and used to calculate the cross-section of elementary particle interactions. Various ingredients are then needed to produce a prediction at the level of the hadronic interactions. One of the most important is the so called parton model, firstly introduced in the 70s, that prescribes a way to connect the parton cross section, $\hat{\sigma}$, for a certain process, to the inclusive proton-proton cross section, σ_{pp}. The latter is obtained by weighting the the parton cross section by some density functions, $f_{q/g}$, called parton density functions (PDFs), giving the formula:

$$\sigma_{pp} = \sum_{ab} \int_0^1 dx_1 dx_2\, f_a(\mu_F^2, x_1) f_b(\mu_F^2, x_2)\, \hat{\sigma}_{ab} \tag{2.23}$$

where the sum is over all possible proton constituents. In the equation above, the PDFs, $f_{a/b}$, are functions of $x_{1/2}$ that is the fraction of proton momentum carried by the parton a/b, $p_{a/b} = x_{1/2} P_{1/2}$. At leading order, the PDFs can be interpreted as the probability of finding, in a proton with momentum P, a particular quark or a gluon with momentum xP. The PDFs in eq. (2.23) depends also on μ_F^2, an energy scale called the factorization scale. This dependence is a consequence of the QCD corrections to the parton cross section calculations, in particular it arises after a renormalization of divergent contributions to the parton cross-section. More details about the PDFs renormalization are examined in the case of a particular process, the

Drell-Yan process, in section 2.4.2. The value of this scale is, in principle, arbitrary, but to avoid spoiling the perturbative calculation it is chosen equal to the energy scale of the process under analysis.

The PDFs are intrinsically non perturbative and they need to be inferred from experimental observations. The applicability of equation 2.23 depends on the assumption that the PDFs values are *universal* for the proton structure, that means: they can be evaluated from the measurement of a particular process and then used with the equation (2.23) for the prediction of any other process. The strongest inputs for the PDF evaluation come from the deep inelastic scattering (DIS) experiments performed at the HERA collider (an electron-proton collider in operation between 1992 and 2007). In deep inelastic scattering processes a highly energetic electron interacts with a proton through the exchange of an electroweak boson (Z/γ or W). The kinematics of the outgoing electron after the collision give sensitivity to the proton PDFs and allows their determination. The procedure for the PDFs evaluation consists firstly of a parametrization of the functions and then a fit to the data to find the parameters values that best describe the experimental observations. Measurements from other experiments, for example Drell Yan related measurements at Tevatron or LHC, can be included in a global fit together with the HERA data to obtain further constraints on PDFs.

2.4 The Drell-Yan Process

The Drell-Yan (DY) mechanism in hadron-hadron collisions consists of the production of a lepton pair by quark-antiquark annihilation. The name comes from Sidney Drell and Tung-Mow Yan who first introduced the process in 1970 [12]. The quarks annihilate into a virtual photon (γ^*) that decays into the lepton pair ($q\bar{q} \rightarrow \gamma^*/Z \rightarrow l^+l^-$). The diagram of the process is depicted in Figure (2.3). The lepton production is dominated by the photon channel when the invariant mass of the leptons is much lower than the mass of the Z boson ($M_{ll} \ll M_Z$). When M_{ll} approaches M_Z, the Z production resonance starts to interfere in the lepton pair production, and fast becomes dominant. The Drell-Yan process is in fact the main mechanism for production of the Z boson at the LHC. The dilepton production through a boson Z/γ^* decay is also referred the Neutral Current (NC) Drell Yan (due to the neutrality of the boson mediator). A similar process is the Charged Current (CC) Drell Yan in which a quark-antiquark pair annihilates producing a charged boson $W^\pm$ that can decay into a lepton and neutrino pair ($W^- \rightarrow l^-\bar{\nu}$, $W^+ \rightarrow l^+\nu$). Measurements of $W^\pm$ production observables, such as the charge asymmetry in the production, are very important because they are strongly related to the proton structure. Theoretical predictions for DY processes are available at

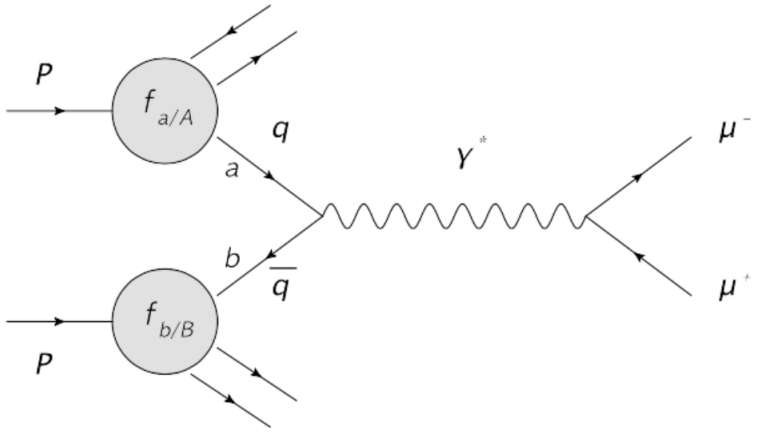

Figure 2.3 Leading order contribution to the Drell-Yan process.

Next-to-next-to-Leading Order (NNLO) in QCD correction [13, 14], and recently also N3LO [15], and up to NLO in ElectroWeak corrections.

2.4.1 The Low Mass Drell-Yan process

In the low mass region, far from the Z peak resonance, the DY process is mediated by the virtual photon only. In this section the leading order DY cross-section is presented.

The lowest order parton level cross-section for a quark-antiquark annihilation into a lepton pair is given by

$$\hat{\sigma}\left(q(p_1)\bar{q}(p_2) \to l^+l^-\right) = \frac{4\pi\alpha^2}{3\hat{s}}\frac{1}{N_c}Q_q^2 \tag{2.24}$$

where $\hat{s} = (p_1 + p_2)^2$ (i.e. the parton energy collision), Q_q is the quark charge and α is the electromagnetic coupling. The factor $1/N_c = 1/3$ comes out averaging over the initial colour states of the quarks. The related diagram is shown in Figure 2.4. The center of mass energy of the interacting quarks, $\sqrt{\hat{s}}$, is equal to the invariant mass, M, of the lepton pair. The cross section of producing a lepton pair of mass M in then given by

$$\frac{d\hat{\sigma}}{dM} = \frac{\hat{\sigma}_0}{M}Q_q\delta(\hat{s} - M^2), \qquad \sigma_0 = \frac{4\pi\alpha^2}{3M^2}. \tag{2.25}$$

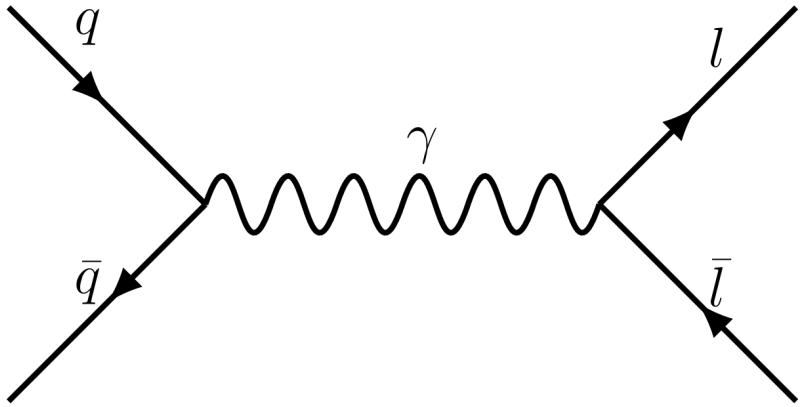

Figure 2.4 Leading order contribution to the Drell-Yan partonic process.

Considering the proton-proton collisions at centre of mass energy s, the partons involved in the process carry the momentum fractions x_1 and x_2, and their momentum are given by

$$p_1 = \frac{\sqrt{s}}{2}(x_1,0,0,x_1), \qquad p_2 = \frac{\sqrt{s}}{2}(x_2,0,0,-x_2). \tag{2.26}$$

Thus the relation between the proton collision energy s and the partons collision energy $\hat{s}$ is

$$\hat{s} = (p_1 + p_2)^2 = x_1 x_2 s. \tag{2.27}$$

To obtain the proton-proton cross section of the process we need to substitute the parton cross section in equation (2.25) in the parton model formula, equation (2.23), obtaining

$$\begin{aligned} \frac{d\sigma}{dM^2} &= \int_0^1 dx_1 dx_2 \sum_q \{f_q(x_1) f_{\bar{q}}(x_2) + (q \leftrightarrow \bar{q})\} \frac{d\hat{\sigma}}{dM^2}(q\bar{q} \to l^+ l^-) \\ &= \frac{\sigma_0}{N_c} \int_0^1 dx_1 dx_2 \, \delta(x_1 x_2 s - M^2) \sum_q Q_q^2 \{f_q(x_1) f_{\bar{q}}(x_2) + (q \leftrightarrow \bar{q})\} \end{aligned} \tag{2.28}$$

The PDFs, $f_{q/\bar{q}}$, in the formula above are independent of M^2 because the QCD corrections are not yet considered. This fact is approximately observed in experiment and is known as scaling. Multiplying both sides of equation (2.28) by M^4, it is possible to express the cross

section as a function of the scaling variable $\tau = M^2/s$ only

$$\begin{aligned} M^4 \frac{d\sigma}{dM^2} &= \frac{4\pi\alpha^2}{3N}\tau \int_0^1 dx_1 dx_2\, \delta(x_1 x_2 - \tau) \sum_q Q_q^2 \{f_q(x_1) f_{\bar{q}}(x_2) + (q \leftrightarrow \bar{q})\} \\ &= \frac{4\pi\alpha^2}{3N}\tau \mathscr{F}(\tau) \end{aligned} \tag{2.29}$$

Experiments show that the DY structure function $\mathscr{F}$ is approximately independent from M and depends only on the scaling variable τ. Violation of this behaviour are explained by including higher-order QCD in the calculation.

Another observable in the experiments is the rapidity y of the lepton pair. The rapidity is often use in the parametrization of a particle four-momentum

$$\begin{aligned} p^\mu &= (E, p_x, p_y, p_z) \\ &= (m_T \cosh y, p_T \sin\phi, p_T \cos\phi, m_T \sinh y) \end{aligned} \tag{2.30}$$

where $m_T = \sqrt{p_T^2 + m^2}$ is the transverse mass. The rapidity is defined by

$$y = \frac{1}{2} \ln\left(\frac{E + p_z}{E - p_z}\right) \tag{2.31}$$

The rapidity is introduced as it is additive under Lorentz boost along the z beam line axis and rapidity differences are invariant under such a transformation. Combining eq. 2.26 and 2.32 the rapidity of the dilepton system is expressed as a function of the fraction x_1 and x_2

$$y = \frac{1}{2} \ln\left(\frac{x_1}{x_2}\right) \tag{2.32}$$

and inverting the above equation

$$x_1 = \sqrt{\tau}\exp(y), \qquad x_2 = \sqrt{\tau}\exp(-y). \tag{2.33}$$

The double differential cross section in mass and rapidity is then given by

$$\frac{d^2\sigma}{dy\,dM^2} = \frac{\sigma_0}{Ms} \sum_q Q_q^2 \{f_q(x_1) f_{\bar{q}}(x_2) + (q \leftrightarrow \bar{q})\}. \tag{2.34}$$

Knowing the value of the PDFs, extracted from Deep Inelastic experiments for example, allows us to calculate the DY differential cross-section. Alternatively, a DY measurement

(a) NLO virtual contributions

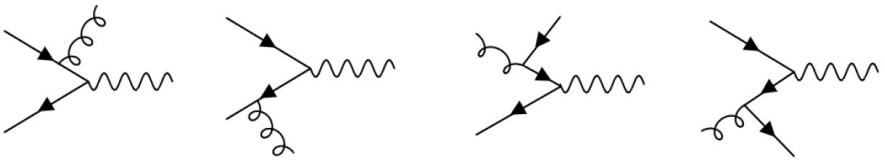

(b) NLO real contributions

Figure 2.5 NLO QCD diagram contributions to the DY process.

itself can be used to constrain the values of the PDFs. and it shows how this quantity is directly related to the quark-antiquark distribution functions. The measurements can provide information on the u- and d-quark valence PDFs [16] and the light-quark sea PDFs, in particular on the s- over $\bar{d}$-quark ratio [17].

The scaling property mentioned in the previous section is only approximate in experiment results, the violation is explained by including higher order QCD correction in the calculation and is ultimately a proof of the QCD theory.

2.4.2 Higher Order QCD Correction

The NLO QCD correction to the DY process regards only the initial state, as the final state leptons have zero color charge. The QCD diagrams are shown in Figure 2.5. The NLO contribution presents three different classes of divergences. Ultraviolet divergences in virtual loops Figure 2.5a, infrared divergences in real and virtual gluon emission in the limit of soft emission, $k^{\mu} \to 0$, and collinear divergences in the $q \to gq$ and $g \to gq$, diagrams Figure 2.5b. Collinear emission refers to the fact that the particle is emitted at small angle. Ultraviolet divergences are treated with the renormalization of the physics parameters. Infrared divergences cancel out when the real and virtual contributions are added together, this happens at each order according to the Kinoshita, Lee, Nauenberg theory [18, 19]. The only divergent contribution that fails to cancel is the collinear term. The treatment of these infinities happens with a new renormalization process in which the PDFs are redefined absorbing the emission terms. This procedure is conceptually similar to the renormalization of the UV singularities: the bare PDFs consider just the leading-order contribution, but what

is measured in the experiments are the renormalized PDFs. This renormalization is possible because the collinear emissions factorize, at each perturbative order, with respect to the cross section and can be absorbed in the PDFs preserving their universality property. The factorisation has been demonstrated for the DY process and few other processes but it is generally assumed when calculating predictions for every process. The collinear emissions are described by the splitting functions $P_{q_i q_j}$. These are the finite part of the term that factorise in the limit of collinear emissions. This is related to the probability that a parton q_i turns into a parton q_j after emitting a third collinear particle. The splitting function are expanded in series of α_S

$$P(z) = P^{(0)}(z) + \frac{\alpha_S}{2\pi} P^{(1)}(z) + \dots \tag{2.35}$$

At leading order the splitting functions are

$$\begin{aligned}
P_{qq}^{(0)}(x) &= C_F \left[\frac{1+x^2}{(1-x)_+} + \frac{3}{2}\delta(1-x) \right], \\
P_{qg}^{(0)}(x) &= T_R \left[x^2 + (1-x)^2 \right], \\
P_{gq}^{(0)}(x) &= C_F \left[\frac{1+(1-x)^2}{x} \right], \\
P_{qg}^{(0)}(x) &= 2C_A \left[\frac{x}{(1-x)_+} + \frac{1-x}{x} + x(1-x) \right] + \delta(1-x)\frac{11C_A - 4n_f T_R}{6}
\end{aligned} \tag{2.36}$$

where x is the fraction of longitudinal momentum carried by the emitted particle. The factors $C_F = \frac{4}{3}$, $C_A = 3$, $T_R = \frac{1}{2}$ are related to the geometrical properties of the $SU(3)$ group. The $+$ in some terms indicates the behaviour of the function when integrated with a smooth function

$$\int_0^1 \frac{f(x)}{(1-x)_+} = \int_0^1 dx \frac{f(x) - f(1)}{1-x}. \tag{2.37}$$

The $+$ distribution are residuals of the soft divergences cancellation. The PDFs renormalization introduces a new arbitrary factorisation scales, μ_F. This scale is unphysical and the results should not depend on it. The dependence of the PDFs on μ_F is not arbitrary but is related to the splitting function and is described by the PDFs renormalization group equation of DGLAP equation

$$\mu_F^2 \frac{\partial}{\partial \mu_F^2} f_i(x, \mu_F^2) = \frac{\alpha_S}{2\pi} \int_x^1 \frac{d\xi}{\xi} P\left(\frac{x}{\xi}\right) f_i(\xi, \mu_F) \tag{2.38}$$

The PDFs are extracted from data at a certain energy scale, and are then propagated to another different scale using the DGLAP equation.

2.5 Resummation

In some regions of the phase space the cancellation between virtual and real emission singularities happens only partially. An example in the Drell-Yan case is when the transverse momentum of the vector boson is much smaller than its mass, $p_T^{\gamma*/Z} \ll M$. In general when two energy scales describing the processes are very different, large logarithms L in the ratio of the two scales appear. In the vector boson transverse momentum case, the logarithms are given by

$$L = \ln\left(\frac{M}{p_T^{\gamma*/Z}}\right). \tag{2.39}$$

The order n in α_S is accompanied by a large coefficient of order L^{2n}. If L is large enough, $\alpha_S L^2 > 1$ and this spoils the convergence of the series. The cross section in these enhanced phase space regions has the structure

$$\sigma(L) \simeq \sigma_{\text{tot}} \sum_{n=0}^{\infty} \sum_{k=0}^{2n} R_{nk} \alpha_S^n L^k \tag{2.40}$$

The converge of the series can be improved with *resummation*. This procedure makes use of known properties of the matrix element in the case of multiple emissions, and the universal structure of the singularities to include the log contributions in calculation at each perturbative order. The accuracy of the procedure depends on the order of the logarithms considered. A leading log (LL) resummation include contributions with $k = 2n$ in the formula above, next-to-leading log (NLL) contributions with $k = 2n-1$, *etc*. A typical result to carry out the resummation is *exponentiation*, the cross section can be written as

$$\sigma(L) \simeq \sigma_{\text{tot}} \exp\left[\sum_{n=1}^{\infty} \sum_{k=0}^{n+1} G_{nk} \alpha_S^n L^k\right], \qquad L \gg 1. \tag{2.41}$$

Exponentiation is a powerful result, the knowledge of G_{12} in the formula for example, allows resummation of the full LL series of equation 2.40.

2.6 Monte Carlo event generators for proton-proton collisions

When calculating theoretical predictions for high energy physics processes, Monte Carlo (MC) techniques are often used. In general the outcome of a certain observable $\langle O \rangle$ is given

by an integral of the type

$$\langle O \rangle = \int d\Phi_n \frac{d\sigma}{d\Phi_n} O(\Phi_n) \tag{2.42}$$

the cross section $d\sigma/d\Phi_n$ is calculated with the parton model, equation 2.28. This step already presents the problem of cancellation of the soft and collinear divergences. Different techniques have been developed to deal with these divergences. These will be discussed in the next chapter where a benchmark study of prediction for the Drell-Yan process at NNLO in QCD is presented. The integration over the n-particles phase space is a multi-dimensional problem and MC techniques are used. The integration is approximated as

$$\langle O \rangle \propto \frac{1}{N} \sum_{i}^{N} \frac{d\sigma_n}{d\Phi_n} \left(\Phi_n^i\right) O(\Phi_n^i), \tag{2.43}$$

the phase space events Φ_i are extracted with MC random generators. When generating proton-proton collision events, the extracted events are stored and together with the weights $d\sigma_n/d\Phi_n$ offer a simulation of the kinematics of the final state particles that can be used to calculate any observable $\langle O \rangle$ afterwards.

In section 2.4.2 it was discussed how the emission of collinear and soft partons in QCD is enhanced. To have a reasonable description of the data, it is necessary to include these contributions, at least in the enhanced limit, at each pertubative order. This can be done analytically for particular observables (see also section 2.5), or with the *parton shower* formalism in event generator. The latter fits well in event generators. The parton shower iteratively adds emissions, from the hardest to the softest, to the event and allows evolution of the system from an energy scale t_0 to a scale t. The starting scale is that of the hard scale of the process and the shower continues until $t \sim 1\,\text{GeV}$, a scale at which perturbative QCD is no longer valid and the process of hadronization takes place. The probability of emitting a parton is described by the *splitting function* in equation 2.36 and the evolution problem is actually equivalent to that of solving the DGLAP equation 2.38. Formally the parton shower gives a solution that resums the leading logarithm contributions at each perturbative order. These logarithms arise when integrating the splitting functions over the phase space. The cross section, in the soft limit, has the structure

$$\sigma \sim \sum_{i=0}^{\infty} \sum_{j=0}^{2i} \alpha_s^i \log^j \frac{t_i}{t_{i-1}} \tag{2.44}$$

where t_i and t_{i-1} are the energy scales of the current and the previous emission. The Leading Logarithms (LL) that are resummed by the parton shower in the evolution between the scales

t_{i-1} and t_i are

$$\sigma^{LL} \sim \sum_i \alpha_s^i \log^{2i} \frac{t_i}{t_{i-1}}. \tag{2.45}$$

A *backward* evolution parton shower algorithm is also used, to implement the shower of parton in the initial state. Here the hard scale of the process is fixed, for example the vector boson invariant mass in the Drell-yan case, and the scale evolution is performed backward, $t_0 > t$.

The next step to obtain a description of the events is hadronization of the partons and subsequent hadron decays. Various models have been developed [20]. After a tuning of parameters to the data, they offer a reasonable description of $p-p$ collision events. Further particle production in the events is related secondary parton interactions, these are referred to as underlying events, and are particularly important when simulating and measuring jets related observable [21, 22].

Chapter 3

High precision Drell-Yan predictions

The level of accuracy reached by the high energy physics experiments imposes the need for high precision in the theoretical predictions. The prime process for precision benchmarking is the Drell-Yan process, this can be both measured and predicted with high accuracy. The calculation needs to take into account extra radiation in the final state and the most important contribution comes from QCD radiation. The experimental results are often extracted within the fiducial region, that corresponds to the application of kinematic cuts on the final state leptons. For a meaningful comparison with the experimental data, the prediction must also implement fiducial cuts. To do this the fully exclusive cross-section for the vector boson production is needed. This is known up to NNLO in QCD for Drell-Yan process [23, 24, 25]. The NNLO calculation considers up to two additional emissions and must deal with the cancellation of the related soft and collinear singularities. To this purpose two main approaches have been developed. These are often referred to as *slicing* and *local* singularity subtraction schemes. Thanks to the success of these methods, the NNLO QCD accuracy for DY is now the state of the art and the predictions can be obtained with various public codes [24, 25, 26, 27]. More recently also inclusive N3LO results have been obtained [15]. Despite the level of precision claimed by the NNLO codes, it has been noticed that the results differ between each other by an amount that can reach the percent level. This has been noticed for example by the ATLAS collaboration in performing the W/Z cross section measurement at 7 TeV [17]. The disagreement is understood to be related to the presence of fiducial cuts applied to final state leptons and the different subtraction schemes adopted in the calculation [28, 29]. The disagreement can be as high as few percent, in some cases this is of the same order as the pure NNLO correction term and, most importantly, is not negligible compared to the experimental uncertainty of some DY measurements. In the case of the ATLAS W/Z measurement mentioned above, for example, the maximum precision

reached is of 0.5%. These differences in the theory predictions can have an impact on PDF extraction where Drell-Yan differential measurements play an important role in constraining the $u-$ and $d-$quark valence distributions.

In this chapter a benchmark study of predictions for the DY process produced with different codes adopting different subtraction schemes is reported. In section 3.1 the idea behind the different subtraction approaches is described. In section 3.1.2 the problem of linear power correction that biases the results of slicing methods, in the presence of fiducial cuts, is explored. The results of the benchmark comparison are reported in section 3.2. The predictions are produced in the fiducial region used in the ATLAS W/Z 7 TeV cross section measurement [17]. The same calculations are used in section 3.3 for a PDF study where the agreement of the predictions in combination with different PDFs and the data is assessed.

3.1 Subtraction methods

In section 2.4.2, Figure 2.5, the different diagrams contributing to the NLO QCD correction for the DY process were presented; in general, two kind of terms are identified: virtual loop correction to the LO vertex and real emission correction. Both contributions present collinear and soft (or infrared (IR)) singularities. General results guarantee the cancellation of the IR singularity when summing up the two contribution [19, 18], and the universal factorisation of the collinear poles, that can be absorbed into a renormalization of the PDFs. These results are valid at each perturbative order. At NNLO the classes of divergent contributions are three: double real emission, real-virtual contribution, and double loop correction. Despite the cancellation of the IR singularities the problem of calculating the exclusive cross section is challenging: fully analytical results for a general phase space integration are not available and numerical results cannot be applied straightforwardly due to the divergent nature of the integrand. In the virtual and real correction terms, the number of final state particles is different, and the phase space integration has to be performed separately, preventing direct cancellation in the sum of the two terms. Two classes of techniques, *local subtraction* and *slicing* methods, have then been developed to isolate and regularize the divergent terms in the integrands. In the next sections the idea behind the two methods is presented.

3.1.1 Slicing methods

Slicing methods identify an IR safe observable that resolves additional emissions. This observable is used to slice the phase space integration into two regions, one containing the

singular term and the other in which the cross section is regular. The regular part can be integrated safely using standard techniques, the singular part is instead approximated thanks to the known universal structure of the singularities.

Typical observables are the transverse momentum q_T of a color singlet [23],[30] and N-jettiness [31]. In the Drell-Yan process q_T is the transverse momentum of the vector boson. The slicing parameter is usually defined as

$$\tau = \frac{q_T^2}{Q^2} \tag{3.1}$$

Q^2 is the hard scale of the born level process, the invariant mass of the exchanged boson in the DY case. When $\tau \to 0$ the cross section $d\sigma/d\tau$ reaches the singular limit. The cross section integration is sliced by introducing a threshold value τ_{cut}

$$\sigma = \int_0^{\tau_{\text{cut}}} \mathrm{d}\tau \frac{\mathrm{d}\sigma}{\mathrm{d}\tau} + \int_{\tau_{\text{cut}}} \mathrm{d}\tau \frac{\mathrm{d}\sigma}{\mathrm{d}\tau} \tag{3.2}$$

The first term in the right hand side contains the singular term, while the second term is regular and can be integrated with standard techniques. The integrand, $d\sigma/d\tau$, can be divided into two contributions, the singular one, that contains the singular contribution as $\tau \to 0$ and a non-singular one

$$\frac{d\sigma}{d\tau} = \frac{d\sigma^{\text{sing}}}{d\tau} + \frac{d\sigma^{\text{nonsing}}}{d\tau}. \tag{3.3}$$

The slicing method relies on the fact that the singular contribution, that dominate the low τ integration part, can be predicted from the factorisation theorem, the structure of the IR singularities and the KLN theorem. The structure is of the type

$$\frac{d\sigma^{\text{sing}}}{d\tau} \sim \delta(\tau) + \sum_i \left[\frac{\ln \tau}{\tau}\right]_+ \tag{3.4}$$

The + distribution, whose definition was given in equation 2.37, indeed represents the structure of the cancellation between the real and virtual IR divergences. This knowledge can be used to approximate the cross section at low τ. Integrating the singular term up to the threshold τ_{cut} one obtains something of the order

$$\sigma^{\text{sing}}(\tau_{cut}) = \int_0^{\tau_{cut}} \frac{d\sigma^{\text{sing}}}{d\tau} \sim 1 + \sum_{j\geq 0} \ln^{j+1} \tau_{\text{cut}}. \tag{3.5}$$

σ^{nonsing} instead includes terms that are at least τ integrable, or that go to zero when $\tau \to 0$. The structure is of type

$$\begin{aligned} \frac{d\sigma^{\text{nonsing}}}{d\tau} &\sim \sum_{m>0}\sum_{j\geq 0} \tau^{m-1}\ln^j \tau \\ \sigma^{\text{nonsing}}(\tau_{\text{cut}}) &= \int_0^{\tau_{\text{cut}}} d\tau \frac{d\sigma^{\text{nonsing}}}{d\tau} \sim \sum_{m>0}\sum_{j\geq 0} \tau^m \ln^j \tau \sim O(\tau) \end{aligned} \tag{3.6}$$

These are considered power corrections ($O(\tau_{\text{cut}}^m)$, $m>0$) to the singular term. The cross section in eq. 3.2 is calculated by adding and subtracting a subtraction term σ^{sub}

$$\sigma = \sigma^{sub}(\tau_{\text{cut}}) + \int_{\tau_{\text{cut}}} d\tau \frac{d\sigma}{d\tau} + \Delta\sigma^{sub}(\tau_{\text{cut}}). \tag{3.7}$$

$\sigma^{sub}(\tau_{\text{cut}})$ approximates the cross section at low τ, while the term $\Delta\sigma^{sub}(\tau_{\text{cut}}) = \sigma(\tau_{\text{cut}}) - \sigma^{sub}(\tau_{\text{cut}})$, that is neglected when doing the computation, represents the error of this approximation. $\sigma^{sub}(\tau_{\text{cut}})$ should include at least the singular term of equation 3.5,

$$\sigma^{sub}(\tau_{cut}) = \sigma^{\text{sing}}(\tau_{cut})[1 + O(\tau_{\text{cut}})] \tag{3.8}$$

so that the error in the calculation is a power correction

$$\Delta\sigma^{sub}(\tau_{\text{cut}}) \sim O(\tau_{\text{cut}}^m) \tag{3.9}$$

The actual value of m depends on how many terms of $\sigma^{\text{nonsing}}(\tau_{\text{cut}})$, equation 3.6, can be included in σ^{sub}. In the case of the inclusive Drell-Yan cross section the $O(\tau_{\text{cut}}^1)$ is known at NLO and can be included in σ^{sub}. The neglected term $\Delta\sigma$ is a power correction $O(\tau_{\text{cut}}^2)$. The presence of fiducial cuts on the final state leptons can introduce additional power dependence of $\mathrm{d}\sigma^{\text{nonsing}}/\mathrm{d}\tau$ on q_T and lower the precision of the approximation.

3.1.2 Fiducial power corrections

The power corrections to the singular term, equation 3.6, represent the intrinsic error of slicing subtraction methods. This error is of order $O((q_{T,\text{cut}}^2/Q^2)^2)$ in the case of DY predictions and for inclusive calculation. A choice of the slicing threshold $\tau_{\text{cut}} = (q_{T,\text{cut}}^2/Q^2)$ small enough makes this bias negligible. The presence of fiducial cuts on the final state leptons, however, can introduce additional power q_T correction that cause a further bias in the predictions. These fiducial power corrections (FPC) arise when considering the final state phase space

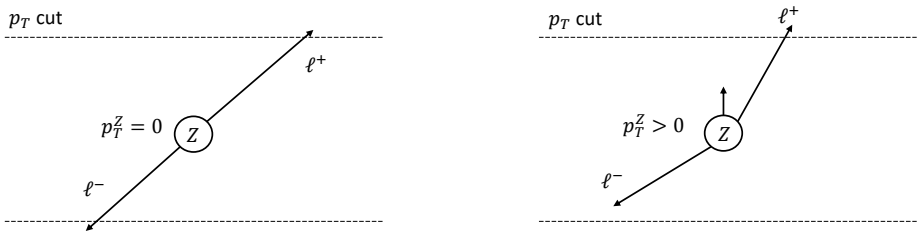

Figure 3.1 Schematic representation of the rising of q_T power corrections due to fiducial cuts on the final state leptons. On left, the case in which the Z boson is at rest and the two lepton are passing the fiducial cuts is shown. When the Z is given a small transverse boost, Figure on the right, one of the two leptons fail to pass the selection.

integration. Using a schematic notation, the phase space integration reads as

$$\frac{d\sigma}{d\tau} = \int d\Phi_F \frac{d\sigma}{d\tau}(\Phi_F) \tag{3.10}$$

where $d\Phi_F$ represent the phase space integration on the final state leptons. The singular term of the cross section depends only on the Born phase space, where no additional emission are considered,

$$\frac{d\sigma^{\text{sing}}}{d\tau} = \int d\Phi_F^{\text{Born}} \frac{d\sigma^{\text{sing}}}{d\tau}(d\Phi). \tag{3.11}$$

When applying fiducial cuts a dependence of the acceptance, $\Phi_F = \int d\Phi_F$, on the boson transverse momentum is introduced. The reason is shown intuitively in Figure where the p_T cut on the leptons coming from the Z decay are shown schematically. When the Z is at rest both leptons pass the requirement $p_{T\,1,2} > p_T^{\text{min}}$. This is no longer the case when the Z boson is given a small transverse momentum. The error introduced in the slicing method can be estimated by comparing the acceptance of the final state with the Born one

$$\Delta\Phi_F = \int d\Phi_F(q_T) - d\Phi_F^{\text{Born}}(q_T = 0) \tag{3.12}$$

It has been shown [28] that

$$\Delta\Phi_F \sim \frac{1}{q_T^2}\left(\frac{q_T^2}{Q^2}\right)^m \tag{3.13}$$

where the value of m depends on the fiducial cut configuration. In the case of a p_T^{ℓ} symmetric cut, $p_T^{\ell_1,\ell_2} > p_T^{\min}$, it is found that $m = 1/2$, that means

$$\Delta\Phi_F\big|_{p_T^{\ell_1,\ell_2} > p_T^{\min}} \sim \frac{1}{q_T^2}\left(\frac{q_T}{Q}\right) \tag{3.14}$$

This linear dependence introduces a bias in the cross section calculation, equation 3.7, that is dominant with respect to the inclusive power corrections, equation 3.9. In the case of additional lepton pseudorapidity cuts, for example a symmetric cut $|\eta_{\ell_1,\ell_2}| < \eta_{\min}$, linear power correction also arise, but effects can be different according to the di-lepton rapidity configuration. A more detailed analysis of the relation between different fiducial cut configurations and the power corrections can be found in Refs [29, 32].

A simple solution in the DY case to avoid this bias is to change the selection configuration. A selection in which different cut thresholds are applied to on the lepton and anti-lepton p_T, also known as *staggered* cuts, is not affected by linear q_T biases [33, 32]. The symmetric cuts are anyway still common in DY measurements and relevant measurements have been performed with this configuration [17]. A way to mitigate the effects of the linear power corrections is then needed. A first possibility is to lower the $q_{T,\text{cut}}$ threshold value, or to have an extrapolation method to small $q_{T,\text{cut}}$ values. Both of these approaches affect the stability and the performance of the calculation. Furthermore the introduction of a dependence of the cross section on q_T introduces some instability in the series expansion due to non perturbative small-q_T effects [32]. These affect any fixed order calculations, regardless of the subtraction scheme. A more feasible approach is then to include the q_T resummation effects in the predictions. It has been shown in Ref. [34] that the implementation of a recoil prescription of the boson transverse momentum as done in the q_T resummation [35, 36, 37, 38, 39, 27], allows the linear power corrections to be resummed at each perturbative order. The residual fiducial biases are quadratic in q_T and so of the same order as in the inclusive case. Starting from this result it is also possible to include the linear power correction in q_T at a given order in α_S. This gives a fixed order result that can be used for a benchmark study with the local subtraction method predictions. This procedure has been implemented in public code such as MATRIX [40] or DYTurbo [41]. In section 3.2 a benchmark study of predictions for the DY process in the case of fiducial cuts is presented and the DYTurbo code is used.

3.1.3 Local subtraction methods

The other strategy to deal with the divergences is the local subtraction method. This aims to correct for the singular contributions in the cross section point by point at the integrand level, so that the phase space integration can be freely performed, without the need of approximations. In the case of NLO calculations, the cross section can be split into the real and virtual contributions, whose phase space integration is performed over a different number of particles in the final state

$$\sigma^{NLO} = \int d\sigma = \int_{N+1} d\sigma^{\mathrm{R}} + \int_{N} d\sigma^{V} \tag{3.15}$$

A subtraction for the real term that encodes all its IR divergences is now constructed. Adding it to the real term eliminates the singularities, so that the $N+1$ phase space integration can be performed

$$\begin{aligned} \sigma^{NLO} &= \int_{N+1} \mathrm{d}\sigma^{\mathrm{R}} - \int_{N+1} \mathrm{d}\sigma^{\mathrm{S}} + \int_{N+1} \mathrm{d}\sigma^{\mathrm{S}} + \int_{N} \mathrm{d}\sigma^{\mathrm{V}} \\ &= \int_{N+1} \left[\mathrm{d}\sigma^{\mathrm{R}} - \mathrm{d}\sigma^{\mathrm{S}}\right] + \int_{N+1} \mathrm{d}\sigma^{\mathrm{S}} + \int_{N} \mathrm{d}\sigma^{\mathrm{V}} \end{aligned} \tag{3.16}$$

The subtraction term is also built in a way that the integral on the extra particle can be factorized and the term can be combined with the virtual contribution. In particular it can be combined with the loop integral in the virtual term from which the infrared singularity arises, hence allowing the cancellation

$$\sigma^{NLO} = \int_{N+1} \left[\mathrm{d}\sigma^{\mathrm{R}} - \mathrm{d}\sigma^{\mathrm{S}}\right] + \int_{N} \left[\int_{\mathrm{loop}} \mathrm{d}\sigma^{\mathrm{V}} + \int_{1} \mathrm{d}\sigma^{\mathrm{S}}\right]. \tag{3.17}$$

The definition of the subtraction term presents a certain freedom, in particular in its finite contribution. Different definition choices is what distinguish the local subtraction methods available for the calculation. At NLO the FKS [42] and the Catani-Seymour [43] schemes are implemented. At NNLO the level of complexity is significantly higher due to the overlapping of singularities. One of the established method is antenna subtraction [44, 45, 46], this is implemented in the NNLOJET code. NNLO Drell-Yan predictions from this program are used in the next section for the benchmark study.

An alternative approach is the *sector decomposition* as implemented in the simulation code FEWZ [24] or in the STRIPPER code [47, 48, 49].

3.2 NLO and NNLO benchmark study

In this section a benchmark study of NLO and NNLO QCD predictions for the DY process is presented. The comparison is performed between the results of two codes: DYTurbo and NNLOJET. These use different subtraction schemes, DYTurbo implements a slicing subtraction in q_T [27], while NNLOJET uses a local subtraction based on the antenna subtraction method. A treatment to include the linear q_T power corrections due to the fiducial cuts is implemented in DYTurbo [41] and is benchmarked in this section. Furthermore, the DYTurbo offers also the possibility to include the q_T resummation effects in the predictions. Also these predictions are used in the comparison. The benchmark is performed in the context of predictions for the ATLAS 7 TeV W/Z measurement. This offers an interesting case in which to evaluate the differences in the theory as this data set reaches an high experimental precision and contributes significantly in the PDF determination. The same predictions will be used in section 3.3 for a comparison of the different theory definitions with the data.

3.2.1 Fiducial region

The predictions are produced in the fiducial region of the ATLAS 7 TeV W/Z cross section measurement [17]. Only the $Z/\gamma^* \to \ell\ell$ cross section is used in the benchmark study.

The ATLAS measurement is performed in two channels. A central channel that selects leptons at central pseudorapidity, $|\eta_\ell| < 2.5$, and a forward channel in which one of the two leptons is required to be produced at high pseudorapidity, $2.5 < |\eta_\ell| < 4.9$. The kinematics requirement applied for the cross section measurement are

$$\begin{aligned} \text{Central } Z/\gamma^* \to \ell\ell : \; & p_{T,\ell} > 20\,\text{GeV}, \\ & |\eta_\ell| < 2.5, \\ & 46 < m_{\ell\ell} < 150\,\text{GeV} \\ \text{Forward } Z/\gamma^* \to \ell\ell : \; & p_{T,\ell} > 20\,\text{GeV}, \\ & \text{one lepton } |\eta| < 2.5, \text{ the other lepton } 2.5 < |\eta| < 4.9, \\ & 66 < m_{\ell\ell} < 150\,\text{GeV} \end{aligned} \tag{3.18}$$

The cross section is measured in three different bins of the dilepton invariant mass

$$m_{\ell\ell} = [46, 66, 116, 140]\,\text{GeV} \tag{3.19}$$

these are referred to as *low mass*, *Z-peak* and *high mass* bins. In the low mass bin only the central channel is measured. In each mass bin the cross section is measured differentially in the dilepton rapidity $|y_{\ell\ell}|$. In the Z-peak region, central channel, the following bins edges are used

$$|y_{\ell\ell}| = [0.0, 0.2, 0.4, 0.8, 1.0, 1.2, 1.4, 1.6, 1.8, 2.0, 2.2, 2.4] \tag{3.20}$$

In the low and high mass bins a binning twice as coarse is used. When measuring the cross section in the forward channel instead, bins with the following boundaries are chosen

$$|y_{\ell\ell}| = [1.2, 1.4, 1.6, 1.8, 2.0, 2.2, 2.4, 2.8, 3.2, 3.6]. \tag{3.21}$$

The same fiducial region and binning schemes are used in producing the predictions. The measurement implements symmetric cuts on the lepton and anti-lepton p_T and both asymmetric and symmetric cuts (according to the channel) on the lepton pseudorapidity η. As discussed in section 3.1.2, an increase in the fiducial power correction when calculating the cross section with slicing subtraction methods is expected in all these configuration .

3.2.2 Simulation setup

The DYTurbo and NNLOJET prediction are calculated with the same input parameters. The G_μ scheme is used: G_F, m_W, m_Z are the input values while $\sin^2\theta_W$ and the QED coupling $\alpha(m_Z)$ are calculated as output. In general, the Standard Model input parameters are set to the following values [50]

$$\begin{aligned} G_F &= 1.1663787 \times 10^{-5}\,\text{GeV}^{-2}, \\ m_Z &= 91.1876\,\text{GeV}, \\ m_W &= 79.936\,\text{GeV}, \\ \Gamma_Z &= 2.4950\,\text{GeV}, \\ \Gamma_W &= 2.091\,\text{GeV}. \end{aligned} \tag{3.22}$$

The CKM matrix elemets are set to [50]

$$\begin{aligned} |V_{ud}| &= 0.97427, \quad |V_{cd}| = 0.2252, \\ |V_{us}| &= 0.2253, \quad |V_{cs}| = 0.97344, \\ |V_{ub}| &= 0.00351, \quad |V_{cb}| = 0.0412 \end{aligned} \tag{3.23}$$

The input PDFs are taken from the NNPDF3.1 set [51]. The values of the renormalization and factorization scale μ_R and μ_F is set to in the dilepton invariant mass in each event, $\mu_R = \mu_F = m_{\ell\ell}$.

DYTurbo implements a slicing subtraction scheme in q_T. The vaule of the slicing cut-off is set to $(q_T/Q)_{\text{cut}} = 0.008$. Additional parameters to include the resummation effects need to be set. The first is the resummation scale μ_{Res} that is set, as the renormalization and factorization scales, to the dilepton invariant mass $m_{\ell\ell}$. The resummation damping function that regulates the vanishing of the resummation effects at high q_T is set to a Gaussian: $f(x) = \exp(-(k\,m_{\ell\ell} - q_T)^2/\Delta m_{\ell\ell}^2)$ with $k = 0.75$ and $\Delta = 0.5$. A term to parametrize non-perturbative QCD effects also needs to be included. This is a Gaussian form factor in the space of the impact parameter b, $G^{\text{NP}}(b) = \exp(-g_1 b^2)$ with $g_1 = 0.8$.

A comparison of the predictions at LO, where no difference due to the subtraction schemes is expected, is carried out to test the simulation setup. Agreement at the level of 0.1per mille is found.

3.2.3 NLO comparison

The predictions at NLO QCD are compared. DYTurbo implements the q_T slicing also at this perturbative order and differences with respect to the NNLOJET results are expected. The fiducial power correction term implemented in DYTurbo is considered, this helps to recover good agreement between the two subtraction scheme calculations.

In figure 3.2 the NLO comparison for the Z-peak bin predictions, in the central and forward channel is shown. A disagreement beetween the fixed order DYTurbo and NNLOJET results is observed. In the central channel the differences are of the order of 6 per mille, these are more severe in the forward channel where the ratio departs from one as much as 7%. The inclusion of the FPC term in the DYTurbo predictions improves the agreement at the level better than 0.5 per mille. Similar observation can be made by comparing the predictions in the high mass bin, Figure 3.3. The effect of fiducial cuts are partially smaller than in the Z-peak bin and again, adding the FPC term to the DYTurbo predictions, increases the agreement at a per mille level. In the low mass bin 3.4 the effect of using different subtraction methods results only in a 2 per mille difference at central rapidity, including the FPC further improves the agreement.

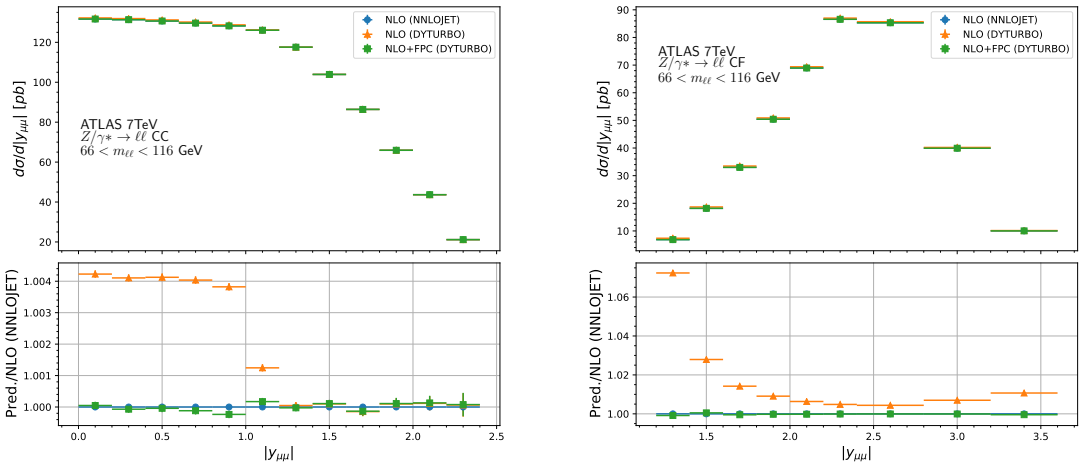

Figure 3.2 NLO QCD predictions for the ATLAS Z-peak central (left) and forward (right) channel. The fixed order DYTurbo prediction shows a disagreement with respect to the NNLOJET. Good agreement is recovered after including the FPC term.

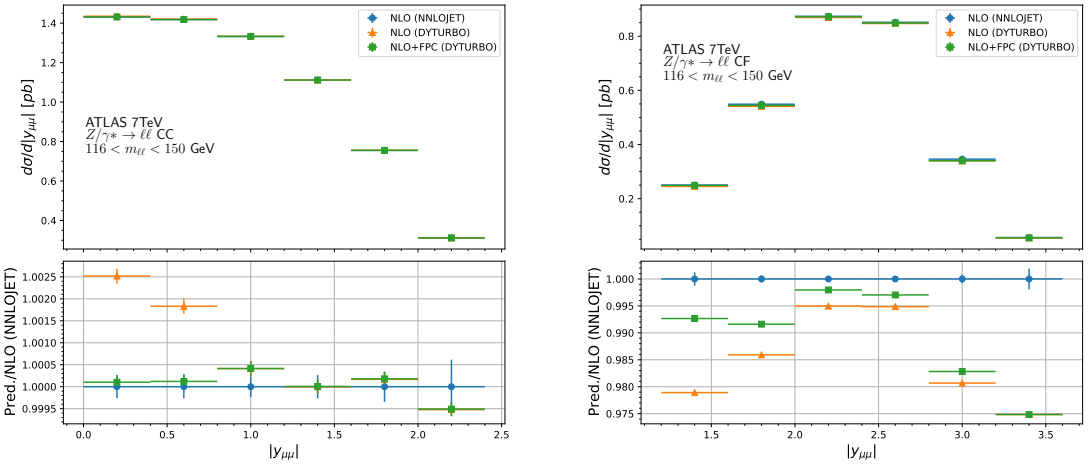

Figure 3.3 NLO QCD predictions for the ATLAS high mass central (left) and forward (right) channel. The fixed order DYTurbo prediction shows a disagreement with respect to the NNLOJET is observe. Good agreement is recovered after including the FPC term. In the forward channel some residual discrepancies are observed at very high rapidity.

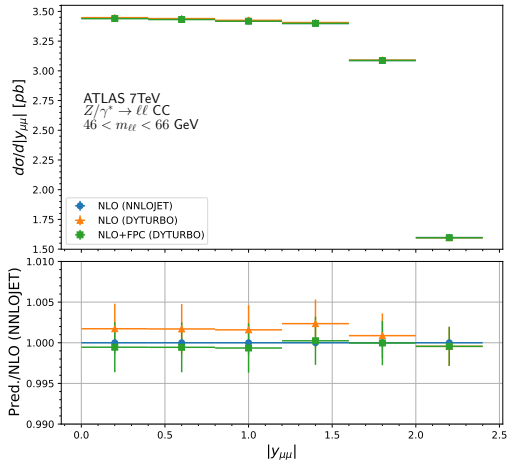

Figure 3.4 NLO QCD predictions for the ATLAS low mass central channel. The fixed order DYTurbo prediction is in slight disagreement with respect to the NNLOJET. Including the FPC term the agreement is further improved.

3.2.4 NNLO comparison

A benchmark study at NNLO precision is performed in this section. In the comparison, also the DYTurbo results that include the q_T resummation corrections are reported, as they will be used in the next section for the PDF study. These prediction correspond to a NNLO+NNLL accuracy. In Figure 3.5 the comparison of the NNLO Z-peak bin predictions is reported. Both in the forward and central channel differences between NNLOJET and the fixed order DYTURBO results are observed. These are of the the same order as those noticed at NLO, Figure 3.2 (but in the opposite direction: at NLO DYTurbo undershoots the NNLOJET cross section, here it overshoots it). Adding the FPC term, DYTurbo is able to recover a per mille level agreement. The NNLO+NNLL result deviates from the fixed order by few per mille in the central channel, with some shape differences for $|y_{\ell\ell}| > 1.2$. In the forward channel the resummation seems to have a bigger effect, and the deviation gets as high as 3%.

In the high mass bin, Figure 3.6, the inclusion of the FPC term doesn't improve the agreement of the DYTurbo results with the NNLOJET ones. For both in the central and forward it actually slightly increases the differences. The reason for this behaviour is yet to be understood. The resummation effects lead to few per mille deviations in the central channel and up to per cent differences in the forward channel.

The comparison for the low mass bin predictions is reported in Figure 3.7. An improvement in the agreement when including the FPC term is observed this time. The differences

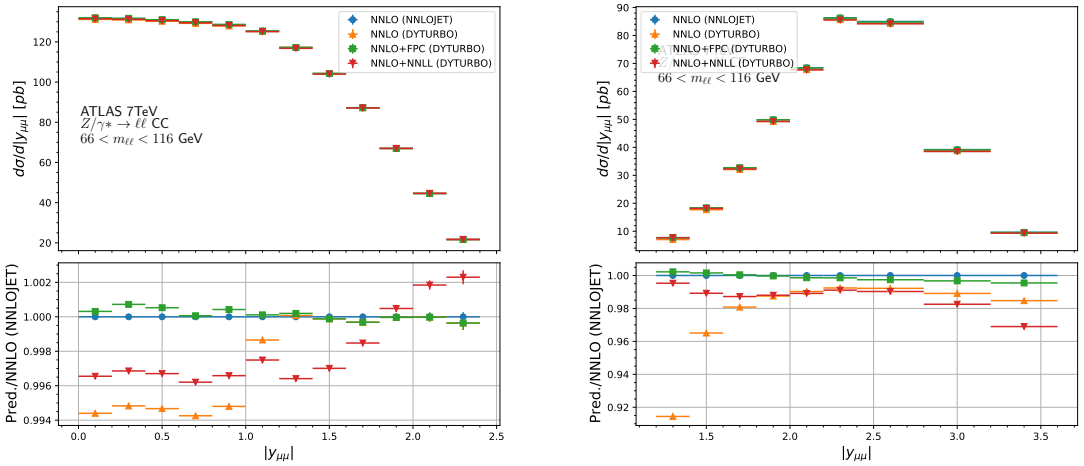

Figure 3.5 Comparison of the NNLO QCD calculations from NNLOJET and DYTURBO. The predictions are for the Z-peak bin in the central (left) and forward (right) channel.

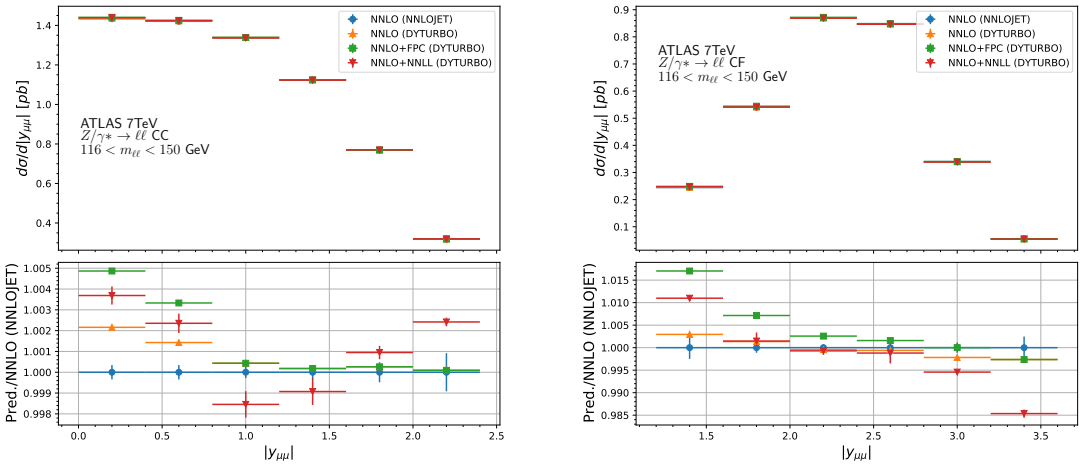

Figure 3.6 Comparison of the NNLO QCD calculations from NNLOJET and DYTURBO. The predictions are for the high mass bin in the central (left) and forward (right) channel.

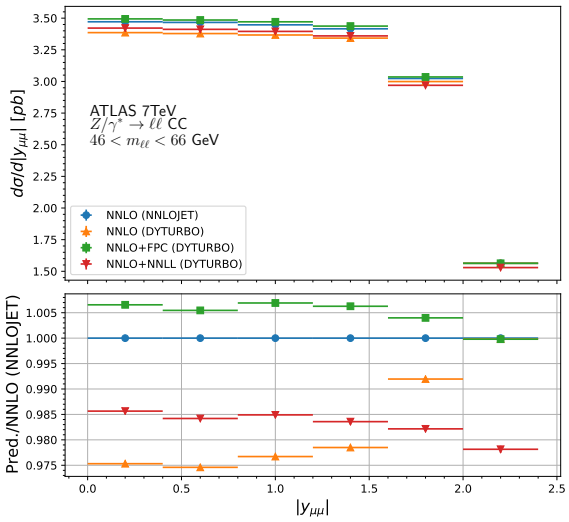

Figure 3.7 Comparison of the NNLO QCD predictions for the low mass bin.

are reduced to a 5per mille level. The resummed DYTurbo result has a shape similar to the fixed order one, but a 2.5% offset difference.

3.3 Data theory comparison

Thanks to the experimental precision and the wide phase space considered, the ATLAS data presented in section 3.2.1 provide a significant constraint on the PDFs [17]. These measurements are usually included in determining modern PDF sets. In this section a study of the compatibility of some modern PDF sets with the ATLAS data when changing the underlying theory is reported. The study is performed with *xfitter* [52], an open source software that offers a framework for PDF determination.

The data theory compatibility is carried out through a χ^2 test. The χ^2 definition takes into account the correlated systematic uncertainties, both experimental and theoretical (from the PDFs), introducing nuisance parameters that are extracted through a χ^2 minimization. The χ^2 at the minimum is equivalent to the more standard definition $\chi^2 = \sum_{ij}(\sigma_i^{\text{exp}} - \sigma_j^{\text{th}})V_{ij}^{-1}(\sigma_j^{\text{exp}} - \sigma_j^{\text{th}})$, where V_{ij} is the uncertainty covariance matrix, see Ref. [53, 54] for the proof. Using the nuisance parameter approach is computationally more feasible because one avoids the inversion of the matrix V_{ij}. Furthermore it allows us to distinguish between

the different sources of systematics. The χ^2 is defined as

$$\begin{aligned}\chi^2(\mathbf{b}_{\rm exp},\mathbf{b}_{\rm th}) = &\sum_{i=1}^{N_{\rm data}} \frac{\left[\sigma_i^{\rm exp} - \sigma_i^{\rm th}(1-\sum_k \gamma_{ik}^{\rm th} b_{k,\rm th} - \sum_j \gamma_{ij}^{\rm exp} b_{j,\rm exp})\right]^2}{\Delta_i^2} \\ &+ \sum_i \log \frac{\delta_{i,\rm uncor}^2(\sigma_i^{\rm th})^2 + \delta_{i,\rm stat}^2 \sigma_i^{\rm exp}\sigma_i^{\rm th}}{\delta_{i,\rm uncor}^2(\sigma_i^{\rm exp})^2 + \delta_{i,\rm stat}^2(\sigma_i^{\rm exp})^2} \\ &+ \sum_{j=1}^{N_{\rm exp.sys}} b_{j,\rm exp}^2 + \sum_{k=1}^{N_{\rm th.sys}} b_{k,\rm th}^2.\end{aligned} \tag{3.24}$$

In the formula, the index i runs over all $N_{\rm data}$ points. For each point, the data measurement $\sigma_i^{\rm exp}$ and theory point $\sigma_i^{\rm th}$ are compared taking into account both the experimental uncertainties and theoretical uncertainties coming from PDF variations. The uncorrelated experimental uncertainties are given by Δ_i. The correlated uncertainty component is included introducing the nuisance parameter vectors $\mathbf{b}_{\rm exp}$ and $\mathbf{b}_{\rm th}$. The impact of the uncertainty source j on the data(theory) point i is described by the matrices $\gamma_{ij}^{\rm data(th)}$. Both the correlated and uncorrelated uncertainties are treated as multiplicative (the uncertainties are proportional to central prediction values). The χ^2 function is minimized as a function of $\mathbf{b}_{\rm exp}$ and $\mathbf{b}_{\rm exp}$. The contribution to the χ^2 for the determination of the nuisance parameters is given by the two sums of b_j^2 over the number of correlated uncertainty sources $N_{\rm exp.sys}$, $N_{\rm th.sys}$. This term is referred to as *correlated* χ^2 contribution when reporting the results of the study. The log term instead is added to minimize biases. Because the χ^2 is quadratic in $\mathbf{b}$ the minimization can be performed analytically. The χ^2 at its minimum gives a test of compatibility between data and theory. The values of the nuisance parameters $b_{k,\rm th}$ at this minimum can be interpreted as an optimization of the PDFs to describe the data, and allows us to determine a new set of PDFs. This procedure is called PDF profiling [55, 56] and can be used to test in a quantitative way the impact of new data measurement on a PDF set without performing a new PDF fit. In this study we limit our self to use the χ^2 at the minimum as a way to check the agreement with the data. The theory points $\sigma_i^{\rm th}$ are calculated using the input PDF and the NLO `APPLGRID` [57] interfaced with the `MCFM` parton level generator [58, 59, 60]. The NNLO accuracy is reached via k-factors (kf) calculated in each observable bin, as the ratio between the higher and lower order QCD calculation

$$kf_i = \frac{\sigma_i^{NNLO}}{\sigma_i^{NLO}}. \tag{3.25}$$

The NNLO DYTurbo results presented in the previous section are used to calculate the k-factors.

3.3.1 Results

Some modern sets of PDFs are used for the comparison with the ATLAS data and using the NNLO theory predictions from DYTurbo. The PDF sets considered are NNPDF3.1_nnlo_as_0118 [51], NNPDF4.0 [61], CT18NNLO, CT18ANNLO [62] and MSHT20nnlo_as118 [63]. In Table 3.1 the χ^2 results using the NNPDF3.1 and NNPDF4.0 for the comparison are reported. In table 3.2 the results using the CT18 and CT18A PDF sets are shown. Finally the results using MSHT20 PDF set are reported in Table 3.3. In each of the result tables, the χ^2 contribution from each data set, the first term on the right hand side of eq. 3.24, is reported, together with the corresponding number of degrees of freedom. At the bottom of the table the correlated and total χ^2 are listed. Different theory predictions from DYTurbo are tested: the fixed order NNLO calculation, the prediction including the FPC term, and the q_T resummed calculation. The results seem to be in line with what exposed in section 3.1.2: the data-theory agreement improves when including the FPC term in the NNLO predictions, obtaining a reasonable χ^2 over degrees of freedom. A further improvement is obtained when considering the q_T resummation effects (third column in Tables 3.1, 3.2, 3.3), resulting in a $\chi^2/ndf \sim 1$. This behaviour of the results is noticeable with each of the PDF sets under consideration.

3.4 Conclusion and outlook

In this chapter, a study regarding high precision QCD predictions for DY was introduced and the differences between the two main calculation methods, local (or slicing) subtraction and global subtraction methods, in the presence of fiducial cuts on the final state leptons, have been explored. Some cut configurations lead the phase space acceptance to have a dependence on the vector boson transverse momentum, q_T, at small values. This induces linear q_T biases in the slicing method predictions and furthermore introduces an instability in the convergence of the series expansion, regardless of the subtraction scheme used. In section 3.2 it has been shown how the inclusion of a fiducial power correction (FPC) term improves the nominal accuracy of the results. This correction allows us to perform benchmark comparison between global and local subtraction scheme calculations. The FPC term comes from the resummation results. The resummation program offers a way to resum the linear q_T bias at each perturbative order and improves the stability of the power expansion. The downside of including resummation effect is the introduction of additional parameters in the calculation. A further investigation should include the theoretical uncertainty effects related to this new parameters.

Table 3.1 Results of compariosn of the NNPDF3.1 and NNPDF4.0 PDF sets with the ATLAS 7 TeV datasets, using different NNLO theories definitions. The NNLO precision is reached with KFactor calcultated from the DYTurbo predicitons.

	NNPDF3.1		
	NNLO	NNLO+FPC	NNLO+NNLL
Data set			
ATLAS 7 TeV y_Z low mass CC	14 / 6	9.8 / 6	8.5 / 6
ATLAS 7 TeV y_Z Z-peak CC	8.4 / 12	6.7 / 12	6.3 / 12
ATLAS 7 TeV y_Z Z-peak CF	5.2 / 9	5.4 / 9	7.1 / 9
ATLAS 7 TeV y_Z high mass CC	5.7 / 6	5.8 / 6	5.3 / 6
ATLAS 7 TeV y_Z high mass CF	4.8 / 6	4.8 / 6	4.6 / 6
Correlated χ^2	16	15	9.7
Log penalty χ^2	-2.28	-2.28	-2.72
Total χ^2 / dof	52 / 39	45 / 39	39 / 39
χ^2 p-value	0.09	0.23	0.48
	NNPDF4.0		
	NNLO	NNLO+FPC	NNLO+NNLL
Data set			
ATLAS 7 TeV y_Z low mass CC	15.2/6	10.2/6	8.7/6
ATLAS 7 TeV y_Z Z-peak CC	12.1/12	8.3/12	6.5/12
ATLAS 7 TeV y_Z Z-peak CF	9.8/9	5.7/9	7.3/9
ATLAS 7 TeV y_Z high mass CC	5.1/6	5.7/6	5.3/6
ATLAS 7 TeV y_Z high mass CF	4.6/6	5/6	4.8/6
Correlated χ^2	8.02	12.6	6.6
Log Penalty χ^2	-2.1	-1.6	-2
Total χ^2/dof	52.7/39	46/39	37.1/39
χ^2 p-value	0.07	0.20	0.56

Table 3.2 Results of the comparison of the CT18 and CT18A PDF sets with the ATLAS 7 TeV datasets, using different NNLO theory definitions. The NNLO precision is reached with KFactor calcultated from the DYTurbo predicitons.

	CT18 NNLO		
	NNLO	NNLO+FPC	NNLO+NNLL
Datasets			
ATLAS 7 TeV y_Z low mass CC	7.2/6	5.7/6	5.9/6
ATLAS 7 TeV y_Z Z-peak CC	12.6/12	8.3/12	7.1/12
ATLAS 7 TeV y_Z Z-peak CF	8.9/9	6/9	7.2/9
ATLAS 7 TeV y_Z high mass CC	5.3/6	5.8/6	5.4/6
ATLAS 7 TeV y_Z high mass CF	4.6/6	5/6	4.6/6
Correlated χ^2	13.6	13.3	10.1
Log Penalty χ^2	-3.5	-3	-3
Total χ^2	48.7/39	41.1/39	36.9/39
χ^2 p-value	0.13	0.38	0.57
	CT18A NNLO		
	NNLO	NNLO+FPC	NNLO+NNLL
Datasets			
ATLAS 7 TeV y_Z low mass CC	7.4/6	5.9/6	6.1/6
ATLAS 7 TeV y_Z Z-peak CC	12.4/12	8.2/12	6.9/12
ATLAS 7 TeV y_Z Z-peak CF	8.7/9	6/9	7.2/9
ATLAS 7 TeV y_Z high mass CC	5.4/6	5.7/6	5.5/6
ATLAS 7 TeV y_Z high mass CF	4.5/6	5/6	5/6
Correlated χ^2	13.2	13.1	9.7
Log Penalty χ^2	-3.5	-2.9	-3.4
Total χ^2	48.1/39	41.1/39	36.6/39
χ^2 p-value	0.15	0.38	0.58

Table 3.3 Results of the comparisong of the MSHT20 PDF set with the ATLAS 7 TeV datasets, using different NNLO theory definitions. The NNLO precision is reached with KFactor calcultated from the DYTurbo predicitons.

	MSHT20 NNLO	NNLO+FPC	NNLO+NNLL
Dataset			
ATLAS 7 TeV y_Z low mass CC	19.9/6	12.1/6	11.3/6
ATLAS 7 TeV y_Z Z-peak CC	14.0/12	7.7/12	7/12
ATLAS 7 TeV y_Z Z-peak CF	10.9/9	6.5/9	8.1/9
ATLAS 7 TeV y_Z Z-mass CC	5.2/6	5.9/6	5.3/6
ATLAS 7 TeV y_Z high mass CF	4.9/6	5.3/6	5.1/6
Correlated χ^2	20.3	15.9	14.1
Log Penalty χ^2	-3.6	-3.1	-3.5
Total χ^2	71.7/39	50.4/39	47.3/39
χ^2 p-value	0.001	0.11	0.17

The theory predictions of chapter 3 are calculated in the same fiducial region as in the ATLAS Z measurement at 7 TeV [17], and are used in section 3.3 for a comparison study with the data. The comparison tests different PDF sets, and the various theory predictions. In particular the fixed order NNLO predictions, the prediction including the FPC term and the resummed results are tested. With the latter two, an improvement of the agreement χ^2 is observed. The ATLAS collaboration performed also a $W^{+/-}$ measurement in the same analysis; to complete the picture, these data and the corresponding predictions could be added to the PDF study of section 3.3. The results of this study is in preparation [64, 65].

The q_T resummation effects can be important in the presence of lepton fiducial cuts. So far these effects have been ignored when determining the parton distribution functions (PDF). To fully assess the variation in the results a PDF fit should be performed varying the underlying theory and comparing the the different outcomes. The study can be a combined fit of deep inelastic scattering data from the HERA experiment [3] and the most relevant Drell-Yan data sets. For some of the DY data it would be important to evaluate the effects of resummation. Other than the ATLAS W/Z measurements at 7 TeV, interesting DY measurements to include are for example the ATLAS W/Z measurements at 5 TeV and 8 Tev [66, 67], the CMS W and Z forward-backward asymmetry measurements at 7 and 8 TeV [68, 69] and also the Drell-Yan analysis performed at Tevatron collider by the D0 [70, 71, 72, 73] and CDF [74, 75, 76, 77] experiments.

Chapter 4

The Large Hadron Collider and the ATLAS detector

The Large Hadron Collider [78] is a 27km accelerator ring for protons and ions built at CERN (Conseil européen pour la recherche nucléaire) near Geneva on the Franco-Swiss border. The construction work lasted between 1998 and 2008 and used the same underground tunnel, at around 100 m depth, where the LEP (Large Electron Proton Collider) collider was operating, but replacing all the magnets and the accelerating structures. The LHC is the largest accelerator in the world, inside the collider, two proton beams are accelerated up to an energy, so far, of 6.5 TeV and collided at four different interaction points. There the detector experiments are built and collect the signals for the particles created in the collisions. Stable LHC operations started in 2009 and since then two data taking run campaigns have been successfully completed: *Run 1* between 2009 and 2013, and *Run 2* between 2015 and 2018. Both runs were followed by a Long Shutdown, an accelerator and detectors upgrade phase. At the time of this thesis the Long Shutdown 2 phase, after *Run 2*, is coming to an end and *Run 3* is expected to start at the beginning of 2022.

The properties of the proton beams at the LHC are explored in section 4.1. Successively, the experiments that operate at the LHC will be introduced. The data samples under study in this thesis have been collected using the ATLAS detector. This will be described in section 4.3.

4.1 The proton beam at the LHC

The proton beams are produced through the scattering of energetic electrons on a hydrogen target. The beam travels then through a chain of accelerators that gradually increase the

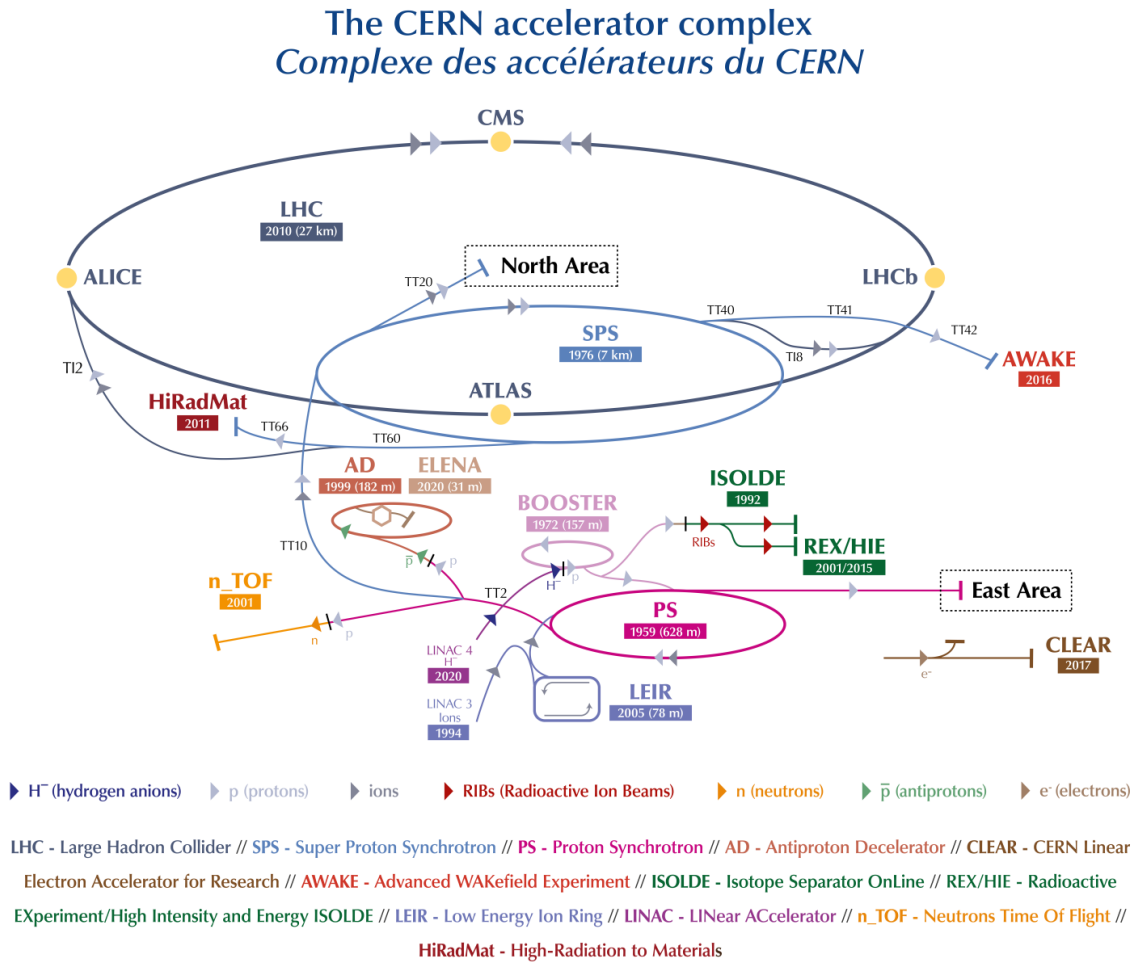

Figure 4.1 Summary of cross section measurements with the ATLAS detector for SM processes and their comparison to the theory predictions.

proton energy and that culminates with the LHC. These machines have provided accelerated particle beams for various important high energy physics experiment in the past and, at the end of the experiment lifetime, have been kept and used as injector for the new, more powerful machines. The accelerator complex at CERN is showed in Fig. 4.1. The machines that accelerate the proton beam before it is injected into the LHC are:

- LINAC 2: linear low energy accelerator, it increases the beam energy from 90keV to 50MeV.
- Proton Synchrotron Booster: it is the first synchrotron of the accelerating chain, it accelerate the beams up to 1.4GeV.

- Proton Synchrotron: it bring the proton beams up to an energy of 25 GeV.
- Super Proton Synchrotron: it is last machine before the injection into the LHC and it accelerate the protons up to 450GeV. This 6.9 km accelerator provided the collisions used for the discovery of the W and Z bosons in 1983 [79].

The last step of the proton acceleration is the LHC. This has been designed to accelerate the beams up to an energy of 7 TeV, but, after a quench incident of one of the magnets during the first months of operation of the accelerator, it was decided to start with a lower energy and gradually reach the maximum beam energy over the years. During Run 1 the collision energy has been increased from 2.76 TeV to 7 TeV and 8 TeV [80]. In Run 2 the collision energy reached the 13 TeV [81]. A slightly higher collision energy of 13.6 TeV is planned to be reached during the next Run, starting in 2022.

4.1.1 Beam properties

The radiofrequency accelerators group the proton beams in bunches, 2808 in total, with around $1.2 \cdot 10^{11}$ protons per bunch. Once the beams are injected into the LHC, a phase that requires around 15 minutes, the protons are accelerated up the final energy in about 20 minutes. After some procedure to increase the beam quality, the physics run, intended here as the data taking time for one beam injection, starts with a collisions rate of 40 MHz. At the LHC the beams are focused thanks to a system of quadrupole and sextupole magnets and collided in four different collision points. The focused beams reach a size of around 16 μm in the dimension transverse to the beam pipe, while the longitudinal beam size is more spread and is of the order of 10 cm. The duration of a single run is of the order of $10-20$ hours. Once the quality of the beam is degraded too much to deliver good physics run conditions, the beam is dumped on a graphite target. A summary of the typical time scales of a beam run are summarized in Fig. 4.2

An important quantity to measure the performance of the accelerator is the *luminosity*, this measures the number of interactions that the collider is able to furnish. Greater the luminosity better it is to study processes with low cross-section. The luminosity L can be calculated through the formula

$$L = N_b f_r \frac{n_1 n_2}{4\pi\sigma_x\sigma_y} \tag{4.1}$$

where

- N_b is the number of bunches

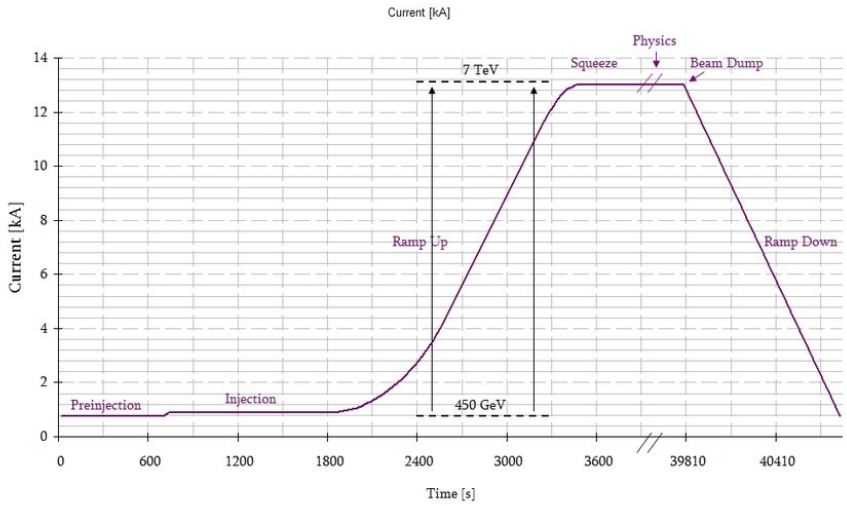

Figure 4.2 Electric current generated by the proton beams in LHC as a function of time, during a typical LHC run. The different stages of the run are highlighted in the Figure.

- f_r is the revolution frequency
- n_1/n_2 are the number of protons in the bunches
- σ_x/σ_y are the transverse dimensions of the beam

The number of bunches N_b and the revolution frequency f_r are known given the accelerator parameters. The number of protons per bunch is obtained measuring the electromagnetic current induced by the beam. The beam transverse sizes are usually obtain via a Van der Meer scan: the scan consists of a measurement of the collision rate performed by varying the beam separation [82]. The Van der Meer scan is adopted for example by the ATLAS experiment and dedicated runs are used to perform this measurement. The methods allows ATLAS to obtain an absolute measurement of the luminosity. The evolution of the instantaneous luminosity with time can be extracted from the number of observed inelastic interactions per bunch crossing. This is usually measured with various strategies. The primary way in ATLAS is done using LUCID [83], a dedicated luminosity detector built in the very forward region, $5.6 < |\eta| < 6.0$, on both sides of the ATLAS detector, at a distance of 17 m from the interaction point. LUCID detects the Cherenkov radiation emitted at the collision point. Other measurements used as cross checks are based on track counting [84], calorimetry measurement [85] and counting of standard model production processes such as Z boson production [86]. The instantaneous luminosity, luminosity per unit of time, delivered by the LHC has reached, in Run 2, a value of $10^{33}\,\mathrm{cm}^{-1}\mathrm{s}^{-1}$ [81], while the total delivered

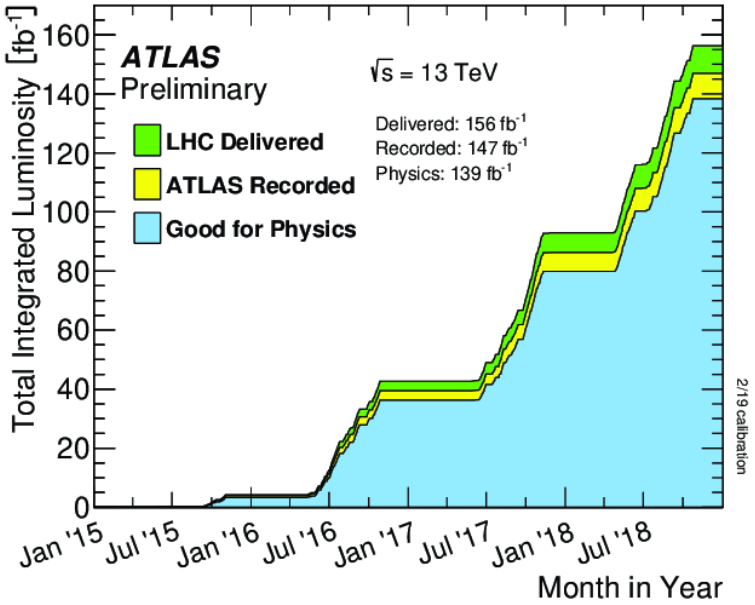

Figure 4.3 Integrated luminosity delivered by the LHC and measured by ATLAS during the run2 data taking period.

luminosity amounts to $156\,\mathrm{fb}^{-1}$. The integrated luminosity during the Run 2 data taking is showed in Fig. 4.3.

4.2 The experiments at the LHC

A total of eight detectors are built along the LHC. The ATLAS [87] and CMS [88] experiments are multipurpose particle detectors. They were built with the main goal to discover the Higgs boson, a success achieved in 2012. ALICE [89] and LHCb [90] focus on more specialized searches: ALICE investigate heavy-ion collision, while LHCb explores b-physics. The other four experiments are LHCf [91], MoEDAL [92], TOTEM [93] and FASER [94]. These are smaller experiments and share the interaction point with the other four.

The analysis presented in this thesis uses the data collected with the ATLAS detector. The ATLAS experiment will be described in the following sections.

4.3 The ATLAS experiment

ATLAS (A Toroidal LHC ApparatuS) is one the experiments at CERN that uses the proton collisions provided by the LHC to perform high energy physics measurements. The data

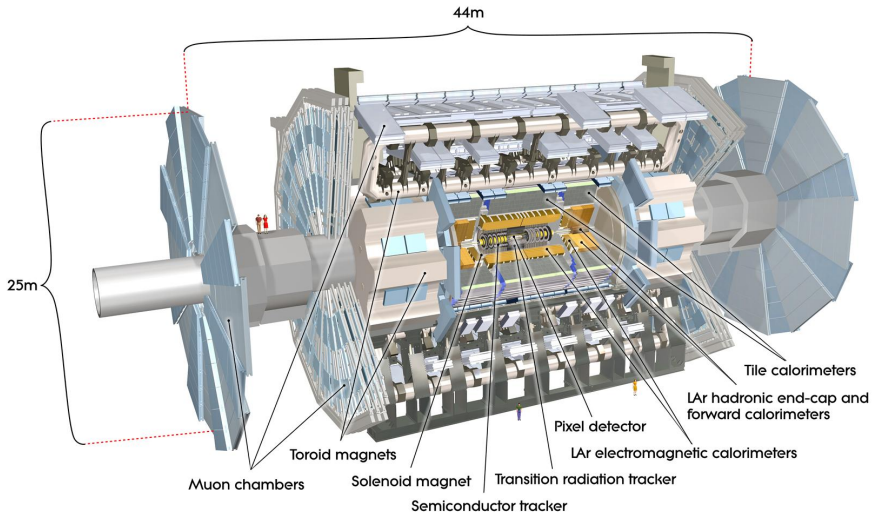

Figure 4.4 An illustration of the ATLAS detector. The different detector substructures are highlighted.

are collected thanks to the ATLAS detector, a multipurpose particle detector built around the proton beam line. The detector has a cylindrical structure, symmetric with respect to the interaction point. This shape is due to the symmetry in the energies of two colliding beams. The detector is composed of three large structures: the barrel, that covers the central region and two end-caps that cover the forward regions. In Figure (4.4) a complete illustration of the detector is shown. Both the barrel and the end-caps have a layered structure with various detector subsystems. Each layer is based on a different technology and have a complementary role in the detection and reconstruction of the particles. A brief description of the composition and the main role of the various substructures are described in the following sections.

4.3.1 The Inner Detector

The first detector substructure, the Inner Detector (ID) [95], measures the tracks of the electrically-charged particles and reconstruct the interaction vertexes. The ID is also embedded in a 2 T magnetic field parallel to the beam pipe, provided by a thin superconductive solenoid that surround the detector. The ID is segmented into a barrel and two end-caps parts, these are divided in three substructures based on different detector technologies: the Pixel detector[96], the SemiConductor Tracker (SCT) [97] and the Transition Radiation Tracker (TRT) [98]. The first ID layer is at around 3 cm from the beam line and the whole ID extends up to 1 m in radius. The tracks are measured in the range $|\eta < 2.5|$ and the coverage in the

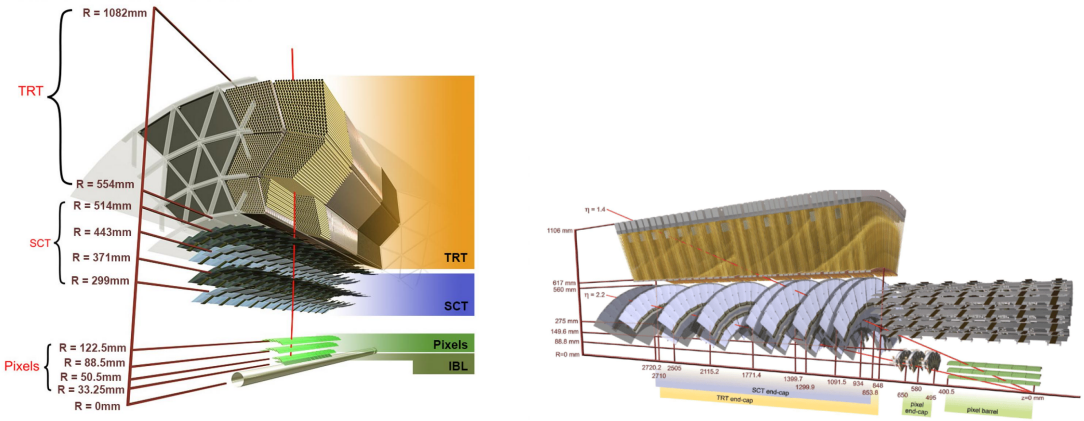

Figure 4.5 The figure shows the inner detector structure in the barrel (left) and in the end-cap (right).

Table 4.1 Resolution, module element sizes and positions of the Inner Detector subsystems.

Subdetector	Element size	Intrinsic resolution [μm]	Radius barrel layers [mm]
IBL	$50\,\mu\text{m} \times 250\,\mu\text{m}$	8×40	33.2
Pixel	$50\,\mu\text{m} \times 400\,\mu\text{m}$	10×115	$50.5, 88.5, 122.5$
SCT	$80\,\mu\text{m}$	17	$299, 371, 443, 514$
TRT	4mm	130	from 554 to 1082

azimuth angle is 2π. Fig 4.5 shows an illustration of the inner detector barrel and end-cap, reporting also the length and distance from the beam pipe of the different detector layers.

The Pixel detector consists of 1744 silicon pixel modules arranged in three cylindrical layers in the barrel and three wheels in each of the end-caps. An additional pixel detector layer, the IBL (Insertable B Layer), consisting of 280 silicon pixels, was added in 2016 as a new B-layer (the detector layer closest to the beam pipe) [99]. With that the minimum distance of the detector from the interaction point was reduced to 3 cm. The IBL improves the ID vertexing and b-tagging performance. An upgrade that was required to deal with the higher pile-up in Run 2 and possible problems in the former B-layer due to the radiation damage. The pixel detector offers good granularity and an intrinsic resolution of $8-10\,\mu$m in the $r-\phi$ plane. The intrinsic resolution for the different ID modules are listed in Table 4.1.

As the distance from the interaction point increases, the track density decreases and a lower granularity of the detector can be used. The Silicon strips modules provide a good performance for the successive layers of the ID. Each module consists of 2 silicon strip

sensors glued back to back and tilted with a small angle to increase the resolution along the sensor longer side. The 4088 Silicon strips modules are arranged in four detector layers in the barrel, with the strips arranged parallel to the beam pipe, and nine wheels in the end-caps, where the modules are placed radially and perpendicular to the pipe line.

The outermost ID subsystem is the TRT, it consists of about 300000 metal straws filled with gas. The TRT offers a worse resolution than the previous silicon detector layers but provides a larger numbers of measurement points together with some particle identification information. The TRT barrel consist of 52544 tubes, each one 1.5 m long, arranged parallel to the beam pipe. The 122880 straws in each of the end-cap TRT are instead 0.4 m long and placed radially and transverse to the beam line. The gaseous tubes have a diameter of 0.4 mm. They host in the middle a thin, few μm, gold-plated tungsten wire. This is at ground potential, while the walls are kept at -1.5 kV. When a charged particle traverses the detector, it ionizes the gas and the freed electrons are collected by the tungsten wire. The TRT also offers timing information, this improve the single tube resolution to about 130 μm.

The TRT provide particle identification information. In particular the transition radiation emitted by the particles when travelling through non-homogeneous material is exploited. The non-homogenity of the TRT is increased by filling the space between the straw with polymer fibers. The probability of transition radiation depends on the relativistic $\gamma = E/m$ factor and is the larger for lighter particles. This is used to distinguish electron and pions.

4.3.2 Calorimeters

The calorimeters measure the energy of the incoming particles by absorbing their total energy (disruptive measurement). They are usually composed of passive layers of dense material, used to facilitate the interaction and the decay of the incoming particle, followed by sampling layers (for example: scintillator detector) that detect the energy of the decay products.

ATLAS is equipped with two calorimeters structures [100], an EM calorimeter to measure electrons and photons through the electromagnetic interactions and an hadronic calorimeter that measure the energy of hadrons that interact via strong and electromagnetic forces. Both are segmented in a barrel and an endcap part. A Forward Calorimeter (FCAL) is equipped to cover higher rapidity values. A complete illustration of the ATLAS calorimeter is reported in Fig 4.6.

The EM calorimeter is a lead/liquid argon detector composed of successive layers of 2 mm lead, the passive layers, interposed with 2.1mm gaps filled with liquid argon (LAr), the sampling layers. The LAr layers also host the readout electronics consisting in electrodes

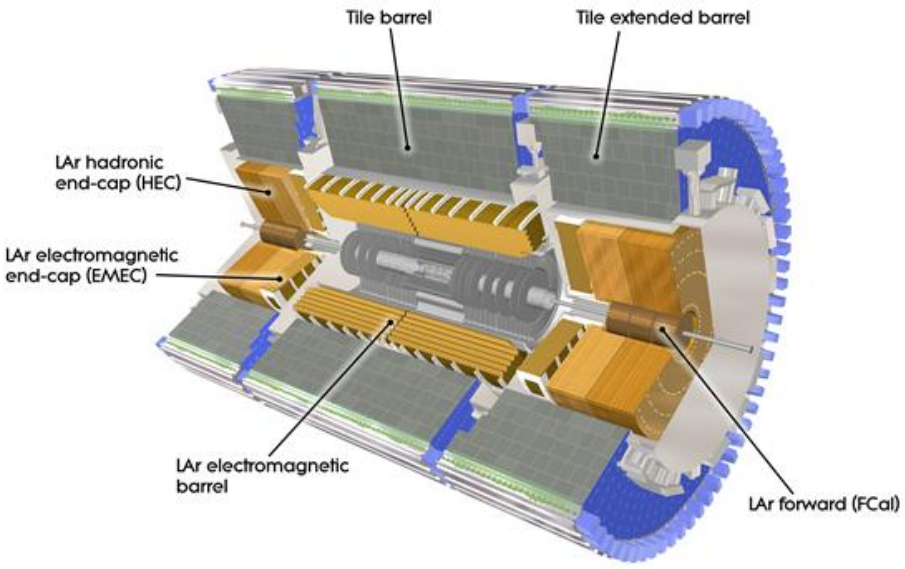

Figure 4.6 ATLAS calorimeters.

that absorb the electrons of the LAr that are ionized by the incoming particles. The EM calorimeter operates at low temperature, about 87 degrees Kelvin, to keep the argon in the liquid state and is embedded in a cryostat that keeps the low temperature, (the barrel cryostat also contains the superconductive solenoid that supplies the 2T magnetic field to the ID tracker detector).

The central part of the hadronic calorimeter, referred to as the tile calorimeter, is based on the same principle as the EM calo, but makes use of different materials. The absorber layers are made of steel while crystal scintillators are used as sampling layers.

In the end-cap and forward parts, all the calorimeters make use of LAr as sampling material, because of its radiation hardness. In the FCAL, placed in the very forward region, the passive layers are made of copper and tungsten.

4.3.3 Muon Spectrometer

The Muon Spectrometer (MS) is the outermost layer of the ATLAS detector [101]. Its role is to furnish an identification and reconstruction system for muons. These particles have high penetration power and typically pass through the previous layers of the detector. The MS is composed of a barrel and two end-cap structures, all equipped with a toroidal magnet system. The magnetic field strength is about 0.5T and 1T in the barrel and end-cap respectively. The barrel MS toroid magnet is made of eight superconducting coils, it is 25m long and extends

from 4.7 m to 10 m in radius. Three measurement planes, one before and after the toroid and one inside it, are built with a combination of Transition Monitored Drift Tubes (MDT) and Resistive Plate Chambers (RPC). Together they provide a good trigger and reconstruction system for muons.

The end-caps toroid magnets are also composed of eight superconducting coils, each 5m long and with a diameter of 10m. The end-caps coils are inserted inside the barrel toroid magnet, as can be seen in the Fig. 4.7. The end-cap is equipped with Cathode Strip Chamber for the forward region around the beam pipe, because of the higher background rate, while MDT are used for the remaining parts. The end-caps are also equipped with a layer of Thin Gap Chambers that provide the trigger signal.

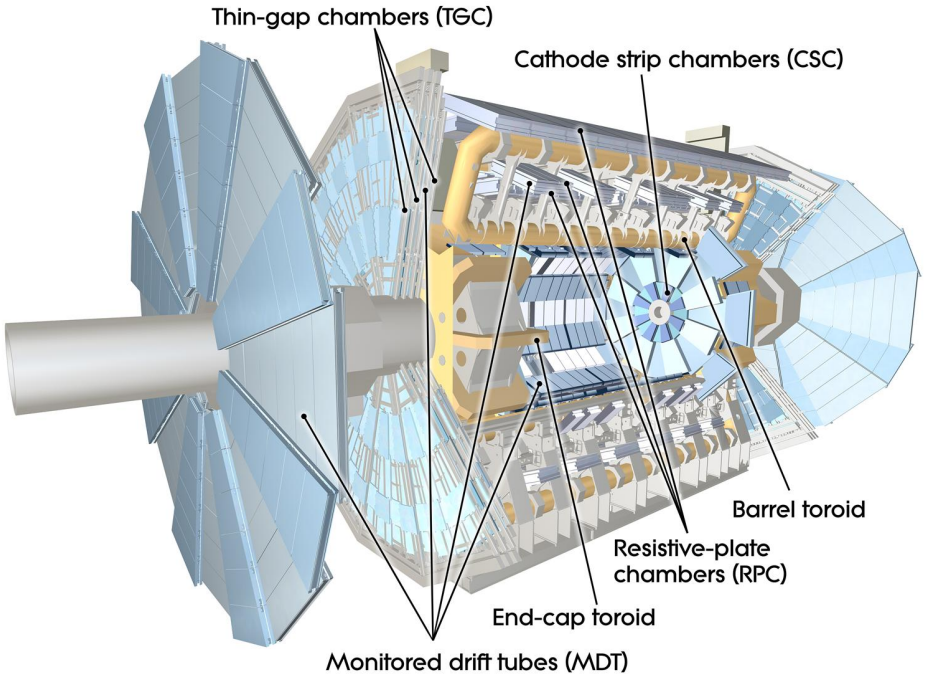

Figure 4.7 ATLAS Muon Spectrometer. The various detector subsystem are highlighted.

Chapter 5

Muon Tracking and Reconstruction

Muons are one of the stable products of the proton collisions at the LHC and are used by many measurements. This chapter presents the main aspects of track reconstruction, with a focus on the momentum determination, both in the Inner Detector, Sec. 5.1, 5.2 and in the Muon Spectrometers. In section 5.3 the problem of detector alignment and how it can degrade the momentum resolution is explored. Finally, in section 5.1, some ATLAS specific aspects of muon identification and reconstruction are presented.

5.1 Momentum reconstruction

The Inner Detector and the Muon Spectrometer is responsible for reconstructing the tracks of the muons traversing the detector. They then work as a spectrometer: they are embedded in a magnetic field (see sec. 4.3.1), that bends the charged particle trajectory into a helical path. From the magnitude of the bending it is possible to reconstruct the momentum of the particle. The curvature of the track is described through the sagitta s, i.e. the maximal distance of the track arc from its chord. A schematic representation of the sagitta of a particle track is shown in Fig 5.1.

Because the magnetic field **B** is directed along the $z-$direction, only the transverse momentum component, p_T, of the particle, is related to the sagitta. In the case of a high momentum particle exiting a detector region of radius L, embedded in magnetic field B, its transverse momentum, p_T, is given by [102]

$$p_T = \frac{8s}{0.3BL^2} \tag{5.1}$$

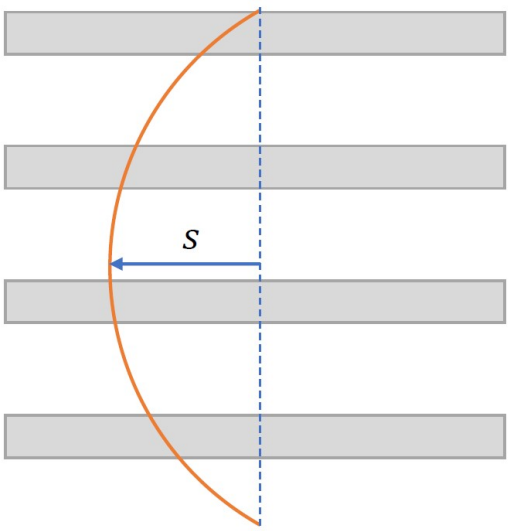

Figure 5.1 Definition of the sagitta s of an helical path crossing the detector.

where the units $B \sim [\mathrm{T}]$, $L \sim s \sim [\mathrm{m}]$ and $p_T \sim [\mathrm{GeV}]$ are used (and the 0.3 factor in the denominator is a unit conversion factor). It is interesting to have an estimate of the of the relative resolution affecting the p_T measurement due to the uncertainty of the detector positional measurements. The actual result depends on the precise structure and composition of the detector and the result has to be computed with numerical and Monte Carlo methods, but in the the case of a high p_T track, traversing N equally spaced detector layers, the result is given by [102, 103]

$$\frac{\sigma(p_T)}{p_T} = \frac{\sigma(s)}{s} = \frac{\sigma_{r\phi}}{0.3BL^2} \cdot \sqrt{\frac{720}{N+4}} \cdot p_T \tag{5.2}$$

where $\sigma_{r\phi}$ is the detector layer spatial resolution (here the same for every layer). A longer path in the bending plane and a more intense magnetic field, together with a larger number of detector layers, increase the p_T resolution. Because the sagitta is inversely proportional to the transverse momentum of the particle, the relative p_T resolution improves linearly with the p_T itself. The intrinsic positional resolution is therefore the dominant effect on the p_T resolution at high p_T. At low p_T another effect dominates the momentum resolution, the multiple scattering: i.e. a series of incoherent elastic scattering the charged particles undergo when crossing the detector material. The effect of the multiple scattering is a net change in the direction of the particle track. Without going into the details of the derivation, it can shown [104] that the relative uncertainty due to multiple scattering (MS) on the transverse

momentum measurement is given by

$$\left(\frac{\delta p_T}{p_T}\right)_{MS} = \frac{1}{0.3B}\frac{0.00136}{\beta}\sqrt{\frac{1}{LX_0}} \tag{5.3}$$

where $\beta = v/c$ is the particle velocity and X_0 the radiation length of the material. The effect of the detector material composition is contained in the dependence on X_0, a short radiation length leads to an higher uncertainty. For the p_T range of the particles reconstructed at the LHC, β, in equation 5.3, is basically one, so the relative uncertainty is constant as a function of p_T. At small transverse momentum, when the relative position uncertainty 5.2 becomes negligible, MS effects become dominant. The positional measurement uncertainty and the MS uncertainty can be assumed independent and the total uncertainty on the momentum is given by

$$\left(\frac{\delta p_T}{p_T}\right)_{\text{tot}} = \left[\left(\frac{\delta p_T}{p_T}\right)_{\text{meas}} \oplus \left(\frac{\delta p_T}{p_T}\right)_{\text{MS}}\right] = a\, p_T \oplus b \tag{5.4}$$

with a and b constants. This equation shows a standard parametrization of the transverse momentum resolution. Other sources of uncertainties come from the knowledge of the magnetic field **B**, in particular in the case of a non perfectly uniform magnetic field, and the alignment of the detector. The latter in particular will be explored for the Inner Detector in section 5.3.

5.2 ID tracking

The hits left by a charged particle on the ID elements are used to reconstruct its trajectory. The tracks are bent by the magnetic field into a helical paths, this can be parametrized with a set of five parameters. A typical choice in ATLAS is $\tau = (d_0, z_0, \phi_0, \theta_0, q/p)$, where d_0 and z_0 are the longitudinal and transverse impact parameters, θ_0 and ϕ_0 are the polar and azimuthal angle of the track. Both the impact parameters and the angles are defined at the perigee, i.e. the point of the track closest to the reference frame $z-$axis, as shown in figure 5.2. Finally q/p is the ratio between the charge of the particle and its momentum.

The first step in track reconstruction is the pattern recognition in which the detector hits belonging to the same particle track are identified. A typical approach is that of propagating the track parameters from one detector layers to the next one, looking for detector hits compatible with the track. A common method is a progressive track fit using Kalman-Filter [105]. This allows the parameter estimate to be updated, each time a new hit is added to the track, by just knowing the estimated parameters at the previous surface.

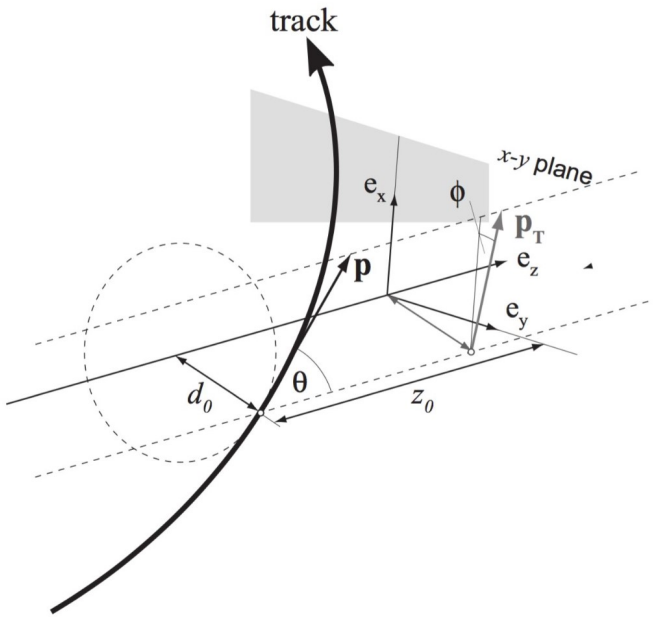

Figure 5.2 Definition of the track parameters. This are defined with respect to the perigee surface, the plane containing the $z-$axis and the perigee point. Other definition can be used, for example with respect to a detector element surface, where the impact parameters become the x and y local coordinates.

After the pattern recognition, the tracks are fitted exploiting the full knowledge from the hits. A typical approach is a least-square fit. The method consists in the minimization of the residual χ^2: the residual r_i of a detector hit is defined as the distance between the recorded hit and the fitted track on the detector element, $r_i = e(\tau)_i - m_i$. The χ^2 quantity from the residuals is given by

$$\chi^2_{\text{track}} = \mathbf{r}(\tau)^T V^{-1} \mathbf{r}(\tau) \tag{5.5}$$

where V represents the covariance matrix of the measurement and the vector notation is used. The approach to fit the track is to minimize the χ^2_{track} with respect to the track parameters τ, $d\chi^2/d\tau = 0$. In order to take into account of multiple scattering effects, additional parameters, representing the multiple scattering angles of the track at each detector layer, can be added to the track parametrization.

5.3 Inner Detector Alignment

Other than the intrinsic resolution of the detector elements, various additional uncertainties can degrade the particle momentum resolution. This section focuses on the alignment of

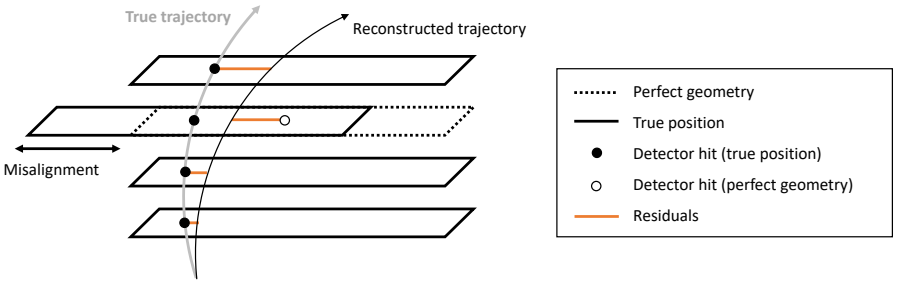

Figure 5.3 A schematic representation of the effect of detector misalignment in track reconstruction.

the detector. An imprecise knowledge of the detector element positions leads to a incorrect reconstruction of the particle track, as schematically shown in Fig. 5.3. The detector alignment is the procedure of determining the real position of the detector elements. The detector configuration can also slightly change in time, due to mechanical and thermal stress, and so the alignment needs to be studied over time. This task, in particular the investigation and monitoring of the momentum biases, Sec. 5.3.4, is a project I collaborated to during my PhD.

5.3.1 Alignment Principles

For the Inner Detector alignment a track-based method is used. A fit to extract simultaneously the track parameters together with positional information of the detector elements is performed. There are six parameters defining and correspond to three translations (T_x, T_y, T_z) and three rotation (R_x, R_y, R_z). As it will be explained later (Sec. 5.3.3), the alignment procedure is performed at various level of granularity. In the first level larger detector substructures, such as the the end-cap wheels, are considered. At the highest level of granularity, the six positional parameters are estimated for each silicon pixel module, silicon strip module and each TRT straw. The number of tracks required for the alignment procedure depends on the level of granularity, at the highest level, a large amount of tracks, of the order of few millions, is used.

5.3.2 Alignment Procedure

The starting point for the alignment procedure is the least square track fit presented in Sec. 5.2. A global χ^2 quantity is constructed by summing the individual track contributions,

χ^2_{track}, defined in eq. 5.5

$$\chi^2 = \sum_{\text{tracks}} \chi^2_{\text{track}} = \sum_{\text{tracks}} \mathbf{r}^T(\mathbf{a},\tau) V^{-1} \mathbf{r}(\mathbf{a},\tau) \tag{5.6}$$

where $\mathbf{a}$ is the vector of all the alignment parameters, and the dependence of the residuals on these quantities is made explicit. The minimization of χ^2 is done with respect to $\mathbf{a}$ ($d\chi^2/d\mathbf{a} = 0$). The problem is generally non linear and it is solved with an iterative procedure. The number of parameters to be extrapolated in eq. 5.6, and consequentially the number of tracks needed, depend on how many detector structures are being aligned. At the highest level of alignment, the position of each detector element is extracted, and the number of parameters is of the order of 10^5 (more details are given in the next section). The number of tracks used to built the global χ^2 in equation 5.6 is of the order of few millions, and the problem of minimization becomes computationally challenging. Various techniques are applied to overcome the problems, the details of the solution methods adopted in ATLAS can be found in Ref. [106].

In order to eliminate possible systematic biases in the track reconstruction due to the *weak modes*, unresolved movements of the detector (see Section 5.3.4), some constraints on the track parameters can be applied adding specific term to the χ^2_{track} definition in equation 5.5. These terms can come from beam spot constraints, constraints from independent momentum measurement (e.g. calorimeter measurements) or constraints from physics event measurements (mass measurement in a resonance decay system).

5.3.3 ATLAS Inner Detector Alignment during Run 2

In ATLAS the alignment procedure is organized in levels of granularity. At different levels larger or smaller detector substructures are aligned. A summary of the alignment configuration used during the Run 2 data taking is shown in Table 5.1. At level three all the detector elements, such as the single detector module, are aligned individually.

The higher the alignment level the higher the time and the computation resources that are needed, as well as the number of tracks required for the convergence of the procedure. The baseline of alignment constants, the starting point configuration for any time dependent improvement, is obtained by performing all the alignment levels listed in Table 5.1 and using a large amount of data ($\sim 2\,\text{fb}^{-1}$).

During data taking, because of thermal and mechanical stress, detector movements of $\mathcal{O}(10\mu\text{m})$ affect the goodness of the alignment. These movements have different time scales that goes from minutes to months. To improve the situation a time-dependent level 1

Table 5.1 Alignment levels definition. This configuration is used to extract the baseline alignment constants.

Level	Description	Structures	DoF
1	IBL	1	All
	Pixel detector	1	All
	SCT end-caps (SCT barrel fixed)	2	All except T_z
	TRT split into barrel and 2 end-caps	3	All except T_z
Si 2	Pixel barrel split into layers	4	All
	Pixel end-caps split into disks	6	All
	SCT barrel split into layers	4	All
	SCT end-caps split into disks	18	All
Si 3	Pixel barrel modules	1736	All
	Pixel end-caps modules	288	T_x, T_y, R_z
	SCT barrel modules	2112	All
	SCT end-caps modules	1976	T_x, T_y, R_z
TRT 2	TRT barrel split into barrel modules	96	All except T_y
	TRT end-caps split into wheels	80	T_x, T_y, R_z
	Pixel and SCT detectors fixed	0	
TRT 3	TRT straws	351k	
	Pixel and SCT detectors fixed		

alignment is performed within the ATLAS data-taking time calibration loop. In particular this is performed every 20 min at the beginning of the run and 100 min for the remaining time.

5.3.4 Momentum Biases

The *weak modes* have small or no effects on the global χ^2 defined in eq. 5.6 and therefore are not corrected by the standard track based alignment procedure. This can cause a wrong reconstruction of the track curvature and induce biases in the particle momentum reconstruction. To investigate them it is necessary to introduce further constraints, such as an independent measurement of the momentum from the calorimeters, or to analyze a system with fixed invariant mass (a resonant decay).

Example of detector *weak modes* are shown in Fig. 5.4. Two categories of distortions are identified

- *sagitta* distortions consists of movements of the detector elements orthogonal to the particle tracks. The consequent momentum bias is sensitive to the direction of the curvature and has opposite effects on positively and negatively charged particles.

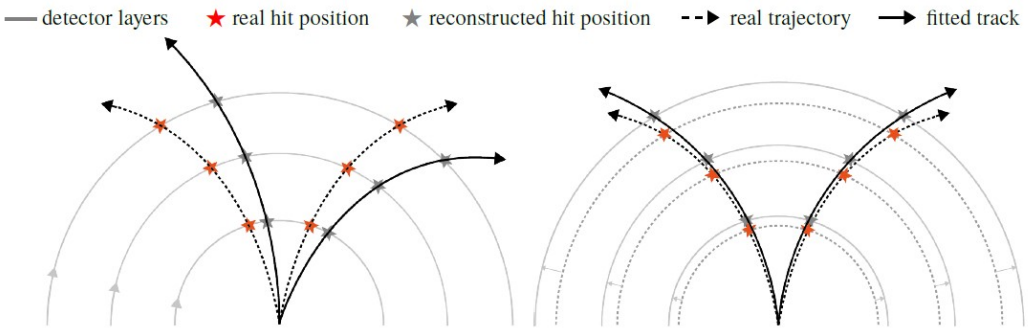

Figure 5.4 A schematic examples of weak modes detector deformations. *Sagitta* biases (left) are caused by deformations perpendicular to particle track. These affect positive and negative charged particles differently (different direction of the track curvature). *Length scale* bias (right) are due to deformations along the track. These affect in the same way positive and negative charges particles.

- *Length scale* biases are due to deformations happening along the particle tracks. In this case the distortion affects positive and negative charged particle momentum in the same way.

Sagitta Bias

Sagitta deformations lead to a bias, indicated as δ_{sagitta}, in the measured track sagitta. This can be used to parametrize the bias in the momentum as

$$p' = p(1 + q\, p_T\, \delta_{\text{sagitta}})^{-1} \tag{5.7}$$

where p is the real momentum of the particle and p' is the reconstructed one, affected by the bias. The charge q of the particle enters in the denominator. $\delta_{sagitta}$ is the parameter that defines the deformation, and can depend on the detector coordinates η and ϕ. Two methods are used to determine the effect of the sagitta biases. The first is to look at the decay of resonant particles, such as Z boson decay particles, reconstructing the invariant mass of the di-lepton final state. Comparing the reconstructed mass to the true one, known with high precision, it is possible to identify the effect of the bias. In particular, using eq. 5.7, and calculating the invariant mass at first order in $\delta_{sagitta}$, one obtains

$$m^2_{\mu\mu} - m^2_Z \approx m^2_Z\,(p^{'+}_T \delta_{\text{sagitta}}(\eta^+, \phi^+) - p^{'-}_T \delta_{\text{sagitta}}(\eta^-, \phi^-)) \tag{5.8}$$

wehre $m_{\mu\mu}$ is the reconstructed mass and m_Z is the true value. An iterative procedure is used to decouple the negative and positive contribution and obtain a detector map of $\delta_{sagitta}$ values.

The second method consists of using the energy measurement of the EM calorimeters for electrons and positrons. This measurement is independent from the ID tracking and any possible bias in the measurement would affect positively and negatively charged particles in the same way. A comparison of the ratio between the calorimeter energy E and the ID momentum p for oppositely charge particle gives an estimation on the δ_{sagitta}. In particular

$$\delta_{\text{sagitta}} = \frac{(E/p')^+ - (E/p')^-}{2(E_T)} \tag{5.9}$$

where E_T is the calorimeter transverse energy (supposed to be the same, on average, for opposite charged particles).

The residual sagitta biases are studied and cross-checked with these two methods. A correction is performed applying some constrains on the track parameters during the alignment procedure, sec. 5.3.2.

During run 2, for example, the residual sagitta bias have been reduced to less than $\sim 0.1\,\text{TeV}^{-1}$ (corresponding to a 1% bias for a 100 GeV track).

Length Scale Biases

Displacement of the detector elements parallel to the particle track induce a charge-symmetric bias in the momentum. The combination of two types of distortions can be identified. A *radial expansion*, i.e. a change in the radius of the detector, $R \to R(1+\varepsilon_r)$, leads to a bias on the transverse momentum, while leaving the the longitudinal momentum component unbiased

$$p'_T = p_T(1+\varepsilon_r) \tag{5.10}$$

On the contrary a *longitudinal expansion* of the detector, $z \to z(1+\varepsilon)$, leaves the transverse momentum unchanged, but induces a bias in the longitudinal momentum component

$$p'_Z = p_Z(1+\varepsilon_z) \tag{5.11}$$

Similarly to what is done for the sagitta bias, a comparison of the reconstructed Z mass to the true value allows the length scale biases to be extracted. Because they affect different components of the momentum, it is possible to distinguish between the longitudinal and

radial biases. An analysis of the ATLAS run 2 data found a bias of $\varepsilon_r \approx \varepsilon_z \sim 0.9 \times 10^{-3}$ [106]. An ambiguity in this study is given by the fact that length scale biases are indistinguishable by the effect of a non perfect knowledge of the magnetic field in the ID. It will continued to be considered in future how best to resolve between these two effects.

5.4 Muon reconstruction

The signature of muon tracks is given by signals in the muon spectrometer or by characteristic signal in the calorimeter (that of minimum-ionising particles). Muon tracks are reconstructed independently both by the ID and by the MS. The ID tracks are reconstructed just as any other charged particles. Additional information can come also from the calorimeters. According to which detector information are used to determine the final muon tracks, different muon track types are defined:

- Combined muons (CB): Muon tracks are reconstructed independently by the ID and the MS. The two results are then combined with a global refit of the tracks. Usually the refit is performed starting from the hits in the MS and proceeding back to the inside of the detector. The opposite inside-out fit can be used as a complementary approach.

- Segmented-tagged (ST) muons: muons are identified as ST if the ID track, extrapolated to MS, is associated with at least one track segment in the MS. ST muons are used when the particle crosses only one layer of the MS either because they are low p_T muons, or because the tracks fall in a low efficiency region of the MS.

- Calorimeter-tagged (CT) muons: an ID track is identified as a muon if it is associated with a calorimeter deposit consistent with that of minimun-ionizing particle. It is the category of muons with the lowest purity, but it recovers some efficiency in the detector region where the MS is poorly instrumented.

- Extrapolated muon (ME) muons: the muon tracks are reconstructed using only the hits recorded in the MS and applying a loose requirement on the Impact Parameter of the tracks. An estimate of the energy loss by the muon traversing the calorimeters layer is also taken into account. ME muons are typically used to extend the reconstruction acceptance to higher rapidity, $2.5 < |\eta| < 2.7$, a region not covered by the ID.

These muon *types* are defined to maximise the muon efficiency offered by the detector. Eventually each muon track will belong to only one particular type. In the case of overlapping

between muon types, algorithms to solve the ambiguity are used. If the various algorithms share the same ID track, the overlap is resolved giving preference first to CB muons, then to ST muons and finally to CT muons. A track quality based decision is used instead to resolve the overlaps between the ME muons types.

5.5 Muon Identification

Muon identification criteria are defined to reject the background, mainly from pions and kaon decay, and, at the same time, to select prompt muons with good momentum resolution. Non prompt muons usually present in the tracks a characteristic *kink* topology, due to the in-flight decay of the mother particle. This track topology is expected to give a poor fit quality of the ID and MS combined track and to be rejected. To guarantee a good momentum measurement a requirement on the number of hits in the ID and in the MS is applied. Four identification selection working points are provided in order to satisfy the specific needs of the various physics analysis: *Medium*, *Loose*, *Tight* and *High-p_T*. *Medium*, *Loose* and *Tight* are inclusive categories, that means, muons identified in the stricter category are included in the looser ones.

- *Medium Muons* are designed to minimize the reconstruction and calibration systematic uncertainties. These are the default selection in ATLAS. Only CB and ME muons are considered

- *Loose muons* are defined to maximises the reconstruction efficiency, still offering a good muon momentum resolution. This working point is optimized for the Higgs analysis in the four lepton final state [107]. All muon type are considered. The *Medium* muons are included in the *Loose* selection.

- *Tight Muons* maximise the purity at the cost of a lower reconstruction efficiency. In particular more stringent selection criteria are required at low p_T where the probability of misidentification is higher.

- *High p_T Muons* maximise the momentum resolution for tracks with p_T greater than 100 GeV. This working point is optimized for high mass Z' and W' searches.

Table 5.2 Definition of the isolation working points.

Isolation WP	Discriminating variable(s)	Definition
LooseTrackOnly	$p_T^{\text{varcone30}}/p_T^{\mu}$	99% efficiency constant in η and p_T
Loose	$p_T^{\text{varcone30}}/p_T^{\mu}$, $E_T^{\text{topocone20}}/p_T^{\mu}$	99% efficiency constant in η and p_T
Tight	$p_T^{\text{varcone30}}/p_T^{\mu}$, $E_T^{\text{topocone20}}/p_T^{\mu}$	96% efficiency constant in η and p_T
Gradient	$p_T^{\text{varcone30}}/p_T^{\mu}$, $E_T^{\text{topocone20}}/p_T^{\mu}$	$\geq 90(99)\%$ effciency at $25\,(60)\,\text{GeV}$
GradientLoose	$p_T^{\text{varcone30}}/p_T^{\mu}$, $E_T^{\text{topocone20}}/p_T^{\mu}$	$\geq 95(99)\%$ efficiency at $25\,(60)\,\text{GeV}$
FixedCutTight	$p_T^{\text{varcone30}}/p_T^{\mu}$, $E_T^{\text{topocone20}}$	$p_T^{\text{varcone30}}/p_T^{\mu} < 0.06$, $E_T^{\text{topocone20}}/p_T^{\mu} < 0.06$
FixedCutTightTrackOnly	$p_T^{\text{varcone30}}/p_T^{\mu}$	$p_T^{\text{varcone30}}/p_T^{\mu} < 0.06$
FixedCutLoose	$p_T^{\text{varcone30}}/p_T^{\mu}$, $E_T^{\text{topocone20}}/p_T^{\mu}$	$p_T^{\text{varcone30}}/p_T^{\mu} < 0.15$, $E_T^{\text{topocone20}}/p_T^{\mu} < 0.30$

5.6 Isolation

A measurement of the isolation of the muon tracks with respect to other particles can be used to discriminate between background and signal. Muons produced in W and Z decays, for example, are usually well isolated from the other particles, while muons coming from hadron semileptonic decays are produced in jets and surrounded by other particles. Isolation is a measure of the physics activity around the tracks. Two isolation variables are available and based on track or calorimeter information:

- The *track based isolation variable*, $p_T^{\text{varcone30}}$, is defined as the scalar transverse momentum sum of the tracks with $p_T > 1\,\text{GeV}$ in a cone of size $\Delta R > \min(10\,\text{GeV}/p_T^{\mu}, 0.3)$ around the muon, excluding the muon track itself.

- The *calorimeter isolation variable*, $E_T^{\text{topocone20}}$, is defined as the sum of the transverse energy of topological cluster in a cone of a size $\Delta R = 0.2$ around the muon, after subtracting the muon signal and correcting for the pileup contribution.

Using the isolation variables defined above, various working points, optimized for different physics analysis, are defined. These are listed, together with their definition, in table 5.2.

Chapter 6

Low Mass Drell-Yan Selection

Measurements of the Drell-Yan process provide a sensitive test of perturbative and non-perturbative QCD effects and allow us to improve the knowledge of the parton distribution functions. Drell-Yan dilepton production is the simplest process from the point of view of QCD calculation: at leading order QCD enters only via the PDFs. To enhance the sensitivity to the PDFs, a measurement of the exchanged boson rapidity can be performed, as this observable is correlated to x_1 and x_2, the fraction of proton momentum carried by the partons. Another interesting variable is the dilepton transverse momentum: this distribution is difficult to predict as the higher part of the spectrum requires higher perturbative order contributions in the calculation, while the lower part needs the inclusion of resummation effects. Many Drell-Yan measurements, reaching an high level of precision, have been performed at the LHC, the ATLAS collaboration for example in Ref. [17, 66, 108], the CMS collaboration in Ref. [68, 109], or LHCb in Ref. [110, 111].

Starting from this chapter a Drell Yan cross-section measurement in the low invariant mass region of the final state leptons is presented. Section 6.1 introduces the scope and the motivation of the measurement. Section 6.2 reports the fiducial volume and the binning scheme used for the measurement. Sections 6.3 and 6.4 describe the data and MC samples used in the analysis. In section 6.5 the selection requirements are discussed, while section 6.6 focuses on the triggers adopted in the measurement. Section 6.7 describes the correction applied to the MC samples in order to improve the data modelling. Finally, Section 6.8 describes two control regions used in the analysis.

6.1 The low mass Drell-Yan Measurement

The low mass Drell-Yan measurement is performed using the data collected with the ATLAS detector during the LHC Run 2 in proton-proton collision at the centre of mass energy of 13 TeV. The data set is a subset of the full Run2 data; it includes the data taken in 2015 that corresponds to $1.28\,\text{fb}^{-1}$ of recorded luminosity. The invariant mass region considered in this analysis is below the Z peak, specifically between 7.3 GeV and 56 GeV, with the exclusion of the window between 8.7 GeV and 12 GeV. This range is complementary to the interval explored by ATLAS in other DY analysis that usually focus on the Z mass peak region. The analysis targets a muon anti-muon pair in the final state. Muons, thanks to the performance of the MS, are reconstructed with good momentum resolution in this kinematic range.

The measurement consists of the extraction of the Drell-Yan process inclusive cross section binned differentially in various dilepton kinematic variables. The differential cross section is measured in bins of the invariant mass of the dilepton final state. For each mass bin a measurement in bins of the absolute dilepton rapidity $|y_{\mu\mu}|$ and, alternatively, in bins of the dilepton transverse momentum $p_T^{\mu\mu}$, is performed. The rapidity measurement brings sensitivity to x, the momentum fraction carried by the partons, and it is interesting for PDF and phenomenology studies, for example for testing small-x non-perturbative dynamics such as BFKL dynamics [5]. In Figure 6.1 the phase space of the analysis is reported on the $x - Q^2$ plane, where Q^2 is the hard energy scale of the process. The $p_T^{\mu\mu}$ result offers instead novel measurement of the DY transverse momentum spectrum at high pp energy collision but low invariant mass of the dilepton final state. The measurement is of particular interest as a test of the different p_T resummation calculations in this new kinematic region.

This measurement extends a previous ATLAS analysis performed with data at 7 TeV [4]. The new analysis explores lower x values thanks to the extension to lower mass and to the higher centre of mass energy of the collisions. Furthermore it explores double differential measurements useful to extract more physical information, while the 7 TeV analysis only presented a mass single-differential measurement. Another LHC measurement of the DY process at a low mass range is the single differential mass measurement performed by CMS [112]. The LHCb DY measurement presented in Ref. [110] analyses masses around the Z boson mass peak, but considers a very high di-muon rapidity range, and thus has sensitivity to low-x values.

The main challenges of the measurement come from the large fraction of background events, in particular in the lowest mass bins where there is a big component of QCD background events. This fraction is difficult to describe in MC simulation and the estimation

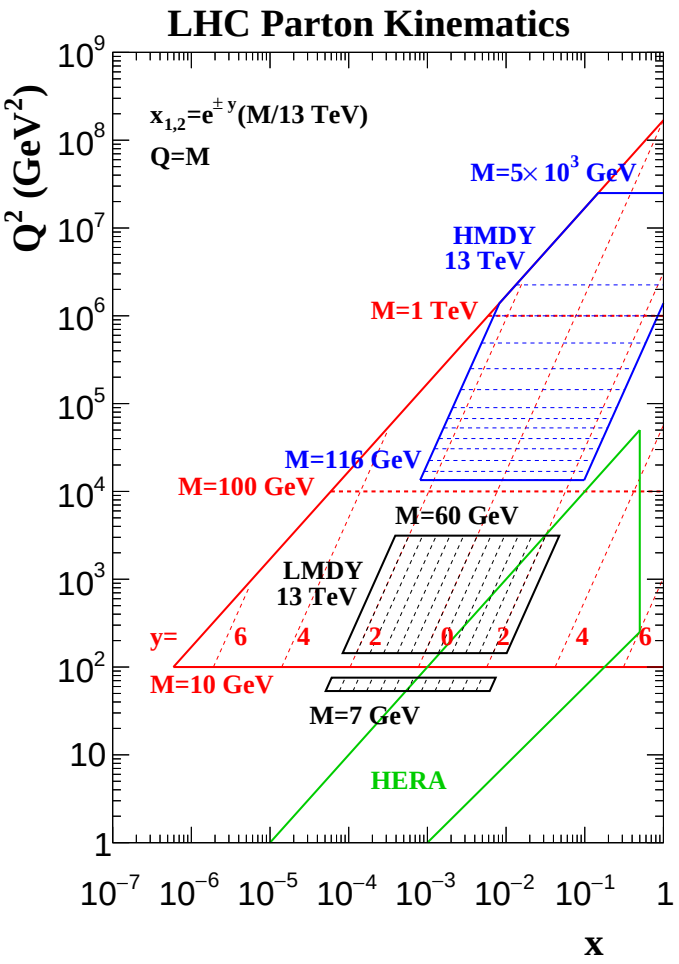

Figure 6.1 In the black and blue boxes the kinematic phase space explored by the low mass DY and high mass DY respectively is shown. This is an estimation at Leading Order in QCD. In red is instead shown the phase space covered at the LHC.

needs to be tuned to the data. Studies related to the background estimation are the subject of chapter 7 and 8.

6.2 Fiducial Selection and Cross-Section definition

The cross-section is measured single and double differentially. It is binned in mass, absolute rapidity and transverse momentum of the dilepton pair. Other processes that can give two muons in the final state are subtracted to the data selection as background. The fiducial selection region is chosen as close as possible to the experimental selection, in order to reduce extrapolation effects. The kinematic requirements for the fiducial selection are

- $p_T^{\mu} > 4.5\,\text{GeV}$
- $|\eta_{\mu}| < 2.4$
- $7.3 < m_{\mu\mu} < 8.7\,\text{GeV}$ and $12 < m_{\mu\mu} < 56\,\text{GeV}$
- $|y_{\mu\mu}| < 2.4$
- $p_T^{\mu\mu} > 10\,\text{GeV}$ in the mass bin $7.3 < m_{\mu\mu} < 8.7\,\text{GeV}$

The cross section is extracted at Born level, that means, the kinematics of the particles is considered prior to the QED final state radiation. The radiation effects are corrected with MC when extracting the cross section, see Chapter 9 for more details.

The mass bins considered are

$$m_{\mu\mu} = [7.3, 8.7] + [12, 14, 17, 22, 28, 36, 46, 56]\,\text{GeV} \tag{6.1}$$

for each $m_{\mu\mu}$ bin the measurement is performed in bins of $|y_{\mu\mu}|$

$$|y_{\mu\mu}| = [0.0, 0.4, 0.8, 1.2, 1.6, 2.0, 2.4] \tag{6.2}$$

Alternatively, for each mass bin, a measurement in $p_T^{\mu\mu}$ is performed, with the following binning

$$p_T^{\mu\mu} = [0.0, 1.5, 3, 5, 10, 16, 22, 30, 40, 55, 85]\,\text{GeV} \tag{6.3}$$

6.3 Data samples

The data events used for this measurement were recorded in 2015. The energy of the proton beams circulating inside the LHC was 6.5 TeV, and the beam bunch spacing was 25 ns. The peak instantaneous luminosity for this period has been recorded to be $\mathscr{L} = 5.1 \cdot 10^{33}\,\text{cm}^{-1}s^{-1}$ while the average number of pileup events, multiple interactions per bunch crossing, was $\langle\mu\rangle = 13.5$. The total recorded luminosity for the data set is $L = 1.28\,\text{fb}^{-1}$. The events considered for the selection belong to a Good Run List (GRL). A GRL consist of a series of luminosity block in which the beams circulating in the LHC were in stable conditions and the detector components were functioning properly [113].

6.4 MC samples

Monte Carlo samples are used in the measurement to simulate signal and background events. These help to optimize the analysis, to perform the cross section unfolding and to evaluate the systematic uncertainties. Some of the samples are also used to estimate the number of background events entering the analysis selection. The samples are produced centrally by the ATLAS collaboration. The signal events correspond to Drell-Yan $\gamma^*/Z \to \mu\mu$ events. For a detailed description of the background processes refer to chapter 7, here only the MC generators are described.

Almost all the signal and the electroweak samples are generated with the `Powheg` Monte Carlo program [114, 115, 116]. The Drell-Yan samples $pp \to \gamma^*/Z \to l^+l^- + X$ with $l = \tau, \mu$ are produced at NLO+NLL in α_S with `Powheg-Box v2` interfaced with the `Pythia v8.1` parton shower program [117]. The program used the CT10nlo PDF set [118] and the AZNLO CTEQ6L1 tune for `Powheg+Pythia` [119]. This tune was obtained to better describe the $Z-$boson p_T spectrum [120]. The signal $\gamma^*/Z \to \mu\mu$ events are also reweighted to NNLO in α_S using NNLO to NLO KFactor as a function of the dilepton invariant mass (and only for mass greater the 10 GeV, below the KFactor were not available). The NNLO QCD prediction is calculated with `VRAP v0.9` [121] and the CT14NNLO PDF set [122]. Two loop EW corrections, calculated with the `MCSANC` program [123], are also applied through the KFactor method.

The $t\bar{t}$ sample is generated with the `Powheg+Pythia8` generator at NLO+LL. The total cross section is normalized to the NNLO+NNLL prediction from the `Top++ v2.0` program [124]. A di-lepton filter is applied to the generated sample.

The exclusive $\gamma\gamma \to \mu\mu$ events are generated using `Herwig++ v2.5.1` [125]. The single dissociative process is simulated using `LPair v4.0` [126]. The proton dissociation is modelled with the Suri-Yenni [127] or Brasse [128] structure functions, depending on the virtuality of the emitted photon. For the final state of the dissociated proton, `LPair` is interfaced to `Jetset v7.408` [129], that implements the `Lund` fragmentation model [130]. The same model was implemented in `Pythia6` version [131]. The double dissociative $\gamma\gamma \to \mu\mu$ events are generated with `Pythia` using the NNPDF2.3QED [132] photon PDF. Depending on the multiplicity of the dissociated protons, the `Pythia` string or mini-string fragmentation model is used.

QCD multijet $b\bar{b}$ and $c\bar{c}$ samples are generated with `Pythia` [117] with the A14 tune [133]. These samples are used for analysis optimizations and evaluation of the uncertainties. The actual number of events for this background is extracted from the data (see section 7.2).

Table 6.1 Summary of the MC generators used in the analysis to simulate signal and background events.

Channel	Generator	Order
$\gamma^*/Z \to \mu\mu$	Powheg-Box v2+Pythia8	NLO+LL (+NNLO kF)
$\gamma^*/Z \to \tau\tau$	Powheg-Box v2+Pythia8	NLO+LL
diboson	Powheg-Box v2+Pythia8	LO+LL
$\gamma\gamma \to \mu\mu$	Herwig v2.5.1	LO
Sd $\gamma\gamma \to \mu\mu$	LPair v4.0	LO
Dd $\gamma\gamma \to \mu\mu$	Pythia8	LO
$t\bar{t}$	Powheg-Box v2+Pythia8	NLO+LL (norm. to NNLO+NNLL)
$\Upsilon_{1S/2S/3S}$	Pythia+Photos	LO+LL
W+jets	Powheg-Box v2+Pythia8	LO+LL

The Υ resonance decay to two muon are a background in this analysis. The three Υ excited states and consecutive decays, $\Upsilon(1S) \to \mu\mu$, $\Upsilon(2S) \to \mu\mu$, $\Upsilon(3S) \to \mu\mu$, are simulated with `Pythia 8.1` [117].

All the generators are interfaced with the `Photos++` program [134] that implements QED radiation of the final state.

The multiple interactions per bunch crossing (pile-up) are modelled by overlying the soft QCD activity over the hard scattering events. The soft QCD is generated with `Pythia 8` using the ATLAS dedicated tune AU2 [135] and the CT10NLO PDF [118].

The generated events go through a simulation of the detector response. This is simulated with the `GEANT4` toolkit [136][137]. The reconstruction algorithm is then the same for data and MC.

6.5 Event Selection

The analysis targets muons in the final state. Muons are reconstructed combining MS and ID information, these objects are referred to as combined muons, as explained in section 5.4. Among the recorded events various selection criteria are applied, in order to have good quality reconstructed particles and to maximise the number of signal events in the event selection. The kinematic region of the selected events is also referred to as Signal Region (SR).

At first an event level selection is applied

- Each selected event is in the list of good runs, runs in which the condition of the detector and the beam were stable.

- the event is required to pass one of the following High Level Trigger (HLT) chain [138]
  - `HLT_mu6_iloose_mu6_11invm24_noos`
  - `HLT_mu6_iloose_mu6_24invm60_noos`
  - `HLT_mu4_iloose_mu4_7invm9_noos`
  - `HLT_mu4_iloose_mu4_11invm60_noos`

The property of the HLT triggers are explored in the next section. After the muon candidates are reconstructed as combined muons, the following selections are applied

- The event must contain at least two combined muons
  - if more than two muons are found in the event, the particles with highest p_T are considered.
- Each muon must have $p_T^{\mu} > 4.5\,\text{GeV}$
- Each muon must have $|\eta^{\mu}| \leq 2.4$
- Each muon passes the *Medium* identification working point, the definition of *Medium* muon is given in section 5.5.
- Muon passes the *FixedCutTight* isolation working point. Definition in section 5.6.

The dimuon triggers considered in the analysis select muons with transverse momentum as low as 4 GeV. In order to avoid the turn on phase of the trigger efficiency a cut at $p_T^{\mu} > 4.5\,\text{GeV}$ is imposed. The muon rapidity requirement is instead imposed by the limit of the muon spectrometer fiducial acceptance.

The isolation requirement is important in particular to reduce the heavy flavour multijets events. The muons in these events are produced within jets, so at small angular separation from other physics activity. This isolation requirement greatly reduces this background component.

Finally a selection on the kinematics of the dimuon system is applied

- The dimuon invariant mass is between $7.3 < m_{\mu\mu} < 8.7\,\text{GeV}$ or $12 < m_{\mu\mu} < 56\,\text{GeV}$
- in the first invariant mass bin, $7.3 < m_{\mu\mu} 8.7 <$ GeV, a cut on the dimuon transverse momentum, $p_T^{\mu\mu} > 10\,\text{GeV}$, is applied: in this part of the spectrum, because of the $p_T^{\mu} > 4.5\,\text{GeV}$ cut, the signal events are highly suppressed and it has decided to exclude these events from the selection.

The low invariant mass selection range excludes the mass window $8.7 < m_{\mu\mu} < 12\,\text{GeV}$. This is because of the presence in this region of the hadronic Υ particle resonances. The Υ is a meson composed by a b quark and its antiparticles. Various excited state of the Υ are produced in this range, and the meson immediately decay (Υ life time $\sim 1.21 \times 10^{-20}\,\text{s}$) through the annihilation of the $b\bar{b}$ pair. One possible decay channel is the annihilation into a photon that then decays into two lepton. This mass window is then excluded by the measurement because the Υ events would have dominated the event selection. The dimuon final state of the Υ decay is instead used as a control region for the measurement, more details are given in section 6.8.1.

The Drell-Yan process produces two opposite charged leptons in the final state, but a requirement on the muon pair to be opposite sign in charge is not applied in the first place as the distribution in the analysis studies are plotted after performing a same-sign opposite-sign subtraction. This is done in order to reduce multijet fake muon contribution, that is distributed symmetrically in charge. This is discussed in more details in section 7.1.2.

6.6 Triggers

The requirements of the `2mu4` (`2mu6`) triggers listed in the previous section are the following

- detection of two muons with the following kinematic requirements
  - $p_T > 4(6)\,\text{GeV}$
  - the dimuon invariant mass is between the range defined by the term `AinvB` in the trigger name: $A < m_{\mu\mu} < B$
- a compatibility of the two muons tracks with the same vertex, 2-tracks vartex $\chi^2(ndf = 3) < 20$.
- at least one muon passes a loose track-based isolation requirement in a cone $\eta - \phi$ of radius 0.12 (`iloose`).
- no opposite-charge requirement is applied at HLT

The triggers were active for instantaneous luminosities below $3 \cdot 10^{33}\,\text{cm}^{-1}\text{s}^{-1}$. During the active period, the analysis triggers were operating with different, fixed prescale. The integrated luminosity recorded by the triggers `HLT_mu6_iloose_mu6_11(24)invm24(60)_noos` (`HLT_mu4_iloose_mu4_7(11)invm(24)_noos`) is $1280.28 pb^{-1}$ ($319.68\,\text{pb}^{-1}$). The recorded luminosity and the trigger prescale are summarized in table 6.2.

Table 6.2 List of the analysis triggers with the corresponding prescale and recorded luminosity. A prescale of 0.25 means that, on average, only one event out of four was recorded. The triggers in the list were active only for instantaneous luminosities below $3 \cdot 10^{33} cm^{-1} s^{-1}$.

Trigger Chain Name	Average Prescale	Recorded Luminosity [pb^{-1}]
HLT_mu4_iloose_mu4_7invm9_noos	1	319.68
HLT_mu6_iloose_mu6_24invm60_noos	1	319.68
HLT_mu6_iloose_mu6_11invm24_noos	0.25	1280.28
HLT_mu6_iloose_mu6_24invm60_noos	0.25	1280.28

Table 6.3 The table shows how the events in MC simulation to which apply the additional 0.25 reconstruction weight are selected. This additional weight mimic the different prescale between the 2mu4 and 2mu6 triggers during data taking.

	Fired Trigger		
Subleading muon p_T	Pass 2mu4	Pass 2mu4 AND 2mu6	Pass 2mu6
$p_T^{Sub} > 6.5\,\text{GeV}$	Apply PS weight = 0.25	-	-
$p_T^{Sub} < 6.5\,\text{GeV}$	Apply PS weight = 0.25	Apply PS weight = 0.25	-

The MC simulation of the 2mu4 and 2mu6 triggers does not take into account the different prescale. This is instead implemented at analysis level by multiplying the MC reconstruction weight by an additional 0.25 factor that mimics the prescale. The additional prescale weight is applied to the MC events that are recorded by the 2mu4 trigger. A more detailed description of the class of events to which the prescale weight is applied is given in table 6.3. The cross section results (chapeters 9, 11) are normalized to the luminosity recorded by the 2mu6, $L_{\texttt{2mu6}} = 1280\,\text{fb}^{-1}$. The lower luminosity recorded by the 2mu4 triggers is taken into account as an additional detector inefficiency (the factor 0.25 mentioned above).

6.6.1 Trigger Efficiency

In this section a study of the trigger efficiencies as a function of the reconstructed invariant mass of the dimuon pair is presented. The study is performed using Monte Carlo DY ($\gamma^*/Z \to \mu\mu$) samples only and it is important in defining the mass range of the analysis. The trigger efficiency, ε, in a bin i, is defined as the number of events reconstructed in the bin dived by the number of events generated in the same bin.

$$\varepsilon_i = \frac{N_i^{Reco}}{N_i^{Gen}} \tag{6.4}$$

The turn-on phase of the triggers efficiencies, before reaching the efficiency plateau, is avoided by the reconstruction selection because the MC detector simulation could behave differently with respect to the data in this region and the differences are not covered by the trigger efficiency scale factor. In this section it is shown that, because of double invariant mass requirement in the trigger chain, the trigger efficiency turn-on is of the order of few GeV, wider than expected.

The Monte Carlo signal samples used for the study are the same used in the low mass DY analysis (see section 6.4)

- $\gamma^*/Z^* \to \mu\mu$ `Powheg+Pythia8` $6 < m_{\mu\mu} < 10$
- $\gamma^*/Z^* \to \mu\mu$ `Powheg+Pythia8` $10 < m_{\mu\mu} < 60$
- $\gamma^*/Z^* \to \mu\mu$ `Powheg+Pythia8` $m_{\mu\mu} > 60$

The triggers studied are the same described in section 6.5.

Additional requirement at final recostructed level are imposed to mirror the requirements in the analysis

- The event should contain two muons with opposite charge sign
- Muon reconstruction working point is *medium*
- $\eta_{\mu_1,\mu_2} < 2.4$
- $p_T^{\mu_1,\mu_2} > 4.5\,\text{GeV}$ for `HLT_2mu4` triggers
- $p_T^{\mu_1,\mu_2} > 6.5\,\text{GeV}$ for `HLT_2mu6` triggers
- The invariant mass range analysed is contained between $5\,\text{GeV} < m_{\mu\mu} < 70\,\text{GeV}$

The *trigger efficiency* is defined as the ratio of the number of events reconstructed in a bin over the number of events generated in the same bin. This quantity is studied as a function of the invariant mass of the dimuon pair. In figure 6.2 the efficiency of the trigger `HLT_2mu4_7invm9` `OR` `HLT_2mu4_12invm60` is plotted, while the efficiencies of the trigger `HLT_2mu4_12invm24` and the trigger `HLT_2mu6_24invm60` separately are shown in figure 6.3. The efficiency of the `OR` operation of the two `HLT_2mu6` triggers is instead reported in figure 6.4.

The turn on phase in which the trigger efficiencies reach the plateau is of the order of few GeV, larger than what expected. This behaviour is evident in figure 6.4 where it causes a loss

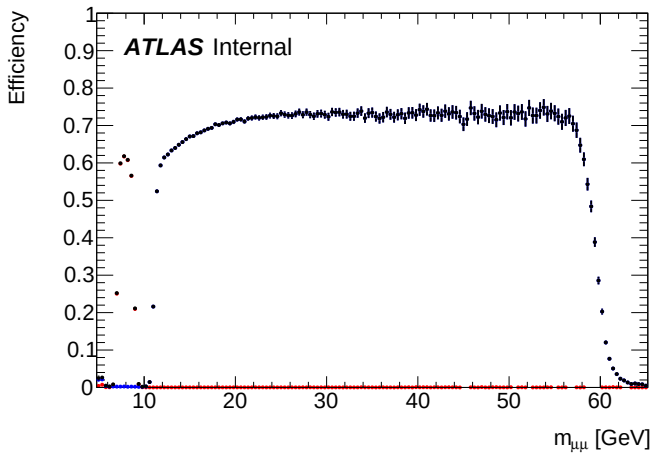

Figure 6.2 Efficiency of the `HLT_2mu4_7invm9` `OR` `HLT_2mu4_12invm60` triggers.

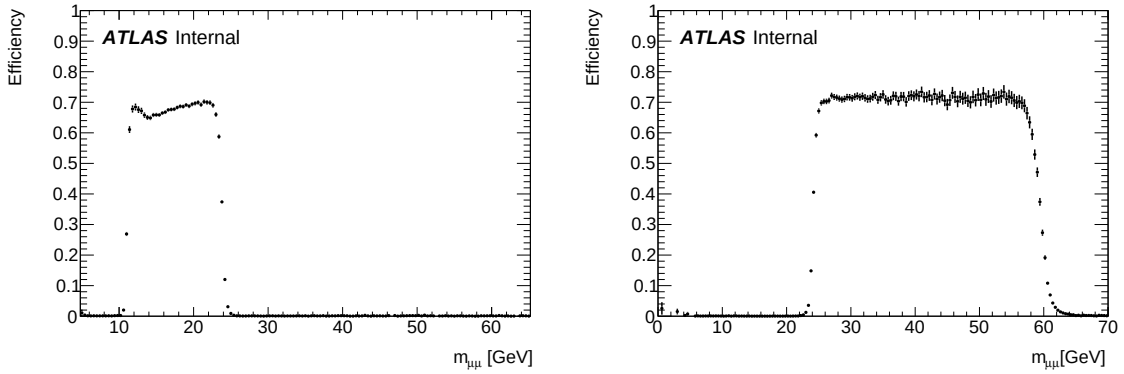

Figure 6.3 The efficiency as a function of the dimuon invariant mass of the trigger `HLT_2mu6_12invm24` on the left and of the trigger `HLT_2mu6_24invm60` on the right.

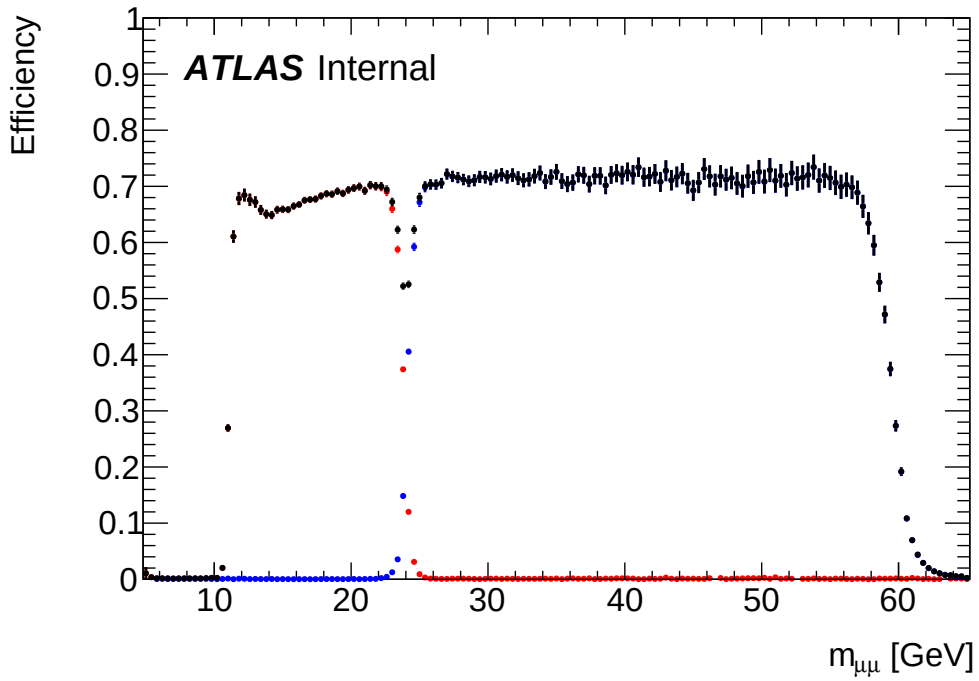

Figure 6.4 Efficiency of the HLT_2mu6_12invm24 OR HLT_2mu6_24invm60 triggers. The loss of efficiency around 24 GeV is due to the long turn on phase of the triggers.

of efficiency around 24 GeV, the mass edge value for the two HLT_2mu6 triggers. The long turn on of the trigger efficiency is due to the double invariant mass requirement in the trigger chain [138], the first at the *Level2* (L2) and at the second at the *Event Filter* (*EF*), both at the same reconstructed mass value. The mass reconstruction at *L2* is not as precise as the *EF* one and some events, that would have passed the *EF* selection, are instead discarded at the first mass cut, thus leading to a loss of efficiency. A schematic representation of this effect is given in Figure 6.5. The figure 6.6 shows the trigger efficiency for the OR selection of all the analysis triggers. The dashed line in the Figure mark the edges of the invariant mass selection, $7.3 < m_{\mu\mu} < 8.7$ GeV and $12 < m_{\mu\mu} < 56$ GeV. As it can be seen from the plot, this is chosen to be inside the plateau region of the trigger efficiency. The rise of efficiency around 12 GeV is actually due to the prescale factor applied on the low p_T, 2mu4, triggers, as explained in section 6.6.

6.7 Corrections to the MC samples

Monte Carlo samples are used to simulate background and signal events in the analysis. A brief description of general event generator framework was given in section 2.6. The

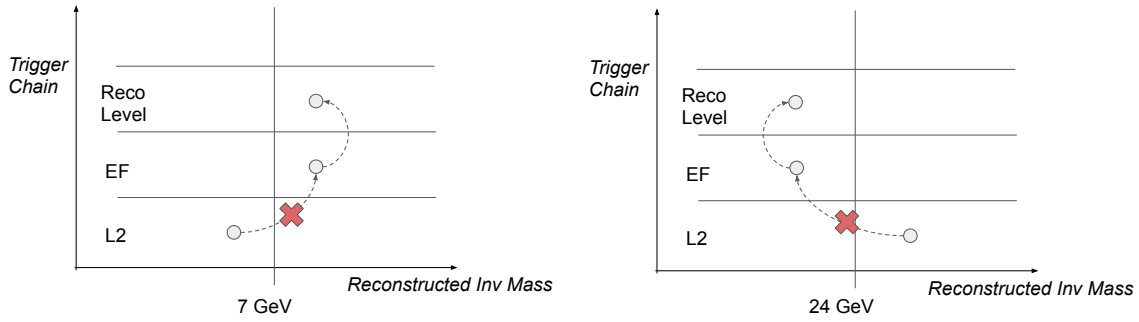

Figure 6.5 Sketch of the trigger behaviour in the proximity of the mass turn on. Events that would have reconstructed inside the trigger mass window are discarded because of a less precise reconstruction at trigger *Level2*.

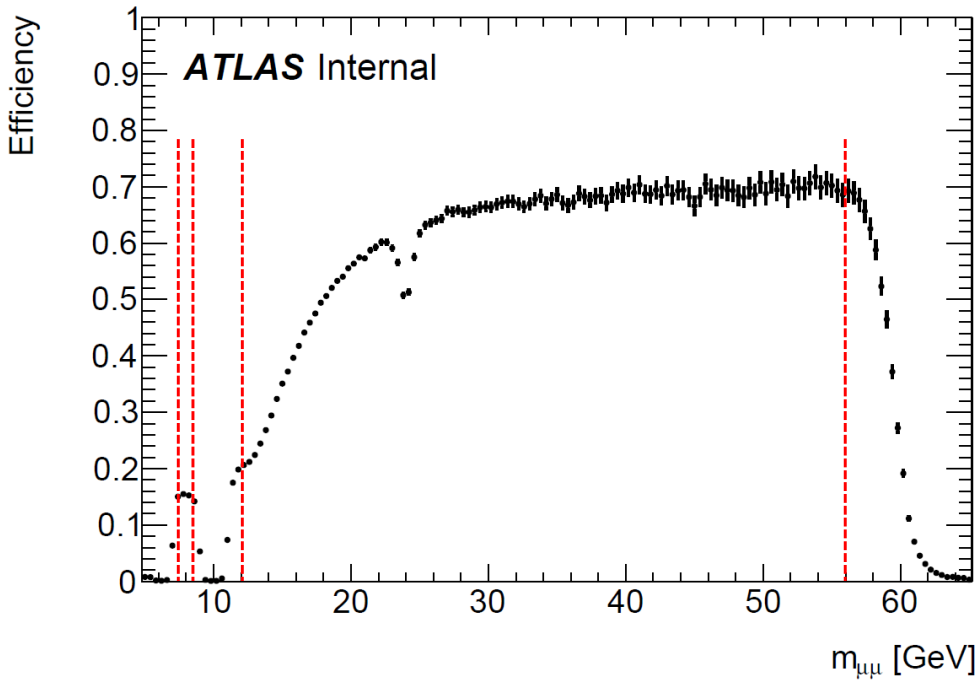

Figure 6.6 Efficiency of the OR operation of all the analysis trigger signals. The red dashed lines represent the edge of the mass selection and shows how this is well inside the plateau of the trigger efficiency. The rise of efficiency around 12 GeV is due to the trigger pre-scale factor applied on the low p_T triggers (see section 6.6).

programs used to generate the signal ($pp \to \gamma^*/Z \to \mu\mu$) were described in section 6.4. All the generated events then go through a simulation of the ATLAS detector performed with the GEANT4 program [136]. Various corrections are applied to the MC samples used in the analysis in order to improve the theory modelling and the detector simulation modelling.

6.7.1 Corrections to the signal MC

The DY events are generated with the Poweg+Pythia program with an accuracy of NLO+LL in QCD (the LL comes from the parton shower as discussed in section 2.6), and with the CT10 at NLO PDF set [118]. To improve the accuracy, NNLO QCD K-factors ($K_{QCD/EW}$) are applied as additional weights to the MC signal events. The NNLO predictions are calculated with the `VRAP 0.9` [121] software and using the newer CT14NNLO PDF set [122]. The K_{QCD} are calculated as a function of the invariant mass, and only for $m_{\mu\mu} > 10\,\text{GeV}$. The values are given by

$$K_{QCD} = \frac{\sigma^{NNLO,CT14}}{\sigma^{NLO,CT10}}. \tag{6.5}$$

Furthermore NLO EW corrections calculated with the MCSANC program [123] are considered. The NLO electroweak predictions are based on the LO QCD, and the EW K-factors are defined as

$$K_{EW} = \frac{\sigma^{NLOEW}_{LOQCD}}{\sigma^{LOEW}_{LOQCD}} \tag{6.6}$$

The combination of the NNLO QCD and NLO EW corrections is achieved with the *additive* approach. This assumes the absolute EW corrections, given by

$$\sigma^{EW\,\text{corr}} = \sigma^{NLOEW}_{LOQCD} - \sigma^{LOEW}_{LOQCD}, \tag{6.7}$$

to be independent of the underlying QCD order of calculation. The $\sigma^{NLOEW}_{NNLOQCD}$ cross section is then obtained as

$$\begin{aligned} \sigma^{NLOEW}_{NNLOQCD} &= \sigma^{LOEW}_{NNLOQCD} + (\sigma^{NLOEW}_{LOQCD} - \sigma^{LOEW}_{LOQCD}) \\ &= \sigma^{LOEW}_{NNLOQCD} \cdot \left(1 + \frac{K_{EW} - 1}{K_{QCD}}\right) \end{aligned} \tag{6.8}$$

The K-factor weights as a function of the invariant mass are shown in Figure 6.7

The DY signal samples poorly describe the vector boson transverse momentum distribution at high values. At high transverse momentum the NLO QCD prediction used (the NNLO K-factors are applied only as a function of mass) is effectively LO in QCD. The $p_T^{\mu\mu}$

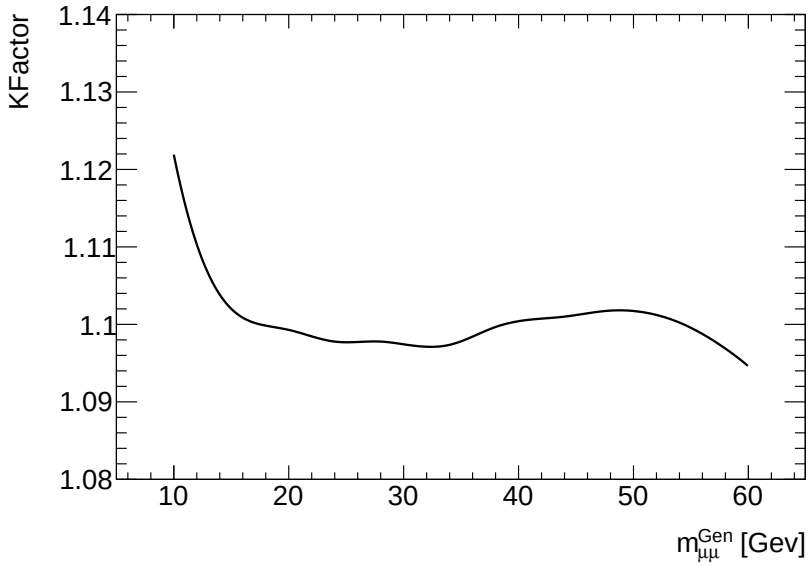

Figure 6.7 K-factor applied to improve the modelling of the Poweg+Pythia signal samples. The K-factors are applied as a function of the generated invariant mass and include NNLO QCD + NLO EW corrections.

differential cross section is one of the measurements performed in this analysis. This result is used to reweight the transverse momentum distribution in MC when extracting the mass and $m_{\mu\mu} - |y_{\mu\mu}|$ differential cross section. The mismodelling of some hidden variable can induce a bias in the result. The $p_T^{\mu\mu}$ reweighting procedure and its effects will be reported in section 9.4, after that the background estimation, chapter 7, and cross section unfolding strategies, chapter 9, are presented.

6.7.2 Pileup reweighting

The high instantaneous luminosity delivered by the LHC results in a large number of proton proton collisions per bunch crossing. The average number of collisions is referred to as *pileup*, $\langle\mu\rangle$. The amount of pileup is important as it can affect the reconstructed distributions. It is simulated in the MC samples by adding additional pp inelastic interactions. Residual differences with respect to the data are corrected by reweighting the MC samples in order to match the observed pileup in data. In Figure 6.8 the number of reconstructed vertices, in data and MC, and before and after reweighting to data is shown. This observable is sensitive to the pileup modelling; before reweighting a disagreement between data and MC is observed, after reweighting, instead, a good modelling is obtained.

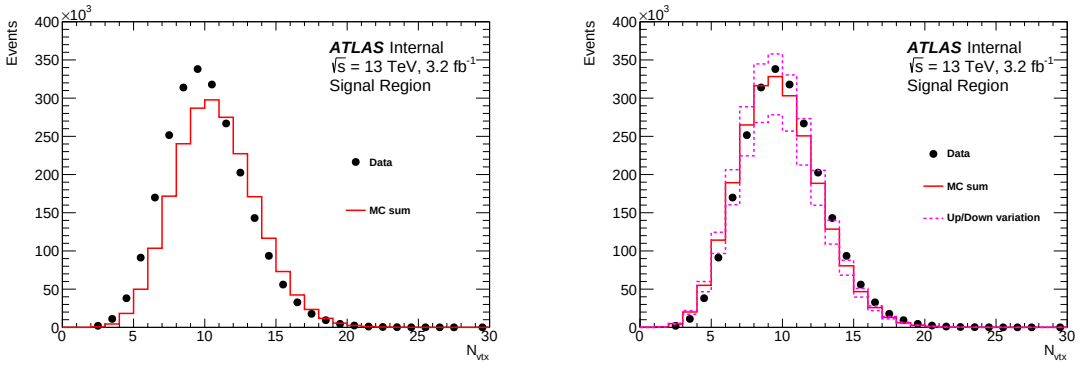

Figure 6.8 Distribution of the number of reconstructed vertices in data and MC. On the left the distribution before applying the pileup reweight to the MC events on right after the reweight. The magenta line show the distribution in MC after varying the overall scaling to data by 10%

6.7.3 Detector modelling corrections

The muon detector performance in simulation needs to be tuned to the data. In particular the detector efficiency and the momentum scale and resolution are corrected to match the values observed in data.

The detector efficiencies are estimated in data and MC with the *tag-and-probe* method. Resonance decays from the J/ψ or Z particles are used [139]. One of the leptons from the decay is identified via a tight selections, this furnishes a *tag* to the event. The other lepton, the *probe*, is instead selected with a looser criteria. The probes offer a sample of particles in which to test the efficiency of particular selection requirements. *Scale factors* (SF) are then calculated as the ratio of the efficiency estimated in data over the one observed in the simulation. The SF are applied to the MC reconstructed events as additional weights. Scale factors for the muon reconstruction and isolation efficiencies are used as well as for the trigger efficiencies.

The reconstructed momentum in simulation is corrected to agree better with the performance observed in data. The muon momentum calibration is evaluated by comparing the mass spectrum of resonance decays (such as Z boson or J/ψ particle) in data and MC. In particular the width of the mass resonance peak is related to the momentum resolution, while the mean of the distribution is sensitive to the momentum scale.

The detector performance estimation is affected by uncertainties. These are taken into account and propagated to the cross section results. The discussion is presented in chapter 10.

Other quantities related to the muon tracks and used in the analysis are the *impact parameters* (IP). These represent the longitudinal and transverse distance of the track from the primary interaction point. The IP distributions are used in the estimation from the data of the multijets background component, section 7.2. A correction to the MC simulation to improve the data modelling is discussed in chapter 8.

6.8 Control Regions

In the low mass DY analysis two Control Regions (CRs) are taken into account. In this analysis the CRs consist of events with two muons in the final state that are excluded by the signal selection, mainly because of the invariant mass cut. The first CR selects dimuon events in the Υ resonance mass range, $m_{\mu\mu} \sim [9-12]\,\text{GeV}$. The other CR looks for Z boson resonance decays into two muons, so DY events, but at a higher invariant mass than the one selected in the analysis.

The Υ CR is used in order to extrapolate a normalization directly using the experimental data for the $\Upsilon(1S)$, $\Upsilon(2S)$, $\Upsilon(3S)$ MC samples (see section 6.4 for a list of the generators). The $Z \to \mu\mu$ together with the Υ CR events are used for a study of the Data MC agreement of the Impact Parameters distributions, d_0 and z_0 in Chapter 8. These quantities are used in the background extrapolation method, Sec. 7.2, and good modelling is important to rely on the estimation. The study is reported in chapter 8. In the next two sections a more detailed definition of the Control Region event selections is reported.

6.8.1 Upsilon Control Region

In the analysis event selection the invariant mass range between 8.7 and 12 GeV is excluded because of the presence of Υ particle decay. These events are instead used as a Control Region. The Υ is a colourless meson composed of a $b\bar{b}$ quark pair. Three excited states, with slightly different masses, are observed

- $m_{\Upsilon(1S)} = 9.46\,\text{GeV}$
- $m_{\Upsilon(2S)} = 10.02\,\text{GeV}$
- $m_{\Upsilon(3S)} = 10.36\,\text{GeV}$

when the invariant mass of the interacting partons in pp collisions approaches the Υ mass, the Υ meson production cross section is enhanced and a resonance peak in the mass spectrum of

the final state is observed. The life time of the Υ is very short, $\tau_\Upsilon \sim 10^{-20}s$, and the particle immediately decays. The decay channel into two muons, $\Upsilon \to \mu^+\mu^-$ is the one considered for this control region.

The HLT trigger used for the selection is `HLT_2mu4_bUpsimumu`, as the analysis triggers were disabled in this region. The selection requirements for the events are the following

- at least two combined muons must be present in the events. If more than two muons are present, the ones with highest transverse momentum are considered.
- Each muon must pass the *Medium* reconstruction working point
- Each muon must pass the *Fixed-Cut-Tight* isolation working point
- the kinematics requirements are
  - $p_T^\mu > 4.5\,\text{GeV}$
  - $|\eta_\mu| < 2.4$
- the selected invariant mass range is $7.5 < m_{\mu\mu} < 12\,\text{GeV}$

The main background to the dimuon Υ events are DY events, and multijets events.

The normalization of the LO `Pythia` MC Υ samples used in the analysis is not accurate and needs to be tuned to the data. The normalizations are extracted using the `TFractionFitter` [140]. The method fits the data distribution using the input MC as template shapes and obtains a normalization factor for each of them. The method brings the advantage of taking into account both the data and MC statistical uncertainties. The templates given as input to the fit are

- MC sample for $\Upsilon(1S) \to \mu^+\mu^-$
- MC sample for $\Upsilon(2S) \to \mu^+\mu^-$
- MC sample for $\Upsilon(3S) \to \mu^+\mu^-$
- sum of all the other MC background samples (except the DY, $\gamma^*/Z \to \mu\mu$ sample)

the DY $\gamma^*/Z \to \mu\mu$ sample normalization is not fitted and it is assumed correct from the MC simulation. This component is subtracted to the data sample before performing the fit. The normalization factors, n, found with `TFractionFitter` for the Υ samples and the background are

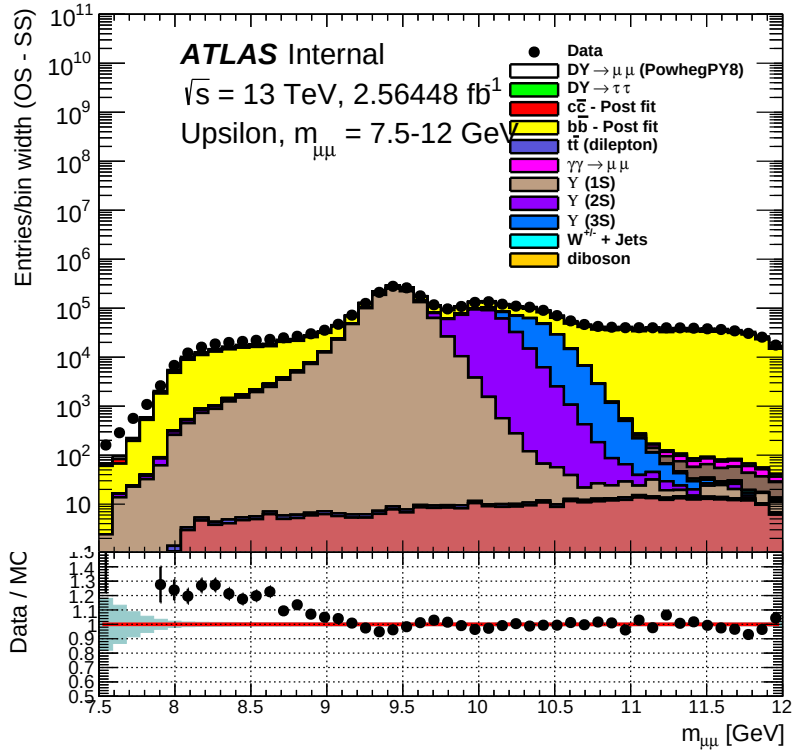

Figure 6.9 Distribution of the dimuon invariant mass system, for the Υ CR, after applying the normalization to the MC samples retrieved with the `TFractionFitter` method.

- $n(\Upsilon_{1S}) = 0.2647 \pm 0.0007$
- $n(\Upsilon_{2S}) = 0.552 \pm 0.002$
- $n(\Upsilon_{3S}) = 0.176 \pm 0.004$
- $n(\text{background}) = 0.545 \pm 0.002$

the error represents the statistical uncertainty of the data and MC combined. The invariant mass spectrum in the Υ region after applying the normalization factors is shown in Figure 6.9. In the bulk of the Υ resonance peaks and in the high part of the spectrum, a good agreement is obtained. Below $m_{\mu\mu} = 9\,\text{GeV}$ the agreement between data and MC gets worse. The normalization factor extracted for the background does not give a good description of the data in this region. In the studies of the impact parameter modelling in Chapter 8 only the events with $m_{\mu\mu} > 9\,\text{GeV}$ are considered.

6.8.2 Z Control Region

The events in this control region are required to pass one of the following single muon HLT

- `HLT_mu20_iloose_L1MU15`
- `HLT_mu50`

The first trigger has the HLT requirement on the muon transverse momentum, $p_T^{\mu} > 20\,\text{GeV}$, while the second covers high p_T^{μ} region and requires $p_T^{\mu} > 50\,\text{GeV}$. The events are required to contain at least two combined muons. The reconstruction working point is *Medium* and the Isolation working point is *FixedCutTight* as in the signal region selection. The kinematic requirements on the events are the following

- $66 < m_{\mu\mu} < 116\,\text{GeV}$
- $p_T^{\text{Leading}} > 25\,\text{GeV}$, $p_T^{\text{Subleading}} > 15\,\text{GeV}$

Using single muon triggers it is possible to lower the cut on the subleading muon transverse momentum (the cut is set to 15GeV in this case). A plot of the dimuon invariant mass in the Z control region is shown in Figure 6.10.

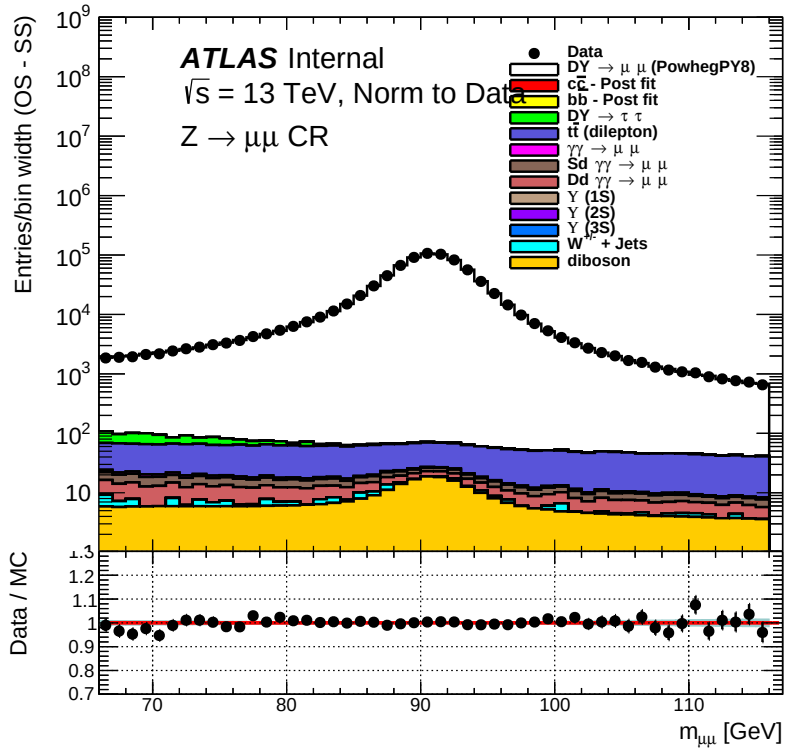

Figure 6.10 dimuon invariant mass distribution for the events in the $Z \rightarrow$ CR.

Chapter 7

Background Estimation

The background processes that affect the low mass Drell-Yan event selection are described. To perform the cross-section measurement these events are subtracted from the data distributions, so every background component needs to be estimated. All sources of background affecting the analysis are described together with the strategy for their estimation. In section 7.1 the EW and QCD sources of background are described, in section 7.2 the method for the estimation of the heavy flavour multijets background, the *Supefitter* method, is presented.

7.1 Background Events for the low mass Drell-Yan process

The analysis selection targets DY events with two muons in the final state, any processes that has two muons in the final state can represent a background for the analysis. Most of these processes have a cross-section that is much lower than the DY one and their contribution is usually (in most of the phase space) lower than 1%. Multijet events, instead, represent a big source of background, around 30% of the total selected events come from this background. This is because of the very high cross-section for these events in the low invariant mass range considered. Multijets events can enhance the number of fake muons in the selection, because of hadrons in the final state that are reconstructed as muons. Furthermore the heavy flavour $b\bar{b}$ and $c\bar{c}$ multijets events can produce highly energetic opposite charge muons in the final state.

7.1.1 Electroweak background

The electroweak background sources for the process $\gamma^*/Z \to \mu^+\mu^-$ are:

- $\gamma^*/Z \to \tau\tau$

Table 7.1 Fraction of Electroweak background events in the total selection (signal plus all background events) as estimated by the MC simulations.

	Fraction in event selection % MC
$\gamma\gamma \to \mu\mu$	1.47%
$\gamma^*/Z \to \tau\tau$	0.77%
EW $t\bar{t}$	0.28%
$W+$Jets	0.07%
diboson	0.04%

- Electroweak $t\bar{t}$
- photon induced dimuon production, in particular the non-dissociative $pp(\gamma\gamma) \to \mu\mu\, pp$ production, the single dissociative production $pp(\gamma\gamma) \to \mu\mu\, pX$ and the double dissociative production $pp(\gamma\gamma) \to \mu\mu\, X$.
- di-boson processes: $WW \to \nu_\mu \mu \nu_\mu \mu$, $ZZ \to \mu\mu ll$
- $W+$Jets events can enter the selection with prompt muon and one fake or non prompt muon from the jet.

These background components are estimated with MC predictions, the MC samples used for the modelling are reported in section 6.3. In Table 7.1 the fraction of EW background events as estimated by the simulation are reported. An uncertainty on each of these background components is evaluated varying the total cross-section normalization for the samples, more detail are presented in Chapter 10.

7.1.2 QCD backgrounds

The lowest mass bin, $7.3 < m_{\mu\mu} < 8.7\,\text{GeV}$, is affected by events coming from the Υ hadron resonance decays. The Υ can decay leptonically, with two muons in the final state. The number of these events is estimated with MC predictions. The normalization of the MC samples is not expected to be accurate and it is estimated from a fit of the MC shape to data in the Υ Control Region, as presented in section 6.8.1. In the first mass bin the fraction of Υ background events is around 16%, in the other mass bins, $12 < m_{\mu\mu} < 56\,\text{GeV}$, this fraction becomes negligible (below 0.05%).

The largest background in the analysis event selection is expected to be due to multijet events. This contributes to the fake muon background component because of charged hadrons in the final state that are reconstructed as muons. The isolation and good track

quality requirements in the event selection, section 6.5, greatly reduce this background. The remaining component that still affects the signal selection is assumed to be charge symmetric, namely

$$N_{Fake}^{+-} + N_{Fake}^{-+} \simeq N_{Fake}^{++} + N_{Fake}^{--} \tag{7.1}$$

where $N_{Fake}^{q_1 q_2}$ is the number of fake muon pairs with charge q_1 and q_2. A selection of same-sign charge dimuon events offers a pure sample of fake muons and serves as an estimation of the opposite charge fake muons contribution. The fake muon component is then eliminated in the physics distributions by subtracting the number of same charge events.

Heavy flavour $b\bar{b}$ and $c\bar{c}$ multijets events can give an excess of opposite charge muons in the final state. The produced heavy flavour hadrons (B and D hadrons for example) decay semileptonically through the weak interaction, leading to a muon and neutrino in the final state, $gg \to \mu^+ \nu_\mu X, \mu^- \bar{\nu}_\mu X$. The muons are produced together with other QCD activity inside a jet and the isolation requirement in the selection greatly reduces this background, but the cross-section for the heavy-flavour jets process is very large and a fraction of these events enter the analysis selection. This background component is difficult to predict with the MC simulation, in particular it is complicated to estimate the fraction of $b\bar{b}$ and $c\bar{c}$ muons that can elude the isolation and pass the selection requirements. This background is estimated using real data distributions from a control region where the number of background events is enhanced. The details of this data-driven approach, that takes the name of *Superfitter*, are explained in the next section.

7.2 Superfitter Method

The idea of the superfitter method is to use a data selection, different from the nominal one, where the number of multijets events is enhanced and the signal is suppressed, to obtain a data template that describes the background distribution shapes. The normalization factor for the background is then fitted to the data using a distribution that has some discriminating power in distinguishing signal and background events.

The control region with enhanced background consists of the same kinematics requirements as in the signal region, section 6.5, but inverting the isolation requirement of detecting other particles in a cone around the muon track (see section 5.6 for the isolation variables definition)

- $p_T^{\text{varcone30}} / p_T^{\mu} < 0.06$
- $p_T^{\text{topetcone20}} < 0.06$

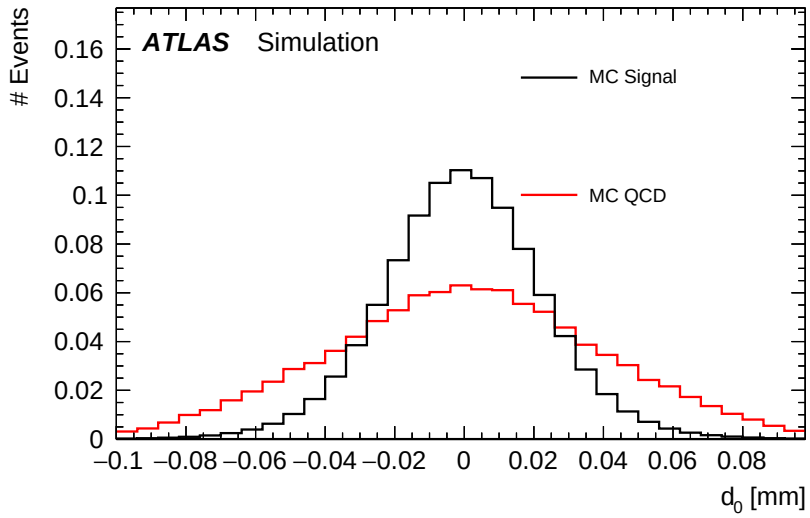

Figure 7.1 Transverse impact parameter d_0 distribution, from MC simulations, for Signal like events and for multijets backgroud events. The distributions are normalized to one to show the different shape in signal and background events distribution.

In this way, muons, most likely produced inside multijets events, are selected. In the *not-isolated* control region the fake muon component is again canceled out by performing the same-sign opposite-sign subtraction for the distributions, as described in sec. 7.1.2.

Given the template for the background, a normalization factor needs to be evaluated by fitting the signal region data selection. The impact parameter d_0 and z_0 distributions, the transverse and longitudinal distance of the muon track from the primary interaction point, are used in the fit (see section 8.1 for a more detailed definition of the impact parameters). Signal and background have a different shapes for these quantities. Signal events consist of two prompt muons, that are muons coming from the primary interaction point. For these, the impact parameter distributions have a Gaussian shape due to the resolution of the detector, with some possible deviation in the tails of the distribution. The heavy flavour hadrons instead have a non-negligible life time, and they travel some tens of μm before decaying. The particles are produced displaced from the primary vertex interaction (non-prompt muons) and consequently the impact parameters are systematically different from zero. This leads the background distribution to have more populated tails. As an example, the d_0 distribution shapes for multijets background events and for signal like events, as predicted by MC simulation, is shown in Figure 7.1.

The discriminating distribution used in the *SuperFitter* is a combination of the d_0 and z_0 impact parameters. For the longitudinal impact parameter the difference between the leading

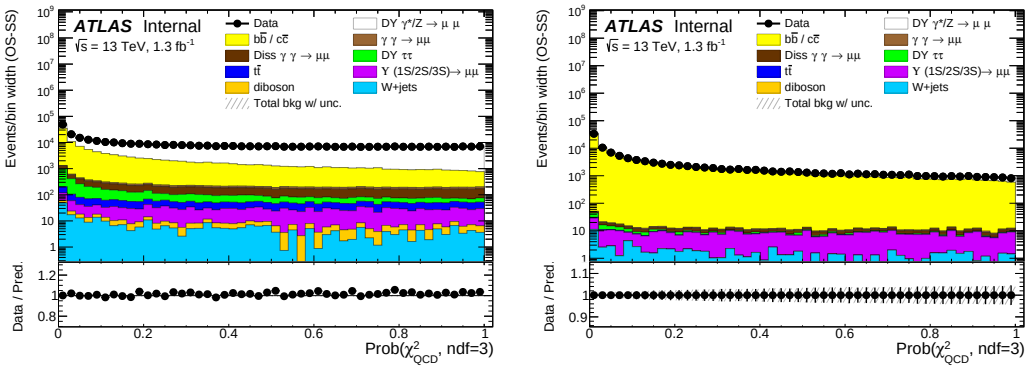

Figure 7.2 $Prob(\chi^2_{QCD}, ndf = 3)$ distribution for the signal region (left) and the not-isolated control region (right). The $b\bar{b}$ and $c\bar{c}$ components are extracted with the *Superfitter* method. The shape is extracted from the not-iso control region, and this explains the perfect data MC agreement in the right plot, and a normalization factor is fitted to the data.

p_T and the subleading p_T muon z_0 is considered

$$\Delta z_0 = z_0^{\text{Lead}} - z_0^{\text{Sub}} \tag{7.2}$$

In fact, in this analysis, the IP are defined with respect to the beam spot or luminous region, that represents the average position of the primary vertex over a few minutes of data-taking. The longitudinal impact parameter z_0 is then the track distance from the primary interaction point convoluted with the longitudinal beam spot size. Considering the difference in equation 7.2 the contribution of the beam spot size is cancelled out.

To combine the d_0 and Δz_0 quantities, the related significance, the ratio of the IP quantity over its resolution, are used. In particular, the sum of the squared IP significance is considered

$$\chi^2_{QCD} = \left(\frac{d_0(\mu_1)}{\sigma_{d_0}(\mu_1)}\right)^2 + \left(\frac{d_0(\mu_2)}{\sigma_{d_0}(\mu_2)}\right)^2 + \left(\frac{\Delta z_0(\mu_1,\mu_2)}{\sqrt{\sigma_{z_0}(\mu_1)^2 + \sigma_{z_0}(\mu_2)^2}}\right)^2. \tag{7.3}$$

For signal like events, the above quantity is approximately a χ^2 distribution with three degrees of freedom. Finally, the distribution used in the background estimation fit is the $Prob(\chi^2_{QCD}, ndf = 3)$. This distribution is limited between 0 and 1 and for prompt muon events is approximately flat, while for non-prompt background events it is peaked at zero. An example of the inclusive $Prob(\chi^2_{QCD}, ndf = 3)$ is shown in Figure 7.2. In particular the distributions for the (isolated) signal region and the non-isolated control region are shown. In the plot, the $b\bar{b}$ and $c\bar{c}$ contribution are obtained with the following fit procedure. The $Prob(\chi^2_{QCD}, ndf = 3)$ distribution is built in each measurement $m_{\mu\mu} - |y_{\mu\mu}|/p_T^{\mu\mu}$ bin, for the

isolated signal region (N_j^{ii}) and for the *not-isolated* control region (N_j^{nn}). In order to perform the fit, the distributions are parameterized as follows

$$N_j^{nn}(k_{DY}, N_j^{nn,QCD}) = k_{DY} \cdot N_j^{nn,DY(MC)} + N_j^{nn,EW(MC)} + N_j^{nn,QCD} \tag{7.4}$$

$$N_j^{ii}(k_{DY}, b_{nn\to ii}, N_j^{nn,QCD}) = k_{DY} \cdot N_j^{ii,DY(MC)} + N_j^{ii,EW(MC)} + b_{nn\to ii} \cdot N_j^{nn,QCD} \tag{7.5}$$

The index j represents the bin of the $Prob(\chi^2_{QCD}, ndf = 3)$ distribution. $N_j^{nn,DY(MC)}$ and $N_j^{nn,EW(MC)}$ is the number of DY events and Electroweak background (section 7.1.1) plus Υ background events as estimated from the MC simulation. The DY and EW background distribution shapes are then obtained from MC. $N_j^{nn,QCD}$ is the number of heavy flavour multijets events in the bin j and is fitted to the data. k_{DY} is a normalization of the DY MC sample and $b_{nn\to ii}$ is the transfer factor that represent the fraction of $b\bar{b}$ and $c\bar{c}$ events that pass the isolation selection. Both factors are fitted to the data.

The *isolated* and *not-isolated* distributions are fitted simultaneously through the minimization of the following χ^2 distribution

$$\begin{aligned}\chi^2\left(k_{DY}, b_{ii\to nn}, \{N_j^{nn,QCD}\}\right) = &\sum_j \frac{\left(N_j^{ii,DATA} - N_j^{ii}(k_{DY}, b_{ii\to nn}, N_j^{nn,QCD})\right)^2}{(\sigma_j^{ii})^2} + \\ &\sum_j \frac{\left(N_j^{nn,DATA} - N_j^{nn}(k_{DY}, N_j^{nn,QCD})\right)^2}{(\sigma_j^{nn})^2}\end{aligned} \tag{7.6}$$

where the error σ in the denominator represents the statistical error of Data and MC distributions

$$\begin{aligned}(\sigma_j^{ii})^2 &= (\sigma_j^{ii,DATA})^2 + (\sigma_j^{ii,MC})^2 \\ (\sigma_j^{nn})^2 &= (\sigma_j^{nn,DATA})^2 + (\sigma_j^{nn,MC})^2\end{aligned} \tag{7.7}$$

The factors k_{DY}, $b_{nn\to ii}$ and the not-isolated background distribution, $\{N_j^{nn,QCD}\}$, are extracted from the fit. Given N_{bins} the number of bins for the $Prob(\chi^2_{QCD}, ndf = 3)$ distribution, the number of degrees of freedom of the fit is equal to

$$ndf = 2 \cdot N_{bins} - (N_{bins} + 2) = N_{bins} - 2 \tag{7.8}$$

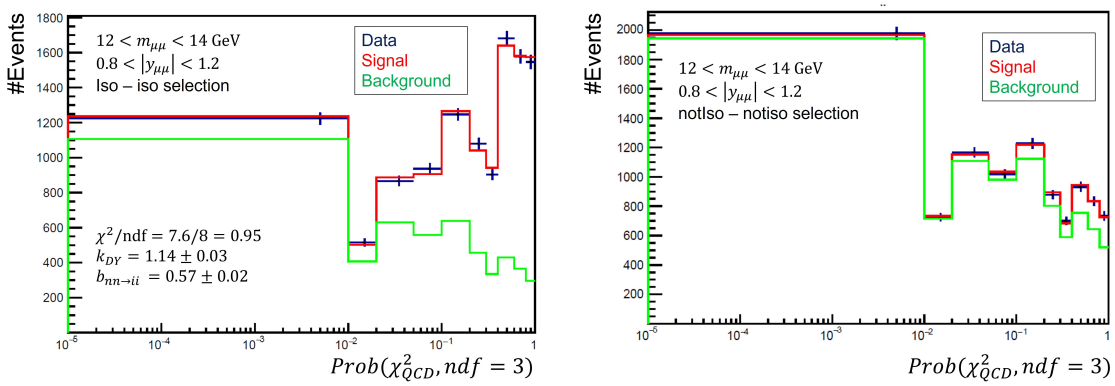

Figure 7.3 Fitted $Prob(\chi^2_{QCD}, ndf = 3)$ distribution in one of the measurement bins. The isolated (left) and non-isolated distribution (left) are fitted simultaneously. The fitted parameters are reported in the left plot. Additionally, also the number of multijets events in each bin of the non-isolated distribution are extracted from the fit.

A non-homogeneous binning is chosen for the fitted distribution, with finer bins at low values of $Prob(\chi^2_{QCD}, ndf = 3)$. This is a range with higher discrimination power between signal and background events. An example of the fitted results in on the measurement bins in reported in Figure 7.3.

The *SuperFitter* method relies on two assumptions that, if not satisfied, can lead to a bias in the result. The first assumption is that the DY MC samples describe well the $Prob(\chi^2_{QCD}, ndf = 3)$ distribution in data, in fact the signal shape in the fit, eq. 7.4, is taken from the simulations and only an overall normalization factor is extracted from the data. This assumption coincides with having a good modelling of the IP distributions and is verified in Chapter 8. Mismodelling is actually observed and a data-driven correction is obtained from two control regions. The results in this chapter already take into account this correction.

The second assumption is that the *not-isolated* QCD background shape is the same as the *isolated* one, or equivalently that the transfer factor $b_{nn\to ii}$ does not depend on the bin of the fitted distribution. This assumption is the subject of a MC study later in this chapter, in section 7.2.2.

7.2.1 Results

The *SuperFitter* presented in the previous section is applied in each measurement bin.

In Figure 7.6 the k_{DY} factors, as extracted from the fit in the $m - |y_{\mu\mu}|$ bins, are shown. Similarly, the results in the $m_{\mu\mu} - p_T^{\mu\mu}$ bins are shown in Figure 7.7. Each k_{DY} is a normalization factors for the DY MC `Powheg+Pythia` samples used in the analysis, in order

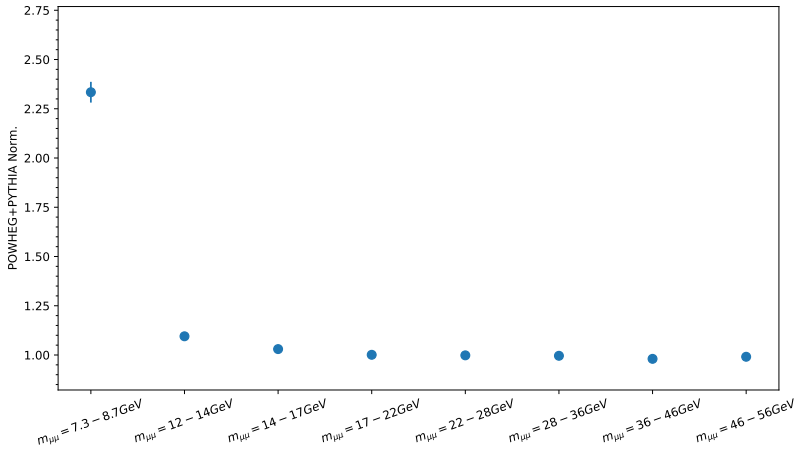

Figure 7.4 `Powheg+Pythia` normalization factors, k_{DY}, as extracted from the *SuperFitter*, in the $m_{\mu\mu}$ measurement bins. The error bars represent the statistical uncertainty on data and MC samples combined.

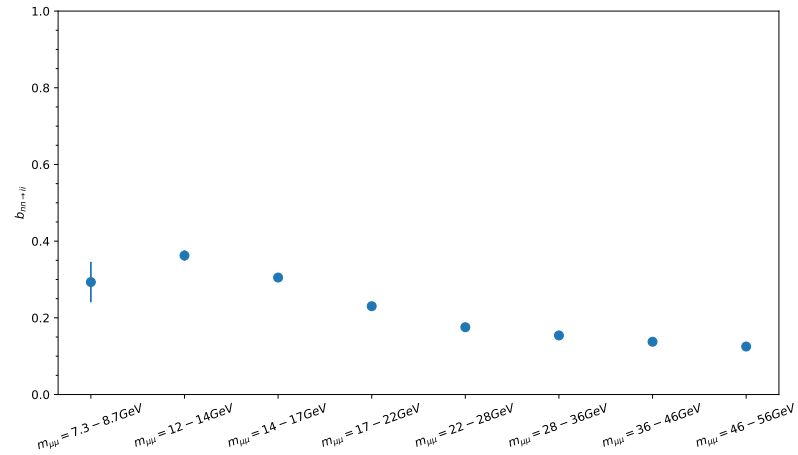

Figure 7.5 Fractions, $b_{nn\to ii}$, of multijets background events that pass the isolation requirement, in the $m_{\mu\mu}$ measurement bins. The error bars represent the statistical uncertainty on data and MC samples combined.

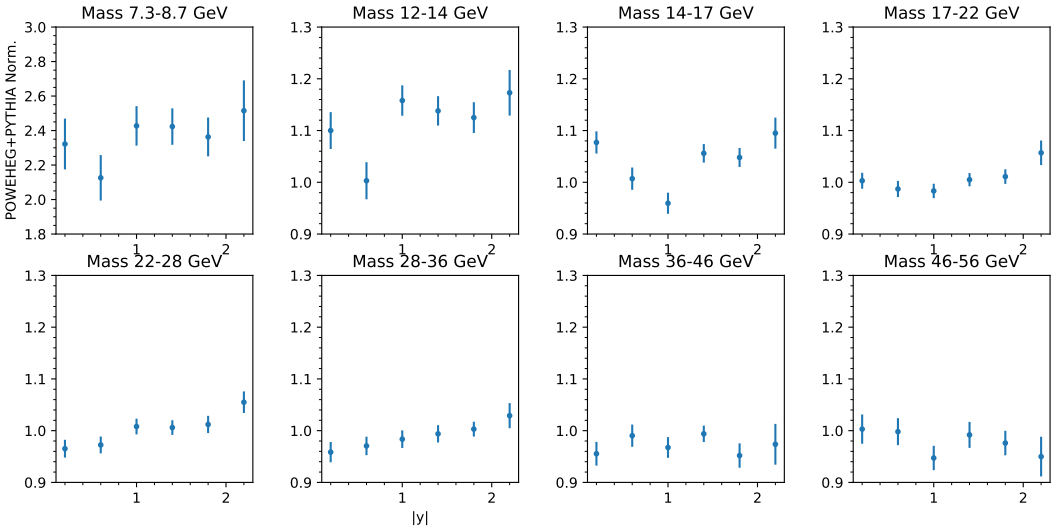

Figure 7.6 `Powheg+Pythia` normalization factors, k_{DY}, as extracted from the *SuperFitter*, in the $m_{\mu\mu} - |y_{\mu\mu}|$ measurement bins. The error bars represent the statistical uncertainty on data and MC samples combined.

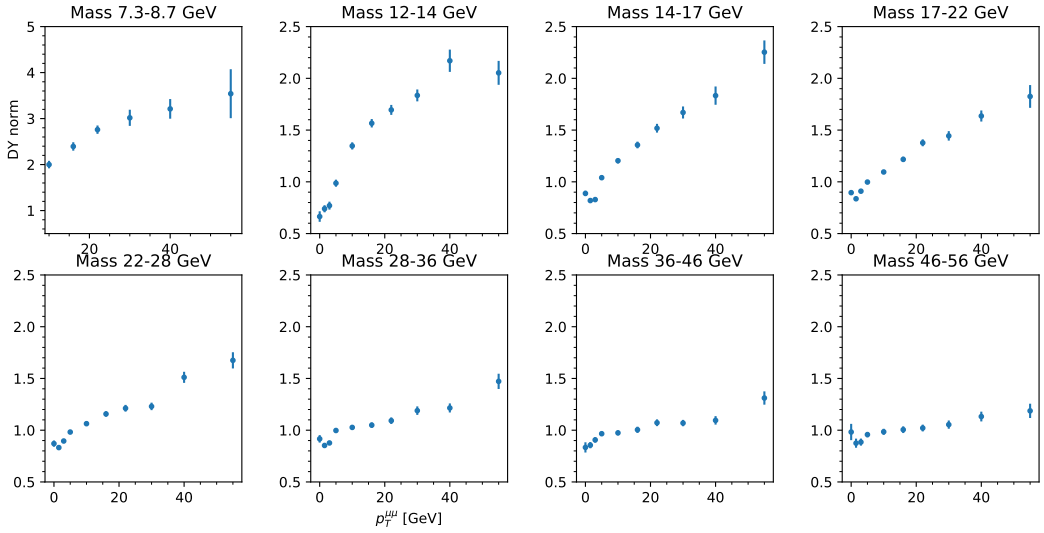

Figure 7.7 `Powheg+Pythia` normalization factors, k_{DY}, as extracted from the *SuperFitter*, in the $m_{\mu\mu} - p_T^{\mu\mu}$ measurement bins. The error bars represent the statistical uncertainty on data and MC samples combined.

to match with the data. The product $k_{DY} \cdot N_{\text{Reco}}^{DY(MC)}$ represents the estimated number of DY events in data and is equivalent, within the fluctuations of the fit results, to the number of background subtracted data events

$$k_{DY} \cdot N_{\text{Reco}}^{DY(MC)} \approx N^{\text{Data}} - N^{\text{Background}} \tag{7.9}$$

The $p_T^{\mu\mu}$ results in Figures 7.7 show how the modelling of the MC generator `Powheg+Pythia` is not accurate at high $p_T^{\mu\mu}$, in particular in the low mass bins. This mismodelling is explained by the fact that the NLO `Powheg+Pythia` predictions are only LO at high $p_T^{\mu\mu}$, where at least one hard emission is required. The k_{DY} factors in $m_{\mu\mu} - |y_{\mu\mu}|$ bins are instead closer to one, except in the very first mass bin, $7.3 < m_{\mu\mu} < 8.7\,\text{GeV}$, where $k_{DY} \sim 2$. This is explained by the $p_T^{\mu\mu}$ mismodelling, because of the cut $p_T^{\mu\mu} > 10\,\text{GeV}$ applied in the first mass bin (see section 6.5).

The Figures 7.8 and 7.9 show the fitted $b_{ii\to nn}$ factors in the $m_{\mu\mu} - |y_{\mu\mu}|$ and $m_{\mu\mu} - p_T^{\mu\mu}$ bins respectively. The $b_{ii\to nn}$ are the transfer factors for the *not-isolated* background distribution to the *isolated* signal region and are interpreted as the fraction of heavy flavour multijets events that eludes the isolation selection. The bigger the $b_{ii\to nn}$ the worse the background rejection through the isolation requirement is working. For example, the $b_{ii\to nn}$ values in Figure 7.9 decrease as $p_T^{\mu\mu}$ increases. At low $p_T^{\mu\mu}$ the heavy flavour jets have, on average, low transverse momentum. Thus they are more spread out and not all the particles are well reconstructed; as a result, the muons are more likely to pass the isolation requirement.

7.2.2 Shape Comparison

As mentioned before, the *SuperFitter* relies on the assumption that the $Prob(\chi^2_{QCD}, ndf = 3)$ shape is the same for *not-isolated* and *isolated* QCD background events. This assumption is studied in this section using the `Pythia` MC samples.

The $Prob(\chi^2_{QCD}, ndf = 3)$ shape comparison for the fully inclusive event selection is showed in Figure 7.10. With the idea of retrieving a smooth correction for possible shape differences, the ratio in Figure 7.10 is fitted with the following function

$$f(x) = p_0 \cdot \left(1 + p_1 \cdot exp\left(-\frac{1}{2}\left(\frac{x}{p_2}\right)^2\right)\right) \tag{7.10}$$

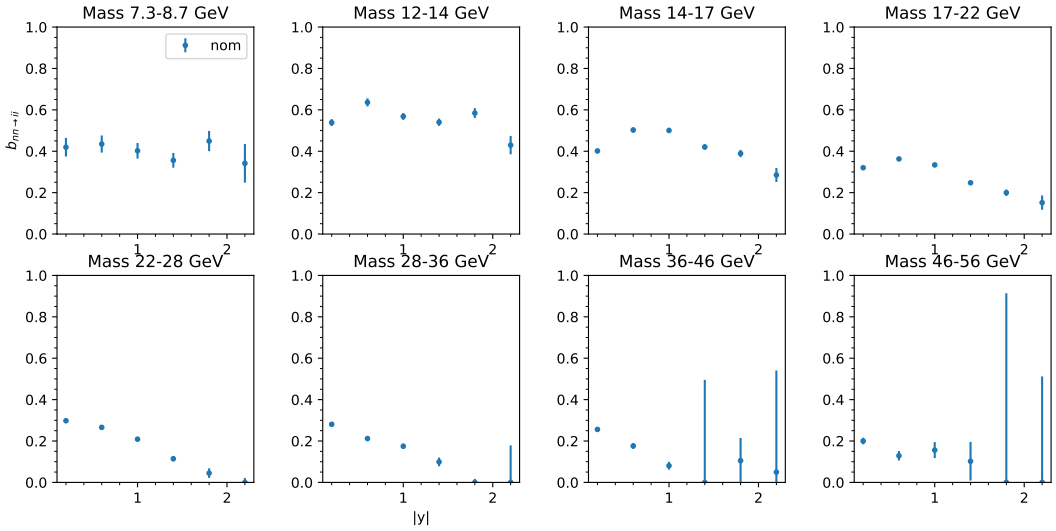

Figure 7.8 Fractions, $b_{nn\to ii}$, of multijets background events that pass the isolation requirement, in the $m_{\mu\mu} - |y_{\mu\mu}|$ measurement bins. The error bars represent the statistical uncertainty on data and MC samples combined.

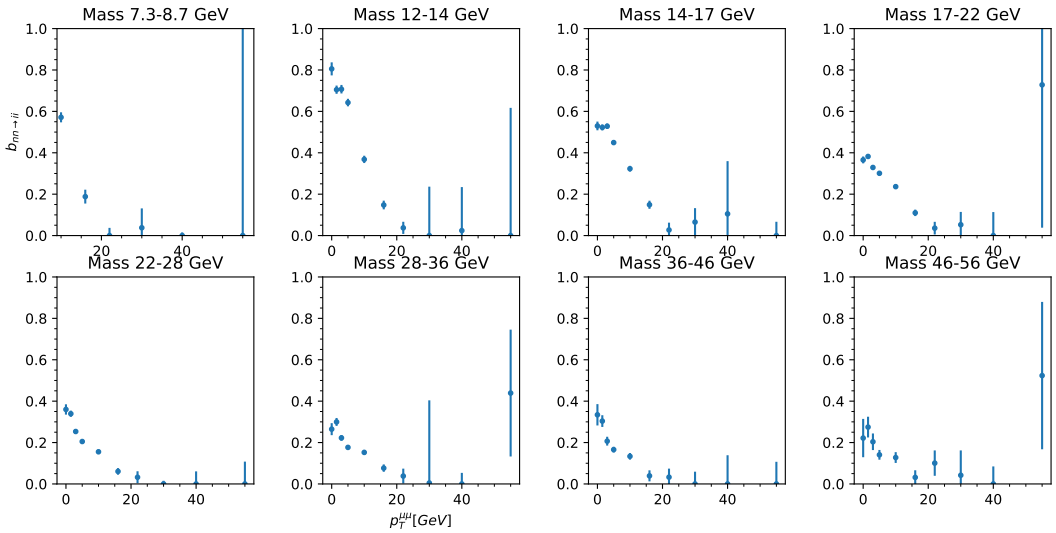

Figure 7.9 Fractions, $b_{nn\to ii}$, of multijets background events that pass the isolation requirement, in the $m_{\mu\mu} - p_T^{\mu\mu}$ measurement bins. The error bars represent the statistical uncertainty on data and MC samples combined.

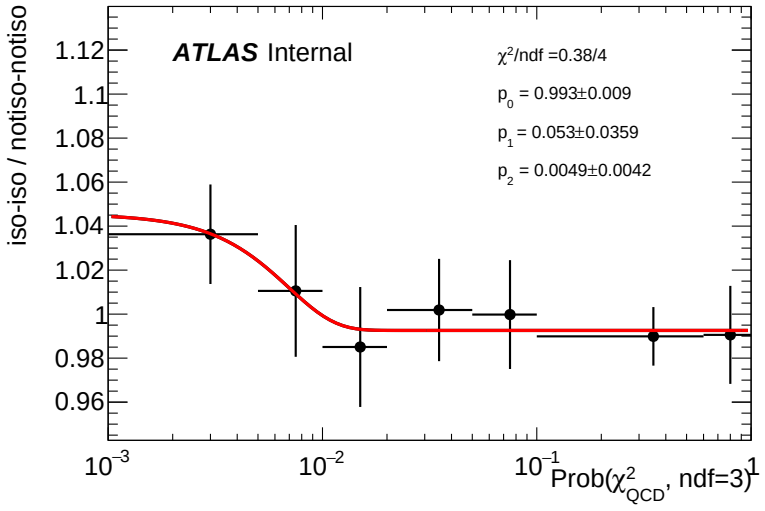

Figure 7.10 Fit results for the *iso/not-iso* $Prob(\chi^2_{QCD}, ndf = 3)$ shape comparison.

This functional form is peaked at zero and is more sensitive to shape differences at low values of $Prob(\chi^2_{QCD}, ndf = 3)$, the most relevant region in discriminating between signal and background events.

The inclusive fit results in Figure 7.10 are used to fix the width of the function when performing the same study but differentially in the variables of interest of the measurement: $m_{\mu\mu}$, $|y_{\mu\mu}|$, $p_T^{\mu\mu}$. Due to the limited statistics of the MC samples a fit in each measurement bin is not feasible and only three mass windows are considered. For each mass range two $|y_{\mu\mu}|/p_T^{\mu\mu}$ regions are taken into account. The fit results in the $m_{\mu\mu} - |y_{\mu\mu}|(p_T^{\mu\mu})$ bins are showed in Figure 7.11(7.12).

The fitted functions are plotted with the 1σ uncertainty band from the fit (the band is plotted in blue). Superimposed, coloured in red, the fit results merging the $|y_{\mu\mu}|$ $(p_T^{\mu\mu})$ region in each mass bin are also shown. These show how no clear dependence in $|y_{\mu\mu}|$ or $p_T^{\mu\mu}$ is observed, as the fitted functions are compatible with the merged result.

The fitted functions in the three different mass windows are used to re-weight the *not-isolated* background distribution to the *isolated* one

$$N_j^{nn,Data} \rightarrow f(\bar{x}_j) \times N_j^{nn,Data} \tag{7.11}$$

where f is the function in eq. 7.10 with the parameter extracted from the fit, $\bar{x}_j$ is the central value of the distribution bin j. This correction is retrieved with a fully MC study, but it is applied to the data distributions. A conservative uncertainty on this correction is estimated

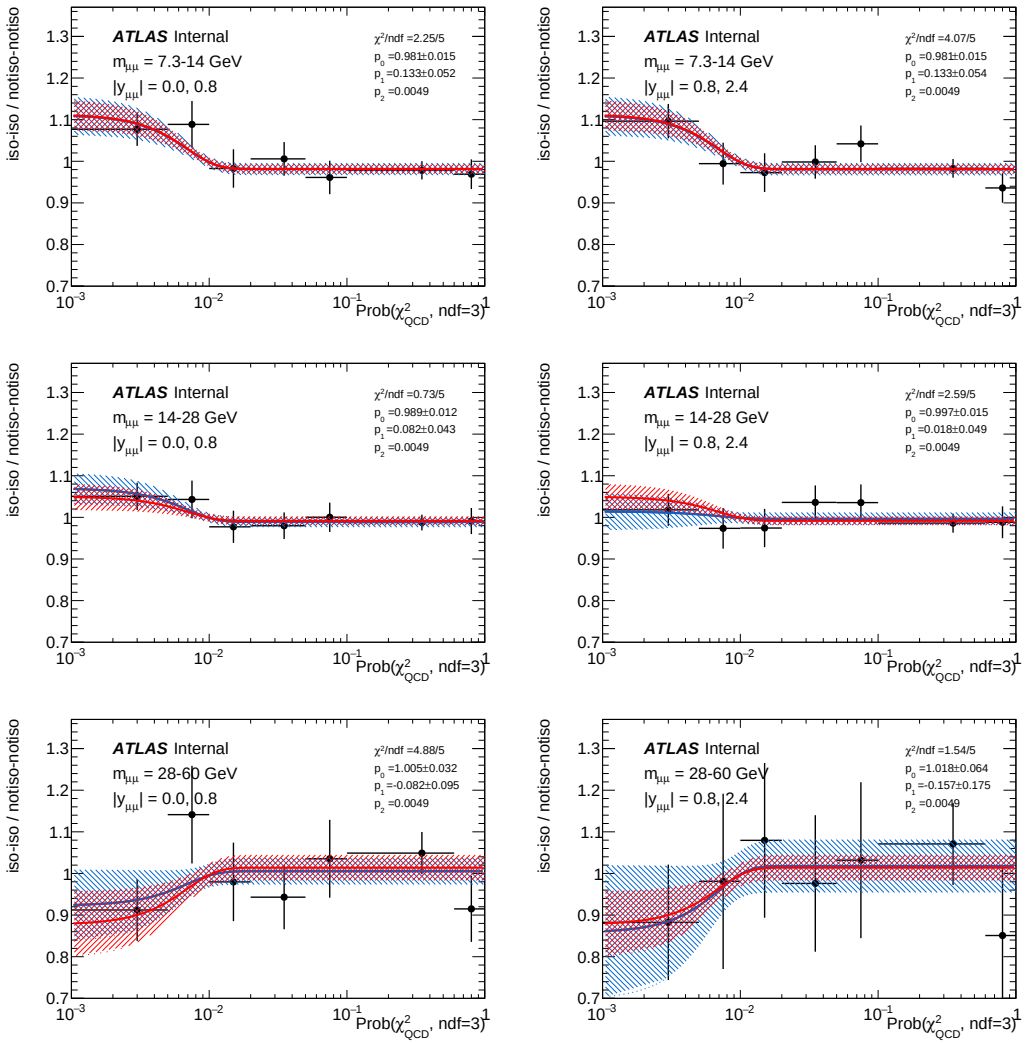

Figure 7.11 Fit results for the shape comparison study in the different mass and rapidity regions. In blue the results in each of the bins (the blue hatched band represents the 1σ uncertainty on the fit). In red are instead the results after merging the two rapidity bin in each of the mass bins. The rapidity differential and the merged results are compatible with each other.

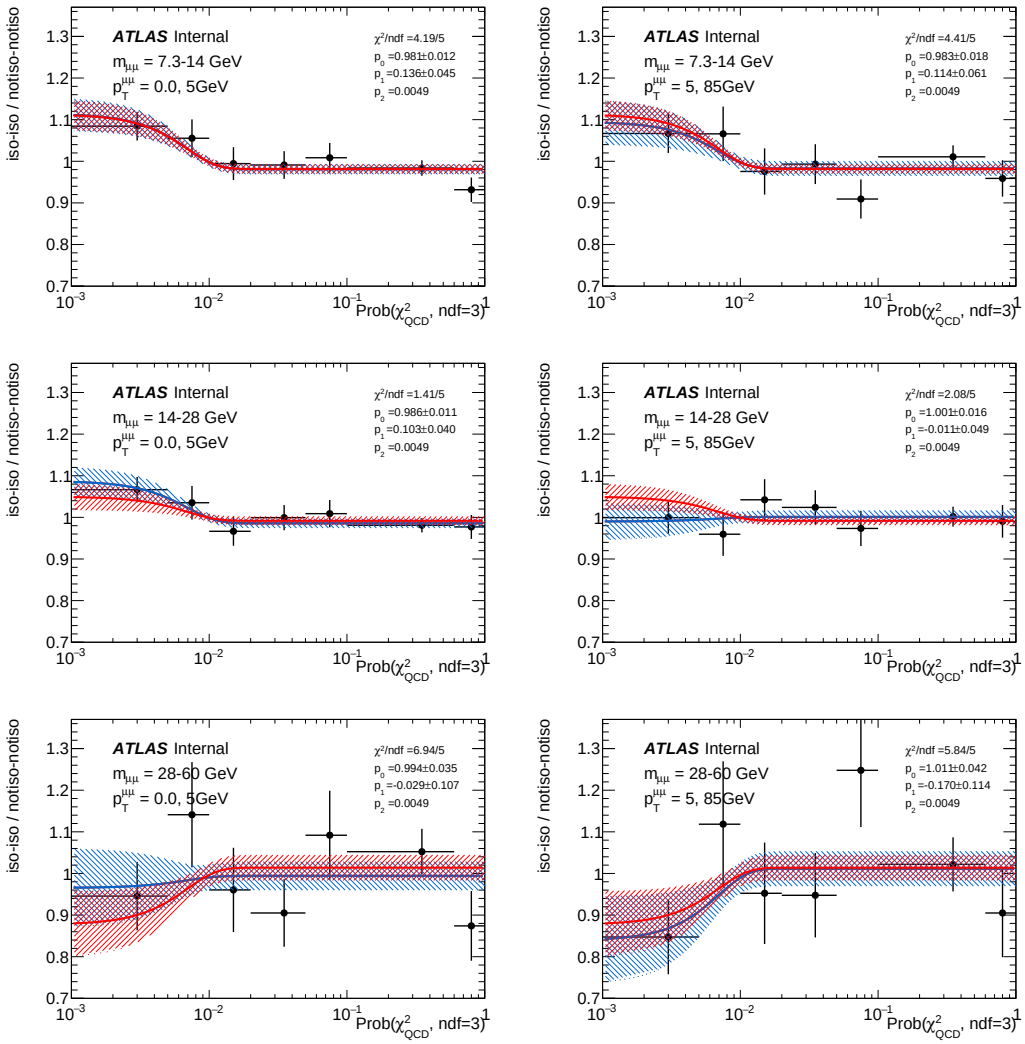

Figure 7.12 Fit results for the shape comparison study in the different mass and transverse momentum regions. In blue the results in each of the bin (the blue hatched band represents the 1σ uncertainty on the fit). In red are instead the results after merging the two rapidity bin in each of the mass bins. The transverse momentum differential and the merged results are compatible with each other.

by considering the differences with respect to the results with no correction applied. The magnitude of this uncertainty is presented in the Chapter 10.

The fit results in the low mass window, Fig. 7.11 and 7.12 seem to show that the relative fraction of QCD background, at low values of $Prob(\chi^2_{QCD}, ndf = 3)$, is higher in the *isolated* selection than in the *not-isolated* one. Physically, this can be related to the fact that more spread heavy flavour jets events produce, on average, muons with higher IP values (low $Prob(\chi^2_{QCD}, ndf = 3)$) that more easily pass the isolation selection. In the highest mass window, $28 < m_{\mu\mu} < 56\,\text{GeV}$ the fitted function peak at zero in the opposite direction. There is no real physical explanation for this behaviour and in this case the *no correction* alternative is chosen as nominal result. The difference with respect to the corrected case is used, in the highest mass window, as an estimation of the uncertainty on possible shape differences.

7.3 Control Plots

To check an overall good behaviour of the data modelling by the MC simulations, control kinematic plots with the events in the signal region are shown in this section. When plotting the distributions, the heavy-flavour multijets component is estimated using the *non isolated* data selection and the results of *superfitter* in section 7.2. In each distribution bin the number of $b\bar{b}$ and $c\bar{c}$ events is obtain as

$$N^{b\bar{b}/c\bar{c}} = b_{nn\to ii} \cdot (N^{nn,DATA} - N^{nn,EW(MC)}) \tag{7.12}$$

where $b_{nn\to ii}$ represent the fraction of background events that elude the isolation selection. These are estimated from the χ^2 minimization in equation 7.6 in each $m_{\mu\mu} - |y_{\mu\mu}|/p_T^{\mu\mu}$ bins of the measurement.

In Figure 7.13 the invariant mass spectrum of the selected events is reported. The disagreement between data and MC in lowest mass bin has been already noticed in the background fit results, Figure 7.6. This is due to the poor MC description of the high $p_T^{\mu\mu}$ tail and the presence of the cut, $p_T^{\mu\mu} > 10\,\text{GeV}$, in the lowest mass bin. The inclusive $p_T^{\mu\mu}$ and $|y_{\mu\mu}|$ distributions are shown in Figure 7.14. The disagreement at high $p_T^{\mu\mu}$ values is here shown directly. When extracting the cross-section in the $m_{\mu\mu} - |y_{\mu\mu}|$ bins, a $p_T^{\mu\mu}$ reweight-to-data operation is performed in order to correct for MC mismodelling effects. The details of this study are given in section 9.4. The muon pseudorapididty and muon transverse momentum distributions are showed in Figure 7.15.

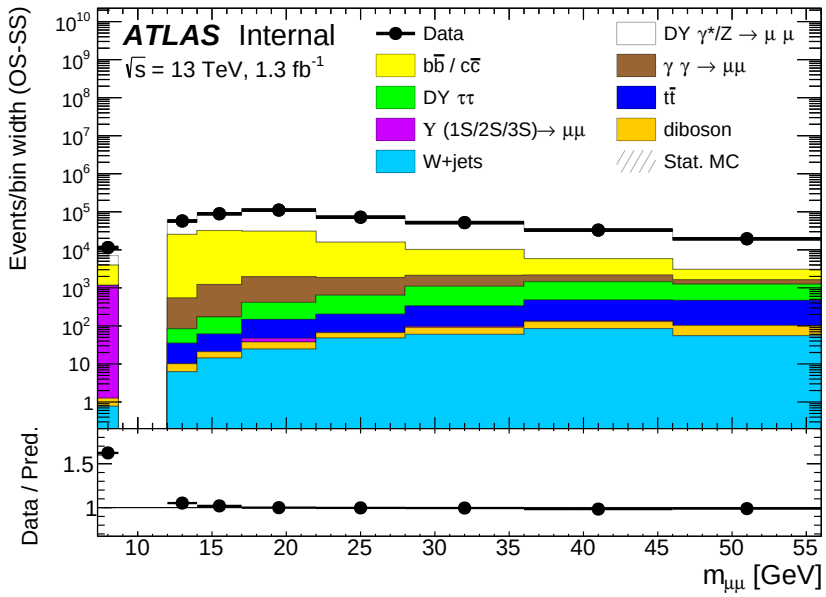

Figure 7.13 Dimuon invariant mass spectrum, in data and MC, of the selected events. The error bars represent the statistical uncertaintiesa only.

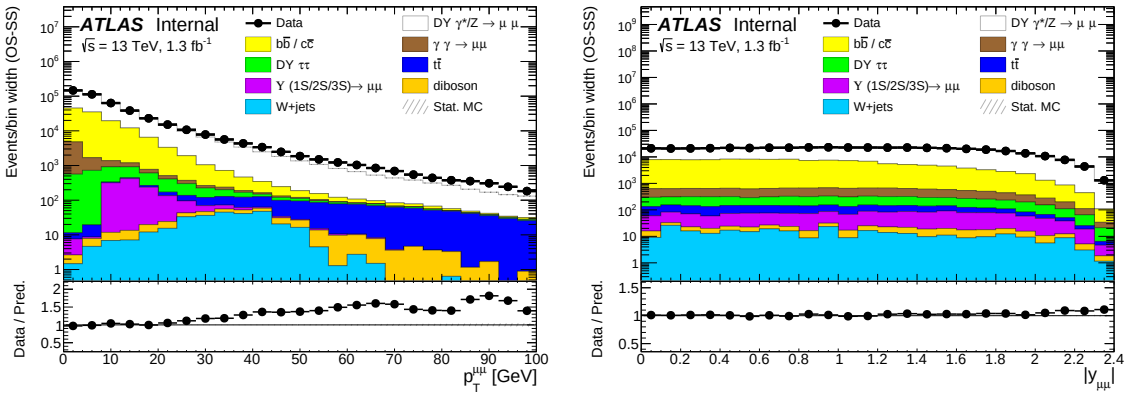

Figure 7.14 $p_T^{\mu\mu}$ (left) and $|y_{\mu\mu}|$ (right) distribution of the selected dimuon events. The error bars represent the statistical uncertainties only.

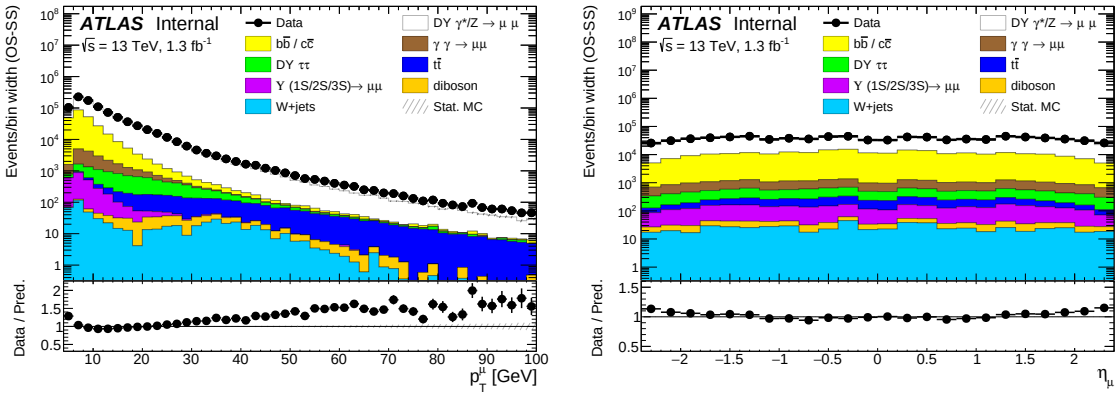

Figure 7.15 Muon transverse momentum (left) and muon pseudorapidity (right) distributions, the error bars represent the statistical uncertainties only.

Chapter 8

Impact Parameter Correction

The background estimation method presented in section 7.2, relies on the assumption that the Impact Parameter distributions are well described by the MC simulation. In fact, in each measurement bin, the shape for the signal distribution is taken from MC simulation, and an overall normalization factor is fitted to the data. This assumption is investigated in this chapter comparing the data and MC distributions. Mismodelling of the MC is observed. The discrepancy is the subject of detailed studies to understand its origin and to obtain an effective correction that improves the description of the data. The correction is obtained by comparing the data and the simulation in two control regions that cover different ranges of muon transverse momentum, namely the $\Upsilon \to \mu\mu$ and $Z \to \mu\mu$ control regions.

In section 8.1 the definition of the Impact Parameter quantities as adopted in this analysis is presented. In section 8.2 the discrepancies observed between data and MC for the IP distributions are shown, similar studies are executed in the analysis control regions in section 8.3. Section 8.4 presents the data-driven correction retrieved from the control regions, that is applied to the signal region events in section 8.5.

8.1 Impact Parameter definition

The track impact parameters d_0 and z_0 are defined at the perigee, the point of closest approach of the track to the reference frame $z-$axis and represent the transverse and longitudinal distance of the point from the axis origin. A graphical representation of the definition is shown in Figure 8.1. The origin of the axis is chosen to be the beam spot center. The beam spot, or luminous region, is defined by the distribution of the primary vertexes over a certain time period, usually of the order of two minutes, of data taking. It represents the pp collision area. The transverse size of the luminous region reflects the beam focusing at the interaction

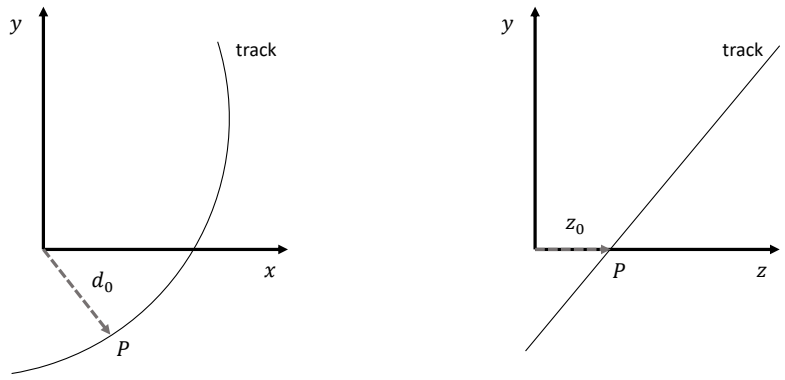

Figure 8.1 Definition of the Impact Parameters d_0 and z_0 on the transverse (on the left) and longitudinal (on the right) plane with respect to the beam line. The perigee P is defined as the point of closest approach of the track to the $z-$axis.

point, the typical size observed in Run2 is $\sim 15\,\mu$m. The longitudinal size is instead much larger, around 50 mm, as it is determined by the bunch lengths (and the angle between the colliding beams). When considering the longitudinal IP for the dimuon events, the difference between the leading and subleading z_0, $\Delta z_0 = z_0^{Lead} - z_0^{Sub}$ is used.

In order to combine the information about the longitudinal and transverse impact parameters in the background fit, section 7.2, the corresponding significances are considered. These are defined as the IP quantity divided by its resolution. In the case of d_0

$$d0\,\text{significance} = \frac{d_0}{\sigma_{d_0}} \tag{8.1}$$

where σ_{d_0} takes into account both the tracking and the beam spot resolution

$$\sigma_{d_0} = \sqrt{(\sigma_{d_0}^{track})^2 + (\sigma_{d_0}^{BS})^2}. \tag{8.2}$$

The Δz_0 significance is defined as

$$\begin{aligned} \Delta z_0\,\text{significance} &= \frac{\Delta z_0}{\sigma_{\Delta z_0}} \\ &= \frac{\Delta z_0}{\sqrt{(\sigma_{z_0^{lead}})^2 + (\sigma_{z_0^{sub}})^2}} \end{aligned} \tag{8.3}$$

8.2 First IP correction and residual discrepancies

Following the recommendation of the Inner Detector group, a first smearing correction is applied to the MC d_0 and z_0 distributions. This correction should compensate for the effect of detector mismodelling in simulation, that can lead to a bias in the IP description. The mismodelling can arise from a not fully accurate detector material description, or from residual misalignment of the detector. The correction values are determined by comparing data and MC distributions in Z boson decay events and minimum bias events, in order to cover a wide range in the lepton transverse momentum. The correction corresponds to a Gaussian random smearing

$$\begin{aligned} d_0^{MC} &\to r \cdot d_0^{MC} \\ r &\sim \exp\left(-\frac{1}{2}(x-d_0^{MC})^2/(\sigma^{smear})^2\right) \end{aligned} \tag{8.4}$$

where r is a random number extracted according to a Gaussian distribution centered in d_0^{MC} and with standard deviation equal to σ^{smear}. This last parameter represents the magnitude of the smearing. It is calculated as

$$\sigma^{smear} = \sqrt{\sigma^2_{\text{data}} - \sigma^2_{\text{MC}}} \tag{8.5}$$

and it is mapped as a function of the rapidity η and transverse momentum p_T of the particle. The detector mismodelling can in fact depend on the position of the track within the detector volume and on the detector energy response.

Furthermore, a bias in the d_0 mean value was observed in data because of residual misalignment of the detector. For this reason a shift correction is applied event by event to the data d_0 values

$$d_0^{data} \to d_0^{data} + s(\eta, p_T) \tag{8.6}$$

where the shift parameter, s, is again mapped in bins of η and p_T.

The smearing correction improves the data description, as can be seen in Figure 8.2 (8.3) where the inclusive d_0 (Δz_0) distribution, before and after the smearing correction and d_0 shift, is shown. Nevertheless, some residual discrepancies after the correction are observed both for the d_0 and Δz_0 distribution. Additional studies to investigate this disagreement are presented in the next sections.

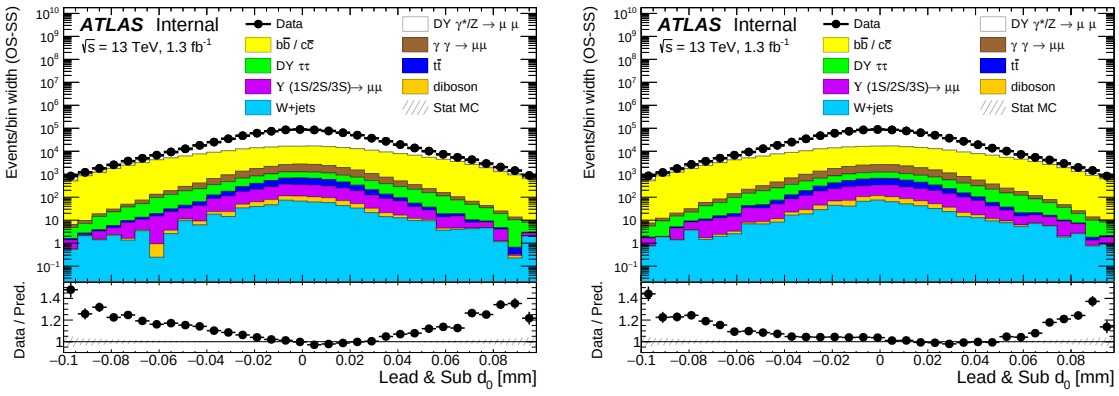

Figure 8.2 Data MC comparison for the d_0 distribution before (left) and after (right) applying the *ID* smearing and shifting correction.

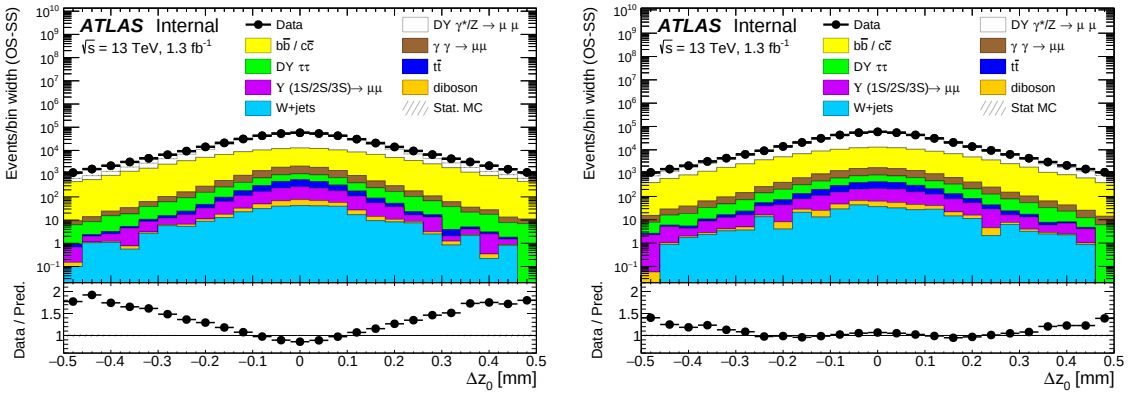

Figure 8.3 Data MC comparison for the Δz_0 distribution before (left) and after (right) applying the *ID* smearing correction.

8.3 IP studies in $\Upsilon \to \mu\mu$ and $Z \to \mu\mu$ Control Regions

The residual discrepancies in the IP quantity description are investigated in this section. The fitted quantity in the background estimation fit, eq. 7.3, depends on the impact parameter significances, so these will be the quantities mostly studied in this section, rather than the bare d_0 and Δz_0. Eventually a disagreement is observed and a data-driven correction is evaluated to improve the modelling, this will be presented in section 8.3.1. In order not to introduce a bias in the background estimation, the correction cannot be retrieved using the signal region events. Instead two control regions, where the multijet background is negligible or can be estimated in other ways, are used to investigate the discrepancies and retrieve the correction. In particular the $\Upsilon \to \mu\mu$ and $Z \to \mu\mu$ resonance regions are used. The two regions offer complementary information: the Υ CR covers a low p_T region, $p_T \lesssim 15\,\text{GeV}$, while the Z allows a higher p_T range to be explored. The detailed selection definition for the two CRs is given in section 6.8.1 and section 6.8.2. In the Z control region the QCD background component is negligible and no data-driven estimation is needed. In the Υ CR the the multijets events are estimated by fitting the mass spectrum shape, as explained in section 6.8.1.

8.3.1 Data MC comparison

The IP significance modelling is investigated as a function of the rapidity η and transverse momentum p_T of the muons. In a particular η and p_T bin, the d_0 and Δz_0 distributions are fitted with a Gaussian function. The tails of the distribution are avoided, as they present a non-Gaussian behaviour, and only a range around the distribution mean of about ± 1.5 standard deviations is considered for the fit. The mean and the width of the fitted Gaussian are then compared between data and MC. As an example, Figure 8.4 shows the fit results in a particular η bin.

A comparison of the d_0 distribution mean in data and MC, as function of η and p_T, is reported in Figure 8.5. A small residual difference, around $0.5\,\mu\text{m}$, almost constant in the two variables analysed, is observed. A similar result is observed in the Z CR as shown in Figure 8.6.

Figure 8.7 shows a study of the IP significance widths in the $\Upsilon \to \mu\mu$ CR. The data-MC comparison is performed as function of η_μ and p_T^μ. The observed disagreement, both for the d_0/σ_{d_0} and $\Delta z_0/\sigma_{\Delta_{z_0}}$ distributions, shows a clear η_μ dependence with a different behaviour in the barrel ($|\eta| \lesssim 1.5$) and in the endcap ($|\eta| \gtrsim 1.5$). The p_T^μ dependence is instead milder.

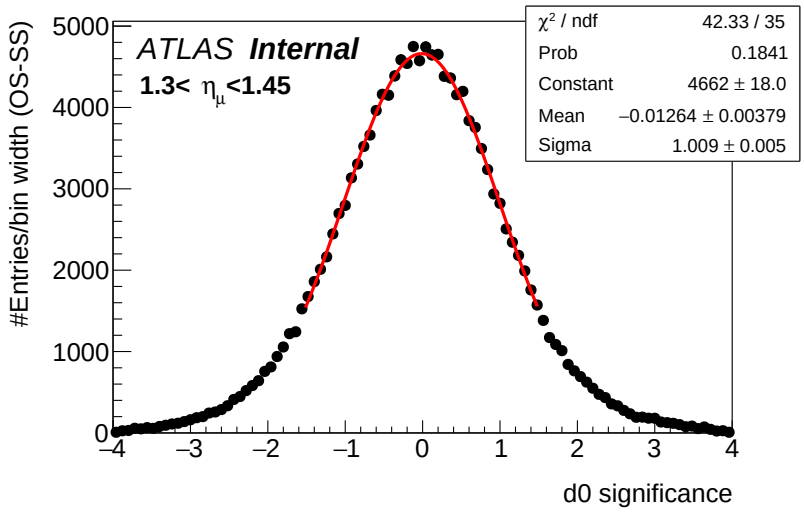

Figure 8.4 Example of the fit of the data d_0 significance distribution. The fit is performed in different bins of η_μ ($1.3 < \eta_\mu < 1.45$ in this example). The fit results in data and MC are then compared.

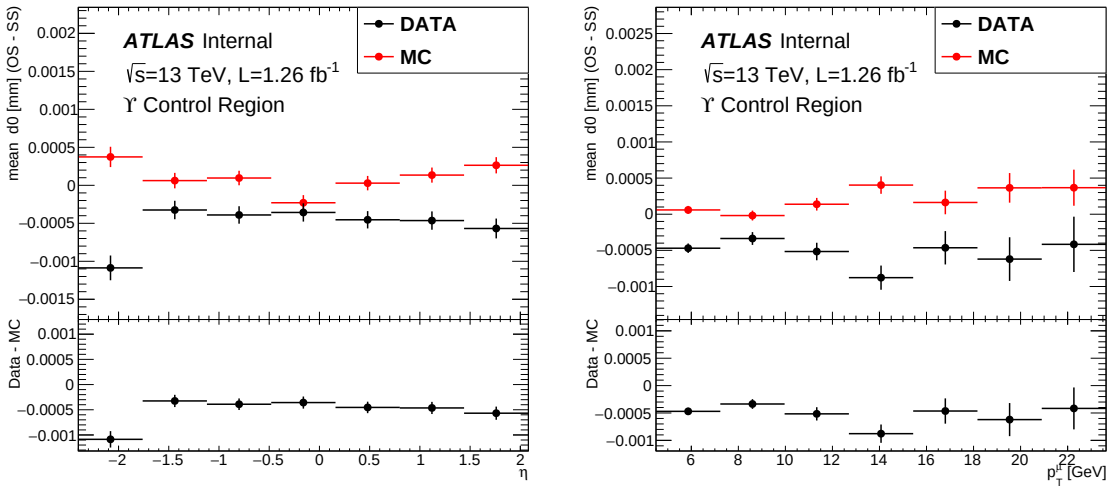

Figure 8.5 d_0 mean comparison as function of η (left) and p_T (right) in the $\Upsilon\mu\mu$ CR. A shift of about 0.5 μm, between data and MC, is observed.

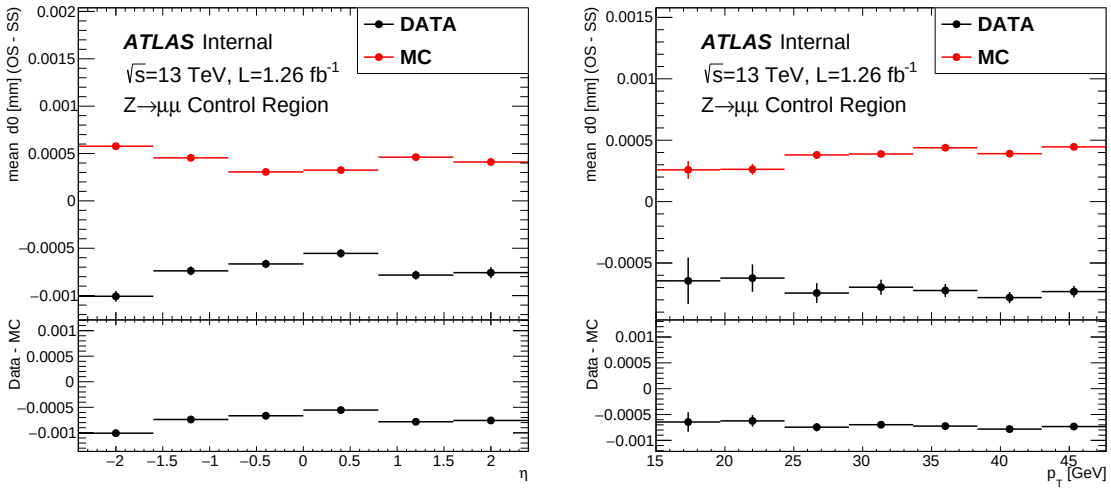

Figure 8.6 d_0 mean comparison as function of η (left) and p_T (right) in the $Z \to \mu\mu$ CR. A shift of about 0.5 μm, between data and MC, is observed.

The same study, but for the $Z \to \mu\mu$ CR is reported in Figure 8.8. Also in this case a similar level of disagreement is observed.

8.4 Impact Parameter correction

Using the events in the Υ and Z Control Regions, a data-driven correction for the IP distributions to apply to the MC simulation is obtained.

Firstly, from the study of the d_0 mean, Figures 8.5, 8.6, a global shift to the MC d_0 distribution is applied

$$d_0^{MC} \to d_0^{MC} + s \quad \text{with} \quad s = -0.55 \mu\text{m} \tag{8.7}$$

the value of s is obtained by comparing the mean of the inclusive d_0 distribution between data and MC.

A correction to the d_0 significance is obtained comparing the width of the distribution in data and MC. A correction value, c, is obtained in bins of η and p_T as

$$c(\eta, p_T) = \frac{\sigma_{d_0}^{Data}(\eta, p_T)}{\sigma_{d_0}^{MC}(\eta, p_T)} \tag{8.8}$$

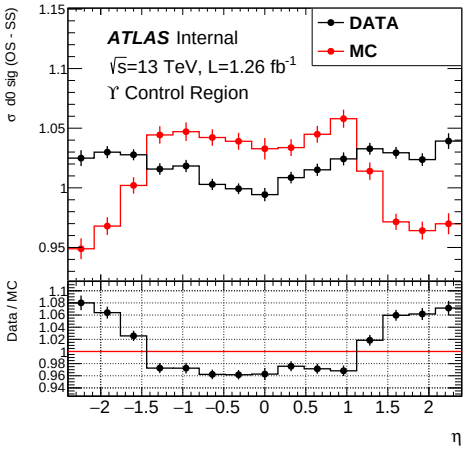

(a) d_0 significance width vs η

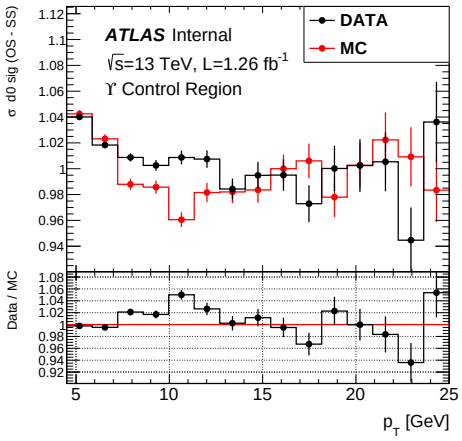

(b) d_0 significance width vs p_T

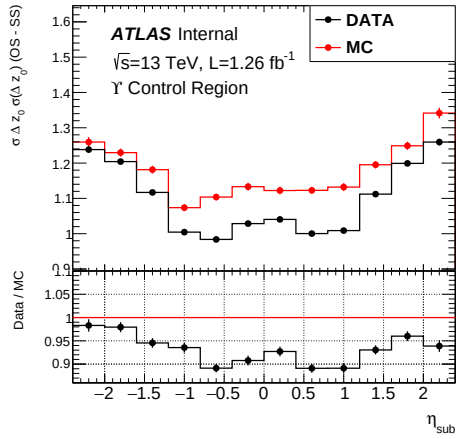

(c) Δz_0 significance width vs η^{sub}

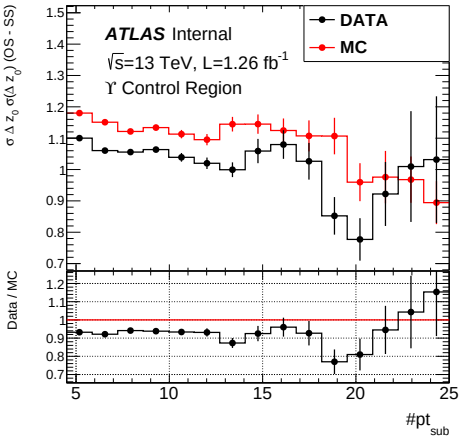

(d) Δz_0 significance width vs p_T^{sub}

Figure 8.7 IP significance width comparison for the $\Upsilon \to \mu\mu$ CR. The width is obtained from a Gaussian fit like the one in Figure 8.4. The data and MC comparison shows a disagreement with a clear η dependence.

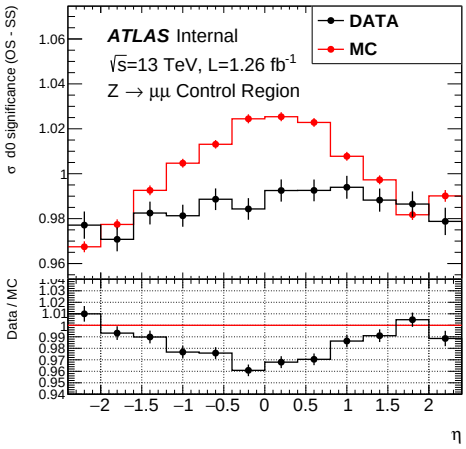

(a) d_0 significance width vs η

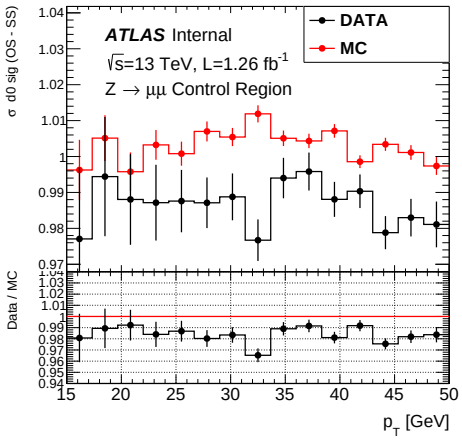

(b) d_0 significance width vs p_T

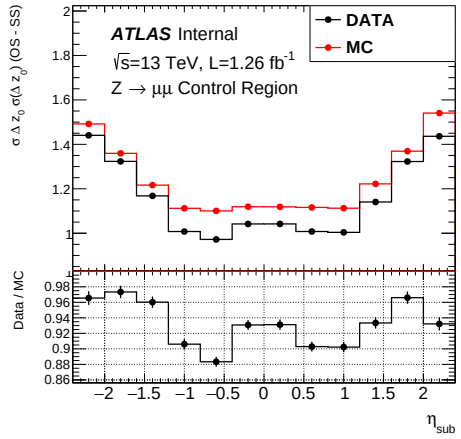

(c) Δz_0 significance width vs η^{sub}

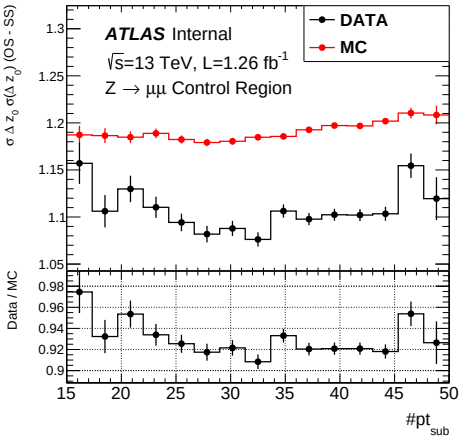

(d) Δz_0 significance width vs p_T^{sub}

Figure 8.8 IP significance width comparison for the $Z \to \mu\mu$ CR. The width is obtained from a Gaussian fit like the one in Figure 8.4. The data and MC comparison shows a disagreement with a clear η dependence.

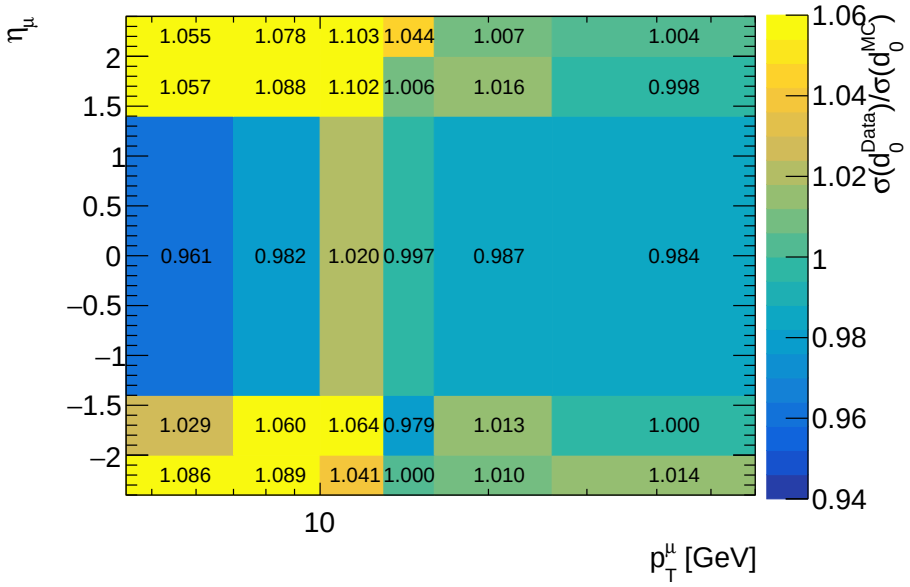

Figure 8.9 $\eta - p_T$ d_0 significance correction map. The correction is obtain by comparing the width of the d_0 significance in data and MC

where σ is the width of the d_0 distribution obtained from the Gaussian fit procedure presented in the previous section. The correction is applied to the MC simulation

$$d_0^{MC} \rightarrow c(\eta, p_T) \cdot d_0^{MC}. \tag{8.9}$$

This operation corresponds to rescaling the width of the MC distribution to the value observed in data. The correction values are shown in the $\eta - p_T$ map in Figure 8.9. The map binning is decided using the information from the one dimensional studies, Figure 8.7 and 8.8. The information from the two control regions are combined producing a correction map that spans a wide range of muon p_T. The Υ CR events are used to obtain the low p_T correction values, in particular for $p_T < 15\,\text{GeV}$. The higher p_T bins instead make use of the events from the $Z \rightarrow \mu\mu$ CR.

For the Δz_0 distribution a similar approach is used. In this case though there is an ambiguity when deciding the variable in which the correction is binned. In fact, the Δz_0 significance value in a dimuon event depends on the kinematics (η, p_T) of both particles and it is not possible to disentangle the two. In order to maximise the sensitivity of the correction, the correction values are binned in bins of η^{sub}, η^{lead} and p_T^{sub}. The correction is applied to

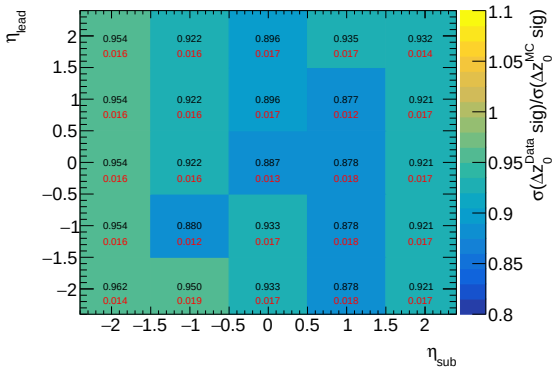

(a) Δz_0 significance correction map for the range $4.5 < p_T^{sub} < 7.5\,\text{GeV}$.

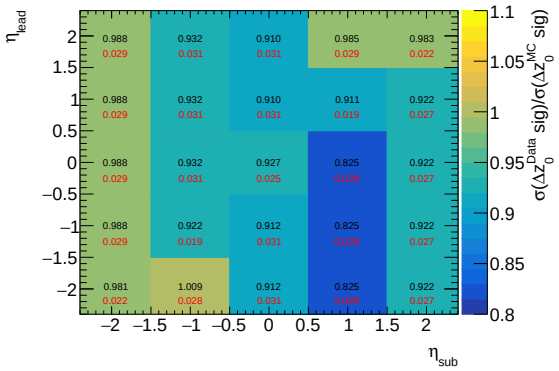

(b) Δz_0 significance correction map for the range $7.5 < p_T^{sub} < 26\,\text{GeV}$.

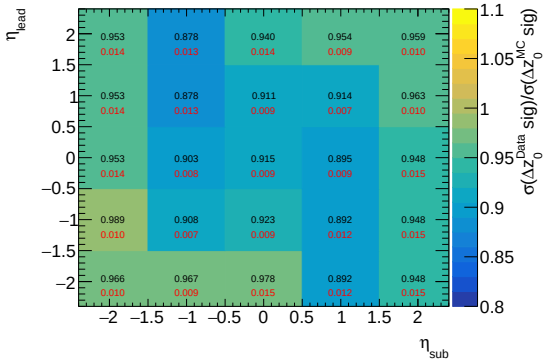

(c) Δz_0 significance correction map for the range $p_T^{sub} > 26\,\text{GeV}$.

Figure 8.10 Δz_0 significance correction maps. Each map is binned in bins of η^{lead} and η^{sub}. Three different maps are used to cover different p_T^{sub} ranges.

the MC events in the same way as for the d_0 distribution

$$\Delta z_0 \to c(\eta^{sub}, \eta^{lead}, p_T^{sub}) \cdot \Delta z_0 \quad \text{with} \quad c = \frac{\sigma^{Data}_{\Delta z_0}}{\sigma^{MC}_{\Delta z_0}}. \tag{8.10}$$

The Δz_0 significance correction maps are reported in Figure 8.10

8.4.1 Closure test

The correction described in the previous section and derived from the events in the $\Upsilon \to \mu\mu$ and $Z \to \mu\mu$ CRs is here applied to the same CRs for a closure test. In particular the correction is applied to the prompt muon MC samples. The data-MC comparison test presented in section 8.2 is performed again expecting an improvement in the level of agreement. The

study for the $\Upsilon \to \mu\mu$ events, after applying the IP correction, is reported in Figure 8.11. The equivalent study, but derived in the $Z \to \mu\mu$ CR, is shown in Figure 8.12. The residual disagreement that is observed is due to variations in the data MC agreement that are not caught by the binning used in the correction maps in Figures 8.9 and 8.10, and that become visible when checking the agreement in a different binning. Additionally, in the Υ CR, the fraction of QCD background events is not negligible, and its relative contribution to the width of the distribution can change after the correction. The IP correction is evaluated fitting the core of the IP distribution, a range dominated by the prompt muon samples and is not applied to the non-prompt samples as the multijet background. As a result an imperfect closure is observed.

The red band in Figures 8.11 and 8.12 is obtained by varying, positively and negatively, the IP correction of 2%. The effect of non closure: the binning choice, and the background component in the Υ CR, are covered in almost all the bins by this band. This variation of 2% on the correction values is used as an estimation of the uncertainty on this operation.

8.4.2 d_0 significance tail reweight

The closure test in the previous section shows an improvement in the description of the data, at least in the central part of the IP distributions. In order to check the behaviour in the tails, the inclusive d_0 significance distribution for the events in the $Z \to \mu\mu$ CR is shown in Figure 8.13. The Figures 8.13a and 8.13b shows the distribution before and after applying the correction of section 8.4. An improvement in the data MC agreement after the correction is observed in the central part of the distribution, $|d_0/\sigma_{d_0}| \lesssim 3$, as expected from the closure test. In the tails, instead, residual mismodelling persists. The distribution tails are still dominated by signal events, so the disagreement is a result of the mismodelling at high values of d_0 significance for signal MC events. A similar result is difficult to isolate in the Υ CR distributions because the tails are dominated by QCD background events.

A tail reweight for the MC samples is obtained from the Z CR. The weights are shown in Figure 8.14. Figure 8.13c shows the data-MC agreement in the Z CR after applying the reweight. The IP correction, together with the d_0 significance tail reweight presented here, are applied to the signal region events in the next section.

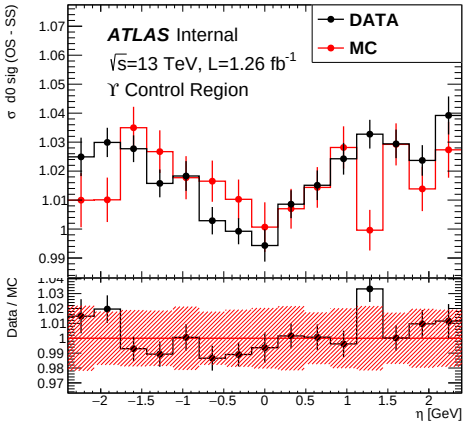

(a) d_0 significance width vs η

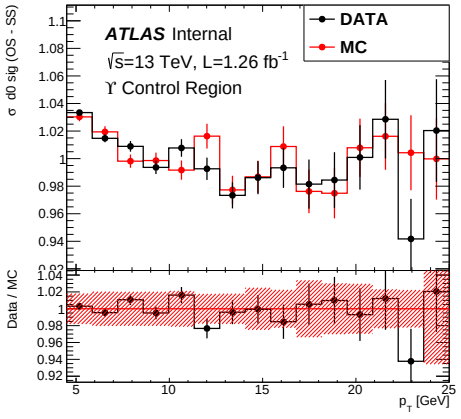

(b) d_0 significance width vs p_T

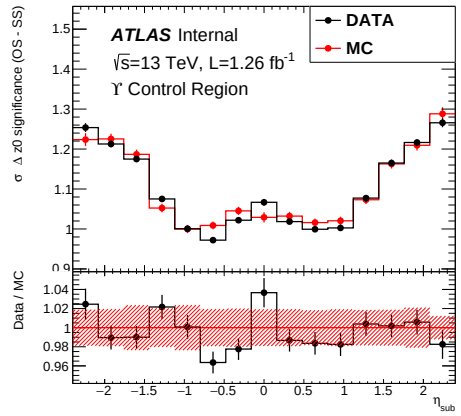

(c) Δz_0 significance width vs η^{sub}

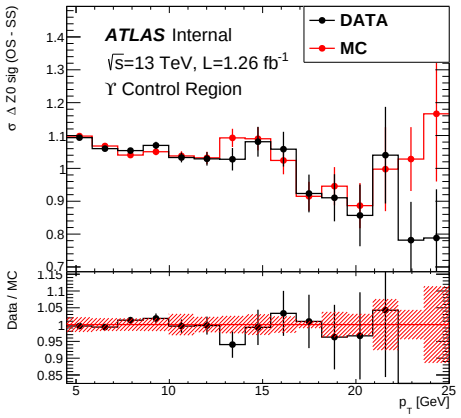

(d) Δz_0 significance width vs p_T^{sub}

Figure 8.11 IP significance width comparison for the $\Upsilon \to \mu\mu$ CR, after applying the IP correction derived in section 8.4. The width is obtained from a Gaussian fit like the one in Figure 8.4. The red band is obtained varying the correction values by 2%. The band covers the residual discrepancies in this closure test.

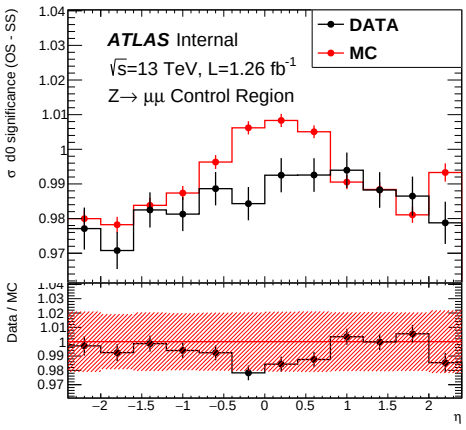

(a) d_0 significance width vs η

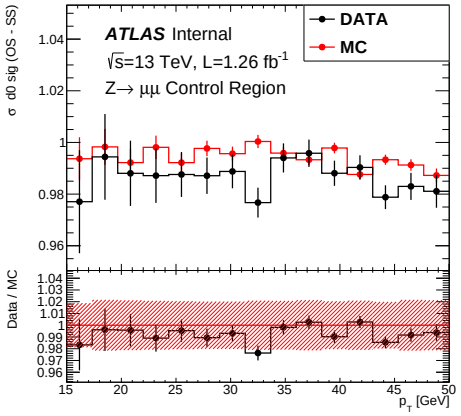

(b) d_0 significance width vs p_T

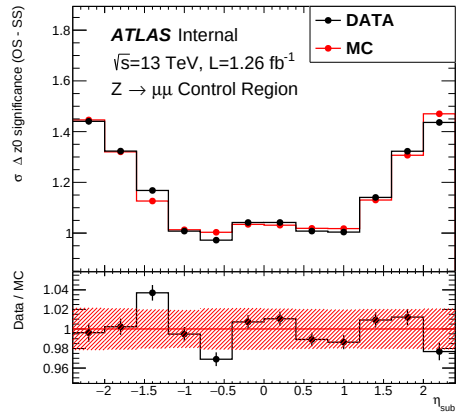

(c) Δz_0 significance width vs η^{sub}

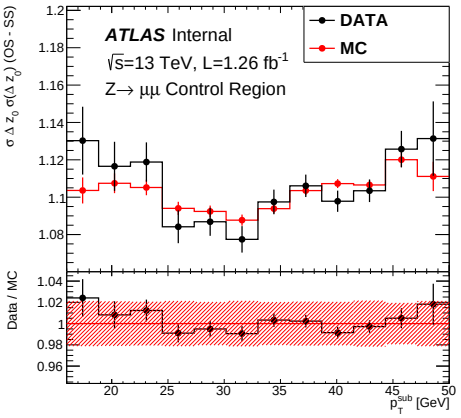

(d) Δz_0 significance width vs p_T^{sub}

Figure 8.12 IP significance width comparison for the $Z \to \mu\mu$ CR, after applying the IP correction derived in section 8.4. The width is obtained from a Gaussian fit like the one in Figure 8.4. The red band is obtained varying the correction values by 2%. The band covers the residual discrepancies in this closure test.

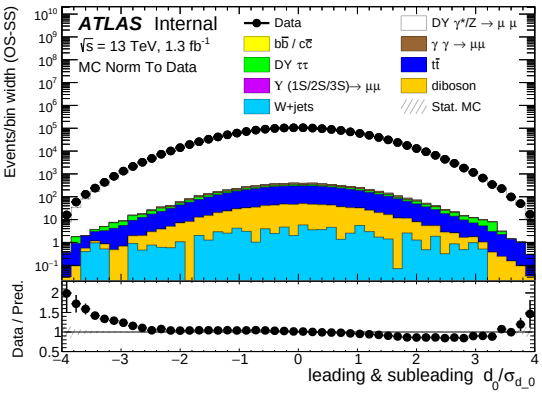

(a) Data and MC comparison after applying the smearing and shifting correction described in section 8.2.

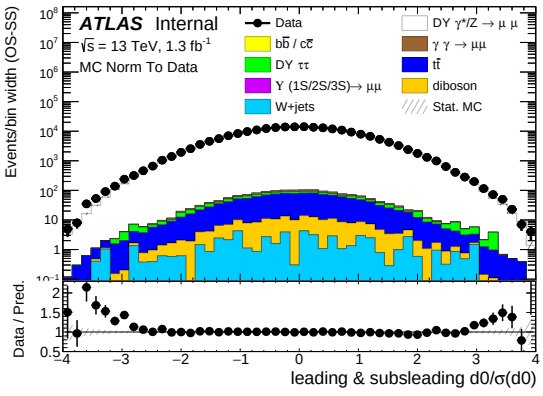

(b) Data and MC comparison after applying the additional correction derived in the analysis and described in section 8.4.

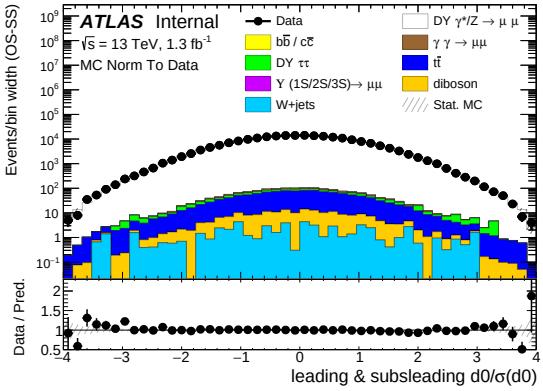

(c) Data and MC after applying the d_0 significance tail reweight of the MC to the data, as described in section 8.4.2.

Figure 8.13 d_0 significance distribution in the Z control region, in data and MC, at various stages of the impact parameter correction.

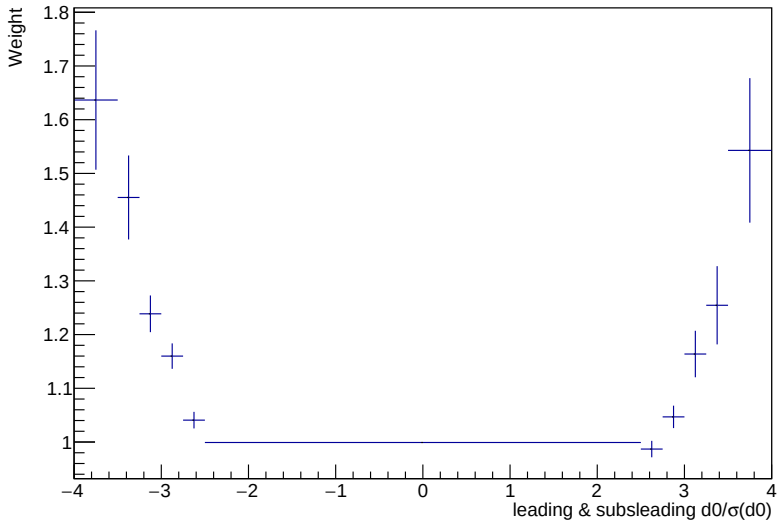

Figure 8.14 Reweight values for the d_0 significance distribution as derived from the Z CR.

8.5 Effects of the correction on the Signal Region

In this section the effect of the Impact Parameter correction on the signal region events are investigated. The correction is applied, as described in section 8.4, to the prompt muon MC samples. After applying the correction, the QCD background estimation is performed, the data-MC agreement for the IP distribution is investigated and the improvement in the modelling is confirmed. In section 8.5.2 the results of the QCD estimation fit are more closely examined.

8.5.1 Data MC comparison

After applying the IP correction to the MC events, the QCD background estimation is performed following the procedure presented in section 7.2. The results are used in the plots in this section. Figure 8.15 shows the d_0 significance distributions, in data and MC, in each of the invariant mass bin considered in the measurement. The plots show good agreement between data and MC. Similar results but for the Δz_0 significance distribution are reported in Figure 8.16. Also in this case good agreement is found.

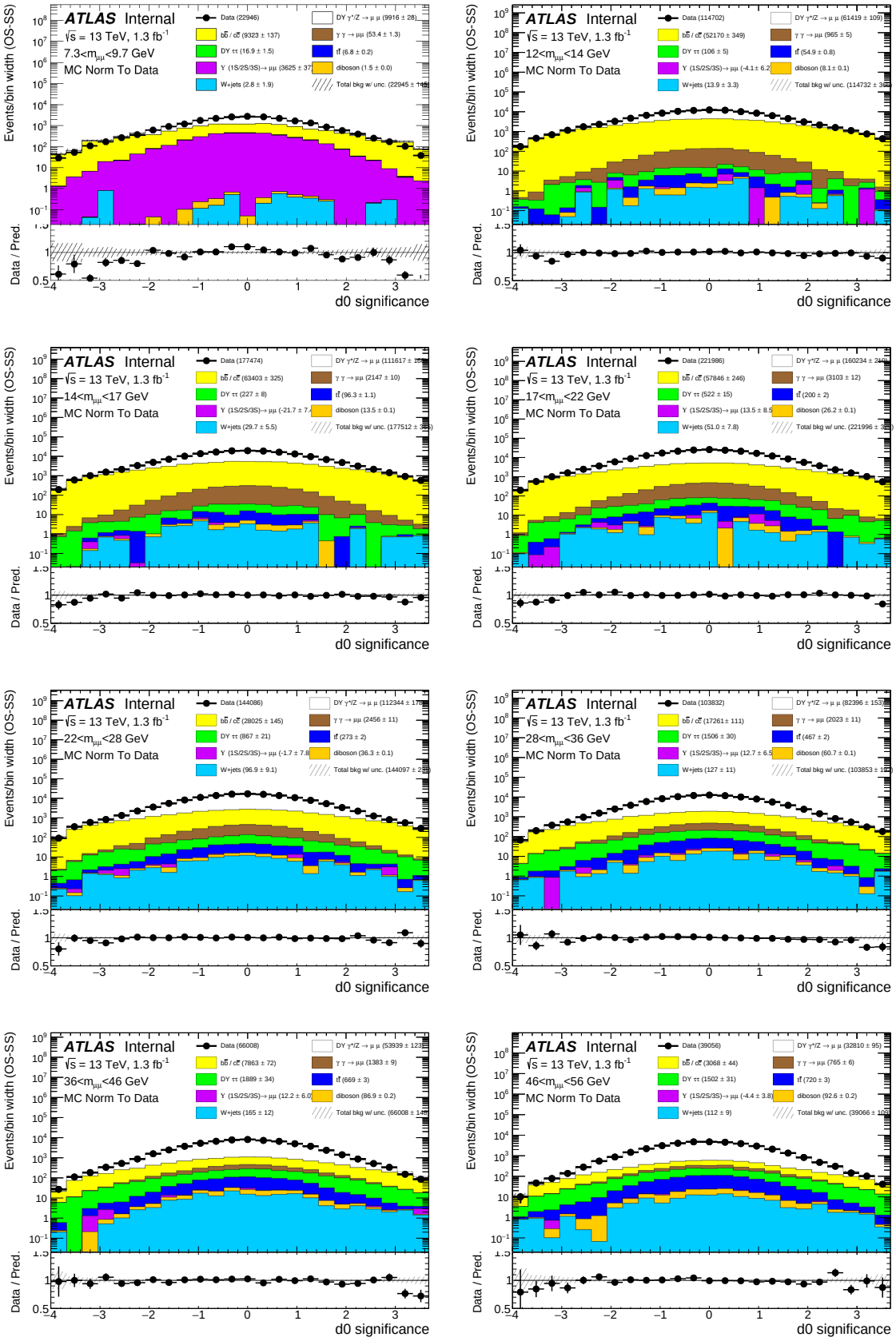

Figure 8.15 Signal region d_0 significance distributions in each of the mass measurement bin. The plots show a good data-MC agreement.

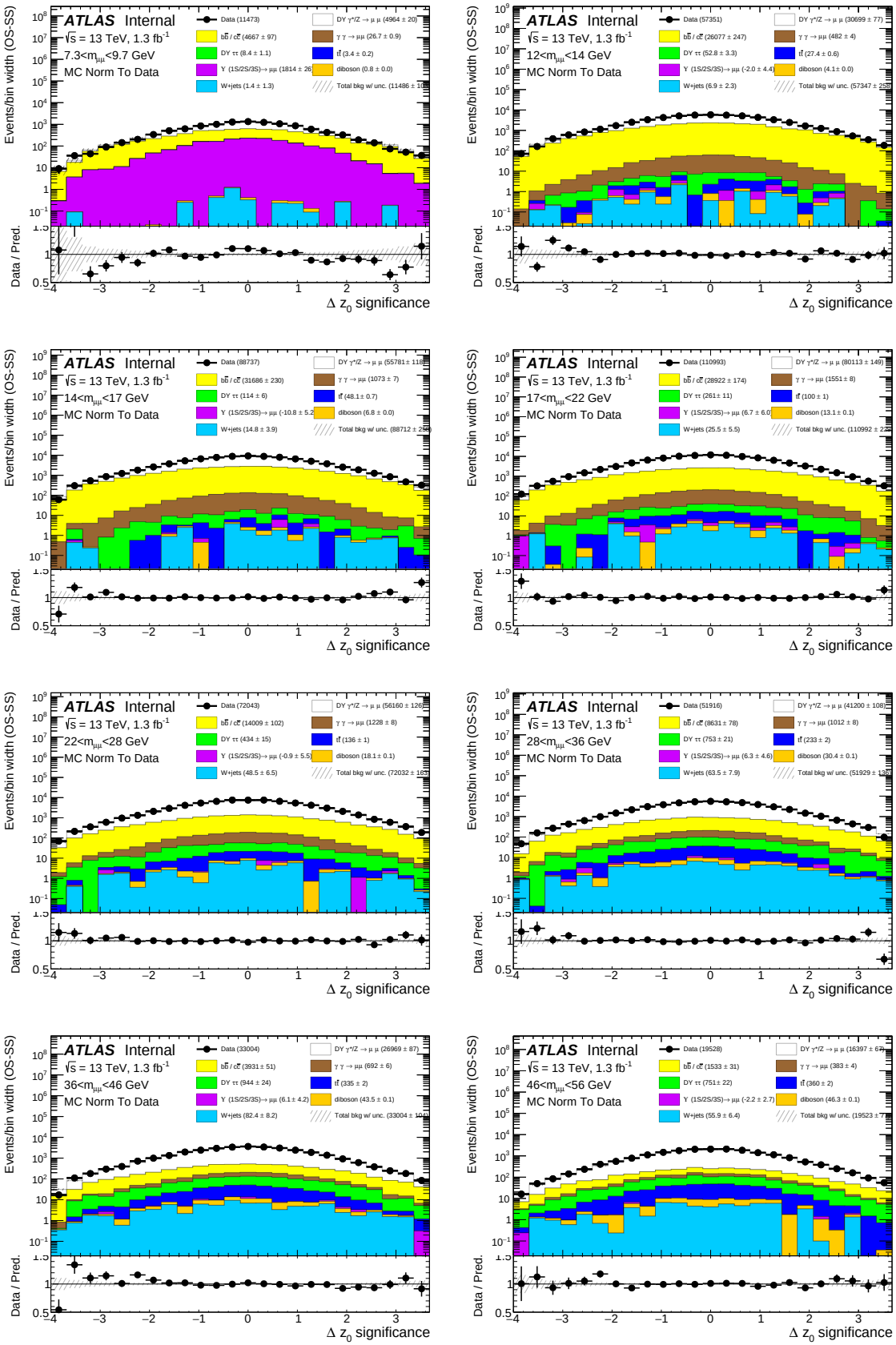

Figure 8.16 Signal region Δz_0 significance distributions in each of the mass measurement bin. The plots show a good data MC agreement.

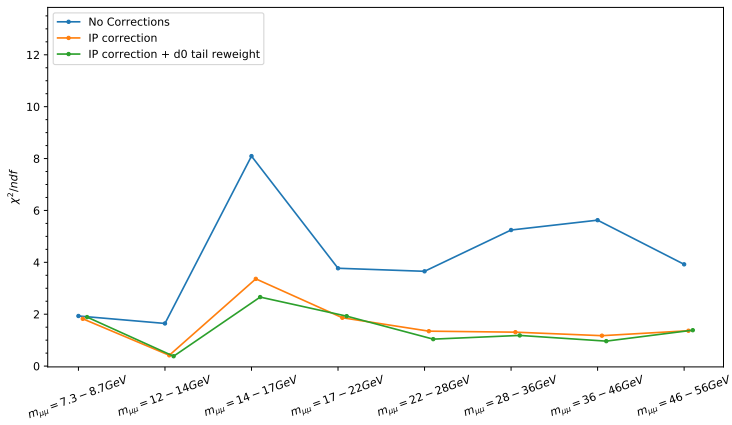

Figure 8.17 Superfitter χ^2/ndf, ndf $= 8$, results at the various stages of the IP correction. The result is shown in each mass measurement bin. A reduction of the fit χ^2 is observed in particular when applying the smearing correction of section 8.4. A smaller improvement is also observed, in most of the bins, after applying the d_0 significance tail reweight, sec. 8.4.2.

8.5.2 *Superfitter* results

The background estimation method, the *superfitter* (section 7.2), performs better after that the IP correction described in this chapter is applied. This can be seen in Figure 8.17 where the fit χ^2, equation 7.6, is compared before and after applying the correction. The reduction of the χ^2 is due to an improved modelling of the fitted distributions.

As mentioned in section 8.4.1, a 2% variation on the correction values is taken as an uncertainty on this MC rescaling procedure. The effect of the 2% variation on one of the output of the superfitter is reported if Figure 8.18. The Figure shows the estimated number of signal events in the data selection, the 2% variation of the IP correction causes a variation in the output of 3% to 4%. This variation contributes to the measurement uncertainty and it is compared to the other source of uncertainty in Chapter 10.

The d_0 significance tail reweight of section 8.4.2 causes a 1% variation in the number of estimated DY events, as shown in Figure 8.19. The result after applying the tail reweight is taken as the nominal. The difference with respect to the case in which no reweight is considered, is used as an estimate of the uncertainty on this correction.

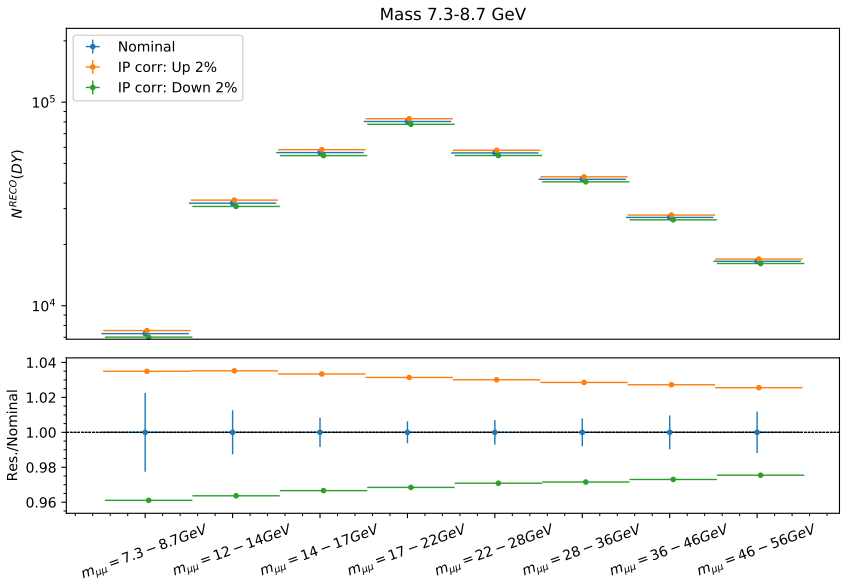

Figure 8.18 Number of signal events in the data selection as estimated from the *superfitter*, in each mass measurement bins. The effect of the 2% variation on the IP correction values cause a change in the fit results of $3-4\%$.

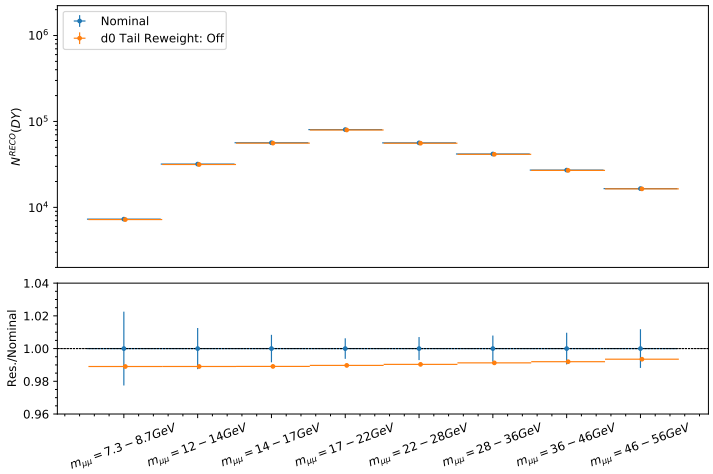

Figure 8.19 Effect of the d_0 significance tail reweight, section 8.4.2, on the *superfitter* result: number of estimated DY events in the data selection. The result is shown in each mass measurement bin. The error bars represent the statistical uncertainty of the data and MC combined.

Chapter 9

Cross section extraction

High energy physics measurements are often based on counting experiments. For a more fruitful comparison with the theory predictions, it is necessary to extract the corresponding cross section of the studied process. In this chapter the studies to extract the Drell-Yan cross section are presented.

The cross section σ can be expressed as the number N of produced DY events in pp collisions, divided by the delivered luminosity L: $\sigma = N/L$. The luminosity is measured by the ATLAS collaboration using van der Meer scans for an absolute measurement and complementary methods for extrapolation at different physics conditions [141, 142]. The number of produced DY events in the collision is extracted from the the number of reconstructed Drell-Yan events candidates in data by correcting for detector inefficiencies and resolution effects. This last procedure is referred to as *unfolding* and is based on MC simulations. In section 9.1 the mathematical problem of unfolding is briefly presented. In the following sections two different approaches, bin by bin unfolding and iterative Bayesian unfolding are presented and applied to the low mass Drell-Yan measurement. In section 9.4, a study of the $p_T^{\mu\mu}$ spectrum in data and MC is presented and the effects of the disagreement when performing the unfolding are explored.

9.1 Unfolding problem

The unfolding procedure uses the reconstructed distribution of events, g, to retrieve the underlying truth distribution f

$$\int R(x^{\text{Truth}}, x^{\text{Reco}}) \cdot f(x^{\text{Truth}}) = g(x^{\text{Reco}}) \tag{9.1}$$

here x is the measured observable, R is the response function that models the detector effects. R is related to the probability distribution that an event with x^{Truth} is reconstructed with value x^{Reco}. The unfolding problem consists of inverting the equation 9.1.

Usually the reconstructed distributions are obtained as histograms and the problem is discretized. In general, the number of detected events in a certain bin of the reconstructed distribution can vary because of the following effects:

- Background events: background processes with similar final state to the process to measure can be misidentified as signal events. The background sources are carefully estimated, but this estimation comes with an uncertainty.

- Detector effects: the imperfect detector efficiency can cause some events to be lost. Because of the finite resolution of the detector, an event can migrate to different bins: at truth level, the event is in one bin, but the it is reconstructed in a different bin.

- Statistical fluctuations: in counting experiments the number of events in a bin is described by a Poisson distribution. The observed number of events is taken as the estimate of the expected number of events and its square root is taken as the statistical uncertainty. This estimate of the uncertainty is a good approximation when the number of events in the bin is large ($N \gtrsim 10^3$) and the Poisson distribution approximate a Gaussian distribution. This is for example the case in the low mass DY measurement.

Considering also the background contribution b_i, equation 9.1 becomes, in the binned case

$$\nu_i = \sum_j R_{ij}\mu_j + b_i \tag{9.2}$$

ν_i and μ_i are the expected number of events in the bin i for the reconstructed and truth histogram respectively. In a general unfolding problem the numbers of reconstructed and truth bins can be different, with $n^{\text{bins reco}} \geq n^{\text{bins truth}}$. ν_i is estimated with the number of observed events n_i and $\sqrt{n_i}$ is used as statistical error. The problem of estimating the number of background events has been discussed in Chapter 7. R_{ij} is the response matrix, it models the detector effect and it gives the probability of observing an event in the bin i given that the truth value is in the bin j. The response matrix is obtained from MC simulation. Given the MC signal samples that simulate the process and detector effects, the matrix elements R_{ij} are given by

$$R_{ij} = \frac{N_{ij}^{MC,\,Reco\wedge Gen}}{N_j^{MC,\,Gen}} \tag{9.3}$$

Here $N_j^{MC,Gen}$ is the number of MC generated events in the bin j. $N_{ij}^{MC,Rec\wedge Gen}$ is the number of events reconstructed in a bin i and generated in the bin j. In the case of weighted MC the number of events is always given by the sum of weights: $N = \sum_i w_i$.

Other than the detector effects, the unfolding can correct also for final state QED effects, according to which generator level particle definition is adopted. In the low mass DY analysis the final state is corrected for the QED final state radiation, and the cross section is extracted at Born level (that refers to leptons prior to QED radiation). The extrapolation at Born level is preferred because the result offers a better versatility in comparison with the theory predictions.

Uncertainties in the knowledge of the response matrix induce uncertainties in the final result. A first source of uncertainty could be non-negligible statistical fluctuations from MC. Furthermore the detector modelling of the resolution and efficiency comes with an uncertainty that can be propagated to the final result as systematic uncertainty. Finally, differences in the underlying theory model used to generate the MC samples can also induce a variation in the result. These sources of uncertainties will be investigated in Chapter 10.

In the next sections the problem of inverting equation 9.2 in the case of the low mass Drell-Yan analysis is faced with two different approaches.

9.2 Bin by bin unfolding

When the number of the truth and reconstructed distribution bins in equation 9.2 are the same, the most straightforward approach to obtain the truth distribution and solve for μ_i in equation 9.2, is given by

$$\mu_i = C_i(n_i - b_i), \quad \text{with} \quad C_i = \frac{N_i^{MC,\text{Reco}}}{N_i^{MC,\text{Gen}}}. \tag{9.4}$$

Here the *correction factors* C_i are obtained from the MC simulations. They are given by the ratio of the number of events reconstructed and generated in a certain bin i. Comparing with equation 9.2, the above result is a solution if

$$\frac{N_i^{MC,\text{Reco}}}{N_i^{MC,\text{Gen}}} = \frac{\nu^{\text{sig}}}{\mu_i} \tag{9.5}$$

Here ν^{sig} is the expect number of events in a bin without background. If the relation above is not perfectly satisfied this unfolding procedure can introduce a bias in the result.

The bin by bin is applied to the low mass Drell-Yan analysis. The cross section, in the single and double differential case, is obtained with the following formulae

$$\frac{d\sigma}{dm_{\mu\mu}} = \frac{n_i - b_i}{C_i \cdot L \cdot \Gamma_{m_{\mu\mu}}} \tag{9.6}$$

$$\frac{d\sigma}{dm_{\mu\mu}d|y_{\mu\mu}|} = \frac{n_i - b_i}{C_i \cdot L \cdot \Gamma_{m_{\mu\mu}}\Gamma_{|y_{\mu\mu}|}} \tag{9.7}$$

$$\frac{d\sigma}{dm_{\mu\mu}dp_T^{\mu\mu}} = \frac{n_i - b_i}{C_i \cdot L \cdot \Gamma_{m_{\mu\mu}}\Gamma_{p_T^{\mu\mu}}} \tag{9.8}$$

where Γ is the bin width and L the luminosity; for the data set considered the recorded luminosity amounts to $L = 1280.28\,\mathrm{pb}^{-1}$.

One can better rely on the assumption in equation 9.5 if there is low migration of events between bins, in this case the effects of data MC differences are mitigated and the bias introduced should be small. The case of no migration corresponds to a response matrix, equation 9.3, with off diagonal elements equal to zero. The relative amount of migration between bins depends on the detector resolution compared to the sizes of the bins used for the unfolding. In the next section, the resolution in reconstructing the unfolded observable is presented. The purity and the stability, quantities that measure the amount of migration, are presented for the unfolding binning scheme, in section 9.2.2.

9.2.1 Resolution study

The study in this section is performed with the MC signal samples (see section 6.4). In Figure 9.1, a study of the detector resolution in reconstructing the dimuon invariant mass is shown. The distribution of the difference between the reconstructed and the generated observable value, $m_{\mu\mu}^{\mathrm{Reco}} - m_{\mu\mu}^{\mathrm{Gen}}$, is used to obtain the results. The mean of the distribution gives the bin content values, while the error bars, that represent the actual resolution, are given by the standard deviation of the same distribution. The generator level particle kinematics is defined prior to final state QED radiation (Born level definition). The binning in the mass resolution plot in Figure 9.1 is the same used for extracting the cross section. Overall, resolution 5 to 10 times smaller than bin widths, is observed. This will reflect in relatively small migration effects as observed in the next section. A small bias of 0.2 GeV between the generated and the reconstructed mass is observed in the high mass bins.

Analogous resolution plots, but for the $|y_{\mu\mu}|$ and $p_T^{\mu\mu}$ observables are shown in Figure 9.2 and Figure 9.3 respectively. The results are shown in each $m_{\mu\mu}$-$|y_{\mu\mu}|/p_T^{\mu\mu}$ bin used in

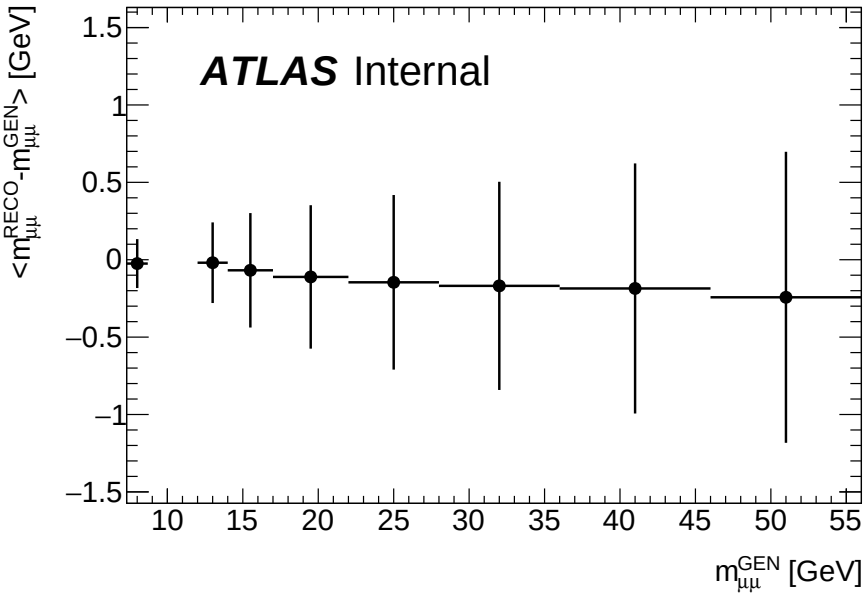

Figure 9.1 Dimuon invariant mass resolution study. The reconstruction resolution correspond to the size of the error bars. A good resolution, much smaller than the bin size is observed.

the unfolding. In both cases good resolution is observed. In the $|y_{\mu\mu}|$ this is at least 10 times smaller than the bin widths. In the $p_T^{\mu\mu}$ distribution, better resolution is observed in particular at low transverse momentum. This is due to the good Muon Spectrometer performance, and allows a fine binning in the lower part of the spectrum when extracting the cross section.

9.2.2 Purity and stability

Two quantities that measure the amount of migration in the unfolding binning, the *purity* and *stability*, are presented in this section. Furthermore the correction factor C_i used to extract the cross section in equations 9.6, 9.7, 9.8 are reported.

Purity

The purity in a bin i is defined as

$$P_i = \frac{N_i^{\text{Reco}\wedge\text{Gen}}}{N_i^{\text{Reco}}}. \tag{9.9}$$

Here $N_i^{\text{Reco}\wedge\text{Gen}}$ is the number of events generated and reconstructed in the same distribution bin i. The purity measures the relative amount of migration into the bin. High purity means

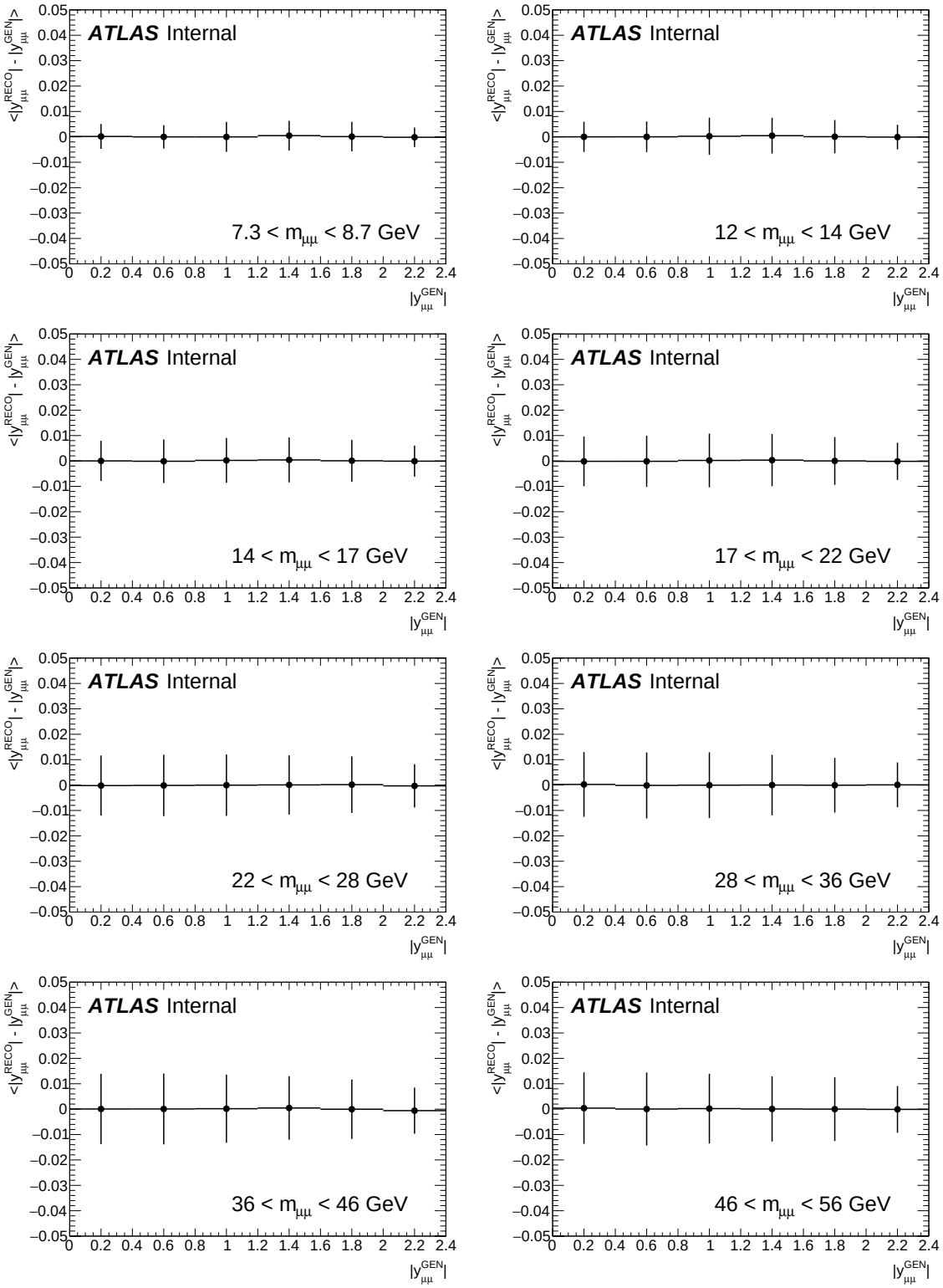

Figure 9.2 Resolution study for the reconstructed dimuon rapidity $|y_{\mu\mu}|$. The estimated resolution is given by the size of the error bars.

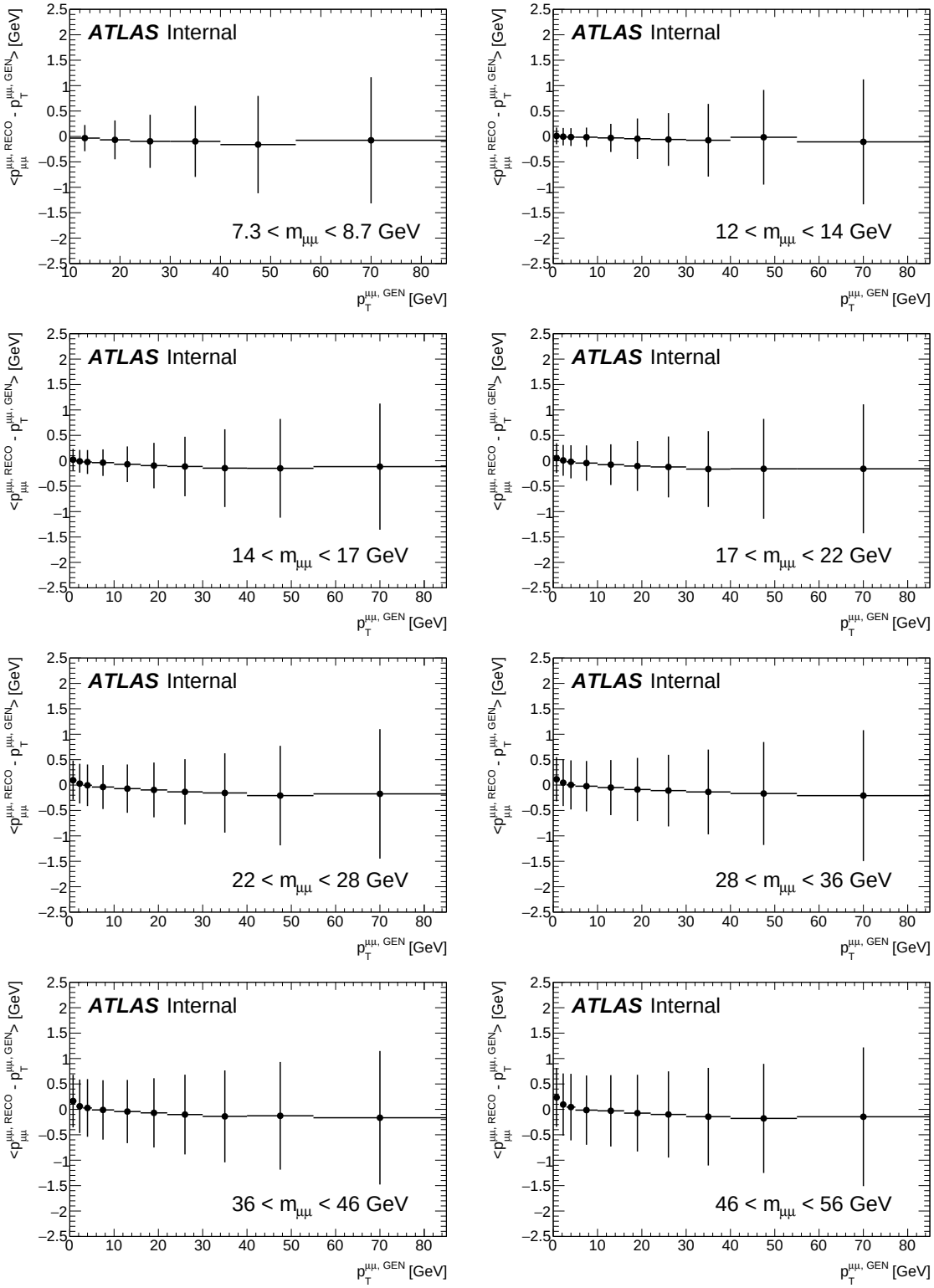

Figure 9.3 Resolution study for the reconstructed dimuon transverse momentum $p_T^{\mu\mu}$. The estimated resolution is given by the size of the error bars.

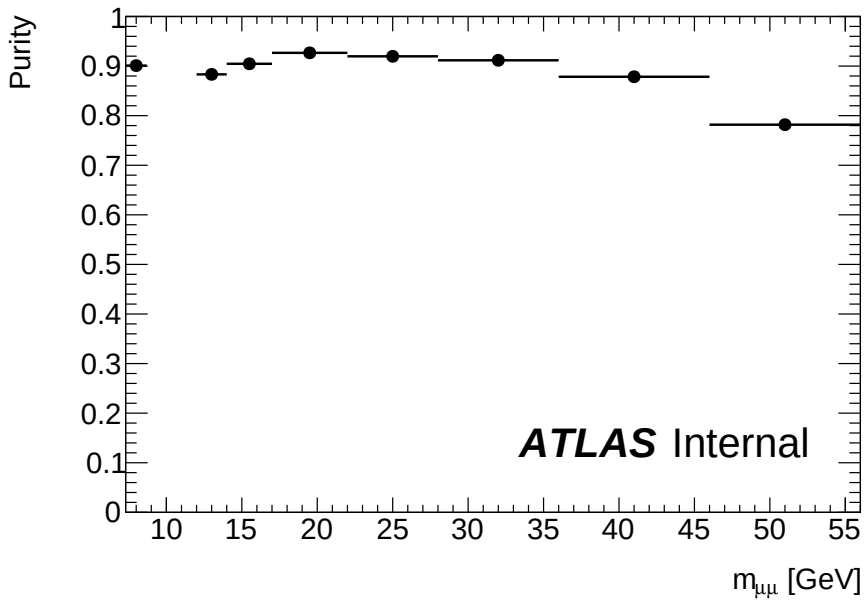

Figure 9.4 Purity in the mass measurement bins. The generator final state definition corresponds to Born level. The decrease of purity in the higher mass bins is due to migration of events from the Z resonance mass peak.

low migration into the bin. The studies are performed using the the MC signal samples. The results for the dimuon invariant mass are shown in Figure 9.4. For the generated particles the Born definition is used. The purity in the mass bins is higher than 85% except that in the last mass bin. The decrease of purity at high mass is due to migration of events from the Z boson mass peak. This is clearly visible in Figure 9.5 where the generated mass spectrum of the events migrating inside the fiducial volume at reconstruction level is shown. The muons coming from the Z decay radiate an highly energetic photon, as a consequence the dimuon invariant mass is reconstructed inside the selection region. When considering the generator level events, this hard photon radiaton is not considered, as the Born level definition consider muons prior to final state radiation.

The purity of the two folded $m_{\mu\mu} - p_T^{\mu\mu}$ bins is shown in Figure 9.6. In the higher mass bins, a dip around $p_T^{\mu\mu} \sim 30-40\,\text{GeV}$ is observed. This is again due to migration of events from the Z pole. Roughly speaking, the transverse momentum of the emitted high energetic radiation is given by

$$p_T^{\gamma} \sim m_Z - m_{\mu\mu}^{\text{Reco}} \approx 30-40\,\text{GeV}. \tag{9.10}$$

This effect of migration due to final state radiation is corrected when extracting the cross section at Born level. An uncertainty related to the modelling of the final state QED radiation

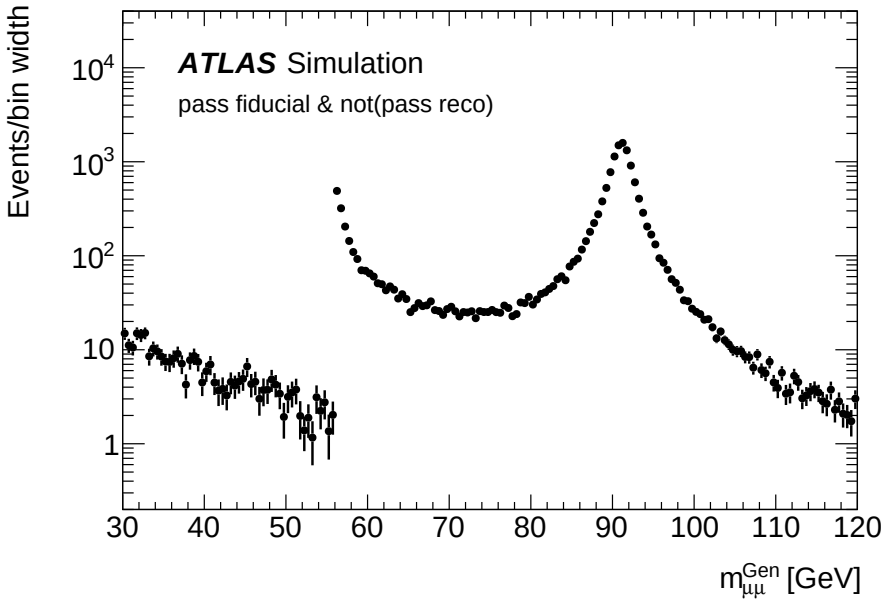

Figure 9.5 Generated mass spectrum of the events migrating into the fiducial volume at reconstruction level. The fraction of the events coming from the Z boson mass peak is visible.

will be taken into account in the final publication and should cover possible differences between data and MC. At low $p_T^{\mu\mu}$, where the binning is finer, the purity is higher than 80% up to $m_{\mu\mu} = 36\,\text{GeV}$. At higher mass it partially decrease and gets around $65-70\%$. This result is due to the good muon momentum resolution of the detector.

To complete the purity study, the results for the two dimensional $m_{\mu\mu} - |y_{\mu\mu}|$ binning are shown in Figure 9.7. Here a purity compatible with mass result in Figure 9.4 is observed.

Stability

The stability of a distribution bin i is defined as

$$S_i = \frac{N_i^{\text{Reco}\wedge\text{Gen}}}{N_i^{Gen}}. \tag{9.11}$$

$1 - S_i$ gives the fraction of events migrating outside of the bin at reconstruction level. The result for the invariant mass bins is reported in Figure 9.8. A very high stability, flat around 90%, is observed. The stability of the two dimensional binning $m_{\mu\mu} - |y_{\mu\mu}|$ and $m_{\mu\mu} - p_T^{\mu\mu}$ are reported in Figure 9.9 and Figure 9.10 respectively. The $|y_{\mu\mu}|$ stability is mostly flat and compatible in each bin with the one dimensional mass result Fig. 9.8. The migration out of the bin is relatively more important at low $p_T^{\mu\mu}$ due to the finer binning adopted. In the low

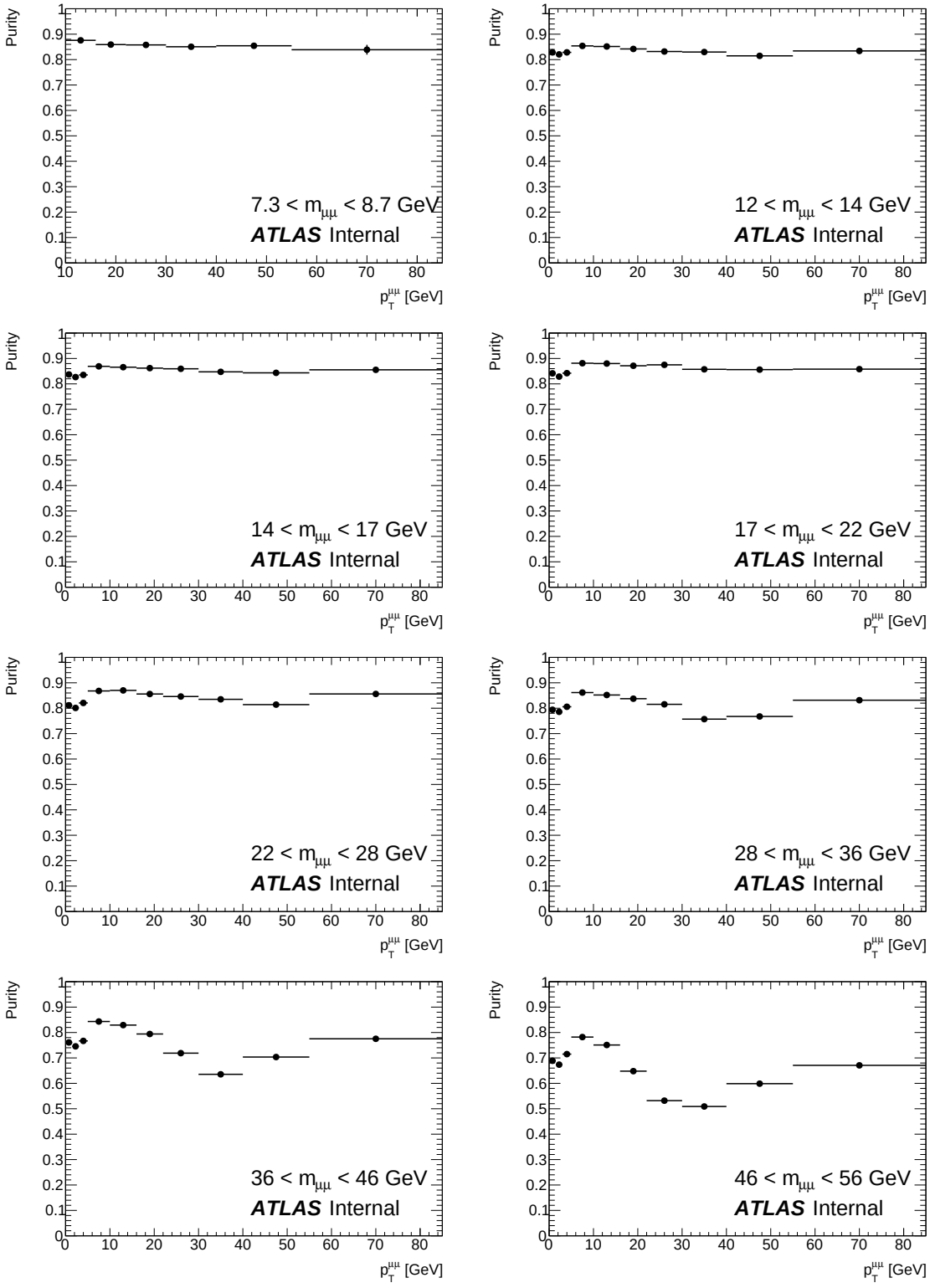

Figure 9.6 Purity study for the $m_{\mu\mu} - p_T^{\mu\mu}$ measurements bins.

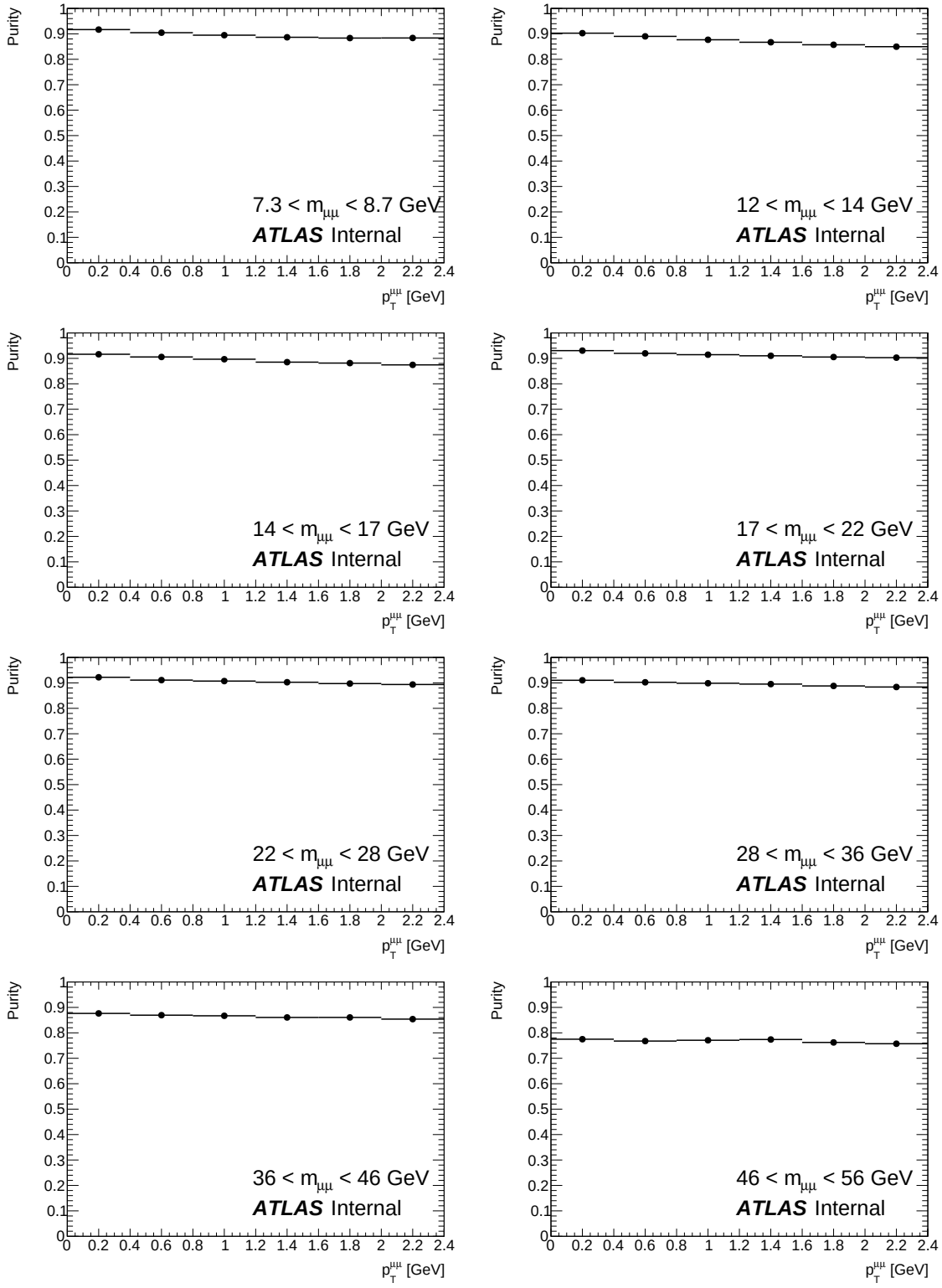

Figure 9.7 Purity study for the $m_{\mu\mu} - |y_{\mu\mu}|$ measurements bins.

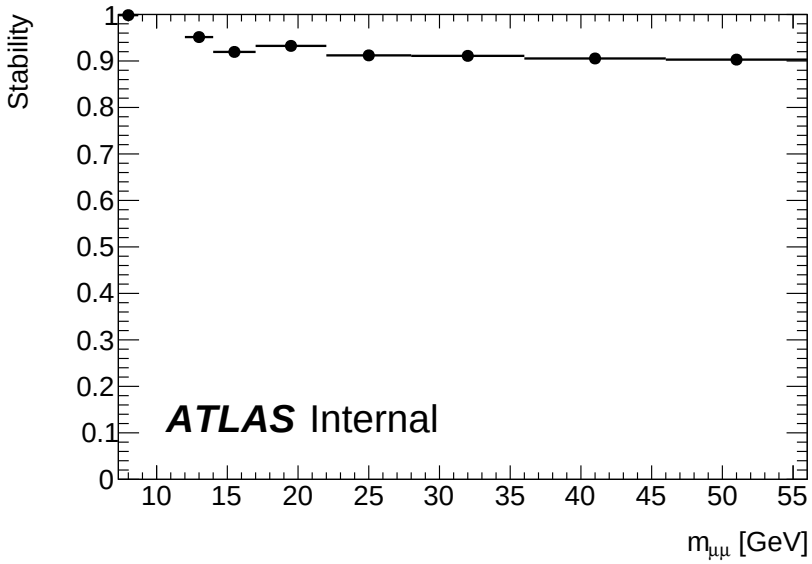

Figure 9.8 Stability study for the dimuon invariant mass distribution.

mass$-p_T^{\mu\mu}$ bins, thanks to the good momentum resolution, the stability is still higher that 80%. In last mass bins it falls as low as 65%.

In general, an high purity and stability is observed for the chosen unfolding binning. This justifies the adopted binning scheme and increases the confidence in the bin by bin unfolded results.

9.2.3 Correction factors

The correction factors C_i in the cross section formulas, equations 9.6-9.8 are defined as the the ratio of the number of events reconstructed and generated in a bin i. They correct for the detector resolution and inefficiency effects. The correction factor for the mass differential cross section are reported in Figure 9.11. The factors also take into account the prescale of one of the triggers in the trigger chain as discussed in section 6.6. This explain the low C_i values at low mass. Analogous plots but for the rapidity and transverse momentum measurements are reported in Fig. 9.12 and Fig. 9.13 respectively. The peak in the C_i values at high mass and around $p_T^{\mu\mu} \sim 40\,\text{GeV}$ is due to the migration of events from the Z resonance peak, as described in section 9.2.2.

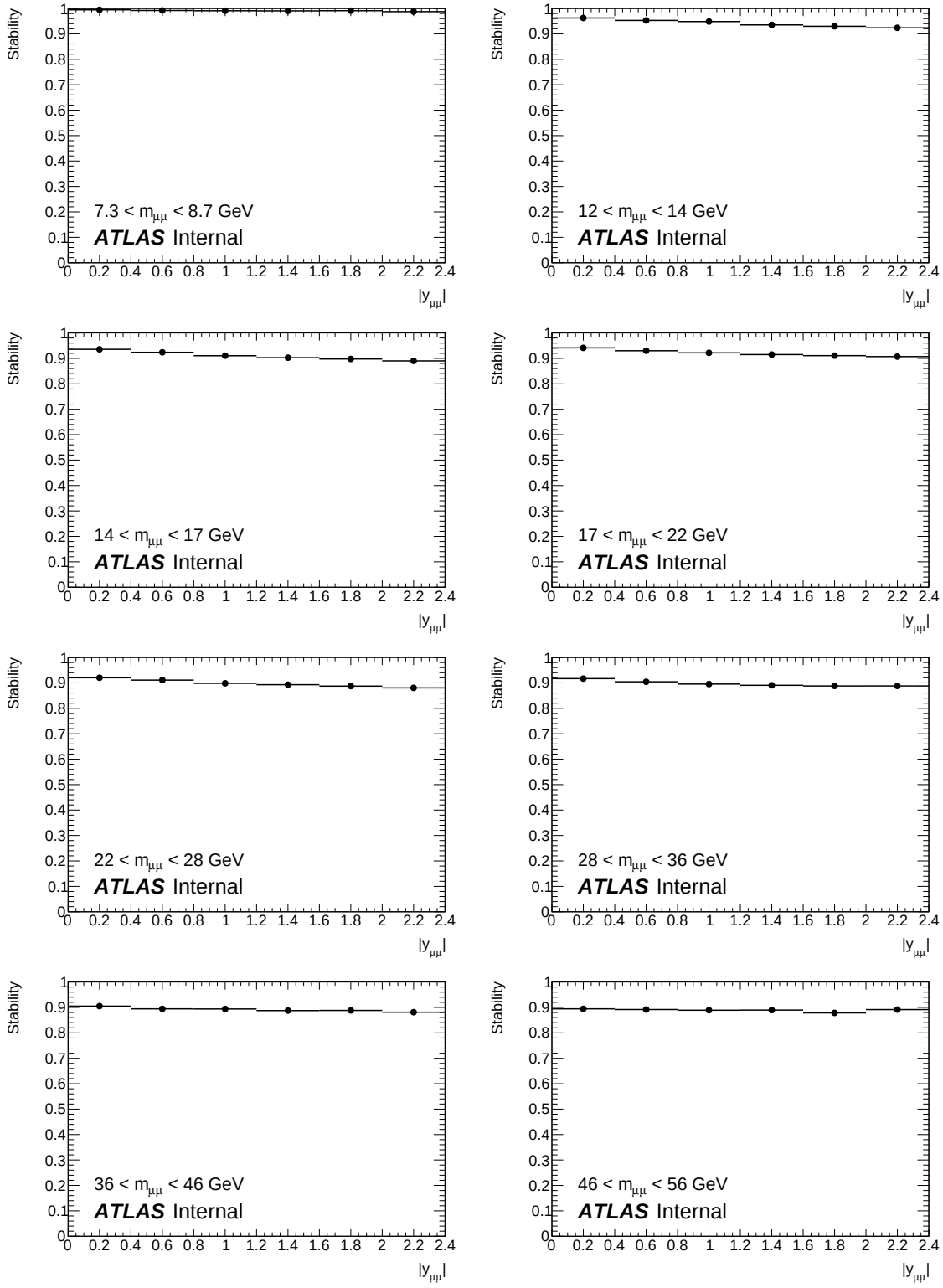

Figure 9.9 Stability of the $m_{\mu\mu} - |y_{\mu\mu}|$ measurements bins.

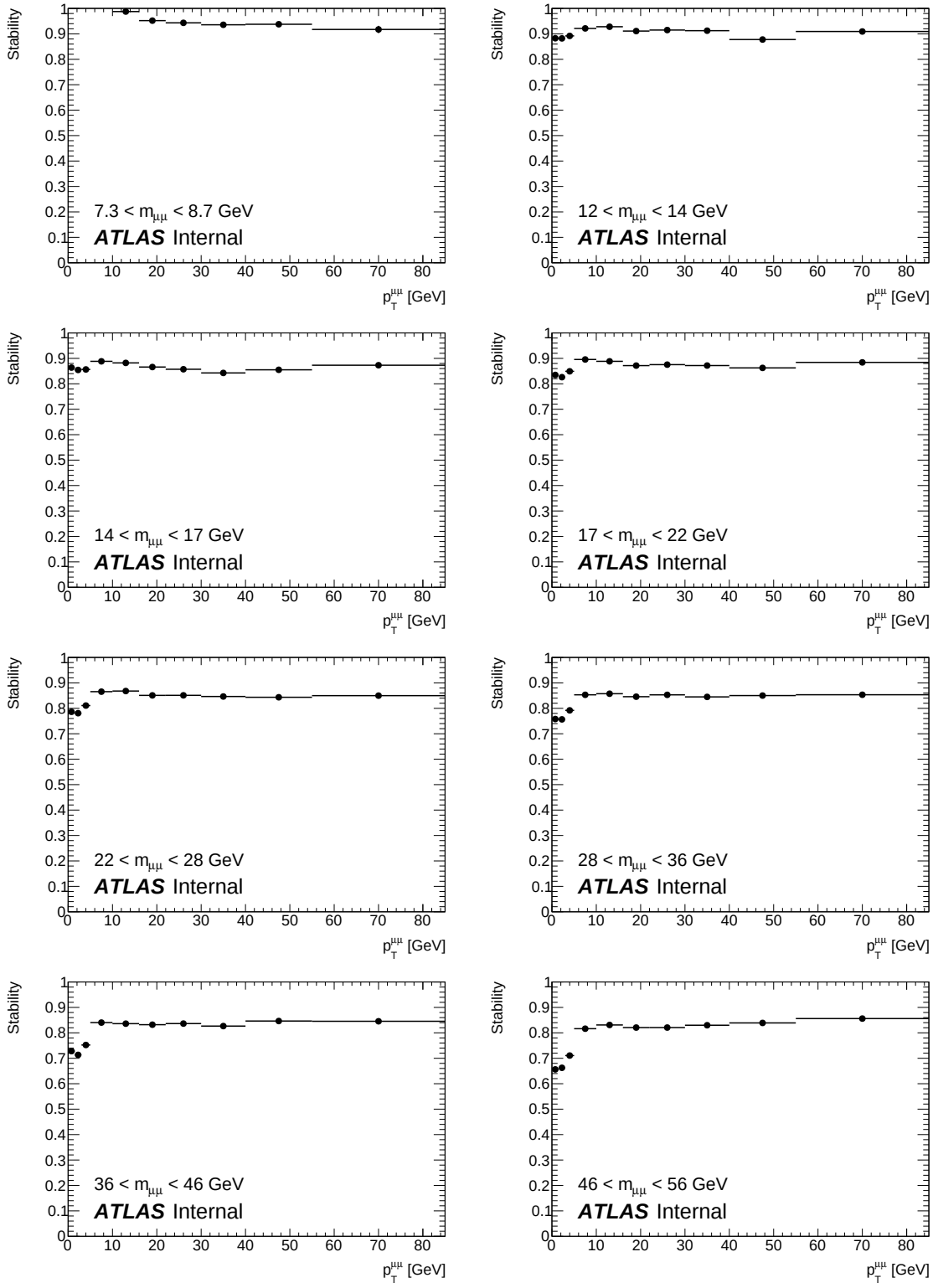

Figure 9.10 Stability of the $m_{\mu\mu} - |y_{\mu\mu}|$ measurements bins.

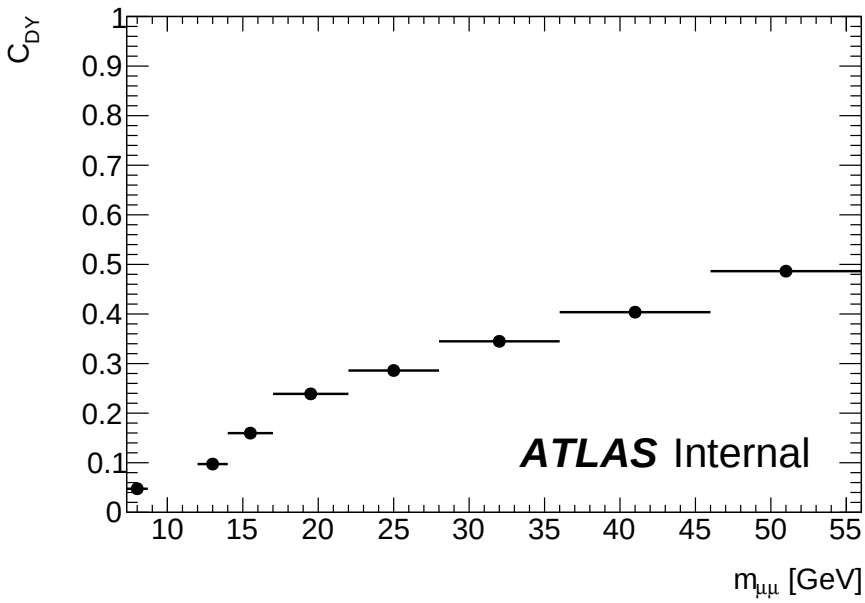

Figure 9.11 Correction factors for the mass cross section extraction.

9.3 Iterative Bayesian unfolding

In this section an alternative unfolding approach, iterative Bayesian unfolding, is applied to extract the DY cross section.

The method uses a probabilistic approach to invert equation 9.2. The entry R_{ij} of the response matrix in equation 9.2 is related to the conditional probability $P(obs_i|truth_i)$, that is the probability of observing an event in the bin i given that the truth value is in the bin j. The exact relation is: $R_{ij} = 1/\varepsilon_i P(obs_i|truth_j)$, where ε_i is the detector efficiency in the bin. As mentioned in section 9.1, the response matrix is extracted from the MC simulations. If one had the 'inverse' of this probability, $P(truth_i|obs_j)$, it would be possible to obtain the truth number of events in a bin i as

$$n_i^{\text{truth}} = \frac{1}{\varepsilon_i} \sum_i P(truth_i|obs_j) \cdot n_j^{\text{obs}} \tag{9.12}$$

Here n_i^{obs} is the observed number of events in data. The Bayesian unfolding make use of the *Bayes* theorem to infer the probability of $P(truth_i|obs_j)$ as

$$P(truth_i|obs_j) = \frac{P(obs_i|truth_j)P(truth_j)}{\sum P(obs_i|truth_j)P(truth_j)} \tag{9.13}$$

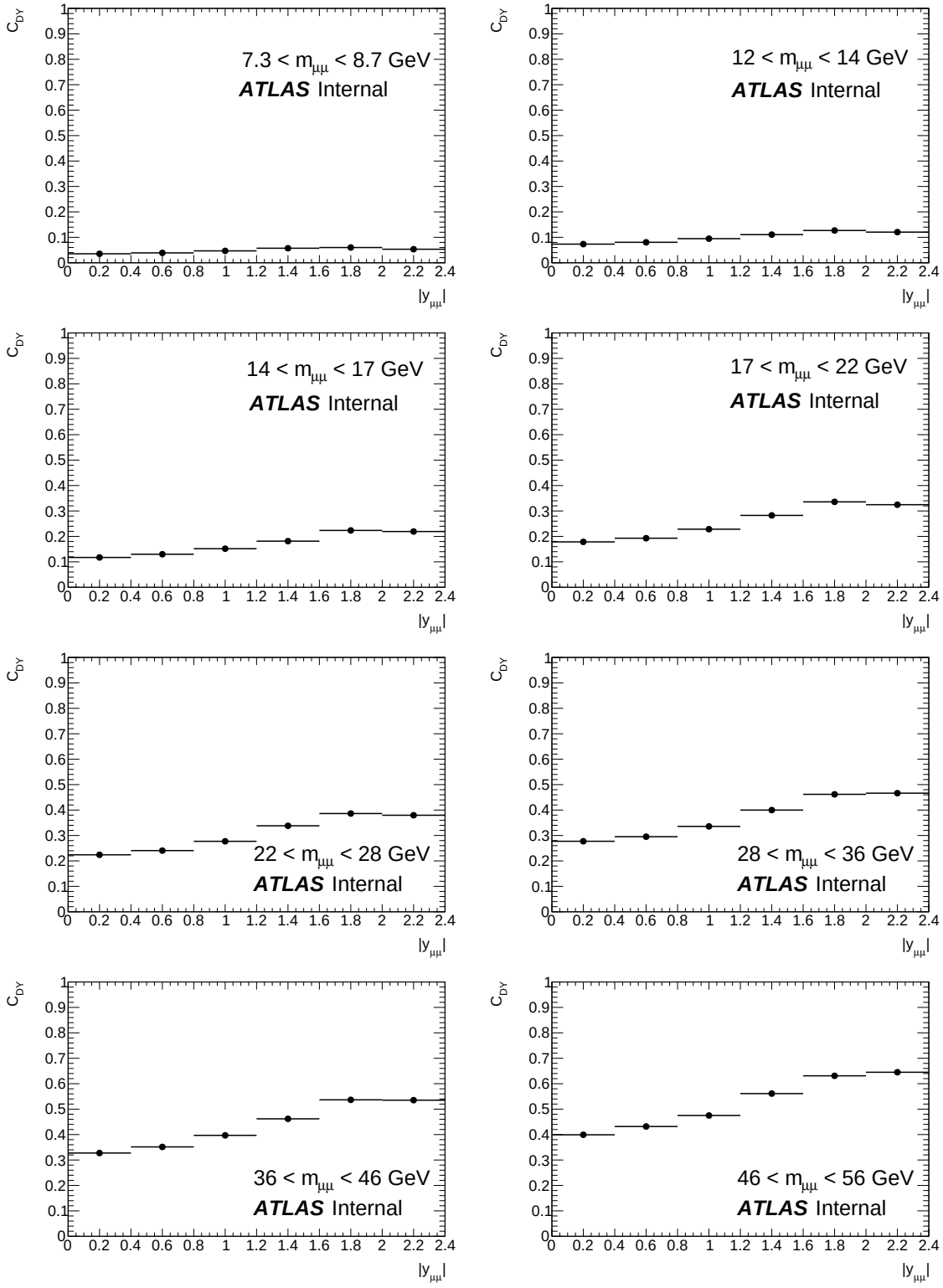

Figure 9.12 Correction factors in the $m_{\mu\mu} - |y_{\mu\mu}|$ measurements bins.

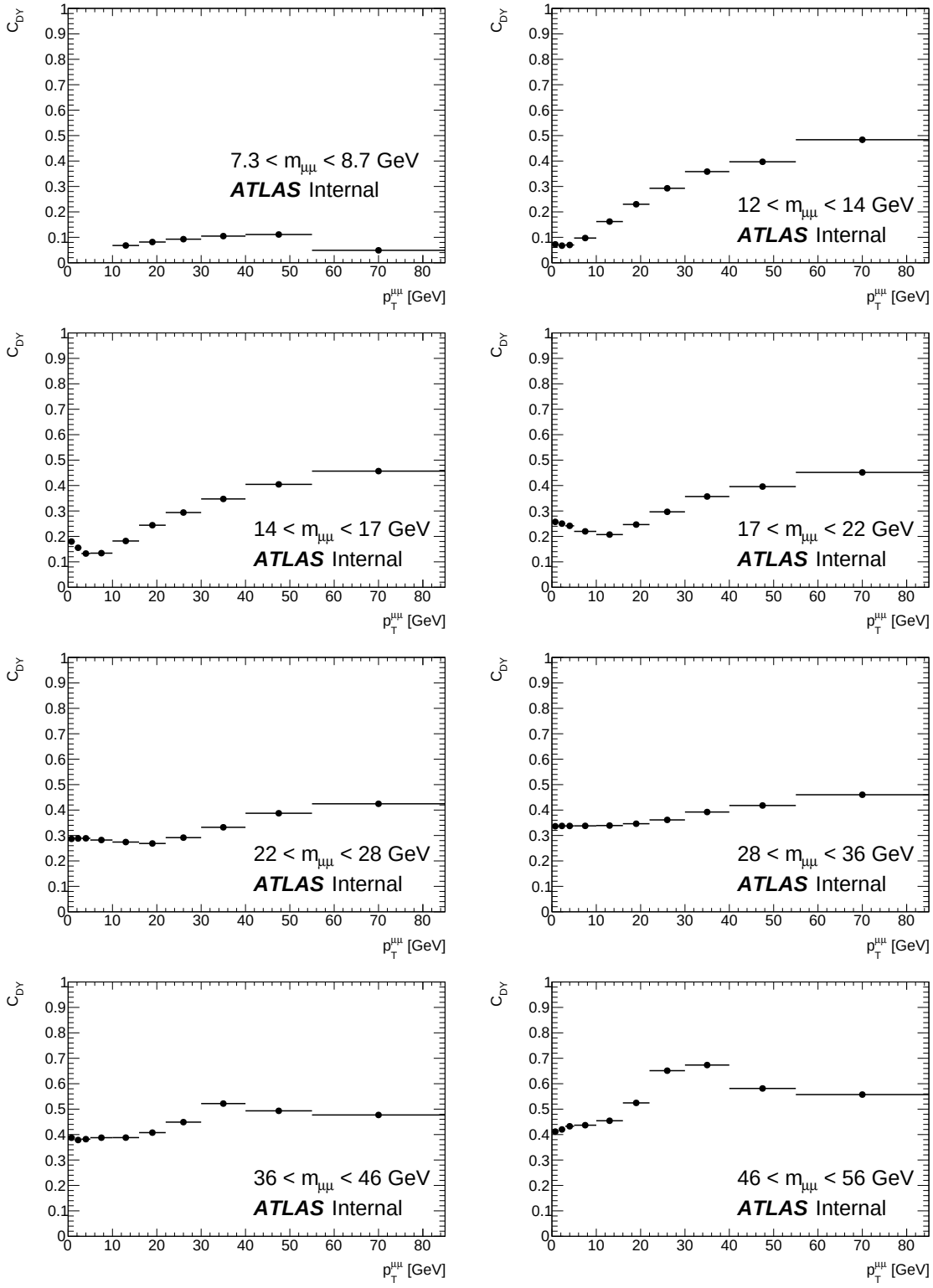

Figure 9.13 Correction factors in the $m_{\mu\mu} - |y_{\mu\mu}|$ measurements bins.

$P(truth_j)$ is the so-called *prior* and in this formulation represents the underlying truth spectrum. Any choice of the prior would bias the result, for this reason the strategy is to solve the problem iteratively and update the prior at each iteration with the information obtained from the previous iteration. At the iteration step $r+1$, $P(truth_i|obs_j)$ is given by

$$P^{r+1}(truth_i|obs_j) = \frac{P(obs_i|truth_j)P^r(truth_j)}{\sum_j P(obs_i|truth_j)P^r(truth_j)}. \tag{9.14}$$

Substituting into equation 9.12 the result is obtained

$$n_i^{\text{truth},r+1} = \sum_j P(obs_i|truth_j)P^r(truth_j) \cdot \frac{n_j^{obs}}{n_j^{\text{obs},r}} \tag{9.15}$$

where $n_j^{\text{obs},r} = \sum_j P(obs_j|truth_i)P^r(truth_i)$. The prior to use in the first iteration, $P^0(truth_i)$, can be chosen to be the normalized spectrum predicted by the MC simulation. Increasing the number of iterations the unfolded solution tends to be unfolded solution. On the other hand an higher number of iterations will make the result more sensitive to structure in n_j^{obs} that originate from statistical fluctuations. A criteria used to decide the number of iterations to perform is to check the stability of the result. The outcome of the $r+1$ iteration is compared with that of the previous iteration, if the agreement is good enough, the algorithm is stopped. In general few iterations are used.

9.3.1 Unfolding results

The results for the low mass DY cross section extracted using the bin by bin method and the Bayesian unfolding method are compared. Both for the single and double differential results, four iterations are used in the Bayesian unfolding procedure.

The result for the invariant mass cross section is reported in Figure 9.14. The bin by bin and the iterative unfolded results agree within 0.6%. The iterative method, already at the second iteration, gives a very stable result. Similar results are observed in the double differential $m_{\mu\mu} - |y_{\mu\mu}|$ cross section, Figure 9.15.

The double differential $m_{\mu\mu} - p_T^{\mu\mu}$ results are reported in Figure 9.16. The bin by bin and the iterative method results presents differences of maximum 1% at low and very high $p_T^{\mu\mu}$. The differences are slightly larger, $2-3\%$, in the higher mass bins. The iterative results also in this case seem to reach a convergence already at the second iteration. One more iteration only seems necessary in some low $p_T^{\mu\mu}$ and high mass parts of the spectrum.

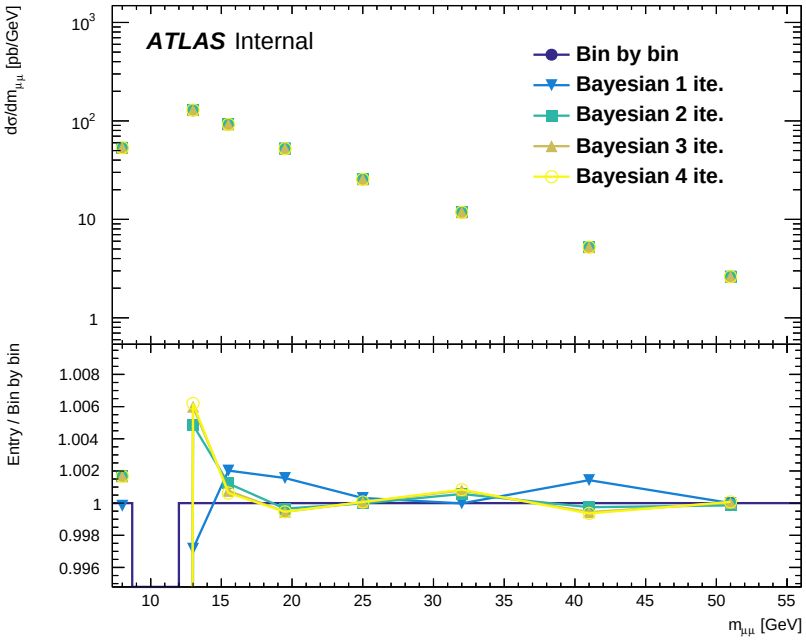

Figure 9.14 Drell Yan cross section results using different unfolding methods: bin by bin unfolding and Bayesian iterative unfolding.

This study shows that no significant bias seems to affect the bin by bin unfolding procedure, at least with respect to the Bayesian unfolding results. The measurement results presented in Chapter 11 are obtained with the bin by bin procedure. Switching to the Bayesian unfolding result will possibly happen in the final publication.

9.4 Transverse momentum reweighting

The signal DY monte carlo samples poorly model the γ^*/Z transverse momentum distribution in the high part of the spectrum. This is due the level of QCD accuracy: Next-to-Leading order and effectively only Leading-Order at high $p_T^{\mu\mu}$. This because at one hard emission is needed for the event to be at high $p_T^{\mu\mu}$. The mismodelling can be observed in Figure 9.17 where the inclusive transverse momentum distribution in data and MC is reported. In order to avoid biases in the cross section result due to the incorrect modelling, a reweight of the MC $p_T^{\mu\mu}$ spectrum to the data is performed. This in particular is applied when extracting the mass differential and $m_{\mu\mu} - |y_{\mu\mu}|$ differential cross section. The reweighting is performed at truth level using a smooth function with the effect of improving the data MC agreement of the reconstructed distributions. To obtain the reweighting function the results of the *superfitter*

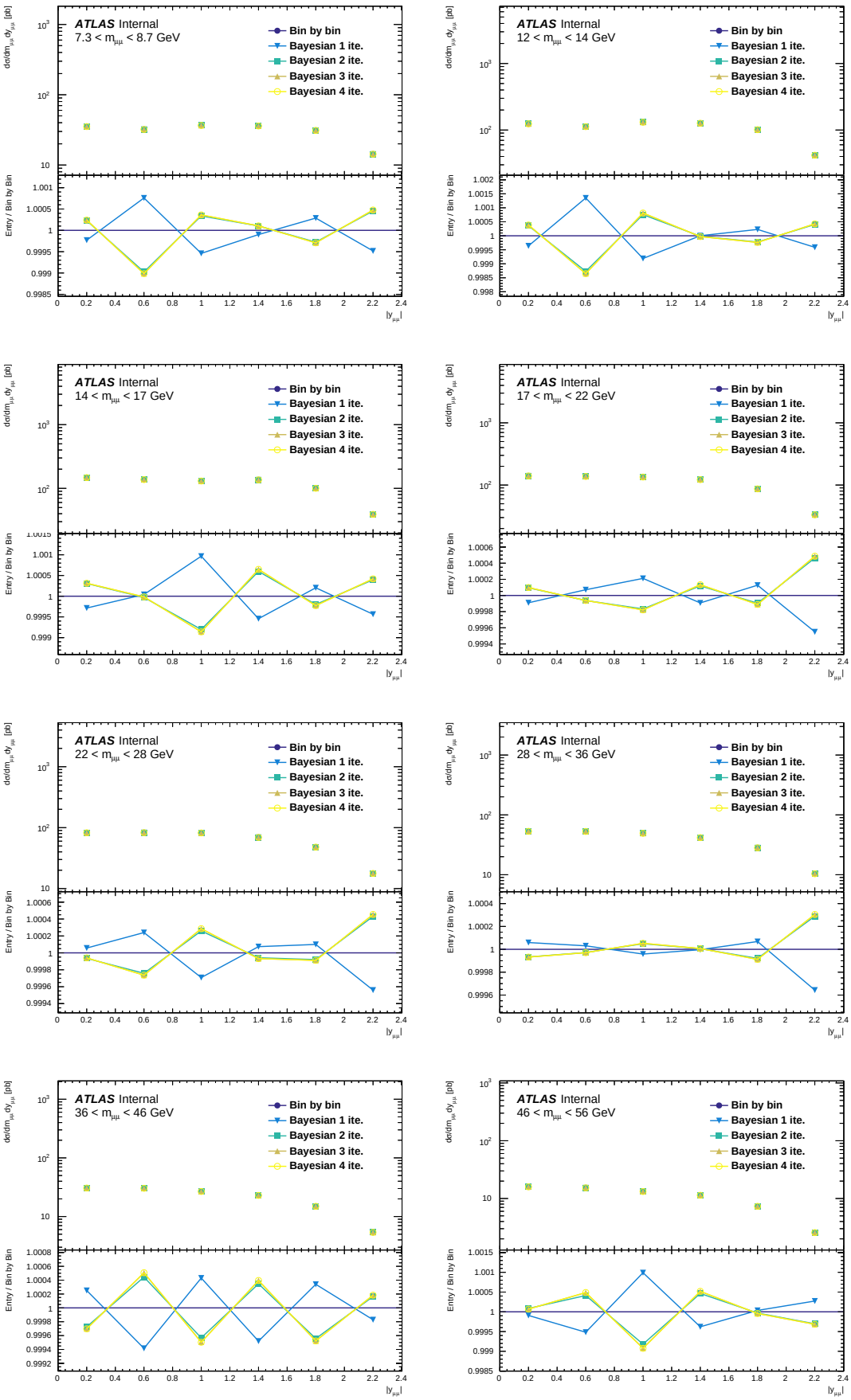

Figure 9.15 $m_{\mu\mu} - |y_{\mu\mu}|$ cross section extracted using the bin by bin method and the iterative Bayesian method.

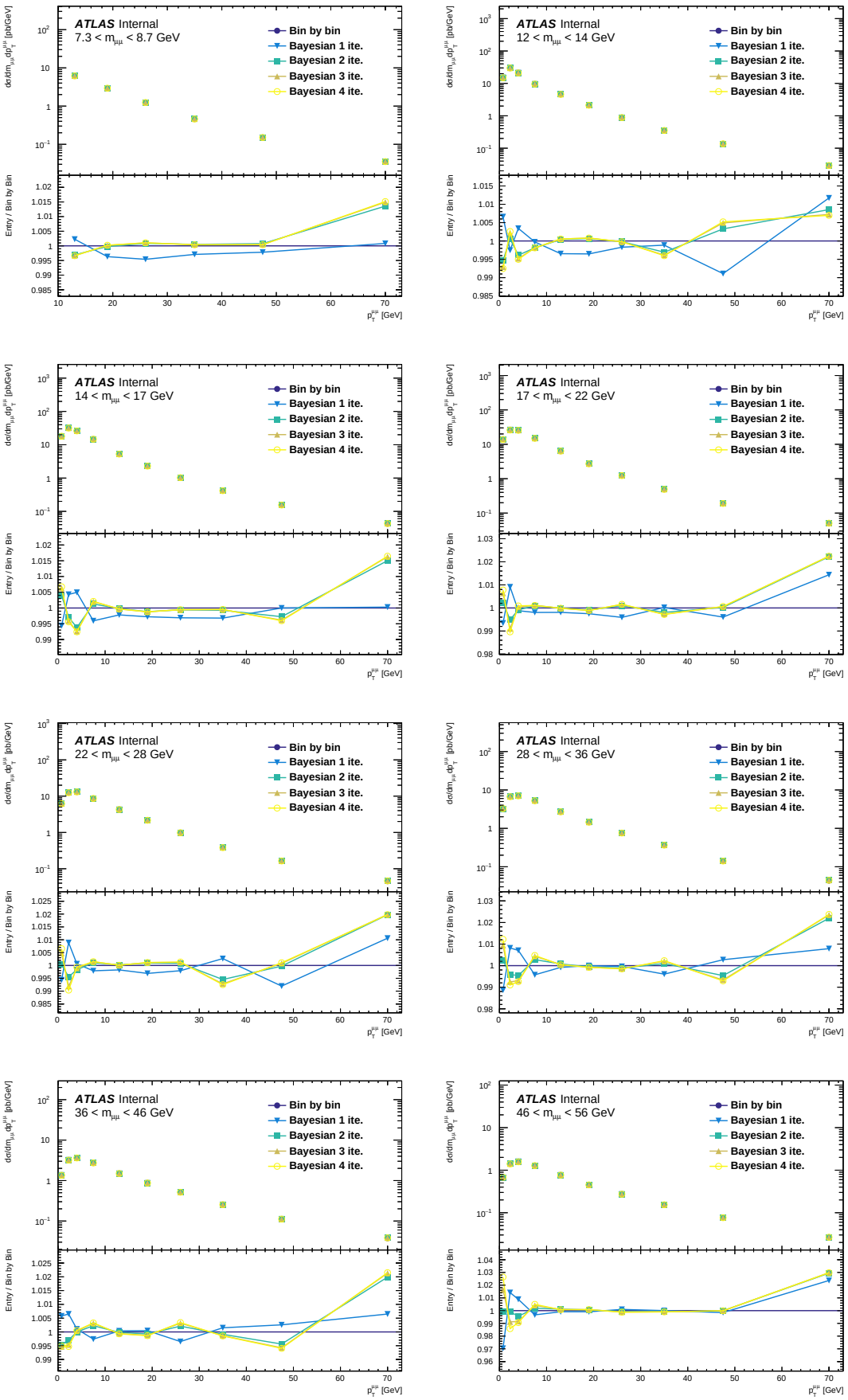

Figure 9.16 $m_{\mu\mu} - p_T^{\mu\mu}$ cross section extracted using the bin by bin method and the iterative Bayesian method.

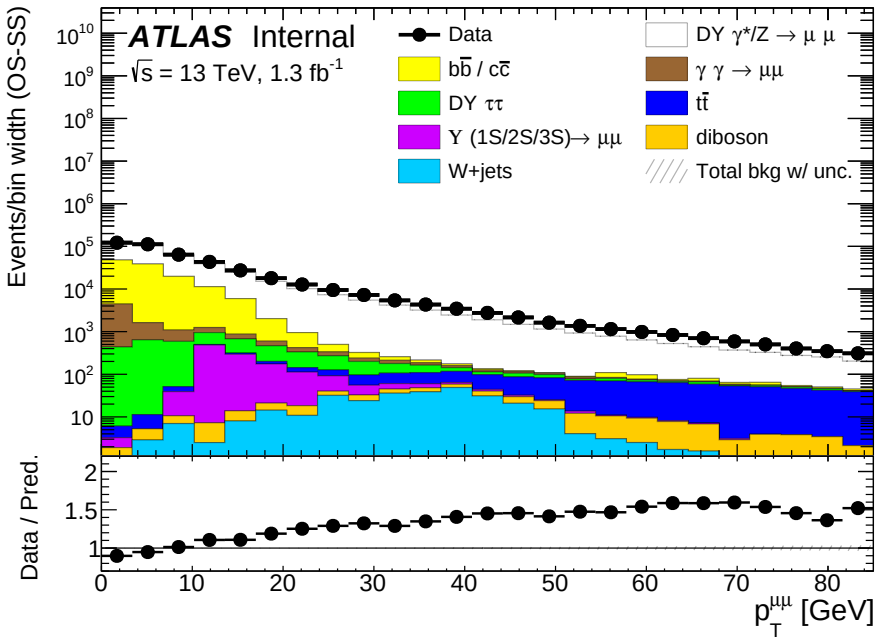

Figure 9.17 Dimuon transverse momentum distribution comparison between data and MC. At medium and high $p_T^{\mu\mu}$ values a mismodelling of the MC is observed.

method in the $m_{\mu\mu} - p_T^{\mu\mu}$ binning scheme are used. The factor k_{DY} from the background fit, see equations 7.4 and 7.6, are equal to the number of reconstructed DY events in data divided by the number of events predicted in MC

$$k_{DY} \approx \frac{N^{\text{data}-N^{\text{BG}}}}{N^{DY,MC}} \tag{9.16}$$

the equivalence holds within fluctuations in the fit results. The functional form chosen to fit the the k_{DY} values is the following

$$f(x) = \begin{cases} p_0 + p_1 \cdot (x - p_2)^2 + \frac{1}{x+\delta} & \text{if } x < p_2 \\ p_0 + \frac{1}{p_2+\delta} & \text{if } x > p_2 \end{cases} \tag{9.17}$$

x is the transverse momentum and the parameters p_i are estimated with the fit. For $x < p_2$, the function is a polynomial of degree two, this is able to catch the raising shape of the data MC ratio, Fig. 9.17. Above p_2 the function is set to a constant. This avoids the polynomial increasing decreasing too much and limits the possibility of very large weight for very high $p_T^{\mu\mu}$ events. The term $1/(x+\delta)$ is added to describe a falling shape of the fitted quantity at

very low $p_T^{\mu\mu}$. The δ term is introduced to avoid the divergence for $p_T^{\mu\mu} \to 0$, its value is set to $\delta = 0.2\,\text{GeV}$. The results of the fit in each mass measurement bin are reported in Figure 9.18 the reweight is applied according to the generated event kinematics

$$w^{\text{rew}} = f(p_T^{\mu\mu,\text{Gen}}), \tag{9.18}$$

The reconstructed $p_T^{\mu\mu}$ distribution is shown in Figure 9.19, after the reweighting good agreement between data and MC is observed.

The effects of the reweighting procedure on the cross section results are due to a change of the correction factors in equation 9.6 (this when considering the bin by bin unfolding procedure, more generally, the changes are in the response matrix, eq. 9.3). The effects on the mass differential cross section, due to the reweight are shown in Figure 9.20. The biggest difference, up to 20%, is observed in the first three mass bins, this is where the reweighting function around the bulk of the $p_T^{\mu\mu}$ distribution, low $p_T^{\mu\mu}$ values, are most different from one. The effect on the double differential $m_{\mu\mu} - |y_{\mu\mu}|$ distributions is of similar size and mostly flat in rapidity. In figure the $|y_{\mu\mu}|$ spectrum in the $12 < m_{\mu\mu} < 14\,\text{GeV}$ mass bin is shown as an example.

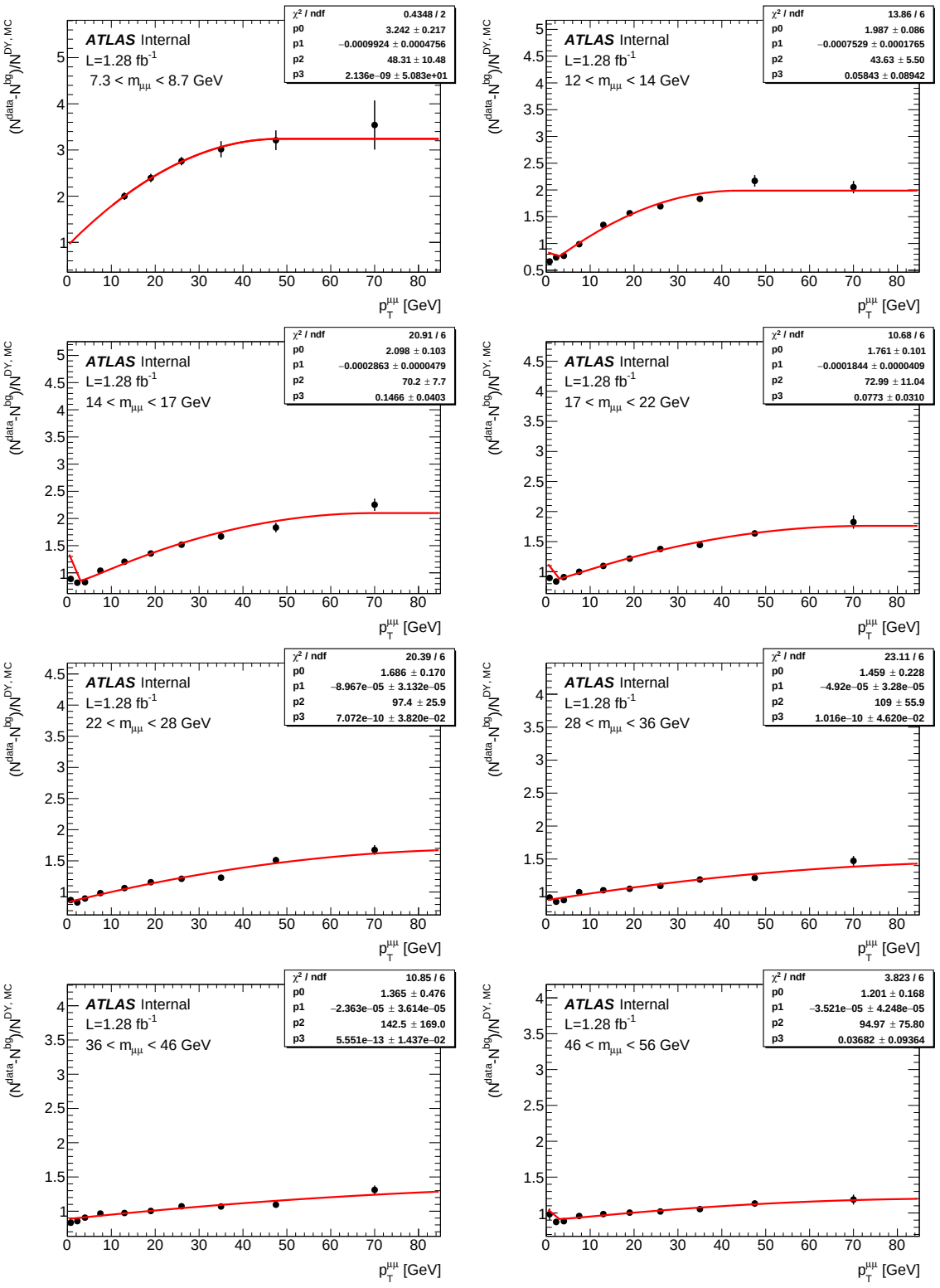

Figure 9.18 $p_T^{\mu\mu}$ reweighting function fit results.

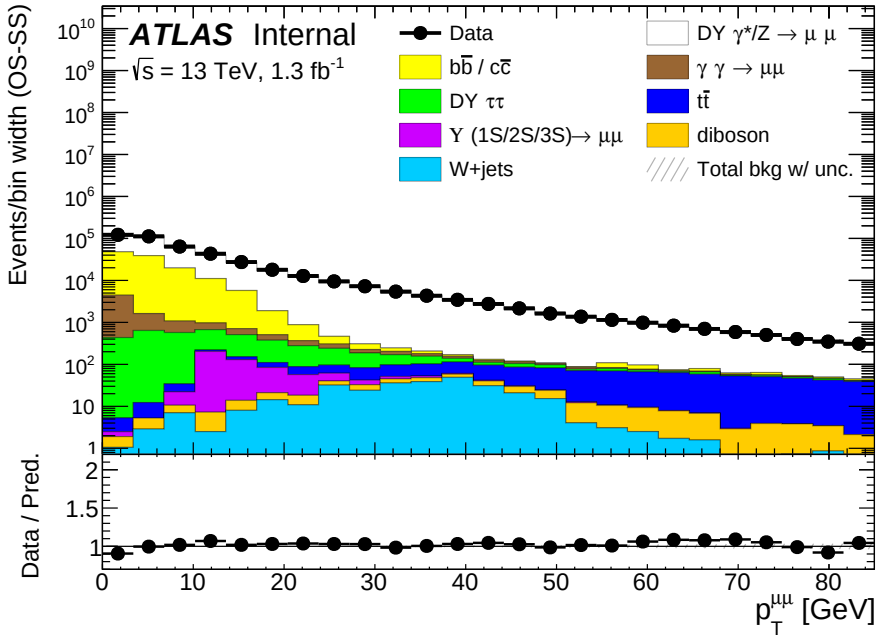

Figure 9.19 Reconstructed dimuon transverse momentum distribution after the $p_T^{\mu\mu}$ reweight of MC events. A good agreement between data and simulation is obtained.

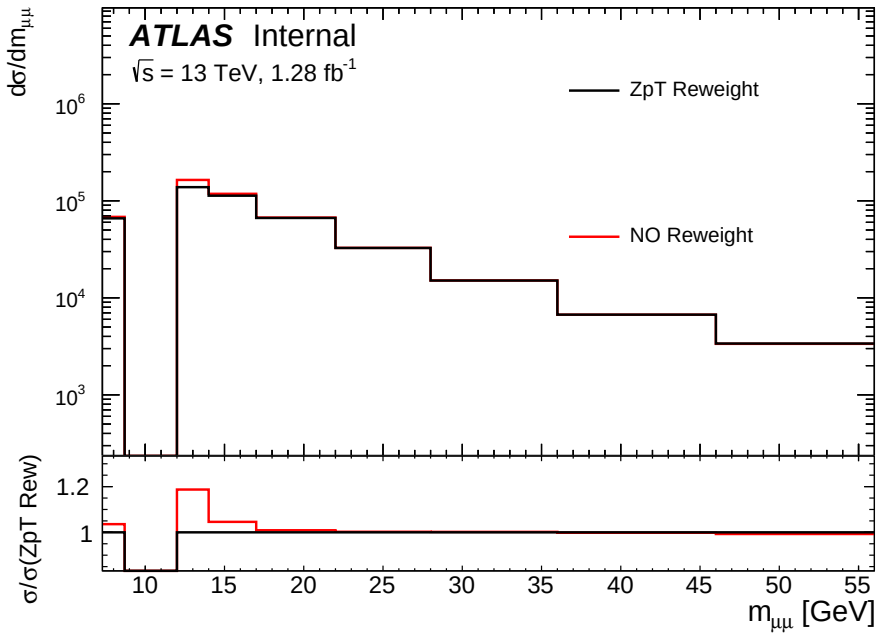

Figure 9.20 Unfolded mass cross section results before and after applying the $p_T^{\mu\mu}$ event reweight to the signal MC.

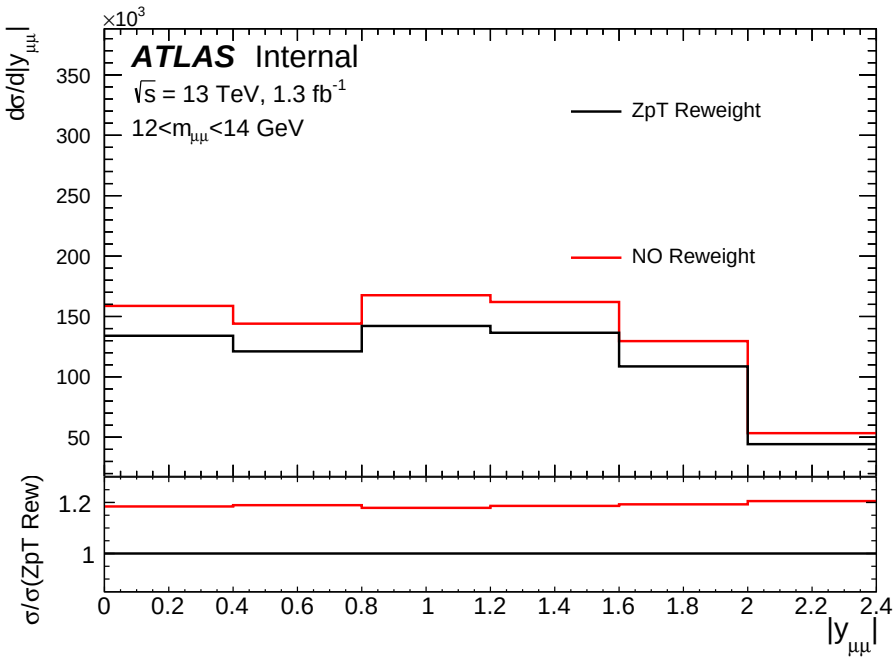

Figure 9.21 Unfolded $|y_{\mu\mu}|$ cross section results before and after applying the $p_T^{\mu\mu}$ event reweight to the signal MC. In particular the cross section in the mass bin $12 < m_{\mu\mu} < 14\,\text{GeV}$ is shown.

Chapter 10

Systematic uncertainties

The different sources of uncertainty affecting the low mass DY measurement are investigated in this chapter. In general, uncertainties that are not related to the data statistics are referred to as systematic uncertainties. A variation of the number of background events or an uncertainty on the momentum resolution of the detector, for example, can induce an uncertainty on the cross section measurement. In the previous chapter the cross section extraction strategy has been presented, the master formula for the calculation is

$$\sigma_i = \frac{N_i^{\text{data}} - N_i^{\text{background}}}{C_i \cdot L \cdot \Gamma_i} \tag{10.1}$$

here i is the distribution bin (see section 9.4 for more details). Any uncertainty affecting one of the terms in the equation above, induces an uncertainty on the cross section. These sources are propagated to the final results and their impact is compared. Other than the statistical uncertainty of the data and MC samples, the uncertainties mainly come from the following effects

- variation in the number of the estimated background events. This is studied in section 10.1. Both the uncertainty on the background estimated with MC and on the multijets background extracted with a data-driven approach are discussed.
- Uncertainty on the momentum scale and resolution of the reconstructed muons and uncertainty in the detector efficiency. These affect the correction factors C_i in equation 10.1. The effects on the results are analysed in section 10.2.
- Luminosity uncertainty. The luminosity in the denominator of equation is measured by the ATLAS collaboration [141]. For the data analyzed in the low mass DY analysis,

the recorded luminosity is $L = 1280.28\,\text{fb}^{-1}$ with a related uncertainty of 2.1%. This reflects on a flat $\sim 2\%$ error on all the extracted distributions.

- Unfolding uncertainty. This takes into account residual bias in the unfolding procedure. The uncertainty can be estimated with some closure tests that check the robustness of the unfolding. This uncertainty is not fully evaluated yet and is not presented in this chapter. Its contribution is anyway expected to be small compared to the other uncertainties considered in the chapter.

- Theory uncertainties. These are related to variations in the underlying theory model used in MC signal samples (the DY$\to \mu\mu$ samples in this case), and affect the estimation of the correction factor C_i in equation 10.1. Theory errors considered are the PDF uncertainty and variation of the parton shower model. These uncertainty are not fully evaluated yet, and are not reported in this chapter. They are expected to be small compared to the other uncertainties considered in the chapter.

10.1 Background uncertainties

The background events to the Drell-Yan process are estimated using both MC simulations, section 7.1, and a data driven approach, section 7.2. For the *EW* backgrounds and the events coming from the Υ decay the simulations are used. In the Υ case the overall normalization is obtained with a fit to the data in the Υ control region 6.8.1. For these backgrounds the uncertainty is estimated by varying the total cross section normalization of the MC samples. The variation is expected to cover the data-MC shape differences in the analysed phase space. The amount of the variation depends on how reliable the MC are in describing the processes. The chosen values for each background sample are summarized in table 10.1. In some cases this might be a conservative choice, but these background components are small, and the relative uncertainties are always 5 to 10 times smaller than other uncertainty contributions. In general a 10% variation is adopted and a more conservative 30% variation is used in two cases. One is the double dissociative $\gamma\gamma \to \mu\mu$ contribution. For the elastic and single dissociative components a variation of 10% of the normalization is chosen. This is justified by the level of agreement between data and MC found in a previous ATLAS measurement for this process [143]. The double dissociative component is instead more difficult to probe and a more conservative variation of 30% is used. This value is chosen also for the W+jets background. In this case the the used generator, Sherpa2.2.1, has been observed to describe the data with disagreement up to $20-30\%$ [144]. The uncertainty on the extracted cross

Table 10.1 Relative variation of the background MC sample normalization used to estimate the uncertainty on the cross section.

Background process	Normalization variation
Elastic & single diss. $\gamma\gamma \to \mu\mu$	10%
Double dissociative $\gamma\gamma \to \mu\mu$	30%
$\Upsilon \to \mu\mu$	10%
DY $\tau\tau$	10%
$t\bar{t}$	10%
diboson	10%
$W+$jets	30%

section due to the background variation is shown in Figure 10.1 for the single differential mass measurement. The error is shown in percent with respect to the cross section value. The background normalization is varied up and down by the values in table 10.1, the shown uncertainty is given by the absolute value of the maximum variation with respect to the central value obtained. The breakdown of all the background uncertainty contributions is plotted. The total uncertainty line is given by the sum in quadrature of all the contributions. In the plot also the statistical uncertainty is reported. This includes the contributions from the data and MC sample statistical errors. The EW backgrounds have a small cross section compared to the Drell-Yan one, or their final states are suppressed by the selection cuts, the respective uncertainties are then small, 2 to 5 times smaller than the statistical error (in the plot a log scale for the y-axis is used, so that the uncertainty lines are visible). Only the Υ uncertainty in the very first mass bin, due to the vicinity to the Υ resonance peaks, gives a non negligible contribution, but the error is still 3-4 times smaller than the other systematic contributions (compare for example to Figure 10.4 where the multijets background uncertainty is shown).

Analogous plots, but for the double differential $m_{\mu\mu} - |y_{\mu\mu}|$ binning scheme, are reported in Figure 10.2. The considered uncertainties give an almost flat contribution in $|y_{\mu\mu}|$, and the errors are compatible with the one observed in the mass case in Figure 10.1. Only the statistical uncertainty, due to the larger number of considered bins, gives a bigger contribution.

The background uncertainties for the $m_{\mu\mu}-$ cross section results are shown in Figure 10.3. Here some effects due to the process $p_T^{\mu\mu}$ shapes are visible. The $\gamma\gamma \to \mu\mu$ contribution is present only at very low $p_T^{\mu\mu}$, and peaks in particular in the first $p_T^{\mu\mu}$ bin. This is due to the kinematics of this process in which the two muons are produced back to back with almost no other activity. At high mass and high $p_T^{\mu\mu}$ instead, the $t\bar{t}$ related uncertainty starts to grow, and reaches a value of 2% with respect to the cross section result. This is due to the higher relative abundance of this background as the considered kinematics gets closer to the bulk of

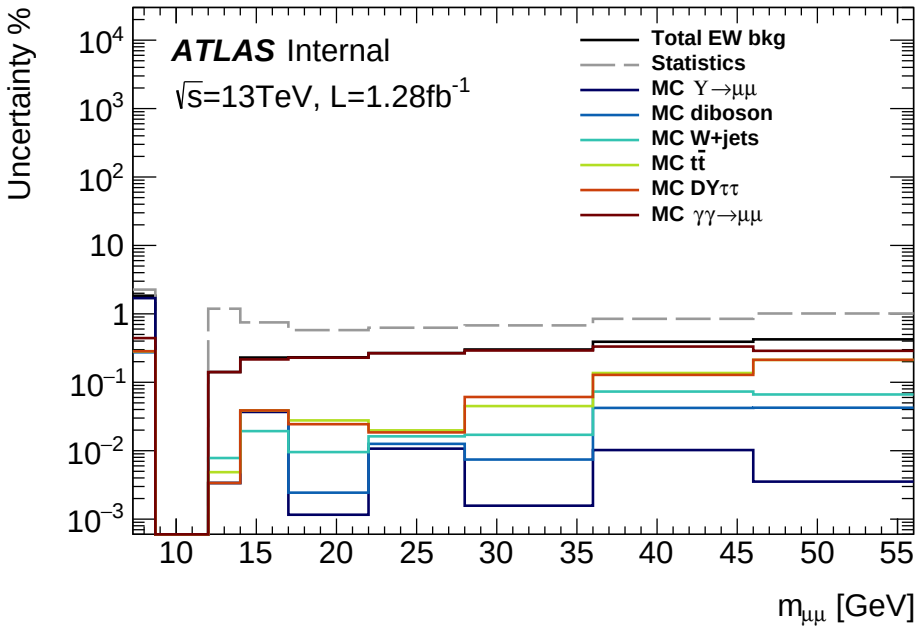

Figure 10.1 Breakdown of the EW background uncertainties on mass differential cross section. Also the statistical uncertainty is shown. The total uncertainty line is obtained by the sum in quadrature of all the background uncertainty components.

the $t\bar{t}$ transverse momentum distribution, but the corresponding uncertainty in those bins is negligible with respect to the other systematic contributions and the statistical error. Note also also that the statistical uncertainty is not flat in $p_T^{\mu\mu}$ due to the intrinsic shape of the distribution and the bin sizes. In particular the uncertainty is higher at low $p_T^{\mu\mu}$ where the binning is finer and at high $p_T^{\mu\mu}$ values were the cross section is smaller. Both in the rapidity and transverse momentum uncertainty plots, Figures 10.2 and 10.3, the uncertainty related to some small backgrounds is quite irregular between bins. This is not a physical effect, but is instead due to the limited statistics of the MC samples. It is planned to mitigate this by fitting the uncertainties with a smooth function.

10.1.1 Multijet background uncertainty

The uncertainties affecting the estimation of the heavy flavour multijet background are discussed here. This background component is estimated with a template fit method. The data selected in the *not-isolated* control region is fitted simultaneously with the signal region selection in order to obtain a background estimation in each of the measurement bin. Two possible sources of bias to the result were investigated. These were related to

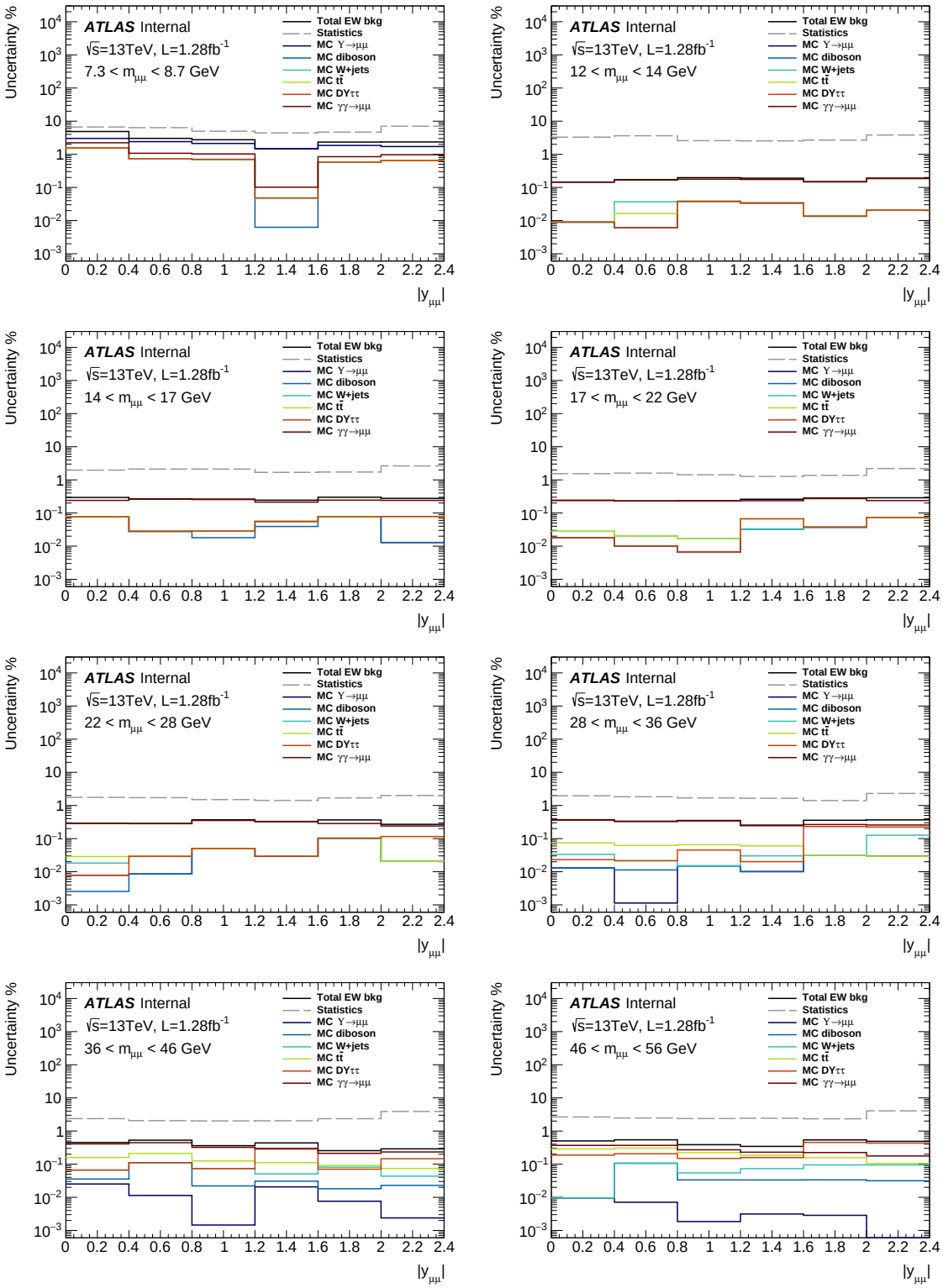

Figure 10.2 Breakdown of the EW background uncertainties on the double differential $m_{\mu\mu} - |y_{\mu\mu}|$ cross section. Also the statistical uncertainty is shown. The total uncertainty line is obtained by the sum in quadrature of all the background uncertainty components.

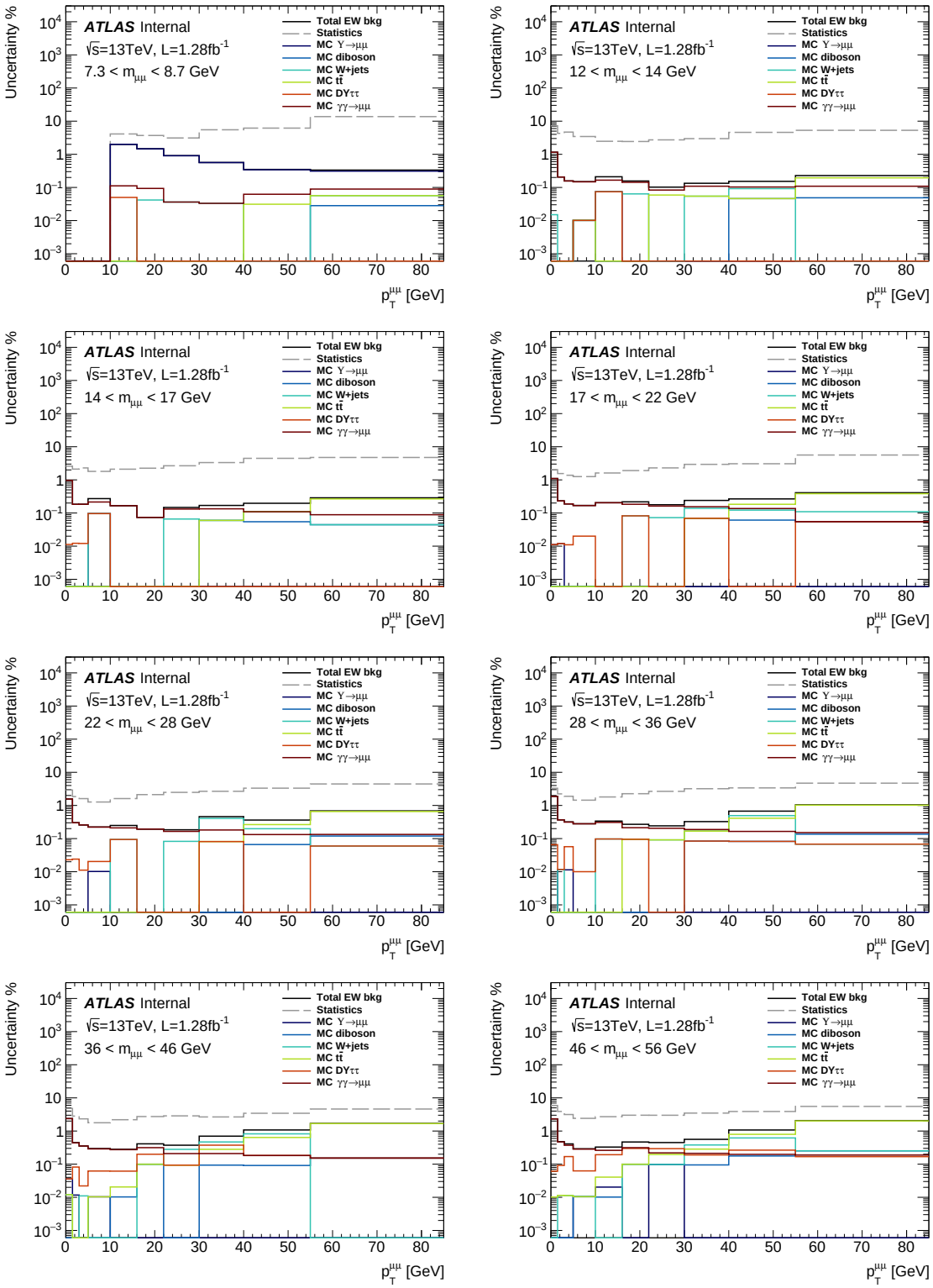

Figure 10.3 Breakdown of the EW background uncertainties on the double differential $m_{\mu\mu} - p_T^{\mu\mu}$ cross section results. The statistical uncertainty is also shown. The total uncertainty line is obtained by the sum in quadrature of all the background uncertainty components.

- **the impact parameter modelling**. The template fit relies on a good modelling of the IP distributions shape in the simulation. Some mismodelling is observed and a data driven correction is then retrieved and applied to the MC samples. The correction corresponds to a smearing of the bulk of the distribution, this was discussed in section 8.4, and a tail reweight of the d_0 significance, discussed in section 8.4.2. An uncertainty on the smearing that covers the residual discrepancies is evaluated by varying the smearing values by $\pm 2\%$. For the tail reweight instead, the difference with respect to the result with no reweight applied is taken as an estimate of the uncertainty.

- **A correction to the shape of the non-isolated data distributions.** The background fit in section 7.2 relies on the fact that the shape of the multijet background for the fitted quantity is similar in the signal region and the non-isolated control region. This assumption was the subject of a MC study in section 7.2.2. A correction to the non-isolated data shape, based on this study is applied. The difference with respect to the result with no shape correction is taken as an uncertainty.

The uncertainty in the fit method is propagated to the cross section results. The multijet uncertainty contributions are shown in Figure 10.4 for the mass differential cross section. The total uncertainty line is given by the sum in quadrature of all the components. The statistical uncertainty is also shown for a comparison. Among the QCD background related uncertainties, the IP modelling gives the biggest contribution. It is higher at low mass, around 4%, due to the larger number of multijet background events in those bins, and it partially decreases at around $2-3\%$ in the higher mass bins. The uncertainty related to the shape correction is also higher at low mass, in particular in the first two mass bins, where the it is around 2%. At higher masses the uncertainty decreases below 1%. The d_0 tail reweight uncertainty instead gives an almost flat 1% contribution. The uncertainty breakdown in the $m_{\mu\mu} - |y_{\mu\mu}|$ bins is given in Figure 10.5. Similar results to the mass one are observed and no strong $|y_{\mu\mu}|$ dependence of the uncertainty is visible. The QCD background uncertainties for the mass-$p_T^{\mu\mu}$ binning scheme are reported in Figure 10.6. The dimuon transverse momentum is sensitive to the number of multijets events, at low $p_T^{\mu\mu}$ more background events are observed. For this reason the IP modelling uncertainty and the shape correction uncertainty give a bigger contribution in lower part of the spectrum. At low $p_T^{\mu\mu}$ this can be as high as $4-6\%$, while it becomes negligible in the higher $p_T^{\mu\mu}$ bins. This set of uncertainties, dominated by the one related to the IP smearing correction, give one the biggest contribution to the total error.

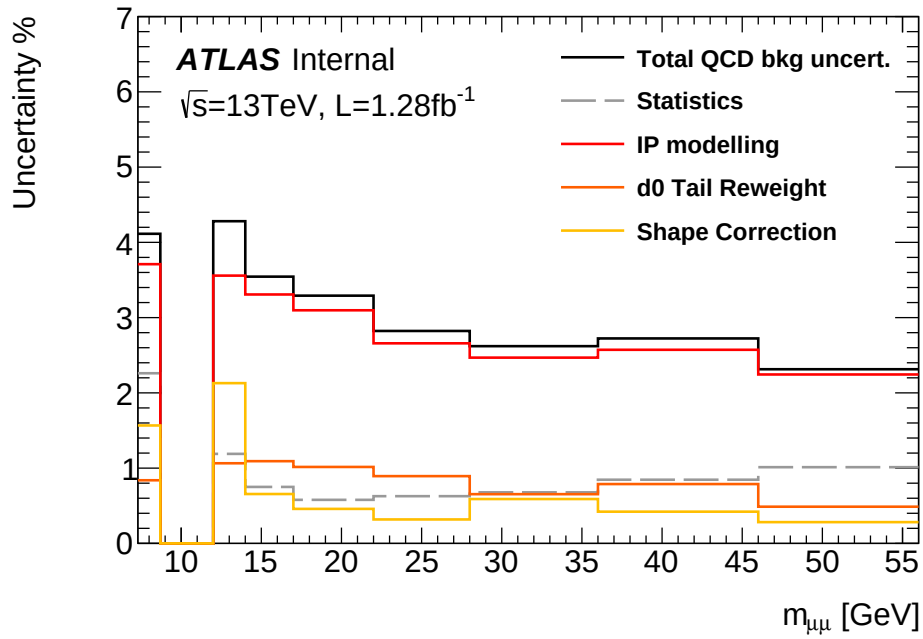

Figure 10.4 Breakdown of the uncertainties on the cross section results related to the multijet background estimation. The mass differential cross section is considered. The statistical uncertainty is also shown. The total uncertainty line is obtained by the sum in quadrature of all the background uncertainty components.

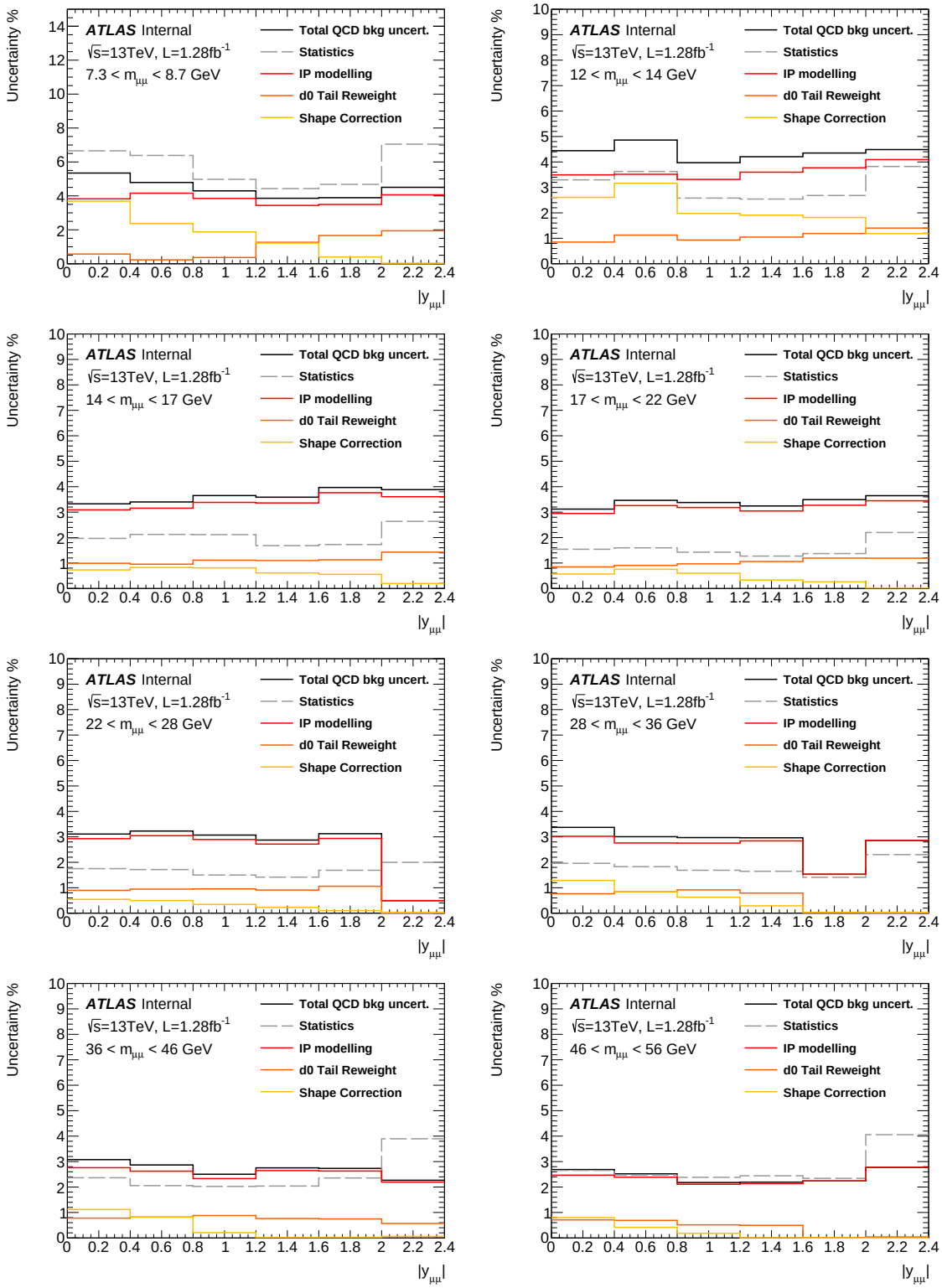

Figure 10.5 Breakdown of the uncertainties related to the multijets background estimation. The error results for the $m_{\mu\mu} - |y_{\mu\mu}|$ differential cross section are shown. The statistical uncertainty is also shown. The total uncertainty line is obtained by the sum in quadrature of all the background uncertainty components.

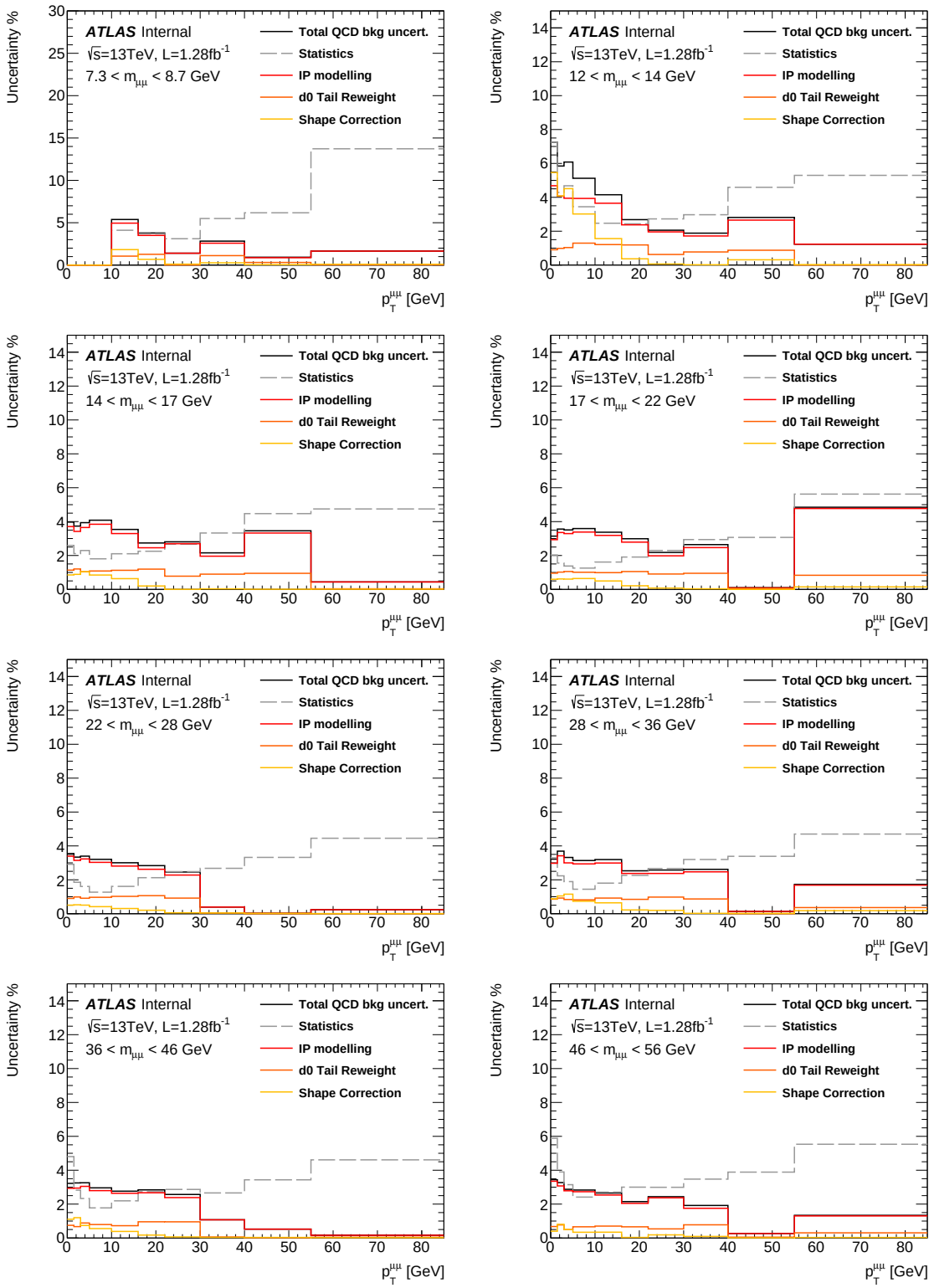

Figure 10.6 Breakdown of the uncertainties related to the multijets background estimation. The results are for the $m_{\mu\mu} - p_T^{\mu\mu}$ differential cross section. The statistical uncertainty is also shown. The total uncertainty line is obtained by the sum in quadrature of all the background uncertainty components.

10.2 Muon performance uncertainties

In extracting the cross section, the detector effects of momentum smearing and detection efficiency are estimated with the MC simulations and corrected through the factor C_i in the cross section formula, equation 10.1. The detector performance in the muon reconstruction is studied in [139]. The detector behaviour in simulation is matched to the real one with smearing factor on the momentum scale and resolution and efficiency scale factors, see section 6.7.3 for a brief description, more details can be found in Ref. [139]. These corrections come with an uncertainty, the nominal values are varied within the error ($\pm 1\sigma$) and the variations are propagated to the correction factors C_i and the cross section results. Usually two uncertainty components are distinguished, a statistical one related to the statistics of the data and MC samples used to evaluate the corrections and a systematic one that include any other effect. The uncertainty contributions considered here are

- **Variation of the muon momentum scale:** the momentum scale calibration is obtained by comparing in data and MC the resonant decay spectrum of Z and J/Ψ particles. The systematic uncertainties on the momentum scale extrapolation come mainly from the background estimation, the selection criteria and variation of the momentum scale correction parametrization.

- **Variation of muon momentum resolution:** the momentum resolution correction is estimated together with the momentum scale. The systematic uncertainties includes effects on the smearing of the Inner Detector reconstructed tracks, and on the smearing of the Muon Spectrometer reconstructed tracks (see section 5.4 for a dscription of the muon reconstruction).

- **Variation of the reconstruction efficiency scale factors** the reconstruction scale factors are obtained with the tag-and-probe method. The systematic uncertainties on the scale factors come mainly from the background estimation and the correction of possible biases in the tag-and-probe procedure.

- **Sagitta correction:** uncertainty related to the correction of the sagitta biases in the muon momentum reconstruction (see section 5.3.4 for more details).

- **Variation of the isolation scale factors.** the isolation scale factor are obtained with the tag-and-probe method. The systematic uncertainties on the scale factor come mainly from the background estimation (in particular at low p_T) and the neglected η

dependence of the scale factors. The relative statistical component is evaluated using toy replicas method.

- **Variation in the trigger scale factors:** the trigger scale factor are obtained with the tag-and-probe method. The systematic uncertainties come mainly from variation of the selection criteria of the tag and probe muons and the background estimation (in particular at low p_T). The statistical component is propagated to the results using the toy replicas method.

More details about the toy replica method are given in Appendix B. This approach allows correct propagation of the uncorrelated statistical uncertainty.

The breakdown of the uncertainties affecting the invariant mass cross section are reported in Figure 10.7. For each uncertainty contribution one line is shown corresponding to the sum in quadrature of its systematic and statistical component. The systematic component is usually the biggest between the two. The biggest contributions are given by the isolation and trigger scale factor uncertainties and the reconstruction efficiency. In the low mass bins, in particular, the isolation uncertainty is the dominant one, and takes values up to 5%. Various contributions are included in the isolation scale factor uncertainty. The dominant one in the low p_T^{μ} range, and that causes the big uncertainty at low mass, is related to the background estimation when calculating the scale factors. The momentum scale and resolution uncertainties are instead negligible. This reflects the good detector performance in reconstructing low p_T muons. A slight raise, up to 1%, of the this component is noticeable only in the last mass bin, where the average muon momentum is higher. The cross section uncertainty breakdown in the $m_{\mu\mu} - |y_{\mu\mu}|$ bins is reported in Figure 10.8, while the effects on the double differential $m_{\mu\mu} - p_T^{\mu\mu}$ cross section are shown in Figure 10.9. The total muon calibration uncertainty is particularly important at low mass and low $p_T^{\mu\mu}$, again the dominant contribution is given by the isolation SF uncertainty. At higher mass the trigger and reconstruction efficiency uncertainties become of the similar magnitude. At high $p_T^{\mu\mu}$ the momentum scale and resolution uncertainties become of the same order as the efficiency errors, but the total contribution is subdominant with respect to the statistical error.

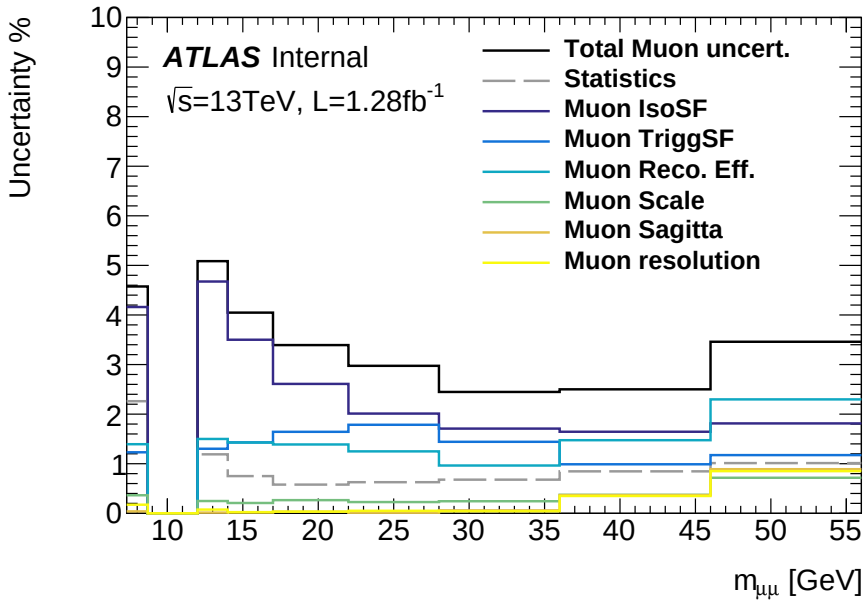

Figure 10.7 Breakdown of the muon calibration uncertainties affecting for the mass differential cross section. The statistical uncertainty is also shown. The total uncertainty line is obtained by the sum in quadrature of all the muon calibration error components.

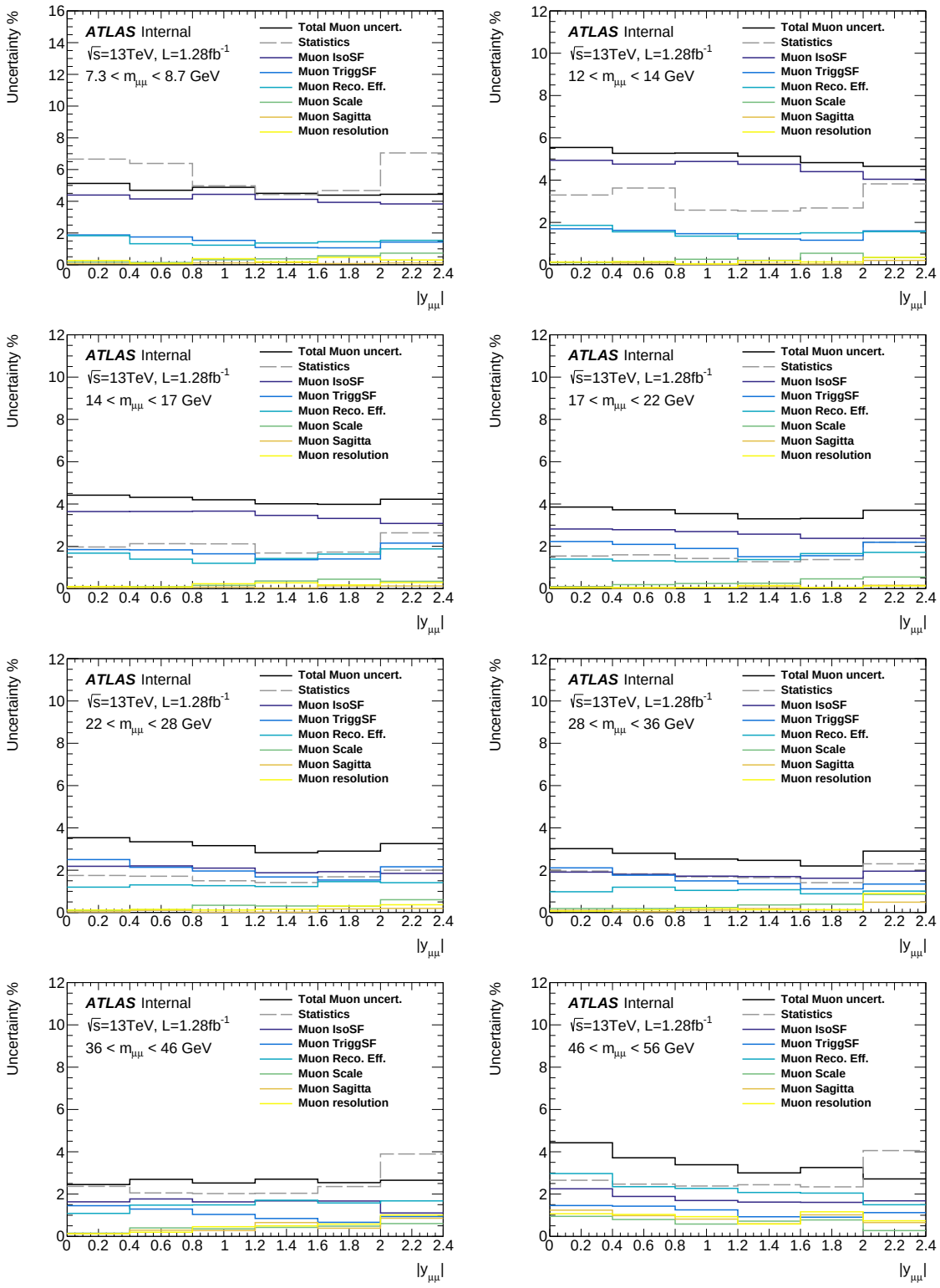

Figure 10.8 Breakdown of the muon calibration uncertainties affecting for the mass differential cross section. The statistical uncertainty is also shown. The total uncertainty line is obtained by the sum in quadrature of all the muon calibration error components.

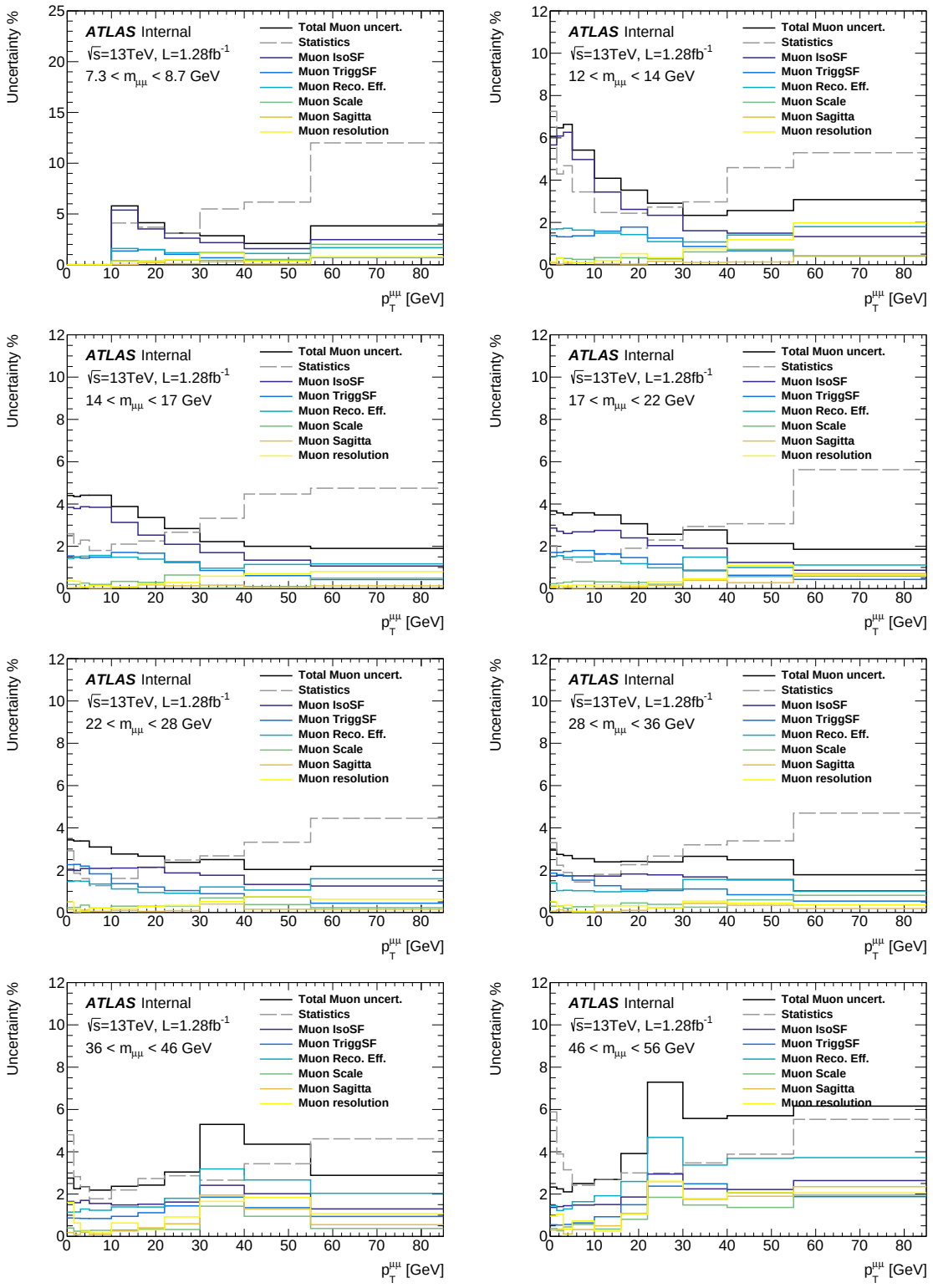

Figure 10.9 Breakdown of the muon calibration uncertainties on the $m_{\mu\mu} - p_T^{\mu\mu}$ cross section results. The statistical uncertainty is also shown. The total uncertainty line is obtained by the sum in quadrature of all the muon calibration error components.

Chapter 11

Results

The low mass DY cross section results are presented in this chapter. The unfolding method has been discussed in chapter 9, in particular the results presented here are obtained with the bin-by-bin unfolding procedure presented in section 9.2. The total uncertainty affecting the cross section results is also reported, the various components were discussed in the previous chapter. The data results are compared with some theoretical predictions.

Firstly, the double differential $m_{\mu\mu} - p_T^{\mu\mu}$ cross section results are presented in section 11.1. These $p_T^{\mu\mu}$ results are used to perform the transverse momentum reweight presented in section 9.4. Then in section 11.2 the extracted distribution for the mass differential and $m_{\mu\mu}-$ differential cross sections are reported. The uncertainty band on the data represents the total systematic plus statistical uncertainty (except the 2.1 % uncertainty on the luminosity)

11.1 Transverse momentum cross section

The double differential cross section in $m_{\mu\mu}$ and $p_T^{\mu\mu}$ is shown in Figure 11.1. The cross section is compared to the prediction of the following MC generators

- *Poweg+Pythia8*: this is the MC event generator used in the low mass DY analysis. The level of accuray is NLO in QCD [114, 115, 116] plus Leading-Log resummation reached with parton shower (simulated with Pythia8 [117]). The total cross section in each mass bin is normalized to an NNLO QCD + NLO EW prediction from the VRAP [121] and MCSANC [123] programs respectively through K-factors, as explained in section 6.7.1. The PDF used in calculating the prediction is CT10NLO [118].

- *DYTurbo* program [27]: DYTurbo offers a framework to calculate DY prediction with high precision in QCD (up to NNLO). It is based on q_T slicing methods described in

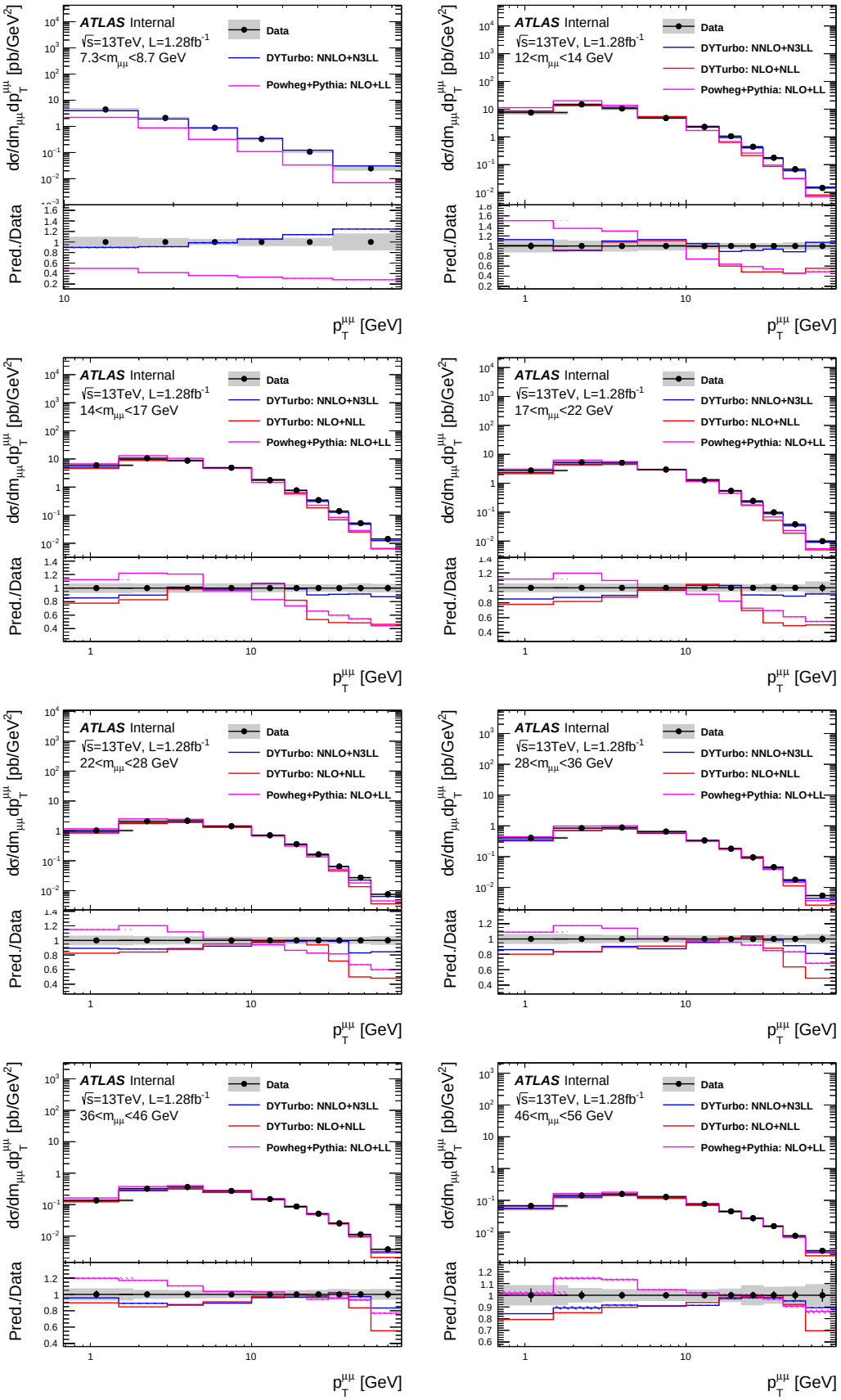

Figure 11.1 Double differential $m_{\mu\mu} - p_T^{\mu\mu}$ cross section results. The measurement is compared to the predictions from the Poweg+Pythia8 and the DYTurbo generators. In the first mass bin a selection cut $p_T^{\mu\mu} > 10\,\text{GeV}$ is applied. The grey band on the data points represents the total uncertainty, while the error bars are the statistical components. The uncertainty on the prediction is statistical only.

section 3.1.1. The slicing formalism makes it easy to include q_T resummation effects [35]. DYTurbo implements a resummation up to N3LL matched with NNLO fixed order prediction [145]. The DYTurbo results are produced using the CT18 NNLO PDF [62].

The inclusion of resummation effects yields a reasonable description of the low part of the $p_T^{\mu\mu}$ spectrum. At high $p_T^{\mu\mu}$ values and in particular in the low mass bins, the NLO QCD prediction, both from Powheg and from DYTurbo are not able to describe the data. Good modelling is restored when including higher order corrections. Some differences between data and MC are noticeable in some mass bins at low $p_T^{\mu\mu}$ but also high transverse momentum, in particular in the highest mass bin. For a more precise comparison, the full set of experimental systematic uncertainties needs to be evaluated. Some minor systematic uncertainties still need to be added, in particular some uncertainties related to the underlying theory modelling, for example the PDF related uncertainties, and unfolding uncertainties are yet to be considered. These are expect to be small and they will be included in the final publication. Furthermore, also the theoretical uncertainties on the predictions due to scale variations, and PDFs needs to be considered. It is also interesting to add other theoretical prediction to the comparison, and test the different resummation algorithm, such as Radish [146], SCETLib [34] and others.

The cross section results are reported in Table 11.1 together with the systematic and statistical total uncertainty.

11.2 Mass and rapidity cross section results

The mass cross section result as extracted from the data is plotted in Figure 11.2. The Poweg+Pythia8 and the DYTurbo predictions are also shown and compared to the data. The characteristic of these prediction are the same described in the previous section. The order of the Powheg+Pythia8 and DYTurbo is formally similar, but the Powheg one includes also NLO EW corrections, and DYTurbo includes effect of resummation up to N3LL. Resummation can have an effect also in *ptmm* inclusive measurements, as explained in section 3. These effects can explain the differences between the two predictions in Figure 11.2, but they need to be fully understood. As commented in the previous section, some minor uncertainties still need to be added, this will be done in the final publication and it will allow a more precise comparison with the theoretical predictions.

The mass and rapidity double differential results are shown in Figure 11.3. Only the Poweg+Pythia preditions are showed for a comparison. In the first mass bin, $7.3 < m_{\mu\mu} <$

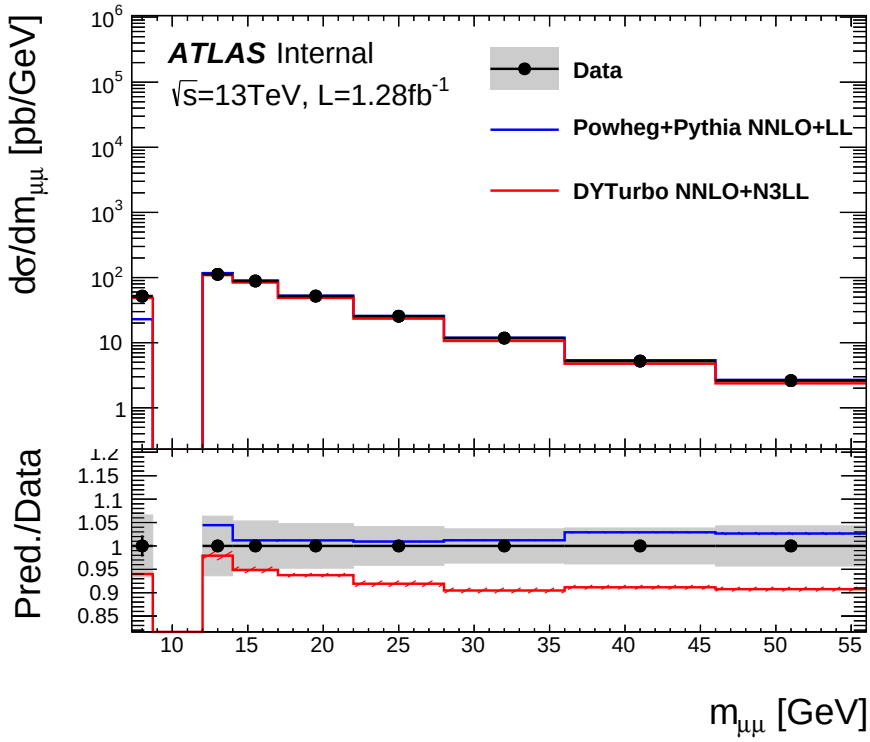

Figure 11.2 Single differential mass cross section results. The error band on data represents the sum in quadrature of statistical and systematic uncertainties. The error band on the predictions represents the statistical error only.

8.7 GeV, the Powheg+Pythia predictions seem to off by a factor two with respect to the data. This is due to the poor modelling of the $p_T^{\mu\mu}$ spectrum by this generator, see also Figure 11.1, and the presence of the fiducial cut $p_T^{\mu\mu} > 10\,\text{GeV}$ in the very first mass bin.

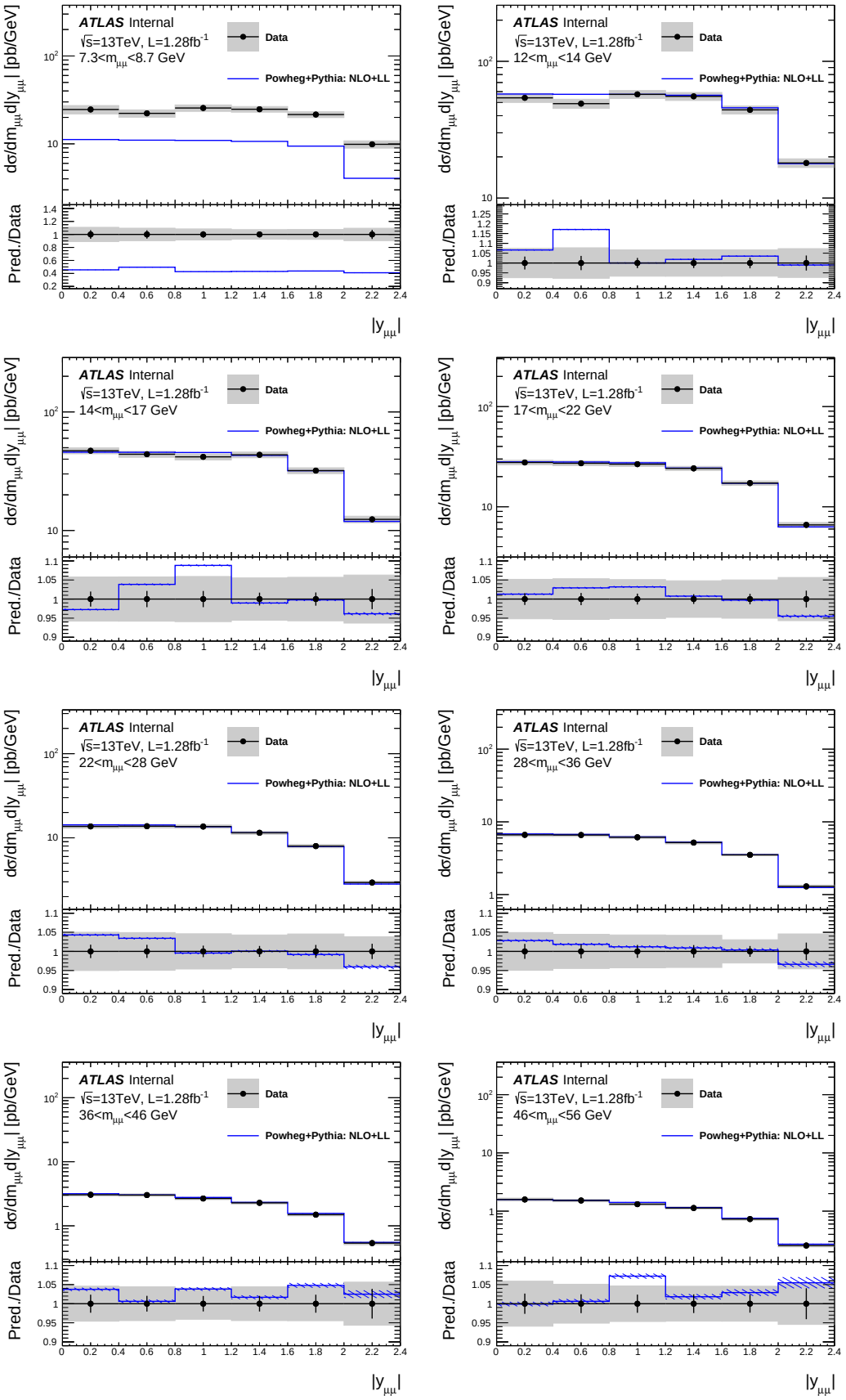

Figure 11.3 Double differential cross section result in mass a rapidity of the final state dileptons.

Table 11.1 Double differential $m_{\mu\mu} - |y_{\mu\mu}|$ cross section results.

$7.3 < m_{\mu\mu} < 8.7$ GeV					
$p_T^{\mu\mu,\min}$ [GeV]	$p_T^{\mu\mu,\max}$ [GeV]	$d\sigma/dm_{\mu\mu}p_T^{\mu\mu}$ [pb/GeV^2]	δ_{stat} [%]	δ_{syst} [%]	δ_{tot} [%]
0.0	1.5	-	-	-	-
1.5	3.0	-	-	-	-
3.0	5.0	-	-	-	-
5.0	10.0	-	-	-	-
10.0	16.0	4.4	4.1	8.2	9.2
16.0	22.0	2.10	3.7	5.9	6.9
22.0	30.0	0.88	3.1	3.8	4.9
30.0	40.0	0.33	5.5	4.4	7.1
40.0	55.0	0.108	6.2	3.4	7
55.0	85.0	0.025	14	7.1	15

$12 < m_{\mu\mu} < 14$ GeV					
$p_T^{\mu\mu,\min}$ [GeV]	$p_T^{\mu\mu,\max}$ [GeV]	$d\sigma/dm_{\mu\mu}p_T^{\mu\mu}$ [pb/GeV^2]	δ_{stat} [%]	δ_{syst} [%]	δ_{tot} [%]
0.0	1.5	7.5	7.2	9.6	12
1.5	3.0	14.9	4.3	8.7	9.7
3.0	5.0	10.6	4.7	9	10
5.0	10.0	4.8	3.4	7.5	8.2
10.0	16.0	2.30	2.5	5.9	6.4
16.0	22.0	1.06	2.4	4.6	5.2
22.0	30.0	0.44	2.7	3.8	4.7
30.0	40.0	0.177	3	3.5	4.6
40.0	55.0	0.068	4.6	4.5	6.4
55.0	85.0	0.0145	5.3	4.3	6.9

$14 < m_{\mu\mu} < 17$ GeV					
$p_T^{\mu\mu,\min}$ [GeV]	$p_T^{\mu\mu,\max}$ [GeV]	$d\sigma/dm_{\mu\mu}p_T^{\mu\mu}$ [pb/GeV^2]	δ_{stat} [%]	δ_{syst} [%]	δ_{tot} [%]
0.0	1.5	6.0	2.6	6.1	6.6
1.5	3.0	10.7	2.1	5.8	6.1
3.0	5.0	8.7	2.3	6	6.4
5.0	10.0	4.88	1.8	6.1	6.3
10.0	16.0	1.75	2.1	5.3	5.7
16.0	22.0	0.76	2.3	4.4	5
22.0	30.0	0.342	2.7	4.1	4.9
30.0	40.0	0.139	3.3	3.4	4.8
40.0	55.0	0.052	4.5	4.4	6.3
55.0	85.0	0.0142	4.7	2.9	5.6

$17 < m_{\mu\mu} < 22$ GeV					
$p_T^{\mu\mu,\min}$ [GeV]	$p_T^{\mu\mu,\max}$ [GeV]	$d\sigma/dm_{\mu\mu}p_T^{\mu\mu}$ [pb/GeV^2]	δ_{stat} [%]	δ_{syst} [%]	δ_{tot} [%]
0.0	1.5	2.75	2	5	5.4
1.5	3.0	5.25	1.6	5.1	5.4
3.0	5.0	5.11	1.4	5	5.2
5.0	10.0	2.98	1.3	5.1	5.2
10.0	16.0	1.27	1.6	4.9	5.1
16.0	22.0	0.54	1.9	4.4	4.8
22.0	30.0	0.245	2.3	3.5	4.2
30.0	40.0	0.098	2.9	4	5
40.0	55.0	0.038	3.1	2.7	4.1
55.0	85.0	0.0099	5.6	5.8	8.1

$22 < m_{\mu\mu} < 28$ GeV					
$p_T^{\mu\mu,\min}$ [GeV]	$p_T^{\mu\mu,\max}$ [GeV]	$d\sigma/dm_{\mu\mu}p_T^{\mu\mu}$ [pb/GeV^2]	δ_{stat} [%]	δ_{syst} [%]	δ_{tot} [%]
0.0	1.5	1.03	2.9	5.3	6
1.5	3.0	2.10	1.9	4.9	5.2
3.0	5.0	2.18	1.6	4.8	5.1
5.0	10.0	1.44	1.3	4.5	4.7
10.0	16.0	0.71	1.6	4.1	4.4
16.0	22.0	0.360	2.1	4	4.5
22.0	30.0	0.164	2.5	3.5	4.3
30.0	40.0	0.064	2.7	2.8	3.9
40.0	55.0	0.0273	3.3	2.8	4.4
55.0	85.0	0.0076	4.5	3.2	5.5

$28 < m_{\mu\mu} < 36$ GeV					
$p_T^{\mu\mu,\min}$ [GeV]	$p_T^{\mu\mu,\max}$ [GeV]	$d\sigma/dm_{\mu\mu}p_T^{\mu\mu}$ [pb/GeV^2]	δ_{stat} [%]	δ_{syst} [%]	δ_{tot} [%]
0.0	1.5	0.40	3.3	5	6
1.5	3.0	0.84	2.2	4.7	5.2
3.0	5.0	0.88	1.9	4.4	4.8
5.0	10.0	0.653	1.4	4.1	4.3
10.0	16.0	0.337	1.8	4	4.4
16.0	22.0	0.181	2.3	3.6	4.2
22.0	30.0	0.095	2.7	3.6	4.5
30.0	40.0	0.046	3.2	3.9	5.1
40.0	55.0	0.0177	3.4	2.9	4.5
55.0	85.0	0.0054	4.7	3.3	5.8

$36 < m_{\mu\mu} < 46$ GeV					
$p_T^{\mu\mu,\min}$ [GeV]	$p_T^{\mu\mu,\max}$ [GeV]	$d\sigma/dm_{\mu\mu}p_T^{\mu\mu}$ [pb/GeV^2]	δ_{stat} [%]	δ_{syst} [%]	δ_{tot} [%]
0.0	1.5	0.136	4.8	5.1	7
1.5	3.0	0.322	2.8	4.1	5
3.0	5.0	0.362	2.3	4.1	4.7
5.0	10.0	0.272	1.8	3.7	4.1
10.0	16.0	0.150	2.2	3.7	4.3
16.0	22.0	0.087	2.7	3.8	4.7
22.0	30.0	0.051	2.9	4.1	5
30.0	40.0	0.0254	2.7	5.5	6.1
40.0	55.0	0.0112	3.4	4.7	5.8
55.0	85.0	0.0038	4.6	3.9	6.1

$46 < m_{\mu\mu} < 56$ GeV					
$p_T^{\mu\mu,\min}$ [GeV]	$p_T^{\mu\mu,\max}$ [GeV]	$d\sigma/dm_{\mu\mu}p_T^{\mu\mu}$ [pb/GeV^2]	δ_{stat} [%]	δ_{syst} [%]	δ_{tot} [%]
0.0	1.5	0.067	5.9	5.9	8.3
1.5	3.0	0.142	3.9	4.4	5.9
3.0	5.0	0.159	3.1	3.8	4.9
5.0	10.0	0.128	2.4	3.9	4.6
10.0	16.0	0.077	2.7	3.9	4.7
16.0	22.0	0.045	3	4.6	5.5
22.0	30.0	0.0274	3	7.7	8.3
30.0	40.0	0.0154	3.5	6	6.9
40.0	55.0	0.0076	3.9	6	7.2
55.0	85.0	0.0026	5.5	7.3	9.1

Table 11.2 Double differential $m_{\mu\mu} - |y_{\mu\mu}|$ cross section results.

$7.3 < m_{\mu\mu} < 8.7$ GeV					
$\|y_{\mu\mu}\|^{\min}$	$\|y_{\mu\mu}\|^{\min}$	$d\sigma/dm_{\mu\mu}\|y_{\mu\mu}\|$ [pb/GeV]	δ_{stat} [%]	δ_{syst} [%]	δ_{tot} [%]
0.0	0.4	25	6.7	8.7	11
0.4	0.8	22	6.4	7.2	9.7
0.8	1.2	26	5	6.9	8.5
1.2	1.6	25	4.4	6	7.4
1.6	2.0	22	4.7	6	7.6
2.0	2.4	9.9	7.1	6.4	9.6
$12 < m_{\mu\mu} < 14$ GeV					
$\|y_{\mu\mu}\|^{\min}$	$\|y_{\mu\mu}\|^{\min}$	$d\sigma/dm_{\mu\mu}\|y_{\mu\mu}\|$ [pb/GeV]	δ_{stat} [%]	δ_{syst} [%]	δ_{tot} [%]
0.0	0.4	54	3.3	6.7	7.5
0.4	0.8	49	3.6	6.9	7.8
0.8	1.2	57	2.6	6.2	6.7
1.2	1.6	55	2.5	6.2	6.7
1.6	2.0	44	2.7	6.1	6.7
2.0	2.4	18.0	3.8	6.3	7.3
$14 < m_{\mu\mu} < 17$ GeV					
$\|y_{\mu\mu}\|^{\min}$	$\|y_{\mu\mu}\|^{\min}$	$d\sigma/dm_{\mu\mu}\|y_{\mu\mu}\|$ [pb/GeV]	δ_{stat} [%]	δ_{syst} [%]	δ_{tot} [%]
0.0	0.4	47.1	2	5.4	5.8
0.4	0.8	44.0	2.1	5.4	5.8
0.8	1.2	41.8	2.1	5.5	5.9
1.2	1.6	43.5	1.7	5.3	5.5
1.6	2.0	32.0	1.7	5.4	5.7
2.0	2.4	12.4	2.6	5.7	6.3
$17 < m_{\mu\mu} < 22$ GeV					
$\|y_{\mu\mu}\|^{\min}$	$\|y_{\mu\mu}\|^{\min}$	$d\sigma/dm_{\mu\mu}\|y_{\mu\mu}\|$ [pb/GeV]	δ_{stat} [%]	δ_{syst} [%]	δ_{tot} [%]
0.0	0.4	27.7	1.5	4.9	5.2
0.4	0.8	27.2	1.6	5.1	5.3
0.8	1.2	26.6	1.4	4.9	5.1
1.2	1.6	24.2	1.3	4.6	4.8
1.6	2.0	17.2	1.4	4.8	5
2.0	2.4	6.6	2.2	5.2	5.7

$22 < m_{\mu\mu} < 28$ GeV					
$\|y_{\mu\mu}\|^{\min}$	$\|y_{\mu\mu}\|^{\min}$	$d\sigma/dm_{\mu\mu}\|y_{\mu\mu}\|$ [pb/GeV]	δ_{stat} [%]	δ_{syst} [%]	δ_{tot} [%]
0.0	0.4	13.7	1.8	4.7	5
0.4	0.8	13.7	1.7	4.6	4.9
0.8	1.2	13.6	1.5	4.4	4.6
1.2	1.6	11.5	1.4	4.1	4.3
1.6	2.0	8.0	1.7	4.2	4.6
2.0	2.4	2.94	2	3.3	3.8
$28 < m_{\mu\mu} < 36$ GeV					
$\|y_{\mu\mu}\|^{\min}$	$\|y_{\mu\mu}\|^{\min}$	$d\sigma/dm_{\mu\mu}\|y_{\mu\mu}\|$ [pb/GeV]	δ_{stat} [%]	δ_{syst} [%]	δ_{tot} [%]
0.0	0.4	6.6	2	4.5	4.9
0.4	0.8	6.6	1.8	4.1	4.5
0.8	1.2	6.1	1.7	4	4.3
1.2	1.6	5.18	1.6	3.9	4.2
1.6	2.0	3.51	1.4	2.7	3.1
2.0	2.4	1.29	2.3	4	4.6
$36 < m_{\mu\mu} < 46$ GeV					
$\|y_{\mu\mu}\|^{\min}$	$\|y_{\mu\mu}\|^{\min}$	$d\sigma/dm_{\mu\mu}\|y_{\mu\mu}\|$ [pb/GeV]	δ_{stat} [%]	δ_{syst} [%]	δ_{tot} [%]
0.0	0.4	3.05	2.4	3.9	4.6
0.4	0.8	3.02	2.1	3.9	4.4
0.8	1.2	2.67	2	3.5	4.1
1.2	1.6	2.28	2	3.9	4.4
1.6	2.0	1.49	2.4	3.8	4.5
2.0	2.4	0.54	3.9	4.1	5.7
$46 < m_{\mu\mu} < 56$ GeV					
$\|y_{\mu\mu}\|^{\min}$	$\|y_{\mu\mu}\|^{\min}$	$d\sigma/dm_{\mu\mu}\|y_{\mu\mu}\|$ [pb/GeV]	δ_{stat} [%]	δ_{syst} [%]	δ_{tot} [%]
0.0	0.4	1.59	2.7	5.3	5.9
0.4	0.8	1.52	2.5	4.5	5.1
0.8	1.2	1.32	2.4	4	4.7
1.2	1.6	1.13	2.4	3.9	4.6
1.6	2.0	0.73	2.3	3.9	4.6
2.0	2.4	0.257	4.1	3.6	5.4

Chapter 12

Conclusion and outlook

Throughout this thesis, studies related to the Drell-Yan process in proton-proton collisions at the LHC were presented. Chapter 3 introduced a study regarding high precision QCD predictions for DY and explored the effects of fiducial cuts on the final state lepton in the calculations results. Conclusions and ideas for further studies were discussed in detail in section 3.4. In the chapter, it was shown how certain cut configurations induce a linear dependence of the cross section on q_T, the vector boson transverse momentum. This dependence affects the stability of the perturbative series expansion and induces an additional bias in q_T-slicing calculation results. Including the resummation of the small q_T effects helps to obtain a stable calculation. Using the resummed result, it is also possible to correct the linear q_T bias in the fixed order calculations and recover the original precision of the slicing method. Various PDFs using the different theory definitions were compared to the data. The results showed an improvement in the agreement when using the theory corrected for the linear q_T biases, in particular when exploiting the full q_T-resummed calculations. The effects of linear q_T corrections and resummation can be investigated for other significant data sets. Modern PDF fits neglect the resummation effects and use only fixed order results. An investigation of the possible implication of including the resummation in the PDF extrapolation can be done exploiting the profiling procedure presented in chapter 3, or with a PDF fit.

Starting from chapter 6, a Drell-Yan measurement using the ATLAS collected data has been presented. The analysis targets a low invariant mass range of the final state leptons and consists of the measurement of the single and double differential cross section for the process. The main challenges of the analysis are presented by the large fraction of multijet background events that enter the data selection, in particular in the low mass bins. This component is extracted exploiting data control regions as explained in chapter 7. The

dominant systematic uncertainties affecting the current measurement (see chapter 10) are related to this background, both directly as the uncertainty on the background estimation method (sec. 7.2 and sec. 10.1.1) and indirectly as the dominating component in the isolation scale factor uncertainty. The total uncertainty affecting the measurement is estimated to be around 7% at low mass and 5% in the higher mass bins. In the double differential schemes the uncertainty is larger due to higher statistical and systematic uncertainty contributions. The $p_T^{\mu\mu}$ spectrum, in particular, is sensitive to the multijet background that gives a larger component at low transverse momentum and induces larger uncertainties in this range. The statistical uncertainty is negligible in the single differential mass measurement, it becomes significant in some of the two dimensional $m_{\mu\mu} - |y_{\mu\mu}|$ and $m_{\mu\mu} - p_T^{\mu\mu}$ binning schemes, in particular in the high mass region. The low mass DY measurement presented here analyses only a small fraction ($L = 1.28\,\text{fb}^{-1}$) of the total ATLAS run2 data. In some of the bins, the measurement could be improved by using more of the run2 data, the extension to the full run2 is challenging due to the complicated trigger prescale configurations.

The set of systematic uncertainties presented in chapter 10 include the most important contributions, but some uncertainties related to the unfolding procedure and underlying theory modelling (e.g. PDF related uncertainty) are yet to be fully estimated (their contributions are expected to be relatively small). The study of these uncertainties is ongoing and they will be soon included in the final pubblication.

The mass and rapidity measurements have sensitivity to low x values of the phase space and can be included in a PDF fit to test this kinematic region. Low x values have been tested at the HERA collider, but this ATLAS measurement offers a complementary result at a higher Q^2 energy scale; $Q^2 \sim 10\,\text{GeV}$ in the HERA results [3] compared to $Q^2 \sim 100\,\text{GeV}$ in the low mass DY analysis. Small-x resummation can have an important role and its effects can be tested with this measurement. The resummation can be performed in the DIS calculations both at the PDF and at the partonic cross section level [147], and a study of the effects on the PDF determination has been performed in Ref. [148]. A similar study can be performed using the low mass Drell-Yan measurement (even though the small-x effects on the DY partonic cross section are not yet available).

The very first mass bin of the analysis ($7.3 < m_{\mu\mu} < 8.7\,\text{GeV}$) is the most sensitive to small-x effects. Unfortunately the muon trigger p_T threshold at 4.5 GeV does not allow us to fully exploit the kinematics of this bin (in particular, as explained in section 6.5, a fiducial cut $p_T^{\mu\mu} > 10\,\text{GeV}$ is applied in the first bin). For improvements in future data taking, some work to lower the p_T threshold of the triggers needs to be done. The LHC

upcoming Run 3 will also provide a slightly higher centre of mass energy of the collisions ($\sqrt{s} = 13.6\,\text{TeV}$), this shifts the phase space region of the analysis to smaller x values. The possibility to fully exploit the lowest mass bin or even, to further reduce the mass range, requires lower thresholds for the triggers. This experimental solution is limited by the high hadronic activity in this kinematic range, and the necessity to keep the overall ATLAS trigger rates below the 1 kHz threshold [149]. A good experimental environment from this point of view are low pile-up (low $\langle\mu\rangle$) runs, i.e. runs with a low number of collisions per bunch crossing. The lower hadron activity in these collisions would allow us to lower the trigger threshold, keeping an overall accessible rate. Furthermore, the low pile up environment helps to reduce the background component related to QCD activity. The ATLAS Run3 physics program includes a running period at low $\mu\rangle$, with $\langle\mu\rangle \sim 1-2$. The expected luminosity to be collected is about $1\,\text{fb}^{-1}$ of data, so compatible with the amount of data used in the current low mass DY analysis. This data set, together with a lower p_T lepton threshold of the triggers, will allow us to perform a precision DY measurement in the mass range between the J/ψ and Υ resonances.

The low mass Drell-Yan analysis also includes the measurement of the vector boson transverse momentum cross section. This effort furnishes a novel measurement for this observable in a low invariant mass range. This can be used to test the agreement of theory predictions that include low q_T resummation effects with the data. In chapter 11 the prediction from DYTurbo has been compared to the data. Many other resummed results can be included for the comparison, for example: the Radish software [146], the SCETlib program [34], the q_T resummation implemented in NangaParbat [150] or the implementation of non perturbative effects in the Transverse Momentum Dependent (TMD) parton branching [151].

The p_T spectrum in the low mass bins gives sensitivity the non-perturbative form factor term used in the resummed calculation [27, 152]. This term helps to describe leading power contributions at non-perturbative impact parameter values. Given a certain physical parametrization, the non-perturbative form factor can be fitted to the data [153]. Usually the measurements around the Z mass pole are used. Double differential mass and transverse momentum measurements offer good sensitivity for the fit and the low mass DY results can be used to extrapolate the form factor at a lower invariant mass region. The results of this study can be important to reduce the uncertainty in the knowledge of these non-perturbative QCD effects and help precision measurements in hadron collisions. An example is the determination of the $W-$boson mass at the LHC: the p_T W distribution enters in the measurement and is determined from precision p_T^Z measurements and accurate prediction

of W/Z ratio [154, 155]. For this last stage, it is important to have under control the non-perturbative effects entering the calculation. Another interesting example of a precision measurement, that would benefit from a more accurate knowledge of the non-perturbative QCD effects, is a novel determination of the strong coupling α_S from the Z-boson transverse momentum spectrum introduced in Ref. [156, 157, 158].

References

[1] ATLAS collaboration. "Observation of a new particle in the search for the Standard Model Higgs boson with the ATLAS detector at the LHC". In: *Physics Letters B* 716.1 (Sept. 2012), pp. 1–29. ISSN: 0370-2693. DOI: 10.1016/j.physletb.2012.08.020. URL: http://dx.doi.org/10.1016/j.physletb.2012.08.020.

[2] CMS collaboration. "Observation of a new boson at a mass of 125 GeV with the CMS experiment at the LHC". In: *Physics Letters B* 716.1 (Sept. 2012), pp. 30–61. ISSN: 0370-2693. DOI: 10.1016/j.physletb.2012.08.021. URL: http://dx.doi.org/10.1016/j.physletb.2012.08.021.

[3] H1 and ZEUS Collaborations. *Combination of Measurements of Inclusive Deep Inelastic $e^{\pm}p$ Scattering Cross Sections and QCD Analysis of HERA Data*. 2015. DOI: 10.48550/ARXIV.1506.06042. URL: https://arxiv.org/abs/1506.06042.

[4] G. Aad et al. "Measurement of the low-mass Drell-Yan differential cross section at $\sqrt{s}$ = 7 TeV using the ATLAS detector". In: *Journal of High Energy Physics* 2014.6 (June 2014). ISSN: 1029-8479. DOI: 10.1007/jhep06(2014)112. URL: http://dx.doi.org/10.1007/JHEP06(2014)112.

[5] Carlo Ewerz et al. "BFKL dynamics at hadron colliders". In: *Journal of Physics G: Nuclear and Particle Physics* 26.5 (Apr. 2000), pp. 696–701. DOI: 10.1088/0954-3899/26/5/329. URL: https://doi.org/10.10882F0954-38992F262F52F329.

[6] $g-2$ collaboration. "Measurement of the Positive Muon Anomalous Magnetic Moment to 0.46 ppm". In: *Phys. Rev. Lett.* 126 (14 Apr. 2021), p. 141801. DOI: 10.1103/PhysRevLett.126.141801. URL: https://link.aps.org/doi/10.1103/PhysRevLett.126.141801.

[7] M. G. Aartsen et al. "Observation of High-Energy Astrophysical Neutrinos in Three Years of IceCube Data". In: *Phys. Rev. Lett.* 113 (10 Sept. 2014), p. 101101. DOI: 10.1103/PhysRevLett.113.101101. URL: https://link.aps.org/doi/10.1103/PhysRevLett.113.101101.

[8] null null et al. "High-precision measurement of the *W* boson mass with the CDF II detector". In: *Science* 376.6589 (2022), pp. 170–176. DOI: 10.1126/science.abk1781. eprint: https://www.science.org/doi/pdf/10.1126/science.abk1781. URL: https://www.science.org/doi/abs/10.1126/science.abk1781.

[9] *Standard Model Summary Plots June 2021*. Tech. rep. All figures including auxiliary figures are available at https://atlas.web.cern.ch/Atlas/GROUPS/PHYSICS/PUBNOTES/ATL-PHYS-PUB-2021-032. Geneva: CERN, July 2021. URL: http://cds.cern.ch/record/2777014.

[10] Nicola Cabibbo. "Unitary Symmetry and Leptonic Decays". In: *Phys. Rev. Lett.* 10 (12 June 1963), pp. 531–533. DOI: 10.1103/PhysRevLett.10.531. URL: https://link.aps.org/doi/10.1103/PhysRevLett.10.531.

[11] Makoto Kobayashi and Toshihide Maskawa. "CP-Violation in the Renormalizable Theory of Weak Interaction". In: *Progress of Theoretical Physics* 49.2 (Feb. 1973), pp. 652–657. ISSN: 0033-068X. DOI: 10.1143/PTP.49.652. eprint: https://academic.oup.com/ptp/article-pdf/49/2/652/5257692/49-2-652.pdf. URL: https://doi.org/10.1143/PTP.49.652.

[12] S.D. Drell and Tung-Mow Yan. "Massive Lepton Pair Production in Hadron-Hadron Collisions at High-Energies". In: *Phys. Rev. Lett.* 25 (1970). [Erratum: Phys.Rev.Lett. 25, 902 (1970)], pp. 316–320. DOI: 10.1103/PhysRevLett.25.316.

[13] Stefano Catani and Massimiliano Grazzini. "Next-to-Next-to-Leading-Order Subtraction Formalism in Hadron Collisions and its Application to Higgs-Boson Production at the Large Hadron Collider". In: *Physical Review Letters* 98.22 (May 2007). ISSN: 1079-7114. DOI: 10.1103/physrevlett.98.222002. URL: http://dx.doi.org/10.1103/PhysRevLett.98.222002.

[14] Stefano Catani et al. "Vector Boson Production at Hadron Colliders: A Fully Exclusive QCD Calculation at Next-to-Next-to-Leading Order". In: *Physical Review Letters* 103.8 (Aug. 2009). ISSN: 1079-7114. DOI: 10.1103/physrevlett.103.082001. URL: http://dx.doi.org/10.1103/PhysRevLett.103.082001.

[15] Claude Duhr, Falko Dulat, and Bernhard Mistlberger. "Drell-Yan Cross Section to Third Order in the Strong Coupling Constant". In: *Physical Review Letters* 125.17 (Oct. 2020). DOI: 10.1103/physrevlett.125.172001. URL: https://doi.org/10.1103%2Fphysrevlett.125.172001.

[16] CMS collaboration. "Measurement of the differential cross section and charge asymmetry for inclusive pp to W + X production at sqrt(s) = 8 TeV". In: *The European Physical Journal C* 76.8 (Aug. 2016). DOI: 10.1140/epjc/s10052-016-4293-4. URL: https://doi.org/10.1140%2Fepjc%2Fs10052-016-4293-4.

[17] ATLAS collaboration. "Precision measurement and interpretation of inclusive W^+/W^- and Z/γ production cross sections with the ATLAS detector". In: *The European Physical Journal C* 77.6 (June 2017). ISSN: 1434-6052. DOI: 10.1140/epjc/s10052-017-4911-9. URL: http://dx.doi.org/10.1140/epjc/s10052-017-4911-9.

[18] Toichiro Kinoshita. "Mass Singularities of Feynman Amplitudes". In: *J. Math. Phys. 3* 3 (1962), pp. 650–677. DOI: https://doi.org/10.1063/1.1724268.

[19] T. D. Lee and M. Nauenberg. "Degenerate Systems and Mass Singularities". In: *Phys. Rev.* 133 (6B Mar. 1964), B1549–B1562. DOI: 10.1103/PhysRev.133.B1549. URL: https://link.aps.org/doi/10.1103/PhysRev.133.B1549.

[20] Bryan Webber. *Hadronization*. 1994. arXiv: hep-ph/9411384 [hep-ph].

[21] ATLAS collaboration. "Charged-particle multiplicities inppinteractions measured with the ATLAS detector at the LHC". In: *New Journal of Physics* 13.5 (May 2011), p. 053033. ISSN: 1367-2630. DOI: 10.1088/1367-2630/13/5/053033. URL: http://dx.doi.org/10.1088/1367-2630/13/5/053033.

[22] ATLAS collaboration. "Measurement of the underlying event in jet events from 7 TeV TeV proton–proton collisions with the ATLAS detector". In: *The European Physical Journal C* 74.8 (Aug. 2014). ISSN: 1434-6052. DOI: 10.1140/epjc/s10052-014-2965-5. URL: http://dx.doi.org/10.1140/epjc/s10052-014-2965-5.

[23] Stefano Catani et al. "Vector Boson Production at Hadron Colliders: A Fully Exclusive QCD Calculation at Next-to-Next-to-Leading Order". In: *Physical Review Letters* 103.8 (Aug. 2009). ISSN: 1079-7114. DOI: 10.1103/physrevlett.103.082001. URL: http://dx.doi.org/10.1103/PhysRevLett.103.082001.

[24] Ryan Gavin et al. "FEWZ 2.0: A code for hadronic Z production at next-to-next-to-leading order". In: *Computer Physics Communications* 182.11 (Nov. 2011), pp. 2388–2403. ISSN: 0010-4655. DOI: 10.1016/j.cpc.2011.06.008. URL: http://dx.doi.org/10.1016/j.cpc.2011.06.008.

[25] Radja Boughezal et al. "Color-singlet production at NNLO in MCFM". In: *The European Physical Journal C* 77.1 (Dec. 2016). ISSN: 1434-6052. DOI: 10.1140/epjc/s10052-016-4558-y. URL: http://dx.doi.org/10.1140/epjc/s10052-016-4558-y.

[26] Massimiliano Grazzini, Stefan Kallweit, and Marius Wiesemann. "Fully differential NNLO computations with MATRIX". In: *The European Physical Journal C* 78.7 (June 2018). ISSN: 1434-6052. DOI: 10.1140/epjc/s10052-018-5771-7. URL: http://dx.doi.org/10.1140/epjc/s10052-018-5771-7.

[27] Stefano Camarda et al. "DYTurbo: fast predictions for Drell–Yan processes". In: *The European Physical Journal C* 80.3 (Mar. 2020). ISSN: 1434-6052. DOI: 10.1140/epjc/s10052-020-7757-5. URL: http://dx.doi.org/10.1140/epjc/s10052-020-7757-5.

[28] Markus A. Ebert and Frank J. Tackmann. "Impact of isolation and fiducial cuts on qT and N-jettiness subtractions". In: *Journal of High Energy Physics* 2020.3 (Mar. 2020). ISSN: 1029-8479. DOI: 10.1007/jhep03(2020)158. URL: http://dx.doi.org/10.1007/JHEP03(2020)158.

[29] S. Alekhin et al. "Precision studies for Drell–Yan processes at NNLO". In: *The European Physical Journal C* 81.7 (July 2021). ISSN: 1434-6052. DOI: 10.1140/epjc/s10052-021-09361-9. URL: http://dx.doi.org/10.1140/epjc/s10052-021-09361-9.

[30] Stefano Catani and Massimiliano Grazzini. "Next-to-Next-to-Leading-Order Subtraction Formalism in Hadron Collisions and its Application to Higgs-Boson Production at the Large Hadron Collider". In: *Physical Review Letters* 98.22 (May 2007). ISSN: 1079-7114. DOI: 10.1103/physrevlett.98.222002. URL: http://dx.doi.org/10.1103/PhysRevLett.98.222002.

[31] Jonathan Gaunt et al. *N-jettiness Subtractions for NNLO QCD Calculations*. 2015. arXiv: 1505.04794 [hep-ph].

[32] Gavin P. Salam and Emma Slade. "Cuts for two-body decays at colliders". In: *Journal of High Energy Physics* 2021.11 (Nov. 2021). ISSN: 1029-8479. DOI: 10.1007/jhep11(2021)220. URL: http://dx.doi.org/10.1007/JHEP11(2021)220.

[33] Massimiliano Grazzini, Stefan Kallweit, and Marius Wiesemann. "Fully differential NNLO computations with MATRIX". In: *The European Physical Journal C* 78.7 (June 2018). ISSN: 1434-6052. DOI: 10.1140/epjc/s10052-018-5771-7. URL: http://dx.doi.org/10.1140/epjc/s10052-018-5771-7.

[34] Markus A. Ebert et al. “Drell-Yan qT resummation of fiducial power corrections at N3LL”. In: *Journal of High Energy Physics* 2021.4 (Apr. 2021). ISSN: 1029-8479. DOI: 10.1007/jhep04(2021)102. URL: http://dx.doi.org/10.1007/JHEP04(2021)102.

[35] Stefano Catani et al. “Vector boson production at hadron colliders: transverse-momentum resummation and leptonic decay”. In: *Journal of High Energy Physics* 2015.12 (Dec. 2015), pp. 1–47. ISSN: 1029-8479. DOI: 10.1007/jhep12(2015)047. URL: http://dx.doi.org/10.1007/JHEP12(2015)047.

[36] Thomas Becher and Monika Hager. “Event-based transverse momentum resummation”. In: *The European Physical Journal C* 79.8 (Aug. 2019). ISSN: 1434-6052. DOI: 10.1140/epjc/s10052-019-7136-2. URL: http://dx.doi.org/10.1140/epjc/s10052-019-7136-2.

[37] Alessandro Bacchetta et al. “Transverse-momentum-dependent parton distributions up to N3LL from Drell-Yan data”. In: *Journal of High Energy Physics* 2020.7 (July 2020). ISSN: 1029-8479. DOI: 10.1007/jhep07(2020)117. URL: http://dx.doi.org/10.1007/JHEP07(2020)117.

[38] Emanuele Re, Luca Rottoli, and Paolo Torrielli. “Fiducial Higgs and Drell-Yan distributions at N3LL+NNLO with RadISH”. In: *Journal of High Energy Physics* 2021.9 (Sept. 2021). ISSN: 1029-8479. DOI: 10.1007/jhep09(2021)108. URL: http://dx.doi.org/10.1007/JHEP09(2021)108.

[39] Wan-Li Ju and Marek Schönherr. “The qT and spectra in W and Z production at the LHC at N3LL+N2LO”. In: *Journal of High Energy Physics* 2021.10 (Oct. 2021). ISSN: 1029-8479. DOI: 10.1007/jhep10(2021)088. URL: http://dx.doi.org/10.1007/JHEP10(2021)088.

[40] Luca Buonocore et al. *Linear power corrections for two-body kinematics in the q_T subtraction formalism*. 2021. DOI: 10.48550/ARXIV.2111.13661. URL: https://arxiv.org/abs/2111.13661.

[41] Stefano Camarda, Leandro Cieri, and Giancarlo Ferrera. “Fiducial perturbative power corrections within the q_T subtraction formalism”. In: (2021). arXiv: 2111.14509 [hep-ph].

[42] Rikkert Frederix et al. “Automation of next-to-leading order computations in QCD: the FKS subtraction”. In: *Journal of High Energy Physics* 2009.10 (Oct. 2009), pp. 003–003. ISSN: 1029-8479. DOI: 10.1088/1126-6708/2009/10/003. URL: http://dx.doi.org/10.1088/1126-6708/2009/10/003.

[43] T. Gleisberg and F. Krauss. “Automating dipole subtraction for QCD NLO calculations”. In: *The European Physical Journal C* 53.3 (Dec. 2007), pp. 501–523. ISSN: 1434-6052. DOI: 10.1140/epjc/s10052-007-0495-0. URL: http://dx.doi.org/10.1140/epjc/s10052-007-0495-0.

[44] Aude Gehrmann-De Ridder, Thomas Gehrmann, and E.W. Nigel Glover. “Antenna subtraction at NNLO”. In: *Journal of High Energy Physics* 2005.09 (Sept. 2005), pp. 056–056. ISSN: 1029-8479. DOI: 10.1088/1126-6708/2005/09/056. URL: http://dx.doi.org/10.1088/1126-6708/2005/09/056.

[45] Alejandro Daleo, Thomas Gehrmann, and Daniel Maître. “Antenna subtraction with hadronic initial states”. In: *Journal of High Energy Physics* 2007.04 (Apr. 2007), pp. 016–016. ISSN: 1029-8479. DOI: 10.1088/1126-6708/2007/04/016. URL: http://dx.doi.org/10.1088/1126-6708/2007/04/016.

[46] James Currie, E. W. N. Glover, and Steven Wells. "Infrared structure at NNLO using antenna subtraction". In: *Journal of High Energy Physics* 2013.4 (Apr. 2013). ISSN: 1029-8479. DOI: 10.1007/jhep04(2013)066. URL: http://dx.doi.org/10.1007/JHEP04(2013)066.

[47] M. Czakon. "A novel subtraction scheme for double-real radiation at NNLO". In: *Physics Letters B* 693.3 (Oct. 2010), pp. 259–268. DOI: 10.1016/j.physletb.2010.08.036. URL: https://doi.org/10.1016%2Fj.physletb.2010.08.036.

[48] M. Czakon. "Double-real radiation in hadronic top quark pair production as a proof of a certain concept". In: *Nuclear Physics B* 849.2 (Aug. 2011), pp. 250–295. DOI: 10.1016/j.nuclphysb.2011.03.020. URL: https://doi.org/10.1016%2Fj.nuclphysb.2011.03.020.

[49] M. Czakon and D. Heymes. "Four-dimensional formulation of the sector-improved residue subtraction scheme". In: *Nuclear Physics B* 890 (Jan. 2015), pp. 152–227. DOI: 10.1016/j.nuclphysb.2014.11.006. URL: https://doi.org/10.1016%2Fj.nuclphysb.2014.11.006.

[50] Particle Data Group et al. "Review of Particle Physics". In: *Progress of Theoretical and Experimental Physics* 2020.8 (Aug. 2020). 083C01. ISSN: 2050-3911. DOI: 10.1093/ptep/ptaa104. eprint: https://academic.oup.com/ptep/article-pdf/2020/8/083C01/34673722/ptaa104.pdf. URL: https://doi.org/10.1093/ptep/ptaa104.

[51] Richard D. Ball et al. "Parton distributions from high-precision collider data". In: *The European Physical Journal C* 77.10 (Oct. 2017). ISSN: 1434-6052. DOI: 10.1140/epjc/s10052-017-5199-5. URL: http://dx.doi.org/10.1140/epjc/s10052-017-5199-5.

[52] S. Alekhin et al. *HERAFitter, Open Source QCD Fit Project*. 2015. arXiv: 1410.4412 [hep-ph].

[53] M Botje. "Error estimates on parton density distributions". In: *Journal of Physics G: Nuclear and Particle Physics* 28.5 (Apr. 2002), pp. 779–789. DOI: 10.1088/0954-3899/28/5/305. URL: https://doi.org/10.1088%2F0954-3899%2F28%2F5%2F305.

[54] D. Stump et al. "Uncertainties of predictions from parton distribution functions. I. The Lagrange multiplier method". In: *Physical Review D* 65.1 (Dec. 2001). DOI: 10.1103/physrevd.65.014012. URL: https://doi.org/10.1103%2Fphysrevd.65.014012.

[55] Hannu Paukkunen and Pia Zurita. "PDF reweighting in the Hessian matrix approach". In: *Journal of High Energy Physics* 2014.12 (Dec. 2014). ISSN: 1029-8479. DOI: 10.1007/jhep12(2014)100. URL: http://dx.doi.org/10.1007/JHEP12(2014)100.

[56] S. Camarda et al. *QCD analysis of W- and Z-boson production at Tevatron*. 2015. arXiv: 1503.05221 [hep-ph].

[57] Tancredi Carli et al. "A posteriori inclusion of parton density functions in NLO QCD final-state calculations at hadron colliders: the APPLGRID project". In: *The European Physical Journal C* 66.3–4 (Feb. 2010), pp. 503–524. ISSN: 1434-6052. DOI: 10.1140/epjc/s10052-010-1255-0. URL: http://dx.doi.org/10.1140/epjc/s10052-010-1255-0.

[58] J. M. Campbell and R. K. Ellis. "Update on vector boson pair production at hadron colliders". In: *Physical Review D* 60.11 (Nov. 1999). ISSN: 1089-4918. DOI: 10.1103/physrevd.60.113006. URL: http://dx.doi.org/10.1103/PhysRevD.60.113006.

[59] John M. Campbell, R. Keith Ellis, and Ciaran Williams. "Vector boson pair production at the LHC". In: *Journal of High Energy Physics* 2011.7 (July 2011). ISSN: 1029-8479. DOI: 10.1007/jhep07(2011)018. URL: http://dx.doi.org/10.1007/JHEP07(2011)018.

[60] John M. Campbell, R. Keith Ellis, and Walter T. Giele. *A Multi-Threaded Version of MCFM*. 2015. arXiv: 1503.06182 [physics.comp-ph].

[61] Richard D. Ball et al. *The Path to Proton Structure at One-Percent Accuracy*. 2021. DOI: 10.48550/ARXIV.2109.02653. URL: https://arxiv.org/abs/2109.02653.

[62] Tie-Jiun Hou et al. "New CTEQ global analysis of quantum chromodynamics with high-precision data from the LHC". In: *Phys. Rev. D* 103.1 (2021), p. 014013. DOI: 10.1103/PhysRevD.103.014013. arXiv: 1912.10053 [hep-ph].

[63] S. Bailey et al. "Parton distributions from LHC, HERA, Tevatron and fixed target data: MSHT20 PDFs". In: *The European Physical Journal C* 81.4 (Apr. 2021). DOI: 10.1140/epjc/s10052-021-09057-0. URL: https://doi.org/10.1140%2Fepjc%2Fs10052-021-09057-0.

[64] Alessandro Guida. *DIS conference 2022 - Drell-Yan cross-sections with fiducial cuts*. 2022. URL: https://indico.cern.ch/event/1072533/contributions/4793108/ (visited on 05/03/2022).

[65] Alessandro Guida et al. "Drell-Yan cross-sections with fiducial cuts". In: (to appear).

[66] ATLAS collaboration. "Measurements of W and Z boson production in pp collisions at $\sqrt{s} = 5.02$ TeV with the ATLAS detector". In: *The European Physical Journal C* 79.2 (Feb. 2019). ISSN: 1434-6052. DOI: 10.1140/epjc/s10052-019-6622-x. URL: http://dx.doi.org/10.1140/epjc/s10052-019-6622-x.

[67] ATLAS collaboration. "Measurement of the cross-section and charge asymmetry of W bosons produced in proton–proton collisions at $\sqrt{s} = 8$ TeV with the ATLAS detector". In: *The European Physical Journal C* 79.9 (Sept. 2019). ISSN: 1434-6052. DOI: 10.1140/epjc/s10052-019-7199-0. URL: http://dx.doi.org/10.1140/epjc/s10052-019-7199-0.

[68] CMS collaboration. "Forward–backward asymmetry of Drell–Yan lepton pairs in pp collisions at $\sqrt{s} = 8$ TeV". In: *The European Physical Journal C* 76.6 (June 2016). ISSN: 1434-6052. DOI: 10.1140/epjc/s10052-016-4156-z. URL: http://dx.doi.org/10.1140/epjc/s10052-016-4156-z.

[69] CMS collaboration. "Forward-backward asymmetry of Drell-Yan lepton pairs in pp collisions at sqrt(s) = 7 TeV". In: *Physics Letters B* 718.3 (Jan. 2013), pp. 752–772. DOI: 10.1016/j.physletb.2012.10.082. URL: https://doi.org/10.1016%2Fj.physletb.2012.10.082.

[70] V.M. D0 collaboration Abazov et al. "Measurement of the Shape of the Boson Rapidity Distribution for $p\bar{p} \to Z/\gamma^* \to e^+e^- + X$ Events Produced at $\sqrt{s}$ of 1.96-TeV". In: *Phys. Rev. D* 76 (2007), p. 012003. DOI: 10.1103/PhysRevD.76.012003. arXiv: hep-ex/0702025.

[71] V.M. D0 collaboration Abazov et al. "Measurement of the Muon Charge Asymmetry in $p\bar{p} \to$ W+X $\to \mu\nu$ + X Events at $\sqrt{s}$=1.96 TeV". In: *Phys. Rev. D* 88 (2013), p. 091102. DOI: 10.1103/PhysRevD.88.091102. arXiv: 1309.2591 [hep-ex].

[72] V.M. D0 collaboration Abazov et al. "Measurement of the W Boson Production Charge Asymmetry in $p\bar{p} \to W + X \to e\nu + X$ Events at $\sqrt{s} = 1.96$ TeV". In: *Phys. Rev. Lett.* 112.15 (2014). [Erratum: Phys.Rev.Lett. 114, 049901 (2015)], p. 151803. DOI: 10.1103/PhysRevLett.112.151803. arXiv: 1312.2895 [hep-ex].

[73] V.M. D0 collaboration Abazov et al. "Measurement of the electron charge asymmetry in $p\bar{p} \to W + X \to e\nu + X$ decays in $p\bar{p}$ collisions at $\sqrt{s} = 1.96$ TeV". In: *Phys. Rev. D* 91.3 (2015). [Erratum: Phys.Rev.D 91, 079901 (2015)], p. 032007. DOI: 10.1103/PhysRevD.91.032007. arXiv: 1412.2862 [hep-ex].

[74] T. CDF collaboration Affolder et al. "Measurement of $d(\sigma)/dy$ for high mass Drell-Yan e^+e^- pairs from $p\bar{p}$ collisions at $\sqrt{s} = 1.8$ TeV". In: *Phys. Rev. D* 63 (2001), p. 011101. DOI: 10.1103/PhysRevD.63.011101. arXiv: hep-ex/0006025.

[75] T. CDF collaboration Aaltonen et al. "Measurement of $d\sigma/dy$ of Drell-Yan e^+e^- pairs in the Z Mass Region from $p\bar{p}$ Collisions at $\sqrt{s} = 1.96$ TeV". In: *Phys. Lett. B* 692 (2010), pp. 232–239. DOI: 10.1016/j.physletb.2010.06.043. arXiv: 0908.3914 [hep-ex].

[76] T. CDF collaboration Aaltonen et al. "Direct Measurement of the W Production Charge Asymmetry in $p\bar{p}$ Collisions at $\sqrt{s} = 1.96$ TeV". In: *Phys. Rev. Lett.* 102 (2009), p. 181801. DOI: 10.1103/PhysRevLett.102.181801. arXiv: 0901.2169 [hep-ex].

[77] T. A. CDF collaboration Aaltonen et al. "Measurement of the charge asymmetry of electrons from the decays of W bosons produced in $p\bar{p}$ collisions at $\sqrt{s} = 1.96$ TeV". In: (July 2021). arXiv: 2107.04678 [hep-ex].

[78] Lyndon Evans and Philip Bryant. "LHC Machine". In: *Journal of Instrumentation* 3.08 (Aug. 2008), S08001–S08001. DOI: 10.1088/1748-0221/3/08/s08001. URL: https://doi.org/10.1088/1748-0221/3/08/s08001.

[79] Luigi Di Lella and Carlo Rubbia. "The Discovery of the W and Z Particles". In: *Adv. Ser. Dir. High Energy Phys.* 23 (2015), pp. 137–163. DOI: 10.1142/9789814644150_0006. URL: https://cds.cern.ch/record/2103277.

[80] R Alemany-Fernandez et al. "Operation and Configuration of the LHC in Run 1". In: (Nov. 2013). URL: https://cds.cern.ch/record/1631030.

[81] Jorg Wenninger. "Operation and Configuration of the LHC in Run 2". In: (Mar. 2019). URL: https://cds.cern.ch/record/2668326.

[82] *Luminosity determination in pp collisions at $\sqrt{s} = 13$ TeV using the ATLAS detector at the LHC*. Tech. rep. All figures including auxiliary figures are available at https://atlas.web.cern.ch/Atlas/GROUPS/PHYSICS/CONFNOTES/ATLAS-CONF-2019-021. Geneva: CERN, June 2019. URL: http://cds.cern.ch/record/2677054.

[83] LUCID collaboration. "LUCID: The ATLAS Luminosity Detector". In: *PoS* ICHEP2018 (2019), p. 280. DOI: 10.22323/1.340.0280.

[84] Patrawan Pasuwan. "Track-counting luminosity measurement in ATLAS". In: (July 2019). URL: http://cds.cern.ch/record/2680903.

[85] Sergio Gonzalez Fernandez. *Measurements of Luminosity in ATLAS with Tile Calorimeter*. Tech. rep. Geneva: CERN, Oct. 2020. URL: https://cds.cern.ch/record/2741127.

[86] *Luminosity Determination using $Z \to ll$ events at $\sqrt{s} = 13$ TeV with the ATLAS detector*. Tech. rep. All figures including auxiliary figures are available at https://atlas.web.cern.ch/Atlas/GROUPS/PHYSICS/PUBNOTES/ATL-DAPR-PUB-2021-001. Geneva: CERN, Feb. 2021. URL: https://cds.cern.ch/record/2752951.

[87] ATLAS Collaboration. "The ATLAS Experiment at the CERN Large Hadron Collider". In: *JINST* 3 (2008). Also published by CERN Geneva in 2010, S08003. 437 p. DOI: 10.1088/1748-0221/3/08/S08003. URL: https://cds.cern.ch/record/1129811.

[88] CMS collaboration. "The CMS Experiment at the CERN LHC". In: *JINST* 3 (2008), S08004. DOI: 10.1088/1748-0221/3/08/S08004.

[89] K. ALICE collaboration Aamodt et al. "The ALICE experiment at the CERN LHC". In: *JINST* 3 (2008), S08002. DOI: 10.1088/1748-0221/3/08/S08002.

[90] LHCb collaboration. "The LHCb Detector at the LHC". In: *JINST* 3 (2008), S08005. DOI: 10.1088/1748-0221/3/08/S08005.

[91] O. Adriani et al. "The LHCf detector at the CERN Large Hadron Collider". In: *JINST* 3 (2008), S08006. DOI: 10.1088/1748-0221/3/08/S08006.

[92] James Pinfold et al. *Technical Design Report of the MoEDAL Experiment*. Tech. rep. June 2009. URL: http://cds.cern.ch/record/1181486.

[93] G. Anelli et al. "The TOTEM experiment at the CERN Large Hadron Collider". In: *JINST* 3 (2008), S08007. DOI: 10.1088/1748-0221/3/08/S08007.

[94] FASER Collaboration et al. *FASER: ForwArd Search ExpeRiment at the LHC*. 2019. arXiv: 1901.04468 [hep-ex].

[95] *ATLAS inner detector: Technical Design Report, 1*. Technical design report. ATLAS. Geneva: CERN, 1997. URL: https://cds.cern.ch/record/331063.

[96] ATLAS Collaboration. "ATLAS pixel detector electronics and sensors". In: *Journal of Instrumentation* 3.07 (July 2008), P07007–P07007. DOI: 10.1088/1748-0221/3/07/p07007. URL: https://doi.org/10.1088/1748-0221/3/07/p07007.

[97] The ATLAS collaboration. "Operation and performance of the ATLAS semiconductor tracker". In: *Journal of Instrumentation* 9.08 (Aug. 2014), P08009–P08009. ISSN: 1748-0221. DOI: 10.1088/1748-0221/9/08/p08009. URL: http://dx.doi.org/10.1088/1748-0221/9/08/P08009.

[98] ATLAS collaboration. "Performance of the ATLAS Transition Radiation Tracker in Run 1 of the LHC: tracker properties". In: *Journal of Instrumentation* 12.05 (May 2017), P05002–P05002. ISSN: 1748-0221. DOI: 10.1088/1748-0221/12/05/p05002. URL: http://dx.doi.org/10.1088/1748-0221/12/05/P05002.

[99] M Capeans et al. *ATLAS Insertable B-Layer Technical Design Report*. Tech. rep. Sept. 2010. URL: https://cds.cern.ch/record/1291633.

[100] ATLAS collaboration. "The ATLAS Experiment at the CERN Large Hadron Collider". In: *JINST* 3 (2008). Also published by CERN Geneva in 2010, S08003. 437 p. DOI: 10.1088/1748-0221/3/08/S08003. URL: https://cds.cern.ch/record/1129811.

[101] ATLAS collaboration. "ATLAS muon spectrometer: Technical design report". In: (June 1997).

[102] Lorenzo Bianchini. *Selected Exercises in Particle and Nuclear Physics*. Jan. 2018. ISBN: 978-3-319-70493-7. DOI: 10.1007/978-3-319-70494-4.

[103] R.L. Gluckstern. "Uncertainties in track momentum and direction, due to multiple scattering and measurement errors". In: *Nuclear Instruments and Methods* 24 (1963), pp. 381–389. ISSN: 0029-554X. DOI: https://doi.org/10.1016/0029-554X(63)90347-1. URL: https://www.sciencedirect.com/science/article/pii/0029554X63903471.

[104] M. Tanabashi et al. "Review of Particle Physics". In: *Phys. Rev. D* 98.3 (2018), p. 030001. DOI: 10.1103/PhysRevD.98.030001.

[105] R. Fruhwirth. "Application of Kalman filtering to track and vertex fitting". In: *Nucl. Instrum. Meth. A* 262 (1987), pp. 444–450. DOI: 10.1016/0168-9002(87)90887-4.

[106] ATLAS collaboration. "Alignment of the ATLAS Inner Detector in Run-2". In: *Eur. Phys. J. C* 80.12 (2020), p. 1194. DOI: 10.1140/epjc/s10052-020-08700-6. arXiv: 2007.07624 [hep-ex].

[107] ATLAS collaboration. "Measurements of the Higgs boson inclusive and differential fiducial cross sections in the 4ℓ decay channel at $\sqrt{s}$ = 13 TeV". In: *Eur. Phys. J. C* 80.10 (2020), p. 942. DOI: 10.1140/epjc/s10052-020-8223-0. arXiv: 2004.03969 [hep-ex].

[108] ATLAS collaboration. "Measurement of $W^{\pm}$-boson and Z-boson production cross-sections in pp collisions at $\sqrt{s} = 2.76$ TeV with the ATLAS detector". In: *The European Physical Journal C* 79.11 (Nov. 2019). ISSN: 1434-6052. DOI: 10.1140/epjc/s10052-019-7399-7. URL: http://dx.doi.org/10.1140/epjc/s10052-019-7399-7.

[109] CMS collaboration. "Measurements of differential Z boson production cross sections in proton-proton collisions at $\sqrt{s}$ = 13 TeV". In: *Journal of High Energy Physics* 2019.12 (Dec. 2019). ISSN: 1029-8479. DOI: 10.1007/jhep12(2019)061. URL: http://dx.doi.org/10.1007/JHEP12(2019)061.

[110] LHCb Collaboration. "Measurement of the forward Z boson production cross-section in pp collisions at $\sqrt{s} = 7$ TeV". In: *Journal of High Energy Physics* 2015.8 (Aug. 2015). DOI: 10.1007/jhep08(2015)039. URL: https://doi.org/10.1007,%2Fjhep08%282015%29039.

[111] LHCb Collaboration. *Precision measurement of forward Z boson production in proton-proton collisions at* $\sqrt{s} = 13$ *TeV*. 2021. DOI: 10.48550/ARXIV.2112.07458. URL: https://arxiv.org/abs/2112.07458.

[112] CMS Collaboration. "Measurements of differential Z boson production cross sections in proton-proton collisions at $\sqrt{s} = 13$ TeV". In: *Journal of High Energy Physics* 2019.12 (Dec. 2019). DOI: 10.1007/jhep12(2019)061. URL: https://doi.org/10.10072Fjhep1228201929061.

[113] ATLAS collaboration. "ATLAS data quality operations and performance for 2015-2018 data-taking". In: *JINST* 15.04 (2020), P04003. DOI: 10.1088/1748-0221/15/04/P04003. arXiv: 1911.04632 [physics.ins-det].

[114] Paolo Nason. "A New Method for Combining NLO QCD with Shower Monte Carlo Algorithms". In: *Journal of High Energy Physics* 2004.11 (Nov. 2004), pp. 040–040. ISSN: 1029-8479. DOI: 10.1088/1126-6708/2004/11/040. URL: http://dx.doi.org/10.1088/1126-6708/2004/11/040.

[115] Stefano Frixione, Paolo Nason, and Carlo Oleari. "Matching NLO QCD computations with Parton Shower simulations: the POWHEG method". In: *JHEP* 11 (2007), p. 070. DOI: 10.1088/1126-6708/2007/11/070. arXiv: 0709.2092 [hep-ph].

[116] Simone Alioli et al. “A general framework for implementing NLO calculations in shower Monte Carlo programs: the POWHEG BOX”. In: *JHEP* 06 (2010), p. 043. DOI: 10.1007/JHEP06(2010)043. arXiv: 1002.2581 [hep-ph].

[117] Torbjörn Sjöstrand, Stephen Mrenna, and Peter Skands. “A brief introduction to PYTHIA 8.1”. In: *Computer Physics Communications* 178.11 (June 2008), pp. 852–867. ISSN: 0010-4655. DOI: 10.1016/j.cpc.2008.01.036. URL: http://dx.doi.org/10.1016/j.cpc.2008.01.036.

[118] Hung-Liang Lai et al. “New parton distributions for collider physics”. In: *Phys. Rev. D* 82 (7 Oct. 2010), p. 074024. DOI: 10.1103/PhysRevD.82.074024. URL: https://link.aps.org/doi/10.1103/PhysRevD.82.074024.

[119] ATLAS Collaboration. “Measurement of the Z/γ^* boson transverse momentum distribution in pp collisions at $\sqrt{s} = 7$ with the ATLAS detector”. In: *Journal of High Energy Physics* 2014.9 (Sept. 2014). DOI: 10.1007/jhep09(2014)145. URL: https://doi.org/10.1007%2Fjhep09%282014%29145.

[120] *Monte Carlo Generators for the Production of a W or Z/γ^* Boson in Association with Jets at ATLAS in Run 2*. Tech. rep. All figures including auxiliary figures are available at https://atlas.web.cern.ch/Atlas/GROUPS/PHYSICS/PUBNOTES/ATL-PHYS-PUB-2016-003. Geneva: CERN, Jan. 2016. URL: http://cds.cern.ch/record/2120133.

[121] Charalampos Anastasiou et al. “High-precision QCD at hadron colliders: Electroweak gauge boson rapidity distributions at next-to-next-to leading order”. In: *Physical Review D* 69.9 (May 2004). ISSN: 1550-2368. DOI: 10.1103/physrevd.69.094008. URL: http://dx.doi.org/10.1103/PhysRevD.69.094008.

[122] Sayipjamal Dulat et al. “New parton distribution functions from a global analysis of quantum chromodynamics”. In: *Physical Review D* 93.3 (Feb. 2016). ISSN: 2470-0029. DOI: 10.1103/physrevd.93.033006. URL: http://dx.doi.org/10.1103/PhysRevD.93.033006.

[123] Sergey G. Bondarenko and Andrey A. Sapronov. “NLO EW and QCD proton–proton cross section calculations with mcsanc-v1.01”. In: *Computer Physics Communications* 184.10 (Oct. 2013), pp. 2343–2350. ISSN: 0010-4655. DOI: 10.1016/j.cpc.2013.05.010. URL: http://dx.doi.org/10.1016/j.cpc.2013.05.010.

[124] Michał Czakon and Alexander Mitov. “Top++: A program for the calculation of the top-pair cross-section at hadron colliders”. In: *Computer Physics Communications* 185.11 (Nov. 2014), pp. 2930–2938. ISSN: 0010-4655. DOI: 10.1016/j.cpc.2014.06.021. URL: http://dx.doi.org/10.1016/j.cpc.2014.06.021.

[125] Manuel Bähr et al. “Herwig physics and manual”. In: *The European Physical Journal C* 58.4 (Nov. 2008), pp. 639–707. DOI: 10.1140/epjc/s10052-008-0798-9. URL: https://doi.org/10.1140%2Fepjc%2Fs10052-008-0798-9.

[126] J. A. M. Vermaseren. “Two Photon Processes at Very High-Energies”. In: *Nucl. Phys. B* 229 (1983), pp. 347–371. DOI: 10.1016/0550-3213(83)90336-X.

[127] Ashok Suri and Donald R. Yennie. “THE SPACE-TIME PHENOMENOLOGY OF PHOTON ABSORPTION AND INELASTIC ELECTRON SCATTERING”. In: *Annals Phys.* 72 (1972), p. 243. DOI: 10.1016/0003-4916(72)90242-4.

[128] F.W. Brasse et al. “Parametrization of the q2 dependence of vp total cross sections in the resonance region”. In: *Nuclear Physics B* 110.4 (1976), pp. 413–433. ISSN: 0550-3213. DOI: https://doi.org/10.1016/0550-3213(76)90231-5. URL: https://www.sciencedirect.com/science/article/pii/0550321376902315.

[129] Torbjorn Sjostrand. *PYTHIA 5.7 and JETSET 7.4 Physics and Manual*. 1995. DOI: 10.48550/ARXIV.HEP-PH/9508391. URL: https://arxiv.org/abs/hep-ph/9508391.

[130] Bo Andersson. *The Lund model*. Vol. 7. Cambridge University Press, July 2005. ISBN: 978-0-521-01734-3, 978-0-521-42094-5, 978-0-511-88149-7. DOI: 10.1017/CBO9780511524363.

[131] Torbjörn Sjöstrand, Stephen Mrenna, and Peter Skands. “PYTHIA 6.4 physics and manual”. In: *Journal of High Energy Physics* 2006.05 (May 2006), pp. 026–026. DOI: 10.1088/1126-6708/2006/05/026. URL: https://doi.org/10.1088%2F1126-6708%2F2006%2F05%2F026.

[132] Stefano Carrazza. *Parton distribution functions with QED corrections*. 2015. DOI: 10.48550/ARXIV.1509.00209. URL: https://arxiv.org/abs/1509.00209.

[133] *ATLAS Pythia 8 tunes to 7 TeV data*. Tech. rep. All figures including auxiliary figures are available at https://atlas.web.cern.ch/Atlas/GROUPS/PHYSICS/PUBNOTES/ATL-PHYS-PUB-2014-021. Geneva: CERN, Nov. 2014. URL: https://cds.cern.ch/record/1966419.

[134] N. Davidson, T. Przedzinski, and Z. Was. *PHOTOS Interface in C++; Technical and Physics Documentation*. 2015. arXiv: 1011.0937 [hep-ph].

[135] “New ATLAS event generator tunes to 2010 data”. In: (Apr. 2011).

[136] S. Agostinelli et. al. “Geant4—a simulation toolkit”. In: *Nuclear Instruments and Methods in Physics Research Section A: Accelerators, Spectrometers, Detectors and Associated Equipment* 506.3 (2003), pp. 250–303. ISSN: 0168-9002. DOI: https://doi.org/10.1016/S0168-9002(03)01368-8. URL: https://www.sciencedirect.com/science/article/pii/S0168900203013688.

[137] ATLAS collaboration. “The ATLAS Simulation Infrastructure”. In: *The European Physical Journal C* 70.3 (Sept. 2010), pp. 823–874. ISSN: 1434-6052. DOI: 10.1140/epjc/s10052-010-1429-9. URL: http://dx.doi.org/10.1140/epjc/s10052-010-1429-9.

[138] ATLAS collaboration. “Performance of the ATLAS trigger system in 2015”. In: *The European Physical Journal C* 77.5 (May 2017). DOI: 10.1140/epjc/s10052-017-4852-3. URL: https://doi.org/10.1140%2Fepjc%2Fs10052-017-4852-3.

[139] ATLAS collaboration. “Muon reconstruction performance of the ATLAS detector in proton–proton collision data at $\sqrt{s} = 13$ TeV”. In: *The European Physical Journal C* 76.5 (May 2016). ISSN: 1434-6052. DOI: 10.1140/epjc/s10052-016-4120-y. URL: http://dx.doi.org/10.1140/epjc/s10052-016-4120-y.

[140] Roger J. Barlow and Christine Beeston. “Fitting using finite Monte Carlo samples”. In: *Comput. Phys. Commun.* 77 (1993), pp. 219–228. DOI: 10.1016/0010-4655(93)90005-W.

[141] ATLAS collaboration. “ATLAS data quality operations and performance for 2015–2018 data-taking”. In: *Journal of Instrumentation* 15.04 (Apr. 2020), P04003–P04003. ISSN: 1748-0221. DOI: 10.1088/1748-0221/15/04/p04003. URL: http://dx.doi.org/10.1088/1748-0221/15/04/P04003.

[142] *Luminosity determination in pp collisions at $\sqrt{s} = 13$ TeV using the ATLAS detector at the LHC*. Tech. rep. All figures including auxiliary figures are available at https://atlas.web.cern.ch/Atlas/GROUPS/PHYSICS/CONFNOTES/ATLAS-CONF-2019-021. Geneva: CERN, June 2019. URL: http://cds.cern.ch/record/2677054.

[143] ATLAS collaboration. "Measurement of the exclusive $\gamma\gamma \to \mu^+\mu^-$ process in proton–proton collisions at $s = \sqrt{13}$ TeV with the ATLAS detector". In: *Physics Letters B* 777 (Feb. 2018), pp. 303–323. ISSN: 0370-2693. DOI: 10.1016/j.physletb.2017.12.043. URL: http://dx.doi.org/10.1016/j.physletb.2017.12.043.

[144] *ATLAS simulation of boson plus jets processes in Run 2*. Tech. rep. All figures including auxiliary figures are available at https://atlas.web.cern.ch/Atlas/GROUPS/PHYSICS/PUBNOTES PHYS-PUB-2017-006. Geneva: CERN, May 2017. URL: https://cds.cern.ch/record/2261937.

[145] Stefano Camarda, Leandro Cieri, and Giancarlo Ferrera. "Drell–Yan lepton-pair production: qT resummation at N3LL accuracy and fiducial cross sections at N3LO". In: *Physical Review D* 104.11 (Dec. 2021). DOI: 10.1103/physrevd.104.l111503. URL: https://doi.org/10.1103%2Fphysrevd.104.l111503.

[146] Wojciech Bizoń et al. "Fiducial distributions in Higgs and Drell-Yan production at N3LLNNLO". In: *Journal of High Energy Physics* 2018.12 (Dec. 2018). DOI: 10.1007/jhep12(2018)132. URL: https://doi.org/10.1007.

[147] Marco Bonvini, Simone Marzani, and Tiziano Peraro. "Small-x resummation from HELL". In: *The European Physical Journal C* 76.11 (Nov. 2016). DOI: 10.1140/epjc/s10052-016-4445-6. URL: https://doi.org/10.1140%2Fepjc%2Fs10052-016-4445-6.

[148] xFitter Developers' team xFitter et al. *Impact of low-x resummation on QCD analysis of HERA data*. 2018. DOI: 10.48550/ARXIV.1802.00064. URL: https://arxiv.org/abs/1802.00064.

[149] The ATLAS collaboration. "Operation of the ATLAS trigger system in Run 2". In: *Journal of Instrumentation* 15.10 (Oct. 2020), P10004–P10004. DOI: 10.1088/1748-0221/15/10/p10004. URL: https://doi.org/10.1088%2F1748-0221%2F15%2F10%2Fp10004.

[150] Alessandro Bacchetta et al. "Transverse-momentum-dependent parton distributions up to N3LL from Drell-Yan data". In: *Journal of High Energy Physics* 2020.7 (July 2020). DOI: 10.1007/jhep07(2020)117. URL: https://doi.org/10.1007%2Fjhep07%282020%29117.

[151] Sara Taheri Monfared et al. *Extending parton branching TMDs to small x*. 2019. DOI: 10.48550/ARXIV.1908.01621. URL: https://arxiv.org/abs/1908.01621.

[152] Anton V. Konychev and Pavel M. Nadolsky. "Universality of the Collins–Soper–Sterman nonperturbative function in vector boson production". In: *Physics Letters B* 633.6 (Feb. 2006), pp. 710–714. DOI: 10.1016/j.physletb.2005.12.063. URL: https://doi.org/10.1016%2Fj.physletb.2005.12.063.

[153] Marco Guzzi, Pavel M. Nadolsky, and Bowen Wang. "Nonperturbative contributions to a resummed leptonic angular distribution in inclusive neutral vector boson production". In: *Physical Review D* 90.1 (July 2014). DOI: 10.1103/physrevd.90.014030. URL: https://doi.org/10.1103%2Fphysrevd.90.014030.

[154] ATLAS collaboration. "Measurement of the W-boson mass in pp collisions at $\sqrt{7}$TeV with the ATLAS detector". In: *The European Physical Journal C* 78.2 (Feb. 2018). DOI: 10.1140/epjc/s10052-017-5475-4. URL: https://doi.org/10.1140%2Fepjc%2Fs10052-017-5475-4.

[155] LHCb collaboration. "Measurement of the W boson mass". In: *Journal of High Energy Physics* 2022.1 (Jan. 2022). DOI: 10.1007/jhep01(2022)036. URL: https://doi.org/10.1007%2Fjhep01%282022%29036.

[156] Richard D. Ball et al. "Precision determination of the strong coupling constant within a global PDF analysis". In: *The European Physical Journal C* 78.5 (May 2018). DOI: 10.1140/epjc/s10052-018-5897-7. URL: https://doi.org/10.1140%2Fepjc%2Fs10052-018-5897-7.

[157] Stefano Camarda, Giancarlo Ferrera, and Matthias Schott. *Determination of the strong-coupling constant from the Z-boson transverse-momentum distribution*. 2022. URL: https://arxiv.org/abs/2203.05394.

[158] Radja Boughezal et al. "The impact of the LHC Z-boson transverse momentum data on PDF determinations". In: *Journal of High Energy Physics* 2017.7 (July 2017). DOI: 10.1007/jhep07(2017)130. URL: https://doi.org/10.1007%2Fjhep07%282017%29130.

Appendix A

Systematic Uncertainties

In this Appendix, the tables with the breakdown of the uncertainties presented in chapter 10 are reported. In table A.1 the uncertainties for the mass measurement are reported. The estimated uncertainties in the mass and rapidity measurement are reported in table A.2. Finally the uncertainties for the mass and $p_T^{\mu\mu}$ measurement are in tables A.3 and A.4.

Table A.1 Statistical and systematic uncertainties for the mass differential cross section measurement.

$m_{\mu\mu}^{\text{min}} - m_{\mu\mu}^{\text{max}}$ [GeV] Variation [%]	7.3-8.7	12.0-14.0	14.0-17.0	17.0-22.0	22.0-28.0	28.0-36.0	36.0-46.0	46.0-56.0
Muon resolution (ID)	0.04	0.08	0.02	0.04	0.06	0.04	0.28	0.57
Muon resolution (MS)	0.10	0.07	0.02	0.04	0.06	0.07	0.19	0.54
Muon scale	0.29	0.20	0.21	0.25	0.25	0.24	0.37	0.71
Sagitta bias	0.01	0.03	0.03	0.02	0.02	0.03	0.30	0.94
Reconstruction eff. (stat.)	0.08	0.07	0.06	0.03	0.06	0.13	0.26	0.39
Reconstruction eff. (syst.)	1.34	1.40	1.37	1.38	1.21	0.97	1.48	2.21
Trigger eff. (stat.)	0.47	0.50	0.60	0.74	0.89	0.79	0.50	0.33
Trigger eff. (syst.)	1.17	1.20	1.30	1.46	1.48	1.18	0.97	1.24
Isolation eff. (stat.)	0.06	0.09	0.07	0.06	0.05	0.03	0.02	0.01
Isolation eff. (syst.)	3.87	4.14	3.37	2.60	2.02	1.72	1.64	1.78
QCD background	4.11	4.28	3.54	3.29	2.82	2.62	2.72	2.31
EWK Background	1.84	0.14	0.23	0.23	0.27	0.30	0.39	0.42
Statistics	2.26	1.19	0.75	0.58	0.63	0.68	0.85	1.01
Total syst	6.23	6.26	5.29	4.72	4.08	3.60	3.75	4.17

Table A.2 Statistical and systematic uncertainties for the mass and rapidity double differential cross section measurement.

$7.3 < m_{\mu\mu} < 8.7\,\text{GeV}$						
$\lvert y_{\mu\mu}\rvert^{\text{min}} - \lvert y_{\mu\mu}\rvert^{\text{max}}$ Variation [%]	0.0-0.4	0.4-0.8	0.8-1.2	1.2-1.6	1.6-2.0	2.0-2.4
Muon resolution (ID)	0.20	0.10	0.08	0.03	0.16	0.08
Muon resolution (MS)	0.12	0.08	0.39	0.21	0.25	0.23
Muon scale	0.18	0.03	0.33	0.38	0.44	0.55
Sagitta bias	0.05	0.02	0.07	0.06	0.16	0.13
Reconstruction eff. (stat.)	0.03	0.07	0.10	0.13	0.14	0.10
Reconstruction eff. (syst.)	1.80	1.36	1.18	1.31	1.34	1.33
Trigger eff. (stat.)	1.10	0.89	0.74	0.45	0.44	0.86
Trigger eff. (syst.)	1.59	1.48	1.46	1.04	0.90	1.16
Isolation eff. (stat.)	0.00	0.00	0.00	0.00	0.00	0.00
Isolation eff. (syst.)	4.13	3.94	4.15	3.90	3.57	3.38
QCD background	5.35	4.79	4.30	3.86	3.89	4.51
EWK Background	4.87	3.02	2.75	1.47	2.34	2.36
Statistics	6.66	6.39	4.98	4.43	4.68	7.05
Total syst	8.75	7.24	6.90	5.95	6.04	6.45

$12 < m_{\mu\mu} < 14\,\text{GeV}$						
$\lvert y_{\mu\mu}\rvert^{\text{min}} - \lvert y_{\mu\mu}\rvert^{\text{max}}$ Variation [%]	0.0-0.4	0.4-0.8	0.8-1.2	1.2-1.6	1.6-2.0	2.0-2.4
Muon resolution (ID)	0.11	0.16	0.04	0.11	0.18	0.24
Muon resolution (MS)	0.13	0.03	0.09	0.21	0.10	0.10
Muon scale	0.11	0.06	0.28	0.14	0.42	0.20
Sagitta bias	0.17	0.08	0.07	0.02	0.15	0.17
Reconstruction eff. (stat.)	0.10	0.09	0.04	0.05	0.13	0.24
Reconstruction eff. (syst.)	1.71	1.43	1.24	1.30	1.46	1.47
Trigger eff. (stat.)	0.96	0.80	0.65	0.54	0.56	1.10
Trigger eff. (syst.)	1.60	1.53	1.35	1.10	1.03	1.34
Isolation eff. (stat.)	0.18	0.20	0.23	0.26	0.30	0.27
Isolation eff. (syst.)	4.35	4.28	4.31	4.20	3.83	3.68
QCD background	4.44	4.86	3.97	4.21	4.35	4.49
EWK Background	0.15	0.17	0.20	0.19	0.15	0.19
Statistics	3.30	3.62	2.58	2.54	2.68	3.82
Total syst	6.72	6.86	6.19	6.22	6.13	6.25

$14 < m_{\mu\mu} < 17\,\text{GeV}$						
$\lvert y_{\mu\mu}\rvert^{\text{min}} - \lvert y_{\mu\mu}\rvert^{\text{max}}$ Variation [%]	0.0-0.4	0.4-0.8	0.8-1.2	1.2-1.6	1.6-2.0	2.0-2.4
Muon resolution (ID)	0.07	0.04	0.10	0.20	0.12	0.20
Muon resolution (MS)	0.04	0.06	0.23	0.14	0.12	0.31
Muon scale	0.06	0.08	0.23	0.42	0.28	0.53
Sagitta bias	0.06	0.06	0.11	0.08	0.10	0.14
Reconstruction eff. (stat.)	0.06	0.04	0.05	0.06	0.09	0.18
Reconstruction eff. (syst.)	1.63	1.34	1.19	1.38	1.43	1.68
Trigger eff. (stat.)	1.12	0.94	0.81	0.67	0.75	1.61
Trigger eff. (syst.)	1.47	1.54	1.47	1.18	1.16	1.41
Isolation eff. (stat.)	0.08	0.09	0.11	0.13	0.16	0.16
Isolation eff. (syst.)	3.51	3.53	3.57	3.31	3.10	3.11
QCD background	3.33	3.40	3.65	3.59	3.97	3.88
EWK Background	0.30	0.27	0.26	0.24	0.30	0.28
Statistics	1.97	2.12	2.12	1.68	1.73	2.64
Total syst	5.44	5.40	5.52	5.28	5.44	5.72

$17 < m_{\mu\mu} < 22\,\text{GeV}$						
$\lvert y_{\mu\mu}\rvert^{\text{min}} - \lvert y_{\mu\mu}\rvert^{\text{max}}$ Variation [%]	0.0-0.4	0.4-0.8	0.8-1.2	1.2-1.6	1.6-2.0	2.0-2.4
Muon resolution (ID)	0.02	0.03	0.03	0.14	0.08	0.10
Muon resolution (MS)	0.00	0.08	0.04	0.04	0.10	0.19
Muon scale	0.13	0.21	0.24	0.28	0.40	0.73
Sagitta bias	0.01	0.02	0.03	0.05	0.15	0.21
Reconstruction eff. (stat.)	0.06	0.04	0.04	0.03	0.12	0.24
Reconstruction eff. (syst.)	1.37	1.32	1.24	1.34	1.65	1.67
Trigger eff. (stat.)	1.33	1.09	0.94	0.76	0.87	1.75
Trigger eff. (syst.)	1.78	1.76	1.67	1.35	1.24	1.42
Isolation eff. (stat.)	0.07	0.06	0.07	0.09	0.10	0.09
Isolation eff. (syst.)	2.78	2.76	2.68	2.54	2.40	2.30
QCD background	3.12	3.46	3.38	3.24	3.49	3.65
EWK Background	0.24	0.23	0.23	0.26	0.28	0.29
Statistics	1.54	1.60	1.43	1.27	1.37	2.20
Total syst	4.94	5.08	4.89	4.62	4.83	5.22

$22 < m_{\mu\mu} < 28\,\text{GeV}$						
$\lvert y_{\mu\mu}\rvert^{\text{min}} - \lvert y_{\mu\mu}\rvert^{\text{max}}$ Variation [%]	0.0-0.4	0.4-0.8	0.8-1.2	1.2-1.6	1.6-2.0	2.0-2.4
Muon resolution (ID)	0.12	0.04	0.04	0.07	0.28	0.34
Muon resolution (MS)	0.07	0.12	0.11	0.14	0.08	0.25
Muon scale	0.10	0.14	0.36	0.36	0.44	0.59
Sagitta bias	0.03	0.05	0.07	0.07	0.16	0.19
Reconstruction eff. (stat.)	0.06	0.03	0.11	0.11	0.13	0.22
Reconstruction eff. (syst.)	1.17	1.26	1.21	1.21	1.25	1.41
Trigger eff. (stat.)	1.53	1.23	1.03	0.89	1.04	1.86
Trigger eff. (syst.)	1.94	1.77	1.61	1.36	1.11	1.03
Isolation eff. (stat.)	0.06	0.07	0.07	0.09	0.10	0.10
Isolation eff. (syst.)	2.20	2.15	2.06	1.96	1.97	1.80
QCD background	3.11	3.23	3.07	2.87	3.12	0.50
EWK Background	0.29	0.29	0.37	0.33	0.37	0.27
Statistics	1.75	1.72	1.50	1.42	1.69	2.00
Total syst	4.70	4.62	4.37	4.06	4.24	3.27

$28 < m_{\mu\mu} < 36\,\text{GeV}$						
$\lvert y_{\mu\mu}\rvert^{\text{min}} - \lvert y_{\mu\mu}\rvert^{\text{max}}$ Variation [%]	0.0-0.4	0.4-0.8	0.8-1.2	1.2-1.6	1.6-2.0	2.0-2.4
Muon resolution (ID)	0.04	0.12	0.06	0.13	0.05	0.67
Muon resolution (MS)	0.01	0.11	0.12	0.10	0.12	0.60
Muon scale	0.16	0.23	0.27	0.35	0.35	0.94
Sagitta bias	0.07	0.10	0.15	0.14	0.11	0.58
Reconstruction eff. (stat.)	0.15	0.15	0.13	0.22	0.15	0.19
Reconstruction eff. (syst.)	1.01	1.17	1.09	0.96	0.93	1.10
Trigger eff. (stat.)	1.26	1.05	0.87	0.81	0.79	1.15
Trigger eff. (syst.)	1.69	1.32	1.24	1.18	0.78	0.83
Isolation eff. (stat.)	0.06	0.06	0.05	0.07	0.07	0.07
Isolation eff. (syst.)	1.88	1.80	1.77	1.72	1.60	1.43
QCD background	3.37	3.01	2.97	2.96	1.53	2.86
EWK Background	0.37	0.33	0.35	0.25	0.36	0.37
Statistics	1.96	1.83	1.69	1.65	1.41	2.30
Total syst	4.54	4.09	3.96	3.88	2.71	3.96

$36 < m_{\mu\mu} < 46\,\text{GeV}$						
$\lvert y_{\mu\mu}\rvert^{\text{min}} - \lvert y_{\mu\mu}\rvert^{\text{max}}$ Variation [%]	0.0-0.4	0.4-0.8	0.8-1.2	1.2-1.6	1.6-2.0	2.0-2.4
Muon resolution (ID)	0.12	0.20	0.42	0.37	0.36	0.93
Muon resolution (MS)	0.13	0.12	0.03	0.32	0.22	1.14
Muon scale	0.15	0.32	0.30	0.51	0.42	0.81
Sagitta bias	0.11	0.28	0.29	0.40	0.39	0.79
Reconstruction eff. (stat.)	0.17	0.19	0.21	0.24	0.58	0.35
Reconstruction eff. (syst.)	1.13	1.45	1.38	1.66	1.71	1.85
Trigger eff. (stat.)	0.78	0.67	0.63	0.55	0.45	0.64
Trigger eff. (syst.)	1.03	1.10	0.85	1.06	0.69	1.31
Isolation eff. (stat.)	0.05	0.04	0.04	0.05	0.05	0.06
Isolation eff. (syst.)	1.65	1.70	1.65	1.67	1.56	1.55
QCD background	3.08	2.87	2.50	2.75	2.73	2.27
EWK Background	0.45	0.53	0.36	0.44	0.26	0.29
Statistics	2.37	2.06	2.02	2.04	2.36	3.90
Total syst	3.93	3.93	3.54	3.93	3.79	4.10

$46 < m_{\mu\mu} < 56\,\text{GeV}$						
$\lvert y_{\mu\mu}\rvert^{\text{min}} - \lvert y_{\mu\mu}\rvert^{\text{max}}$ Variation [%]	0.0-0.4	0.4-0.8	0.8-1.2	1.2-1.6	1.6-2.0	2.0-2.4
Muon resolution (ID)	0.84	0.56	0.77	0.44	0.60	0.51
Muon resolution (MS)	0.45	0.82	0.73	0.52	0.47	0.55
Muon scale	0.93	0.73	0.62	0.80	0.55	0.22
Sagitta bias	1.35	1.00	0.81	0.79	0.94	0.87
Reconstruction eff. (stat.)	0.66	0.42	0.26	0.33	0.48	0.26
Reconstruction eff. (syst.)	2.86	2.18	2.12	2.11	2.13	0.98
Trigger eff. (stat.)	0.51	0.45	0.44	0.35	0.33	0.46
Trigger eff. (syst.)	1.70	1.47	1.17	0.75	1.23	0.92
Isolation eff. (stat.)	0.07	0.04	0.05	0.05	0.05	0.05
Isolation eff. (syst.)	2.22	1.85	1.68	1.76	1.44	1.30
QCD background	2.69	2.52	2.18	2.19	2.24	2.77
EWK Background	0.50	0.54	0.39	0.34	0.54	0.49
Statistics	2.65	2.47	2.38	2.44	2.34	4.06
Total syst	5.27	4.46	4.00	3.87	3.94	3.61

Table A.3 Statistical and systematic uncertainties for the $m_{\mu\mu} - p_T^{\mu\mu}$ double differential cross section measurement (here the first four mass bins are shown).

$7.3 < m_{\mu\mu} < 8.7\,\text{GeV}$										
$p_T^{\mu\mu,\text{min}} - p_T^{\mu\mu,\text{max}}$ Variation [%]	0.0-1.5	1.5-3.0	3.0-5.0	5.0-10.0	10.0-16.0	16.0-22.0	22.0-30.0	30.0-40.0	40.0-55.0	55.0-85.0
Muon resolution (ID)	0.00	0.00	0.00	0.00	0.19	0.27	0.31	1.03	0.12	0.54
Muon resolution (MS)	0.00	0.00	0.00	0.00	0.23	0.17	0.37	0.47	0.35	0.57
Muon scale	0.00	0.00	0.00	0.00	0.39	0.36	0.44	0.43	0.52	2.01
Sagitta bias	0.00	0.00	0.00	0.00	0.04	0.21	0.11	0.28	0.09	0.74
Reconstruction eff. (stat.)	0.00	0.00	0.00	0.00	0.02	0.17	0.18	0.36	0.24	0.48
Reconstruction eff. (syst.)	0.00	0.00	0.00	0.00	1.60	1.48	1.17	1.14	1.08	1.61
Trigger eff. (stat.)	0.00	0.00	0.00	0.00	0.54	0.61	0.44	0.30	0.22	0.32
Trigger eff. (syst.)	0.00	0.00	0.00	0.00	1.24	1.36	0.92	0.61	0.43	0.64
Isolation eff. (stat.)	0.00	0.00	0.00	0.00	0.00	0.00	0.00	0.00	0.00	0.00
Isolation eff. (syst.)	0.00	0.00	0.00	0.00	5.38	3.52	2.62	2.18	1.58	2.47
QCD background	0.00	0.00	0.00	0.00	5.38	3.79	1.40	2.83	0.93	1.65
EWK Background	0.00	0.00	0.00	0.00	2.00	1.47	0.91	0.57	0.35	0.33
Statistics	0.00	0.00	0.00	0.00	4.11	3.70	3.11	5.50	6.17	13.73
Total syst	0.00	0.00	0.00	0.00	8.16	5.80	3.54	4.06	2.32	4.18
$12 < m_{\mu\mu} < 14\,\text{GeV}$										
$p_T^{\mu\mu,\text{min}} - p_T^{\mu\mu,\text{max}}$ Variation [%]	0.0-1.5	1.5-3.0	3.0-5.0	5.0-10.0	10.0-16.0	16.0-22.0	22.0-30.0	30.0-40.0	40.0-55.0	55.0-85.0
Muon resolution (ID)	0.11	0.09	0.14	0.08	0.10	0.31	0.22	0.39	1.08	1.87
Muon resolution (MS)	0.09	0.30	0.05	0.07	0.16	0.42	0.25	0.65	0.47	0.66
Muon scale	0.11	0.32	0.29	0.25	0.34	0.33	0.27	0.61	0.72	0.42
Sagitta bias	0.08	0.03	0.07	0.09	0.05	0.03	0.16	0.11	0.13	0.43
Reconstruction eff. (stat.)	0.03	0.05	0.06	0.04	0.04	0.12	0.30	0.39	0.22	0.45
Reconstruction eff. (syst.)	1.69	1.70	1.72	1.64	1.49	1.42	1.05	1.01	1.39	1.74
Trigger eff. (stat.)	0.66	0.59	0.50	0.51	0.62	0.81	0.64	0.44	0.32	0.22
Trigger eff. (syst.)	1.21	1.18	1.22	1.27	1.46	1.58	1.08	0.74	0.58	0.34
Isolation eff. (stat.)	0.06	0.04	0.00	0.00	0.00	0.00	0.00	0.00	0.00	0.00
Isolation eff. (syst.)	5.66	6.08	6.26	4.97	3.44	2.62	2.34	1.61	1.49	1.33
QCD background	7.25	5.85	6.08	5.12	4.15	2.68	2.06	1.88	2.81	1.23
EWK Background	1.16	0.21	0.16	0.15	0.21	0.16	0.10	0.13	0.15	0.23
Statistics	7.25	4.29	4.68	3.44	2.47	2.43	2.73	2.97	4.59	5.30
Total syst	9.53	8.72	9.00	7.46	5.83	4.43	3.56	3.00	3.81	3.32
$14 < m_{\mu\mu} < 17\,\text{GeV}$										
$p_T^{\mu\mu,\text{min}} - p_T^{\mu\mu,\text{max}}$ Variation [%]	0.0-1.5	1.5-3.0	3.0-5.0	5.0-10.0	10.0-16.0	16.0-22.0	22.0-30.0	30.0-40.0	40.0-55.0	55.0-85.0
Muon resolution (ID)	0.15	0.23	0.06	0.06	0.07	0.12	0.25	0.29	0.53	0.27
Muon resolution (MS)	0.34	0.27	0.05	0.13	0.06	0.17	0.14	0.51	0.46	0.76
Muon scale	0.19	0.20	0.26	0.20	0.34	0.29	0.64	0.04	0.10	0.50
Sagitta bias	0.05	0.05	0.07	0.02	0.07	0.18	0.13	0.17	0.04	0.13
Reconstruction eff. (stat.)	0.06	0.02	0.04	0.01	0.07	0.11	0.40	0.16	0.48	0.37
Reconstruction eff. (syst.)	1.43	1.51	1.53	1.57	1.49	1.39	1.22	0.95	1.04	1.11
Trigger eff. (stat.)	0.84	0.67	0.59	0.57	0.69	0.78	0.61	0.43	0.31	0.23
Trigger eff. (syst.)	1.30	1.31	1.32	1.37	1.57	1.48	1.07	0.74	0.53	0.36
Isolation eff. (stat.)	0.09	0.05	0.00	0.00	0.00	0.00	0.00	0.00	0.00	0.00
Isolation eff. (syst.)	3.84	3.78	3.87	3.84	3.13	2.53	2.10	1.70	1.35	1.07
QCD background	3.97	3.74	3.94	4.08	3.54	2.74	2.81	2.16	3.46	0.44
EWK Background	0.97	0.18	0.18	0.27	0.17	0.07	0.15	0.17	0.20	0.29
Statistics	2.60	2.11	2.29	1.80	2.10	2.25	2.67	3.33	4.47	4.75
Total syst	6.01	5.74	5.92	6.02	5.25	4.34	4.00	3.10	4.00	1.97
$17 < m_{\mu\mu} < 22\,\text{GeV}$										
$p_T^{\mu\mu,\text{min}} - p_T^{\mu\mu,\text{max}}$ Variation [%]	0.0-1.5	1.5-3.0	3.0-5.0	5.0-10.0	10.0-16.0	16.0-22.0	22.0-30.0	30.0-40.0	40.0-55.0	55.0-85.0
Muon resolution (ID)	0.04	0.07	0.06	0.05	0.12	0.04	0.29	0.23	0.74	0.24
Muon resolution (MS)	0.05	0.11	0.12	0.16	0.13	0.17	0.15	0.40	0.81	0.60
Muon scale	0.23	0.26	0.31	0.35	0.32	0.29	0.20	0.83	0.57	0.59
Sagitta bias	0.13	0.02	0.06	0.02	0.04	0.08	0.16	0.40	0.28	0.71
Reconstruction eff. (stat.)	0.08	0.03	0.01	0.03	0.12	0.15	0.18	0.46	0.29	0.20
Reconstruction eff. (syst.)	1.52	1.56	1.48	1.49	1.30	1.17	0.96	1.42	0.95	1.10
Trigger eff. (stat.)	0.95	0.87	0.79	0.76	0.72	0.69	0.58	0.43	0.30	0.23
Trigger eff. (syst.)	1.42	1.48	1.57	1.63	1.48	1.29	1.00	0.76	0.55	0.37
Isolation eff. (stat.)	0.07	0.05	0.00	0.00	0.00	0.00	0.00	0.00	0.00	0.00
Isolation eff. (syst.)	2.86	2.71	2.61	2.68	2.75	2.40	2.03	1.91	1.24	0.87
QCD background	3.14	3.56	3.51	3.59	3.37	2.99	2.18	2.64	0.10	4.85
EWK Background	1.10	0.23	0.19	0.17	0.20	0.22	0.18	0.24	0.27	0.41
Statistics	2.03	1.55	1.38	1.26	1.61	1.91	2.30	2.94	3.07	5.62
Total syst	4.96	5.05	4.95	5.07	4.85	4.29	3.37	3.84	2.15	5.21

Table A.4 Statistical and systematic uncertainties for the $m_{\mu\mu} - p_T^{\mu\mu}$ double differential cross section measurement (here the last four mass bins are shown).

$22 < m_{\mu\mu} < 28\,\text{GeV}$										
$p_T^{\mu\mu,\text{min}} - p_T^{\mu\mu,\text{max}}$ Variation [%]	0.0-1.5	1.5-3.0	3.0-5.0	5.0-10.0	10.0-16.0	16.0-22.0	22.0-30.0	30.0-40.0	40.0-55.0	55.0-85.0
Muon resolution (ID)	0.09	0.12	0.02	0.16	0.14	0.01	0.30	0.33	0.18	0.63
Muon resolution (MS)	0.49	0.11	0.05	0.14	0.11	0.28	0.15	0.41	0.72	0.05
Muon scale	0.24	0.24	0.35	0.21	0.30	0.29	0.31	0.69	0.38	0.23
Sagitta bias	0.15	0.03	0.11	0.05	0.10	0.05	0.09	0.40	0.15	0.15
Reconstruction eff. (stat.)	0.14	0.08	0.05	0.06	0.08	0.23	0.34	0.36	0.22	0.39
Reconstruction eff. (syst.)	1.46	1.49	1.47	1.35	1.11	0.92	0.84	1.15	1.04	1.55
Trigger eff. (stat.)	1.17	1.18	1.14	0.91	0.65	0.57	0.49	0.39	0.30	0.22
Trigger eff. (syst.)	1.93	1.94	1.88	1.58	1.19	1.06	0.91	0.80	0.67	0.38
Isolation eff. (stat.)	0.06	0.04	0.00	0.00	0.00	0.00	0.00	0.00	0.00	0.00
Isolation eff. (syst.)	2.04	1.98	2.08	2.09	2.10	2.14	1.87	1.76	1.33	1.25
QCD background	3.55	3.34	3.40	3.21	3.01	2.84	2.46	0.40	0.03	0.24
EWK Background	1.57	0.30	0.26	0.22	0.25	0.19	0.18	0.46	0.36	0.69
Statistics	2.92	1.85	1.61	1.27	1.61	2.12	2.48	2.68	3.32	4.45
Total syst	5.18	4.76	4.80	4.46	4.09	3.89	3.42	2.57	2.07	2.30
$28 < m_{\mu\mu} < 36\,\text{GeV}$										
$p_T^{\mu\mu,\text{min}} - p_T^{\mu\mu,\text{max}}$ Variation [%]	0.0-1.5	1.5-3.0	3.0-5.0	5.0-10.0	10.0-16.0	16.0-22.0	22.0-30.0	30.0-40.0	40.0-55.0	55.0-85.0
Muon resolution (ID)	0.39	0.30	0.29	0.05	0.16	0.29	0.23	0.38	0.44	0.34
Muon resolution (MS)	0.33	0.04	0.17	0.04	0.28	0.14	0.03	0.39	0.06	0.13
Muon scale	0.30	0.31	0.20	0.27	0.32	0.45	0.39	0.25	0.60	0.81
Sagitta bias	0.06	0.13	0.07	0.03	0.04	0.10	0.23	0.43	0.34	0.18
Reconstruction eff. (stat.)	0.37	0.11	0.12	0.26	0.22	0.28	0.30	0.47	0.44	0.38
Reconstruction eff. (syst.)	1.35	1.03	1.04	1.00	0.96	0.96	1.07	1.49	1.50	0.93
Trigger eff. (stat.)	1.07	1.04	1.00	0.87	0.67	0.54	0.44	0.37	0.29	0.23
Trigger eff. (syst.)	1.52	1.46	1.41	1.25	1.07	0.96	0.94	1.05	0.79	0.49
Isolation eff. (stat.)	0.04	0.02	0.00	0.00	0.00	0.00	0.00	0.00	0.00	0.00
Isolation eff. (syst.)	1.72	1.75	1.73	1.73	1.72	1.82	1.78	1.68	1.54	1.03
QCD background	3.22	3.69	3.32	3.14	3.19	2.53	2.58	2.62	0.14	1.73
EWK Background	1.88	0.37	0.32	0.28	0.34	0.27	0.24	0.33	0.67	1.04
Statistics	3.30	2.23	1.89	1.44	1.80	2.26	2.67	3.20	3.39	4.70
Total syst	4.76	4.62	4.29	4.05	4.01	3.51	3.52	3.74	2.59	2.70
$36 < m_{\mu\mu} < 46\,\text{GeV}$										
$p_T^{\mu\mu,\text{min}} - p_T^{\mu\mu,\text{max}}$ Variation [%]	0.0-1.5	1.5-3.0	3.0-5.0	5.0-10.0	10.0-16.0	16.0-22.0	22.0-30.0	30.0-40.0	40.0-55.0	55.0-85.0
Muon resolution (ID)	1.13	0.61	0.11	0.05	0.46	0.19	0.48	1.07	1.40	0.81
Muon resolution (MS)	1.15	0.15	0.28	0.16	0.44	0.24	0.79	1.26	1.18	0.71
Muon scale	0.40	0.25	0.28	0.29	0.30	0.35	0.33	1.43	0.95	0.37
Sagitta bias	0.18	0.08	0.20	0.09	0.26	0.40	0.59	1.95	1.30	0.55
Reconstruction eff. (stat.)	0.15	0.20	0.37	0.27	0.38	0.56	0.59	1.38	1.26	0.65
Reconstruction eff. (syst.)	1.14	1.14	1.24	1.21	1.34	1.27	1.70	2.88	2.35	1.93
Trigger eff. (stat.)	0.61	0.61	0.59	0.55	0.52	0.50	0.44	0.37	0.29	0.23
Trigger eff. (syst.)	0.62	0.61	0.61	0.64	0.79	1.00	1.37	1.82	1.33	0.91
Isolation eff. (stat.)	0.02	0.02	0.00	0.00	0.00	0.00	0.00	0.00	0.00	0.00
Isolation eff. (syst.)	1.65	1.59	1.70	1.56	1.49	1.52	1.62	2.42	2.02	1.30
QCD background	3.22	3.25	3.26	2.96	2.76	2.84	2.57	1.08	0.52	0.17
EWK Background	2.37	0.45	0.35	0.30	0.28	0.41	0.37	0.70	1.08	1.70
Statistics	4.81	2.82	2.33	1.78	2.19	2.73	2.87	2.66	3.43	4.61
Total syst	4.86	3.98	4.03	3.69	3.65	3.76	4.00	5.45	4.52	3.35
$46 < m_{\mu\mu} < 56\,\text{GeV}$										
$p_T^{\mu\mu,\text{min}} - p_T^{\mu\mu,\text{max}}$ Variation [%]	0.0-1.5	1.5-3.0	3.0-5.0	5.0-10.0	10.0-16.0	16.0-22.0	22.0-30.0	30.0-40.0	40.0-55.0	55.0-85.0
Muon resolution (ID)	0.93	0.76	0.09	0.52	0.17	0.74	1.94	1.24	1.32	1.40
Muon resolution (MS)	0.24	0.73	0.33	0.50	0.19	0.73	1.74	1.30	1.59	1.51
Muon scale	0.37	0.27	0.45	0.57	0.35	0.81	1.85	1.48	1.37	1.95
Sagitta bias	0.30	0.33	0.11	0.32	0.50	1.09	2.59	1.75	1.90	2.35
Reconstruction eff. (stat.)	0.31	0.51	0.43	0.51	0.49	0.89	2.06	1.51	1.67	1.70
Reconstruction eff. (syst.)	1.42	1.11	1.22	1.56	1.86	2.44	4.20	3.02	3.29	3.31
Trigger eff. (stat.)	0.40	0.38	0.38	0.36	0.33	0.33	0.37	0.40	0.34	0.29
Trigger eff. (syst.)	0.38	0.38	0.42	0.52	0.87	1.46	2.35	2.45	2.03	1.86
Isolation eff. (stat.)	0.01	0.01	0.00	0.00	0.00	0.00	0.00	0.00	0.00	0.00
Isolation eff. (syst.)	1.37	1.41	1.45	1.48	1.51	1.86	2.95	2.25	2.22	2.64
QCD background	3.44	3.27	2.87	2.83	2.65	2.15	2.44	1.92	0.27	1.34
EWK Background	2.33	0.48	0.41	0.29	0.33	0.47	0.45	0.56	1.07	2.07
Statistics	5.88	3.90	3.15	2.41	2.71	3.00	2.99	3.47	3.89	5.53
Total syst	4.76	4.00	3.59	3.79	3.79	4.49	7.70	5.92	5.81	6.63

Appendix B

Scale factor uncertainties and toy MC

The scale factors correct the detector performance in simulation to match the behaviour observed in data. The SF values are usually organized in maps that are binned in some relevant kinematic variables, often the transverse momentum and pseudorapidity of the particle. Each bin of the map is affected by a systematic and statistical uncertainty. The latter is due to the finite size of the data and MC samples used to calculate the SF with the tag-and-probe method. This uncertainty is uncorrelated between the different map bins, and to correctly propagate it to the measured observable the toy replica MC approach needs to be implemented. Various toy experiments are generated by varying the scale factor values. Each bin of the map is independently fluctuated around the central value, according to a Gaussian with standard deviation equal to the statistical error affecting the bin

$$w_i^{\mathrm{SF,toy}} \sim \exp\left(0.5(x - w_i^{\mathrm{SF}})^2/(\delta_i^{\mathrm{stat}})^2\right) \tag{B.1}$$

here i indicates the SF map bin. The measurement is then repeated many times, each time with a different SF map replica. The final uncertainty on the measured observable σ is given by the standard deviation of the toy results

$$\delta_\sigma^{\mathrm{SF\,stat}} = \left(\frac{1}{N_{\mathrm{toy}} - 1}\sum_i^{N_{\mathrm{toy}}}(\sigma_i - \langle\sigma\rangle)^2\right)^{1/2} \tag{B.2}$$

where the N_{toy} is the number of random SF maps, σ_i is the outcome toy experiment number i. $\langle\sigma\rangle$ is the mean value of the toy experiments

$$\langle\sigma\rangle = \frac{1}{N}\sum_i^{N_{\mathrm{toy}}}\sigma_i. \tag{B.3}$$

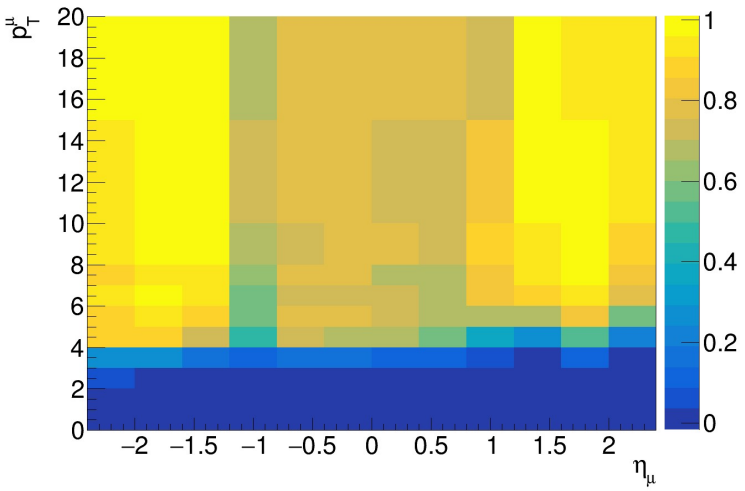

Figure B.1 Trigger efficiency in data as estimated with the tag-and-probe method. This map is used to evaluate the trigger scale factors.

The greater the number of toys the better the uncertainty is estimated. The standard error (SE) on the uncertainty estimated in equation B.2 is given by

$$SE(\delta_\sigma^{\text{SF stat}}) \simeq \sqrt{\frac{2\sigma^4}{N_{\text{toy}}-1}} \cdot \frac{1}{2\sigma} \tag{B.4}$$

and so

$$\delta_\sigma^{\text{SF stat}} / SE(\delta_\sigma^{\text{SF stat}}) \sim \frac{1}{\sqrt{N_{\text{toy}}}}. \tag{B.5}$$

In the low mass Drell-Yan analysis presented in this thesis, the toy MC method is used to propagate the statistical uncertainty of the trigger and isolation scale factors. The number of toy experiments is 500. This allows us to estimate the uncertainty with a relative accuracy of 4%. Figure B.1 show the trigger scale factor map (in particular this cover a low p_T range of the muon kinematics). Toy replicas of this map are produce as explained previously. An example of the distribution of the replica measurements, each one using a fluctuated SF map, is shown in Figure B.2. In particular the outcome of the cross section measurements in a particular mass bin is shown. The standard deviation of this distribution, eq. B.2, represents the estimated uncertainty in this bin. Figure shows the mean value of the toy experiments, B.3, varying the number of toy replicas, in the case of the single differential mass cross section. The first entry in the legend represents the result obtained with the nominal SF values. This agrees with the toy result, as expected by construction. Figure B.4 shows the trigger scale factor uncertainty (the statistical component) as propagated to the invariant

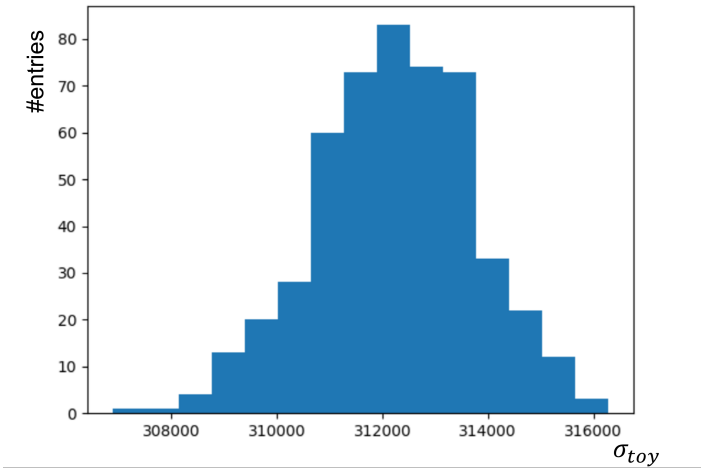

Figure B.2 Distribution of cross section values (for a particular mass bin) from the toy experiments.

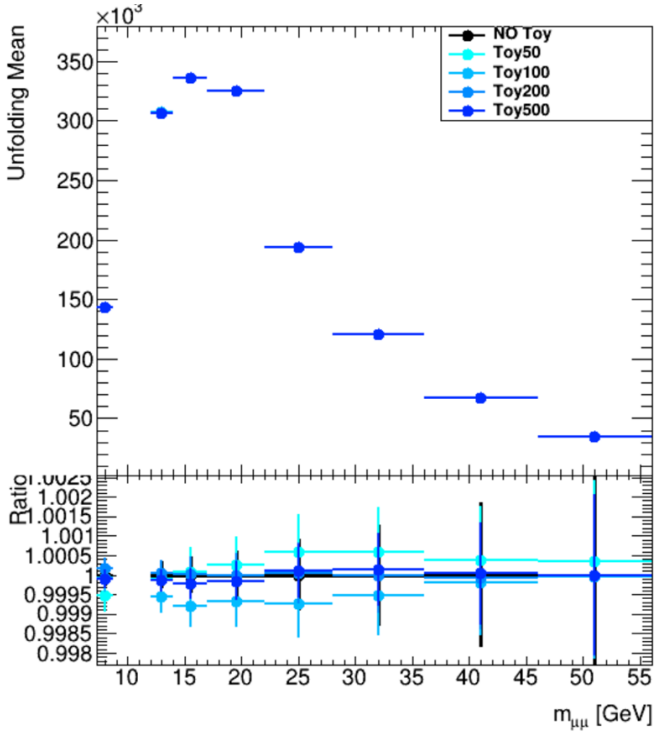

Figure B.3 Mean of the toy experiments outcome. In particular the mass cross section is shown. The first entry represent the nominal result (using the nominal, non-fluctuated SF). This agrees with the toy result, as expected by construction.

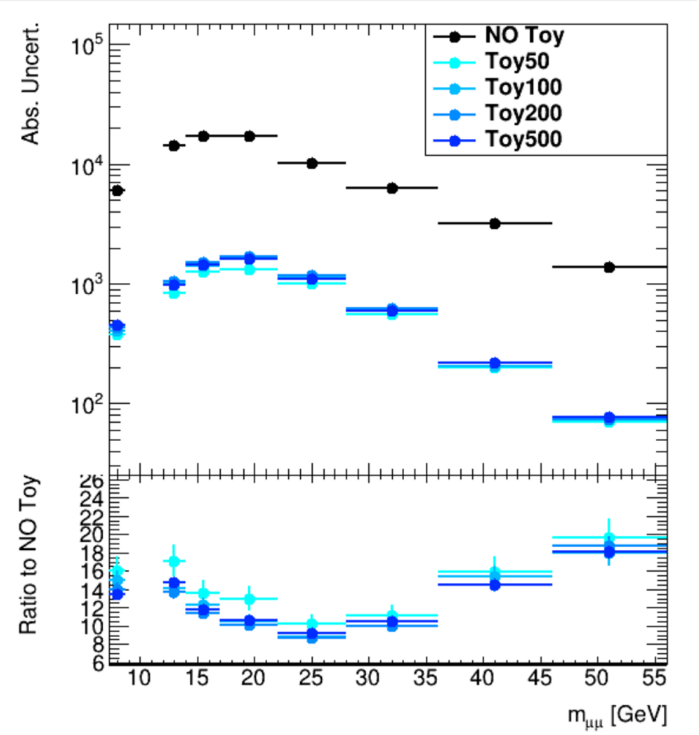

Figure B.4 Trigger SF uncertainty, statistical component as propagated to the cross section result. The first entry in the legend represents the uncertainty in the case the uncertainty between the bins of the SF map are considered fully correlated.

mass cross section result. The black points in the Figure represent the case in which the statistical uncertainty is considered fully correlated between the SF map bins. This is a wrong assumption and would lead to an over estimation of the the related uncertainty.